frontiers | Research Topics

The metabolic pathways of archaea

Edited by
Hannu Myllykallio, Wei Qin and Ivan A. Berg

Published in
Frontiers in Microbiology

ISSN 1664-8714
ISBN 978-2-8325-6642-8
DOI 10.3389/978-2-8325-6642-8

Generative AI statement
Any alternative text (Alt text) provided alongside figures in the articles in this ebook has been generated by Frontiers with the support of artificial intelligence and reasonable efforts have been made to ensure accuracy, including review by the authors wherever possible. If you identify any issues, please contact us.

About Frontiers

Frontiers is more than just an open access publisher of scholarly articles: it is a pioneering approach to the world of academia, radically improving the way scholarly research is managed. The grand vision of Frontiers is a world where all people have an equal opportunity to seek, share and generate knowledge. Frontiers provides immediate and permanent online open access to all its publications, but this alone is not enough to realize our grand goals.

Frontiers journal series

The Frontiers journal series is a multi-tier and interdisciplinary set of open-access, online journals, promising a paradigm shift from the current review, selection and dissemination processes in academic publishing. All Frontiers journals are driven by researchers for researchers; therefore, they constitute a service to the scholarly community. At the same time, the *Frontiers journal series* operates on a revolutionary invention, the tiered publishing system, initially addressing specific communities of scholars, and gradually climbing up to broader public understanding, thus serving the interests of the lay society, too.

Dedication to quality

Each Frontiers article is a landmark of the highest quality, thanks to genuinely collaborative interactions between authors and review editors, who include some of the world's best academicians. Research must be certified by peers before entering a stream of knowledge that may eventually reach the public - and shape society; therefore, Frontiers only applies the most rigorous and unbiased reviews. Frontiers revolutionizes research publishing by freely delivering the most outstanding research, evaluated with no bias from both the academic and social point of view. By applying the most advanced information technologies, Frontiers is catapulting scholarly publishing into a new generation.

What are Frontiers Research Topics?

Frontiers Research Topics are very popular trademarks of the *Frontiers journals series*: they are collections of at least ten articles, all centered on a particular subject. With their unique mix of varied contributions from Original Research to Review Articles, Frontiers Research Topics unify the most influential researchers, the latest key findings and historical advances in a hot research area.

Find out more on how to host your own Frontiers Research Topic or contribute to one as an author by contacting the Frontiers editorial office: frontiersin.org/about/contact

The metabolic pathways of archaea

Topic editors

Hannu Myllykallio — INSERM U1182 Laboratoire d'Optique et Biosciences (LOB), France

Wei Qin — University of Oklahoma, United States

Ivan A. Berg — University of Münster, Germany

Citation

Myllykallio, H., Qin, W., Berg, I. A., eds. (2025). *The metabolic pathways of archaea*. Lausanne: Frontiers Media SA. doi: 10.3389/978-2-8325-6642-8

Table of contents

frontiers | Frontiers in Microbiology

TYPE Editorial
PUBLISHED 08 July 2025
DOI 10.3389/fmicb.2025.1648560

OPEN ACCESS

EDITED AND REVIEWED BY
Sonja-Verena Albers,
University of Freiburg, Germany

*CORRESPONDENCE
Hannu Myllykallio
✉ hannu.myllykallio@polytechnique.edu

RECEIVED 17 June 2025
ACCEPTED 23 June 2025
PUBLISHED 08 July 2025

CITATION
Myllykallio H, Qin W and Berg IA (2025) Editorial: The metabolic pathways of archaea. *Front. Microbiol.* 16:1648560. doi: 10.3389/fmicb.2025.1648560

Editorial: The metabolic pathways of archaea

Hannu Myllykallio[1]*, Wei Qin[2] and Ivan A. Berg[3]

[1]LOB, CNRS, INSERM, École Polytechnique, Institut Polytechnique de Paris, Palaiseau, France, [2]School of Biological Sciences and Institute for Environmental Genomics, The University of Oklahoma, Norman, OK, United States, [3]Institute for Molecular Microbiology and Biotechnology, University of Münster, Münster, Germany

KEYWORDS

archaea, thermoacidophiles, ammonia-oxidizing archaea, genome annotation, mevalonate pathway

Editorial on the Research Topic
The metabolic pathways of archaea

Archaea are fascinating microorganisms that have been recognized as the third domain of life for the past 40 years. Archaea are ubiquitous, inhabiting soil and marine environments, marshlands, engineered systems, and the gastrointestinal tracts of animals, along with some of the most hostile environments on Earth. Although archaea play a crucial role in the global biogeochemical cycle, our understanding of their metabolic diversity is still limited. Research into the metabolic pathways of archaea expands our understanding of the evolution and origins of life and their adaptive and biotechnological potential in diverse environments. The goal of the Research Topic "The Metabolic Pathways of Archaea" was therefore to improve our understanding of their metabolic processes.

Blake et al. studied the growth of the thermoacidophilic archaeon *Metallosphaera sedula* under mixotrophic and heterotrophic conditions. This organism can use a variety of organic and inorganic electron donors to perform oxidative phosphorylation. The authors found that the mixotrophic cells cultured on yeast extract in the presence of soluble iron bifurcated into coccoidal cells of two sizes: smaller cells with an average diameter of 0.6 μm, and larger cells with an average diameter of 1.35 μm. The authors discuss the physiological reasons for this phenotypic heterogeneity.

The metabolomes of the iron- and sulfur-oxidizing thermoacidophilic archaea remain poorly characterized, as the isolation of organic molecules from these microorganisms is challenging. Gfellner et al. developed an improved protocol for their extraction by breaking the tight contacts between cells and the mineral surface, thus facilitating metabolomics analyses of lipophilic compounds using mass spectrometry. This approach led to the identification of molecules implicated in microbial and cell surface interactions through biofilm formation and cell–cell interactions. Moreover, it led to the identification of saturated thiophene-bearing quinones as potential biomarkers for detecting microbial life in extreme environmental conditions in the presence of mineral pyrite (FeS_2).

Karavaeva and Sousa emphasized the importance of curated genomic annotations for understanding the physiology and metabolism of the many recently discovered archaeal lineages at the phylum level. The authors found that despite the extensive use of the different bioinformatics approaches, major portions of archaeal genomes remain unexplored and poorly understood, thus confirming a substantial gap between automatic classification tools and our understanding of archaeal metabolism. This study indicates the need for further functional studies of archaeal genomes by developing more precise computational methods.

Hernández-Magaña and Kraft investigated abundant ammonia-oxidizing archaea (AOA) as a key player in marine nitrogen cycles. They focused particularly on their potential contribution to nitrogen transformation in hypoxic and oxygen-depleted waters. This is of particular interest as AOA produce significant amounts of the potent greenhouse gas nitrous oxide (N_2O) as a byproduct of ammonia oxidation. Using the isotope labeling and oxygen-depleted incubations, the authors tracked the origin and fate of the nitrogen gases N_2O and N_2 during nitric oxide (NO) dismutation. The presented results provide solid evidence for the role of AOA isolates in this reaction. This article builds upon the authors' previous work on a single AOA model species and demonstrates that oxygen production via NO dismutation to support archaeal ammonia oxidation may be widespread across multiple AOA species and lineages, thereby paving the way for future studies to understand the global environmental role of the sources and sinks of N_2O in marine oxygen minimum zones.

Liu et al., collected and analyzed 70 complete genomes to analyze the ability of AOA and bacteria (AOB) to use labile-dissolved organic nitrogen (LDON) compounds as a source of nitrogen. Genomic analyses revealed that urea and cyanates are commonly used by these groups of microbes to satisfy their nitrogen demands, thus potentially influencing the choice of their ecological niches. The authors also performed phylogenetic and bioinformatics analyses that indicated the importance of the lateral gene transfer of the relevant metabolic pathways between bacteria and archaea. The reported results thus indicate that LDON utilization is a common feature among AOA and AOB.

The mevalonate pathway is an essential metabolic pathway that produces two five-carbon building blocks called isopentenyl pyrophosphate (IPP) and dimethylallyl pyrophosphate (DMAPP), which are required for the biosynthesis of a large number of isoprenoids. In archaea, this pathway uses a specific intermediate, *trans*-anhydromevalonate phosphate. The synthesis of this unique intermediate is catalyzed by an archaea-specific phosphomevalonate dehydratase that belongs to the aconitase X family of the aconitase superfamily. Komeyama et al., investigated the poorly understood enzymatic mechanism of the archaeal phosphomevalonate dehydratase by reconstructing the iron–sulfur cluster of phosphomevalonate dehydratase from the hyperthermophilic archaeon *Aeropyrum pernix*. The authors report the biochemical and enzymatic characterization of this enzyme. Detailed biophysical and site-directed mutagenesis studies revealed that three conserved cysteine residues coordinate, surprisingly, a [4Fe-4S] cluster, in contrast to bacterial aconitase X family enzymes harboring a [2Fe-2S] cluster.

Microbial ammonia oxidation is a key and potentially rate-limiting step in the global nitrogen cycle. Melcher et al., reported a number of studies addressing biomass productivity and the physiological response of the model soil AOA species *Nitrososphaera viennensis* to different ammonia and carbon dioxide (CO_2) concentrations under both closed batch and continuous culture conditions. This study revealed quantitative data on the physiology of *N. viennensis* that are important for understanding how biomass production is controlled by AOA. This study also demonstrates that bioprocess technology can be used to understand environmental factors influencing the regulation of archaeal physiology, particularly the interplay between ammonia oxidation and carbon fixation. In addition, since traditional batch cultivation of AOA often yields low biomass, the use of continuous cultivation in chemostats enabled high-biomass production, making previously challenging investigations feasible—such as biofilm composition analysis, purification of key metabolic enzymes, and the subsequent biochemical characterization.

Author contributions

HM: Writing – original draft, Writing – review & editing. WQ: Writing – original draft, Writing – review & editing. IB: Writing – original draft, Writing – review & editing.

Funding

The author(s) declare that financial support was received for the research and/or publication of this article. HM acknowledges funding from the ANR-22-CE12-0042.

Conflict of interest

The authors declare that the research was conducted in the absence of any commercial or financial relationships that could be construed as a potential conflict of interest.

The author(s) declared that they were an editorial board member of Frontiers, at the time of submission. This had no impact on the peer review process and the final decision.

Generative AI statement

The authors declare that no Gen AI was used in the creation of this manuscript.

Publisher's note

frontiers | Frontiers in Microbiology

TYPE Original Research
PUBLISHED 16 February 2023
DOI 10.3389/fmicb.2023.1076342

OPEN ACCESS

EDITED BY
Wei Qin,
University of Oklahoma,
United States

REVIEWED BY
Willm Martens-Habbena,
University of Florida,
United States
Tao Liu,
The University of Queensland,
Australia

*CORRESPONDENCE
Simon K.-M. R. Rittmann, Privatdoz.
✉ simon.rittmann@univie.ac.at

SPECIALTY SECTION
This article was submitted to Biology of Archaea, a section of the journal Frontiers in Microbiology

RECEIVED 21 October 2022
ACCEPTED 17 January 2023
PUBLISHED 16 February 2023

CITATION
Melcher M, Hodgskiss LH, Mardini MA, Schleper C and Rittmann SK-MR (2023) Analysis of biomass productivity and physiology of *Nitrososphaera viennensis* grown in continuous culture.
Front. Microbiol. 14:1076342.
doi: 10.3389/fmicb.2023.1076342

Analysis of biomass productivity and physiology of *Nitrososphaera viennensis* grown in continuous culture

Michael Melcher[1], Logan H. Hodgskiss[1], Mohammad Anas Mardini[1], Christa Schleper[1] and Simon K.-M. R. Rittmann[1,2,3]*

[1]Archaea Biology and Ecogenomics Division, Department of Functional and Evolutionary Ecology, University of Vienna, Vienna, Austria, [2]Arkeon GmbH, Tulln a.d. Donau, Austria, [3]Archaea Physiology & Biotechnology Group, Department of Functional and Evolutionary Ecology, University of Vienna, Vienna, Austria

Microbial ammonia oxidation is the first and usually rate limiting step in nitrification and is therefore an important step in the global nitrogen cycle. Ammonia-oxidizing archaea (AOA) play an important role in nitrification. Here, we report a comprehensive analysis of biomass productivity and the physiological response of *Nitrososphaera viennensis* to different ammonium and carbon dioxide (CO_2) concentrations aiming to understand the interplay between ammonia oxidation and CO_2 fixation of *N. viennensis*. The experiments were performed in closed batch in serum bottles as well as in batch, fed-batch, and continuous culture in bioreactors. A reduced specific growth rate (μ) of *N. viennensis* was observed in batch systems in bioreactors. By increasing CO_2 gassing μ could be increased to rates comparable to that of closed batch systems. Furthermore, at a high dilution rate (*D*) in continuous culture (≥ 0.7 of μ_{max}) the biomass to ammonium yield ($Y_{(X/NH3)}$) increased up to 81.7% compared to batch cultures. In continuous culture, biofilm formation at higher *D* prevented the determination of D_{crit}. Due to changes in $Y_{(X/NH3)}$ and due to biofilm, nitrite concentration becomes an unreliable proxy for the cell number in continuous cultures at *D* towards μ_{max}. Furthermore, the obscure nature of the archaeal ammonia oxidation prevents an interpretation in the context of Monod kinetics and thus the determination of K_S. Our findings indicate that the physiological response of *N. viennensis* might be regulated with different enzymatic make-ups, according to the ammonium catalysis rate. We reveal novel insights into the physiology of *N. viennensis* that are important for biomass production and the biomass yield of AOA. Moreover, our study has implications to the field of archaea biology and microbial ecology by showing that bioprocess technology and quantitative analysis can be applied to decipher environmental factors affecting the physiology and productivity of AOA.

KEYWORDS

archaea, bioreactor, closed batch, batch, fed-batch, chemostat, carbon dioxide, biofilm

Introduction

Nitrification is the oxidation of ammonia (NH_3) to nitrate (NO_3^-) *via* the intermediate nitrite (NO_2^-). Ammonia oxidation is the first and usually rate limiting step in nitrification and is therefore important for the global nitrogen cycle. For over a century ammonia oxidation was thought to be performed by the few bacterial genera *Nitrosomonas*, *Nitrosococcus*, and *Nitrosospira*, until 20 years ago when evidence started to accumulate that archaea might play an important role in this process as well (Venter et al., 2004; Könneke et al., 2005; Treusch et al., 2005). *Nitrosopumilus*

maritimus was the first isolate from a marine aquarium (Könneke et al., 2005; Qin et al., 2017) followed by *Nitrososphaera viennensis* (Tourna et al., 2011; Stieglmeier et al., 2014) from garden soil. Since then multiple isolates and enrichments of ammonia oxidizing archaea (AOA) have been established and characterized to further improve our understanding of these ubiquitously abundant organisms (De La Torre et al., 2008; Blainey et al., 2011; Lehtovirta-Morley et al., 2011, 2016; Lebedeva et al., 2013; Jung et al., 2014; Zhalnina et al., 2014; Santoro et al., 2015; Qin et al., 2017; Sauder et al., 2017, 2018; Abby et al., 2018; Daebeler et al., 2018; Alves et al., 2019; Bayer et al., 2019; Nakagawa et al., 2021). Viable habitats include oceanic crust (Nunoura et al., 2013; Jørgensen and Zhao, 2016; Zhao et al., 2020), deep sea sediments (Francis et al., 2005; Park et al., 2008; Nunoura et al., 2018; Vuillemin et al., 2019; Zhao et al., 2019; Kerou et al., 2021), marine water column (Qin et al., 2017; Bayer et al., 2019; Santoro, 2019), oxygen minimum zones (Bristow et al., 2016), various kinds of soils (Lehtovirta-Morley et al., 2011, 2016; Tourna et al., 2011; Jung et al., 2014; Zhalnina et al., 2014; Alves et al., 2019), fresh water ecosystems (French et al., 2012, 2021; Sauder et al., 2018), waste water treatment plants (Mußmann et al., 2011; Sauder et al., 2017), terrestrial hot springs (De La Torre et al., 2008; Reigstad et al., 2008; Dodsworth et al., 2011; Abby et al., 2018; Daebeler et al., 2018; Luo et al., 2020), and human skin (Probst et al., 2013; Moissl-Eichinger et al., 2017). AOA outnumber their bacterial counterparts, ammonia oxidizing bacteria (AOB), by orders of magnitude in many habitats (Karner et al., 2001; Leininger et al., 2006; Adair and Schwartz, 2008; Nicol et al., 2008; Hollibaugh et al., 2011), but their contribution to the nitrification process is still not completely resolved. While all known AOA and AOB are confined to oxidize NH_3 to NO_2^-, another group of bacteria was recently identified which are able to perform the complete oxidation of NH_3 to NO_3^-, thus given the name Comammox (Daims et al., 2015; van Kessel et al., 2015).

In bacteria, NH_3 is oxidized to hydroxylamine (NH_2OH) by the enzyme ammonia monooxygenase (AMO) (Hollocher et al., 1981; Hyman and Wood, 1985) which is then further oxidized to nitric oxide (NO) by the hydroxylamine oxidoreductase (HAO) (Hooper and Terry, 1979; Caranto and Lancaster, 2017). The enzyme responsible for the oxidation of NO to NO_2^- is still unknown. Unlike the bacterial NH_3 oxidation pathway, the archaeal one is still very poorly characterized. Only the oxidation of NH_3 to NH_2OH is inferred to be catalyzed by an AMO (Vajrala et al., 2013) which is very distantly related to bacterial AMO and all other enzymes of the copper membrane monooxygenase superfamily (CuMMO) (Alves et al., 2018). However, a counterpart to the bacterial HAO is still missing in archaea. Two models are currently proposed, one that mimics the bacterial pathway (Lancaster et al., 2018) and another one where ammonia is oxidized to hydroxylamine which would then be further oxidized to NO_2^- with NO as a co-substrate (Kozlowski et al., 2016). NO would be produced by the reduction of NO_2^- by a proposed nitrite reductase (NirK), which is highly expressed in most AOA, but whose role is still ambiguous as AOA do not perform nitrifier denitrification, unlike AOB (Wrage-Mönnig et al., 2018).

One important factor in niche differentiation of organisms is their substrate affinity, which is described either as reaction rate (v) based on the K_m value (Eq. 1) or as specific growth rate (μ) based on the K_S value (Eq. 2). In a steady state the residual substrate concentration (S) remains constant over time.

$$v = \frac{v_{max} \cdot [S]}{K_m + [S]} \quad \text{Eq. 1}$$

$$\mu = \frac{\mu_{max} \cdot [S]}{K_S + [S]} \quad \text{Eq. 2}$$

AOA are notoriously difficult to grow and produce only very little biomass and therefore most information about AOA is provided in the form of the apparent substrate affinity ($K_{m(app)}$), which is based on whole cell activity measurements of molecular oxygen (O_2) consumption in micro-respiratory chambers (Kits et al., 2017; Jung et al., 2022). Most AOA are considered oligotrophs and their $K_{m(app)}$ values range from 0.1–1 μmol L^{-1} NH_3 and NH_4^+ for marine strains, 1–10 μmol L^{-1} for soil or thermophilic strains to 0.1–10 mmol L^{-1} for the soil clade Nitrosocosmicus. Comammox have $K_{m(app)}$ in the range of 0.1–10 μmol L^{-1} NH_3 and NH_4^+ and are thus considered also oligotrophs while AOB are rather considered eutrophs with $K_{m(app)}$ between 0.1 and 100 mmol L^{-1} NH_3 and NH_4^+ (Jung et al., 2022). In an attempt to measure the K_S value of a fresh water AOA enrichment in batch cultures, no effect of the initial substrate concentration on μ was observed, suggesting that the K_S is much lower than the lowest tested concentration of about 15 μmol L^{-1} NH_4^+ (French et al., 2021). In a chemostat experiment, *N. maritimus* was grown with 150 μmol L^{-1} NH_4^+ and different dilution rates (D) of 0.010, 0.023 and 0.032 h^{-1} (μ_{max} is 0.036 h^{-1}) to investigate the influence of μ on the lipid composition of the organism. NO_2^- concentration only varied by a maximum of 7% (Hurley et al., 2016) but no information was given about the residual substrate concentration.

Nitrososphaera viennensis was isolated from garden soil and grows optimal at 42°C (Stieglmeier et al., 2014) with the addition of pyruvate to scavenge reactive oxygen species (ROS) that are endogenously produced (Kim et al., 2016). Cell concentrations and μ are usually approximated by NO_2^- concentrations, as they have been shown to correlate well (Tourna et al., 2011; Stieglmeier et al., 2014). However, *N. viennensis* produces far too little biomass to measure optical density or dry cell weight.

As the different forms of cultivation systems are rarely discussed in the field of nitrification (except for waste water treatment plants), a short overview of the most commonly used systems shall be given here. In general, systems can be distinguished by the level of which they allow energy and matter to be transferred through them. Closed systems (transfer of energy but not matter) and open systems (transfer of energy and matter) are the extreme cases of reality and the isolated system (no transfer of energy or matter) serves as an important theoretical construct that can only be asymptotically approached by closed systems. Cultivation systems are characterized by the level of transfer of matter and in analogy, closed batch (e.g., serum flask with rubber stopper) is a closed system (Taubner and Rittmann, 2016; Mauerhofer et al., 2019), continuous culture (e.g., bioreactor with gassing and in- and outflow of medium) is an open system, with the openness of the system depending on the transfer rates. Open batch (e.g., Erlenmeyer flask with cotton plug, bioreactor with gassing) and fed-batch (e.g., bioreactor with gassing and inflow of medium) are open system intermediates in between the two extremes (Mauerhofer et al., 2019).

Batch systems are probably the most common cultivation systems used in microbiology, because they are very easy to set up and require little technological infrastructure. Closed batch is usually only used if an atmosphere different from air is required (Mauerhofer et al., 2019; Hanišáková et al., 2022). A major disadvantage of batch systems are the changing substrate concentrations that lead to a very heterogeneous biomass which can complicate analysis. Fed-batch systems consist of a

shorter batch phase followed by a feed phase, where usually a concentrated feed medium is used to increase the biomass concentration but at the same time avoid substrate inhibition. By using an exponential feeding strategy μ can be kept constant and a relatively homogeneous biomass can be produced, as long as no product inhibition or other limitations hamper growth. In continuous culture systems a stable flow of medium is maintained after an initial batch phase and by changing the dilution rate (D, Eq. 3), different steady states can be established by changing the flow rate (Q) or the volume of the culture (V).

$$D = \frac{Q}{V} \quad \text{Eq. 3}$$

A system is usually considered to be in a steady state after five volume exchanges (99.3% of medium exchanged) while all parameters are kept constant. As a result, the produced biomass is very homogeneous, because in a steady state μ is equal to D. Technically speaking, productivities of organisms that are grown in continuous culture are up to tenfold higher compared to batch systems (Herbert et al., 1956), because the system can be stably operated near μ_{max} and downtime for disassembly, sterilization and reassembly of the bioreactor becomes increasingly negligible with longer operation times. Continuous cultures are also excellent tools to study the physiology of microorganisms due to the high level of control and the extended periods of time a steady state can be maintained. A typical application is the determination of the K_S value by varying D and measuring the residual substrate concentration (S), thereby relating μ to S and thus allowing to calculate K_S when assuming Monod kinetics. However, biofilm formation, genetic adaptation or other factors might flaw the determination of such values with extended process runtimes.

In stirred tank reactors gas is usually supplied by a fumigation tube at the bottom of the reactor. The gas transfer rate, which is often a limiting factor for fast growing organisms, can be increased by, e.g., the gassing rate, stirrer speed and operating pressure (Rittmann et al., 2018; Pappenreiter et al., 2019). Due to the low μ_{max} and biomass concentration (X) of AOA the gas transfer rate is not a limiting factor but rather needs to be considered because of the possibility to strip important metabolic intermediates (like NO) from the system.

All cultivated AOA are chemolithoautotrophs and fix CO_2 by a modified version of the hydroxypropionate/hydroxybutyrate cycle (Könneke et al., 2014). For the cultivation of AOA and AOB in bioreactors CO_2 is usually supplied by air and $NaHCO_3$ that is used to titrate the pH and act as C-source (Hurley et al., 2016; Sedlacek et al., 2020; French et al., 2021). Given the fast reaction kinetics of the aqueous carbonate system, the liquid phase in a gassed reactor will tend to be in equilibrium with the supplied gas mix independently of $NaHCO_3$ titration (Wang et al., 2010).

The aim of this study was to investigate the growth behavior of *N. viennensis* in continuous culture systems to develop a biomass production process that would enable biochemical studies of the organism to eventually elucidate the energy metabolism of AOA. Growth conditions were optimized to ensure that only NH_3 acts as a limiting substrate while characterizing process parameters such as K_S, biomass to substrate yield ($Y_{(X/NH3)}$) and the critical dilution rate (D_{crit}) at which the organism will be washed out, for the bioprocess development. To further increase the biomass productivity per reactor volume we also established a continuous culture at a higher substrate concentration.

Materials and methods

Cultivation of *Nitrososphaera viennensis*

Nitrososphaera viennensis was routinely grown as batch cultures in 30 mL Quickstart universal containers (STERILIN) at 42°C in freshwater medium (FWM) (De La Torre et al., 2008; Tourna et al., 2011) amended with non-chelated trace element solution (MTE) (Könneke et al., 2005), 7.5 μmol L^{-1} FeNaEDTA, 2 mmol L^{-1} NH_4Cl, 2 mmol L^{-1} $NaHCO_3$, 1 mmol L^{-1} sodium pyruvate, and 10 mmol L^{-1} HEPES buffer (final pH 7.5). Cultures used as inoculum for bio reactors were inoculated with 1% (v/v), but for regular culture maintenance 1:10^6 (v/v) inoculum was used. Long term storage works best by aliquoting late exponential cultures without any additives and storing them at −70°C. For reviving the culture 5% (v/v) inoculum should be used and a lag phase of 1–2 days need to be expected. Growth was followed by measuring NO_2^- production and NH_3 consumption as described before (Tourna et al., 2011).

Batch

To elucidate the effect of gassing on μ, *N. viennensis* was grown in 2 L all-glass bioreactors (Eppendorf AG, Hamburg, Germany) filled with 1.5 L. The medium composition and conditions were the same as for batch cultures, except for omitting HEPES buffer, and the inoculum was 5% (v/v). The pH was controlled at pH 7.50 (± 0.05 deadband) using 0.5 mol L^{-1} HCl and 0.5 mol L^{-1} NaOH for titration. Dissolved molecular oxygen concentration (dO_2) was measured with optodes (Hamilton) and recorded but not controlled. Cultures were continuously stirred at a rate of 400 rpm and depending on the experiment not gassed (in- and off-gas clamped off), gassed with 2 sL L^{-1} h^{-1} air, gassed with 1 sL L^{-1} h^{-1} air or 1 sL L^{-1} h^{-1} air/N_2 mix (12.6 Vol.-% O_2). In the last batch experiment cultures were gassed with 2 sL L^{-1} h^{-1} air for 63 h, in- and off-gas clamped off and NO-donor 2,2′-(2-Hydroxy-2-nitrosohydrazinylidene) bis-ethanamine (DETA NONOate) added *via* a septum in different concentrations (0.15, 0.6 and 2.4 μmol L^{-1}, sterile H_2O as control). After 25 h one reactor was gassed with 2 sL L^{-1} h^{-1} air, one with 2 sL L^{-1} h^{-1} 99% air 1% CO_2 mixture, one was kept clamped off and one clamped off and 2 mmol L^{-1} $NaHCO_3$ were added *via* a septum.

Chemostat

Chemostat cultures were grown like batch cultures but without $NaHCO_3$ in the medium, instead the cultures were gassed with an air/CO_2 mix of 0.5, 1 or 2 Vol.-% CO_2 with 2 sL L^{-1} h^{-1} gassing rate. The culture volume was 1.5 L but had to be reduced to 1.1 L at the highest D of 0.07 h^{-1} to not exceed the maximum pump rate of 100 mL h^{-1}. The chemostats were started in late exponential growth phase of the batch and due to the relatively low μ of the organism, the minimum volume exchanges for steady states, after every applied or observed change, were reduced from the usual five (99.3% (v/v) exchanged) to three exchanges (95.0% (v/v) exchanged) to speed up the experiment.

Peristaltic pumps were calibrated by weighing feed- and harvest bottles every day to avoid drifting over time and the reactor volume was corrected with every sampling. Deviations of the reactor volume were usually between 1 and 3%. Outliers of BR1 and BR2 at 1,271 h and 1,295 h were caused by technical issues of the outflow pumps

after the reduction of the working volume to 1.1 L, causing a culture volume increase to about 2 L over night and thus a decrease in residual NH_4^+. Outliers of BR2 at 1,343 h and 1,346 h were due to a ripped inflow pump tube, causing a temporary reduction of culture volume to about 0.9 L, a decrease in residual NH_4^+ and a contamination with small rod-shaped microorganisms that was treated with kanamycin.

Washing experiment

To estimate the activity of the biofilm on the reactor walls, the planktonic cells were removed by draining the reactors and refilling them with fresh and sterile medium twice. At a working volume of 1.5 L and 7.5 mL remaining in the bioreactors, a dilution of the planktonic culture of 1:40,000 was achieved (43 nmol L^{-1} NO_2^- remaining). After that the continuous cultures were started again with a D of 0.065 h^{-1}. During the washing procedure, precipitated carbonate detached from the acid/base/medium inlet in BR2 and started to scrape off the biofilm from the reactor wall, thereby creating a constant loss of biofilm to the system.

Fed-batch

The fed-batch experiment started with two batch cultures of 1.1 L gassed with an air/0.5 Vol.-% CO_2 mix of 2 sL L^{-1} h^{-1}. The 400 mL feed medium contained 32 mmol L^{-1} NH_4Cl (10 mmol L^{-1} final), 4.75 mmol L^{-1} pyruvate (2 mmol L^{-1} final), 4.75x MTE (2x final), 4.75x FeNaEDTA (2x final) and was exponentially fed in the beginning to maintain a μ of 0.02 h^{-1}. Due to unreliable pump rates the feed mode was changed to linear with a feed rate of 2 mL h^{-1}. The pyruvate concentration in the feed medium for the continuous culture was increased to 5 mmol L^{-1} to avoid pyruvate depletion which resulted in stagnating cell concentration during the fed-batch.

Sampling

Samples were taken from the bioreactors after the first 2 mL were discarded to remove old culture from the tubing. One micro liter aliquots were pipetted into 1.5 mL reaction tubes and centrifuged at 4°C for 30 min at 23,000 g in a benchtop centrifuge (Eppendorf Centrifuge 5424 R). Supernatant was removed and used directly for NO_2^- and NH_3 measurements while the cell pellets were stored at −20°C for DNA extraction.

Exchanging feed and harvest bottles

Basic FWM was autoclaved in 5 L Schott bottles and supplements were added in a laminar flow hood after room temperature was reached. The GL45 caps with tubing and 0.2 μm filter were always transferred from one bottle to the next, while keeping the inlet and outlet tubes clamped off. After attaching the bottles back to the reactor tubes *via* luer locks, the connections were put into beakers with boiling water for at least 10 min to reduce the contamination risk, before opening the clamps and restarting the pumps. While BR2 was slightly contaminated due to ripped feed pump tubing, BR1 remained clean over the whole run (103 days with 36 bottle exchanges). The contamination of BR2 occurred at 1,343 h and lasted at most up to 2,041 h.

DNA-extraction

DNA from cell pellets was extracted by bead beating using SDS-buffer, phenol/chloroform/isoamylalcohol [25:24:1 (v/v/v), Fisher BioReagents] and chloroform/isoamylalcohol [24:1 (v/v)] as already described elsewhere (Zhou et al., 1996; Griffiths et al., 2000; Rittmann and Holubar, 2014; Abby et al., 2018).

PCR

DNA samples were checked for bacterial contamination using the 16S rRNA primers Eubac27F 5′-AGA GTT TGA TCC TGG CTC AG-3′ and Eubac1492R 5′-GGT TAC CTT GTT ACG ACT T-3′. PCR conditions were 95°C for 5 min as initialization, followed by 35 cycles of 30 s denaturing at 94°C, 30 s primer annealing at 55°C, 2 min elongation at 72°C, and finishing with final elongation at 72°C for 10 min. Reactions were done in 25 μL containing 2 μL sample, 0.15 μL GoTaq Polymerase, 5 μL 5x Flexi Buffer, 2 μL $MgCl_2$ 25 mmol L^{-1}, 0.5 μL dNTP 10 mmol L^{-1}, 0.25 μL BSA 20 mg mL^{-1}, 1.25 μL Primer F 10 μmol L^{-1}, 1.25 μL Primer R 10 μmol L^{-1}, 12.6 μL nuclease free water.

Quantitative PCR

The archaeal 16S rRNA gene was quantified to estimate the cell number using the primers Arch931F 5′-AGG AAT TGG CGG GGG AGC A-3′ (Jackson et al., 2001) and Arch1100R 5‘-BGG GTC TCG CTC GTT RCC-3′ (Øvreås et al., 1997) in triplicate 20 μL reactions containing 10 μL qPCR Master Mix 2x (Luna Universal qPCR Master Mix, NEW ENGLAND BioLabs Inc.), 1 μmol L^{-1} of each primer, nuclease free water and 4 μL DNA sample (diluted to have approximately 10 ng per reaction) or standard. Reactions were performed in a qPCR (BIO-RAD CFX Connect Real-Time System) with the following conditions: initialization at 95°C for 2 min, 40 cycles of 30 s denaturing at 95°C, 30 s joint annealing-extension at 60°C, and extension with fluorescence measurement at 60°C for 30 s. The specificity of qPCR products was confirmed by melting curve analysis. Standards were prepared by amplifying the 16S rRNA gene of *N. viennensis* under the conditions as described above in a 50 μL reaction using 2 μL DNA template and the archaeal 16S rRNA primers A109F 5‘-ACK GCT CAG TAA CAC GT-3′ (Großkopf et al., 1998) and A1492R GYY ACC TTG TTA CGA CTT-3′ (Nicol et al., 2008). PCR product was cleaned up using the Machery-Nagel DNA cleanup kit and DNA concentration was measured with Qubit™ dsDNA BR Assay Kit (Thermo Fisher Scientific) before preparing serial dilutions with nuclease free water. The standard curve had an efficiency of 93.38% and an R^2 of 0.999.

Extrapolating cell number and biomass from DNA concentration

DNA concentration of extracted samples was measured with Qubit™ dsDNA HS Assay Kit (Thermo Fisher Scientific) and several samples with concentrations ranging from 3.58 to

35.5 ng μL^{-1} were quantified by qPCR as described above. Using a linear regression model the mass of DNA was correlated to the cell number, assuming that each cell contained a single copy of the 16S rRNA gene. Using this model one copy of 16S rRNA correlates to 3.42 fg which is 25.6% more than the calculated mass of a *N. viennensis* genome of 2.72 fg (2.52 Mbp genome size). Assuming a cell diameter of 0.75 µm (0.6–0.9 µm cell diameter) and a density of 1.1 g cm^{-3} a theoretical *N. viennensis* cell would weight $2.43 \cdot 10^{-13}$ g or 243 fg.

Harvesting of biomass

The outflow of the continuous cultures was collected in sterile 5 L bottles and usually harvested once a week by concentrating the biomass using a tubular centrifuge (CEPA) at 40,000 rpm and subsequent centrifugation of the cell concentrate in a bucket centrifuge (Thermo SCIENTIFIC Sorvall LYNX 4000 Centrifuge) at 4°C, 24,470 g for 40 min. The pellets were resuspended in a small amount of supernatant and split up into pre-weighted 2 mL reaction tubes which were centrifuged in a benchtop centrifuge (Eppendorf Centrifuge 5424 R) at 4°C for 30 min at 23,000 g. Supernatant was removed, reaction tubes weighed and stored at −70°C.

Equations

Active biofilm estimation

To estimate the amount of biofilm biomass contributing to nitrification, biofilm BR1 was modeled as a continuously stirred tank reactor (CSTR) at the final time point taken. BR1 was chosen based off of its relative stability compared to BR2. The change of substrate with relation to time can be described using the following equation:

$$V\frac{dS}{dt} = QS_i - QS + r_f A_f L_f + r_S V \qquad \text{Eq. 4}$$

Where V is the volume of the reactor, Q is the flow rate, S_i is the concentration of ammonium in the inflow, S is the concentration of ammonium in the outflow, r_s represents the reaction of ammonium to nitrite by the planktonic cells, r_f represents the reaction of ammonium to nitrite by biofilm cells, A_f is the surface area of the reactor covered by biofilm, and L_f is the height of the biofilm. The volume of the biofilm is assumed to be negligible when compared to the planktonic volume (and therefore total volume) of the reactor system.

The reaction of ammonium to nitrite (mmol L^{-1} h^{-1}) can be represented by:

$$r = \frac{-1}{Y_{XS}}\mu X \qquad \text{Eq. 5}$$

Where $Y_{(X/NH3)}$ represents the yield of *N. viennensis* biomass from ammonia oxidation (mg biomass/mmol ammonium), µ is the specific growth rate (h^{-1}), and X represents the respective biomass concentration (mg/L; planktonic or biofilm).

Substituting the reaction rate into the substrate mass balance:

$$V\frac{dS}{dt} = Q(S_i - S) + \left(\frac{-1}{Y_{XS}}\mu_f X_f A_f L_f\right) + \left(\frac{-1}{Y_{XS}}\mu XV\right) \qquad \text{Eq. 6}$$

Assuming steady state ($dS/dt = 0$), a μ that is the same for both biofilm and planktonic cells ($\mu_f = \mu$), and the volume of the biofilm to be surface area multiplied by height ($A_f L_f = V_f$), Equation 6 simplifies to:

$$0 = Q(S_i - S) + \left(\frac{-1}{Y_{XS}}\mu X_f V_f\right) + \left(\frac{-1}{Y_{XS}}\mu XV\right) \qquad \text{Eq. 7}$$

The exact volume of the biofilm is unknown due to the unknown height. Assuming a homogenous biofilm and equilibrium between the biofilm and planktonic biomass, the total amount of biomass (mg) contributing to nitrification from the biofilm can be determined by solving Equation 7 for $X_f V_f$:

$$X_f V_f = \frac{-Y_{XS}}{\mu}Q(S - S_i) - XV \qquad \text{Eq. 8}$$

The right side of the equation is now represented by known variables when using BR1: $Y_{(X/NH3)} = 15$ mg biomass/mmol ammonium (calculated from batch cultures (assumption for calculations)); $\mu = 0.048\ h^{-1}$; $Q = 0.0975\ L\ h^{-1}$ (set parameter); $S_i = 2$ mmol ammonium/L (set parameter); $S = 0.3295$ mmol ammonium/L (measured in effluent); $X = 13.3$ mg biomass/L (measured in effluent); $V = 1.5$ L (set parameter).

Results

Effect of gassing rate and in-gas flow composition in batch and closed batch experiments

Initial experiments of *N. viennensis* grown as batch cultures in 2 L bioreactors showed that gassing with air had a detrimental effect on µ even at low gassing rates such as 2 sL L^{-1} h^{-1} (0.0276 h^{-1}) when compared to cultures without gassing (0.0445 h^{-1}, Supplementary Figure S1). In non-gassed cultures dO_2 decreased to about 50% of its initial concentration. Therefore, growth under decreased gassing rate and reduced dO_2 was tested. As shown in Supplementary Figure S2 reducing the gassing rate to 1 sL L^{-1} h^{-1} did not increase µ (0.0267 h^{-1}) and reducing dO_2 to about 60% did decrease µ to 0.0205 h^{-1}, which contradicted the results of the first experiment. Due to the hypothesized importance of NO for the archaeal ammonia oxidation pathway (Kozlowski et al., 2016) we decided to test if the reduction of µ is a result of stripping NO from the system by gassing. As shown in Figure 1, addition of the NO-donor 2,2′-(2-Hydroxy-2-nitrosohydrazinylidene) bis-ethanamine (DETA NONOate) to early exponential phase cultures (300 µmol L^{-1} NO_2^- produced) did not show any effect on recovering µ. However, adding 1 Vol.-% CO_2 to the in-gas or 2 mmol L^{-1} $NaHCO_3$ to the culture medium, and keeping the bioreactor closed did increase µ from 0.0259 ± 0.0002 h^{-1} to 0.0338 h^{-1} and 0.0395 h^{-1}, respectively. Gassing with air or keeping the reactor closed did not change µ (0.0260 h^{-1}) or even reduced it (0.0234 h^{-1}), respectively. Hence, the above results showed that the organism was carbon limited likely due to the stripping of CO_2 from the supplied gassing.

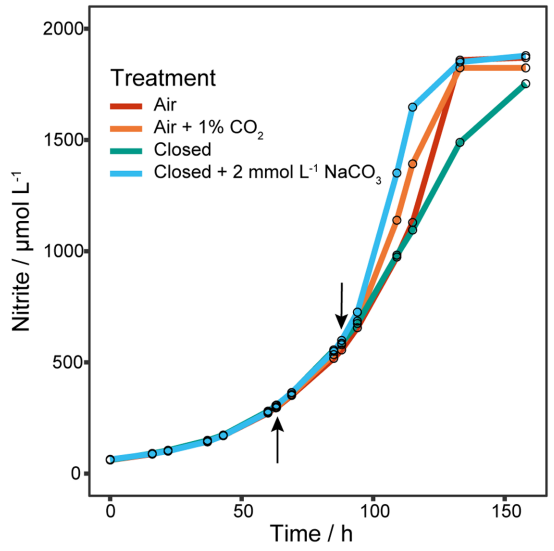

FIGURE 1
Effect of NO-donor and CO_2 on µ. Four 1.5 L batch cultures grown in 2 L bioreactors gassed with 2 sL L^{-1} h^{-1} air (n=1). The upward arrow indicates the addition of different amounts of the NO-donor 2,2′-(2-Hydroxy-2-nitrosohydrazinylidene)bis-ethanamine (DETA NONOate) to early exponential cultures, after which gassing was stopped and reactors clamped off to prevent gas exchange. As no effect on the nitrite production was observed, cultures were tested for CO_2 limitation indicated by the downward arrow. One culture was gassed again with air, one with air plus 1% CO_2, one was kept closed and one was kept closed but with the addition of 2mmol L^{-1} $NaHCO_3$. Addition of CO_2 to the in-gas or $NaHCO_3$ to the culture medium increased µ, while gassing with air or keeping the reactor closed did not change or reduce µ, respectively.

To determine μ_{max} in closed batch systems, *N. viennensis* was grown in serum flasks with 0.5 Vol.-% CO_2 and different dO_2 concentrations (Supplementary Figure S3). A slight increase of µ was observed with decreasing dO_2 from 0.0484 ± 0.0004 h^{-1} to 0.0508 ± 0.0004 h^{-1}at 21 Vol.-% to 5 Vol.-% O_2, respectively (224.7 to 53.5 µmol L^{-1} dO_2 considering a pressure of 1,106 hPa and an incubation temperature of 42°C). Due to the minor effect of dO_2 on µ, 21 Vol.-% O_2 was used to gas the following cultures and a μ_{max} of 0.0484 h^{-1} is therefore considered. Moreover, by using an inoculum of 1:10^6 (v/v), µ was increased from 0.024 h^{-1} (Stieglmeier et al., 2014) to 0.048 h^{-1} (data not shown).

Continuous culture experiments at high dilution rates

To determine the K_S and D_{crit} of *N. viennensis* eight different D (0.035, 0.038, 0.042, 0.046, 0.050, 0.060, 0.065, and 0.070 h^{-1}) were applied in two bioreactors. As shown in Figure 2, at D 0.035 h^{-1} S stabilized at an unexpectedly high level around 750 µmol L^{-1} NH_4^+ and increasing D further only had a marginal effect on S. In section A (D 0.035 to 0.050 h^{-1}, 382 to 990 h) S stabilized at 801.9 ± 43.2 µmol L^{-1} NH_4^+. Activity of both cultures spontaneously increased 58 h after D was set to 0.050 h^{-1} (94.5% of medium exchanged) and S decreased to 575.2 ± 21.2 µmol L^{-1} NH_4^+. The increase of D to 0.060 h^{-1} was responsible for the abrupt increase of S to 690.1 ± 29.9 µmol L^{-1} NH_4^+ which gradually decreased, despite negative outliers, to 456.2 ± 7.9 µmol L^{-1} NH_4^+. Overall S stabilized at 541.6 ± 68.6 µmol L^{-1} NH_4^+ in section B (D = 0.050 to 0.070 h^{-1}, 1,032 to 1,654 h) and negative outliers at 1,271, 1,295, 1,343, and 1,346 h were due to technical issues (see Materials and Methods). Another spontaneous increase of activity occurred in both cultures 11 days after D was set to 0.070 h^{-1} (18 working volume exchanges), which first led to a complete consumption of NH_4^+ in both cultures but subsequently two different S stabilized. As shown in section C of Figure 2 (D = 0.070 and 0.065 h^{-1}, 1,796 to 2,035 h), S of the BR1 culture stabilized at 262.2 ± 19.9 µmol L^{-1} NH_4^+ and at 7.4 ± 11.1 µmol L^{-1} NH_4^+ for the BR2 culture. From section C to section D (D 0.065 h^{-1}, 2,062 to 2,402 h) the reactor volume was increased to minimize the effect of sampling larger volumes which caused S of BR1 to increase from 258 to 356 µmol L^{-1} NH_4^+ (ratio of concentrations matches the ratio of volumes). S of BR2 gradually increased from 4.1 µmol L^{-1} NH_4^+ to 375.0 µmol L^{-1} NH_4^+ probably as a result of the disturbances caused by the repeated sampling process.

The cell concentrations declined gradually with D from $7.67{\cdot}10^7$ ± $2.11{\cdot}10^7$ cells mL^{-1} at D = 0.035 h^{-1} to $4.36{\cdot}10^7$ ± $2.18{\cdot}10^6$ cells mL^{-1} at D = 0.046 h^{-1} (549 to 932 h). µ calculated from measured cell concentrations as shown in Supplementary Figure S4 gradually increased with increasing D from 0.0362 ± 0.0011 h^{-1} at D = 0.035 h^{-1} to 0.0437 ± 0.0007 h^{-1} at D = 0.046 and after the activity increase at D 0.050 h^{-1} µ increased further to 0.0505 ± 0.0003 h^{-1} (1,107 h). Cell concentrations remained surprisingly stable from D = 0.050 to 0.060 h^{-1} at $4.13{\cdot}10^7$ ± $5.30{\cdot}10^6$ cells mL^{-1} (1,032 to 1,419 h) and declined to $3.08{\cdot}10^7$ ± $7.06{\cdot}10^5$ cells mL^{-1} at D = 0.070 h^{-1} (1,654 h) before the second activity increase, after which cell concentrations started to alternate in both reactors. Average NH_4^+ and cell concentrations of sections A to D are shown in Supplementary Figure S5. K_S and D_{crit} could not be determined due to the unusual growth behavior and biofilm formation, respectively.

Ammonia oxidizing activity of biofilm

Over the course of the experiment a biofilm had formed gradually on the reactor walls. To estimate its contribution to the gross activity, the medium was aseptically removed from the reactors, the reactors were washed once with sterile medium and then refilled with fresh medium to restart the continuous culture at D = 0.065 h^{-1}. Only a residual NO_2^- concentration of 43 nmol L^{-1} should have been present at the restart of the continuous culture but instead a starting NO_2^- concentration of about 100 µmol L^{-1} was measured in both reactors. As shown in Figure 3 within 2 days the same steady state as before the washing step was recovered in both reactors.

Almost no change in planktonic cell concentration of BR1 was observed after the washing step and the concentration remained stable afterwards between $4.91{\cdot}10^7$ and $6.19{\cdot}10^7$ cells mL^{-1}. In BR2 the cell concentration increased after the washing step from $3.31{\cdot}10^7$ ± $1.09{\cdot}10^6$ to $1.43{\cdot}10^8$ ± $2.35{\cdot}10^7$ cells mL^{-1} and increased further to $2.43{\cdot}10^8$ ± $6.40{\cdot}10^7$ cells mL^{-1} within the next 3 h as a result of precipitate being washed off of the inlet and subsequently scraping off biofilm from the reactor wall. The cell concentration remained rather stable from there for 36 h up to a concentration of $2.80{\cdot}10^8$ ± $6.88{\cdot}10^7$ cells mL^{-1} and decreased to $1.69{\cdot}10^8$ ± $1.73{\cdot}10^7$ cells mL^{-1} within the following 27 h.

Thus the biofilm was not only highly active but also contributed considerably to the planktonic cell concentration in the bioreactors by seeding cells. Even though BR2 lost substantial biofilm biomass it still had comparable NH_3 oxidizing activity to BR1 in which the biofilm was retained.

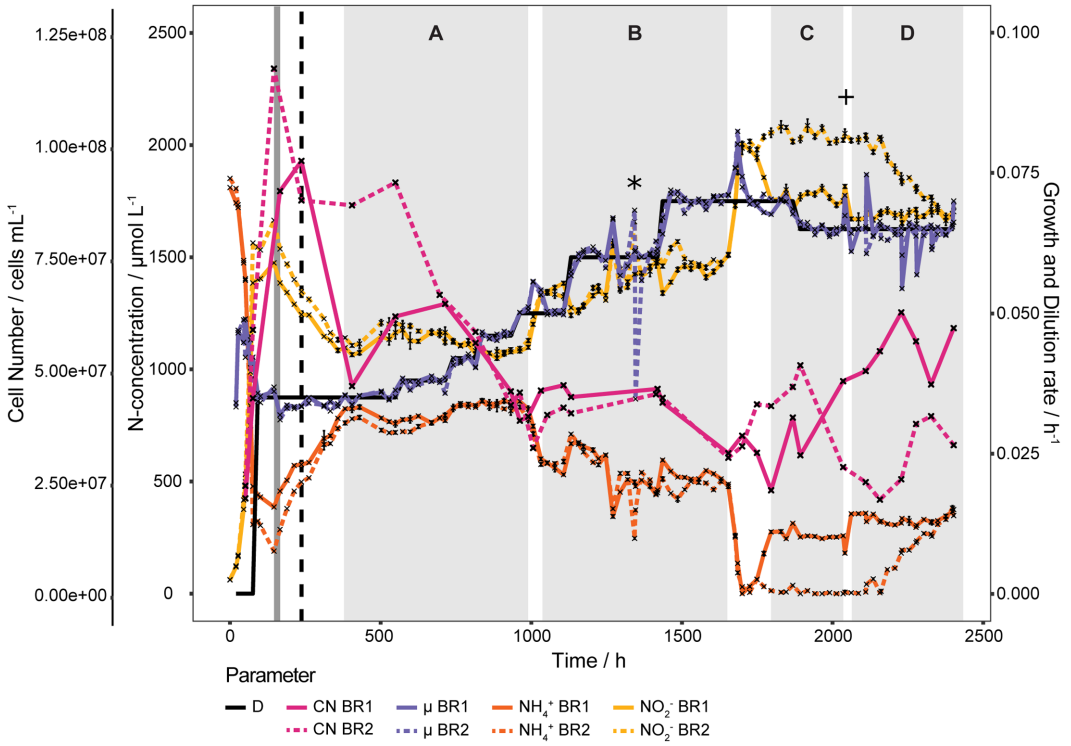

FIGURE 2
Continuous culture of *N. viennensis* at high *D*. Two continuous cultures with *D* ranging from 0.035h^{-1} to 0.070h^{-1} and the development of cell number (CN), NO_2^- derived µ, NH_4^+ and NO_2^- concentrations of the cultures grown in the corresponding reactors BR1 and BR2. Cultures were gassed with 1% CO_2 enriched air at 2 sL L^{-1} h^{-1} gassing rate, except for the period marked in dark grey where the gassing rate was temporarily increased to 10 sL L^{-1} h^{-1}. The black dashed line indicates the increase to 2% CO_2 in the in-gas. Sections A to D signify regions where NH_4^+ concentrations stabilized, even though *D* was increased. Spontaneous increases of activity happened between section A and B and section B and C without external influences. Increase of NH_4^+ of BR1 from section C to D was due to an increase of reactor working volume and the increase of NH_4^+ of BR2 in section D was probably induced by taking larger sampling volumes. The asterisk indicates the point of contamination of BR2 due to a ripped pump tube and the plus sign indicates the point at which the contamination was no longer detectable by PCR of the bacterial 16S rRNA gene. NH_4^+ and NO_2^- curves show mean values of technical triplicates and error bars represent the standard deviation of the mean. Points with small standard deviation may not have visivle error bars.

Estimation of active biofilm biomass in BR1

Based on a substrate mass balance and assuming a steady state at time point 2,402 h (Figure 2), 30.9 mg of *N. viennensis* biomass is contributing to nitrification in the biofilm (see Materials and Methods). This represents approximately 1.55 times as much biomass as would be found in the planktonic phase of the reactor. While this number represents the amount of actively nitrifying biomass, it is plausible that the biofilm itself is much more in terms of weight that could be represented by extrapolymer substances (EPS), precipitated bicarbonate, and cells that are potentially inactive due to substrate limitation. While these calculations demonstrate a significant portion (over half) of the nitrification activity is coming from the biofilm, this number could change if it is determined that certain growth parameters, such as the $Y_{(X/NH3)}$ and µ, are differing between the planktonic and biofilm phases. However, within the presented model, the biofilm is affecting the amount of NH_4^+ oxidized to NO_2^- and could help explain the NO_2^- productivity within these bioreactors. A large portion of activity from the biofilm is also expected due to NO_2^- being produced even though *D* is higher than the predicted μ_{max}. The combined ammonium oxidation of planktonic cells and biofilm, and planktonic cells being seeded from the biofilm, could explain the absence of an expected cellular washout of the reactor.

Estimation of biofilm biomass in BR2

An estimate for the total biofilm biomass was obtained from BR2 under the assumption that all biofilm from the bioreactor wall had been scraped off during the biofilm activity experiment. By summing up all cells washed out and subtracting the cells produced during the time of the experiment, the biofilm biomass at the start can be estimated. To assess the amount of cells produced, the total amount of substrate consumed was calculated and then multiplied by the estimated $Y_{(X/NH3)}$. Total cells washed out was calculated as the area under the curve from 2,402 h to 2,471 h (Figure 3) after converting time to volume using the set flow rate. Total ammonia consumed was calculated by subtracting residual ammonia (area under the curve) from total supplied ammonia during the given time span. Using a $Y_{(X/NH3)}$ of 15 mg mmol^{-1} NH_4^+ and an estimated mass per cell of 2.3·10^{-13} g cell^{-1} (see Materials and Methods) the amount of cells produced during the time span was calculated to be 167.77 mg. The mass of total cells washed out was calculated to be 378.16 mg. Subtracting produced biomass from total washed out biomass gives an estimate biofilm mass of 210.49 mg. Assuming the amount of biofilm in BR2 from the washout experiment to be representative of the amount of biofilm in BR1 at the end of the chemostat experiment (Figure 2), this data can be combined with the active biofilm estimation (30.9 mg, BR1) calculation to determine the percentage of active biomass in the biofilm. According to these estimations and under the assumption that BR1 and BR2 produced

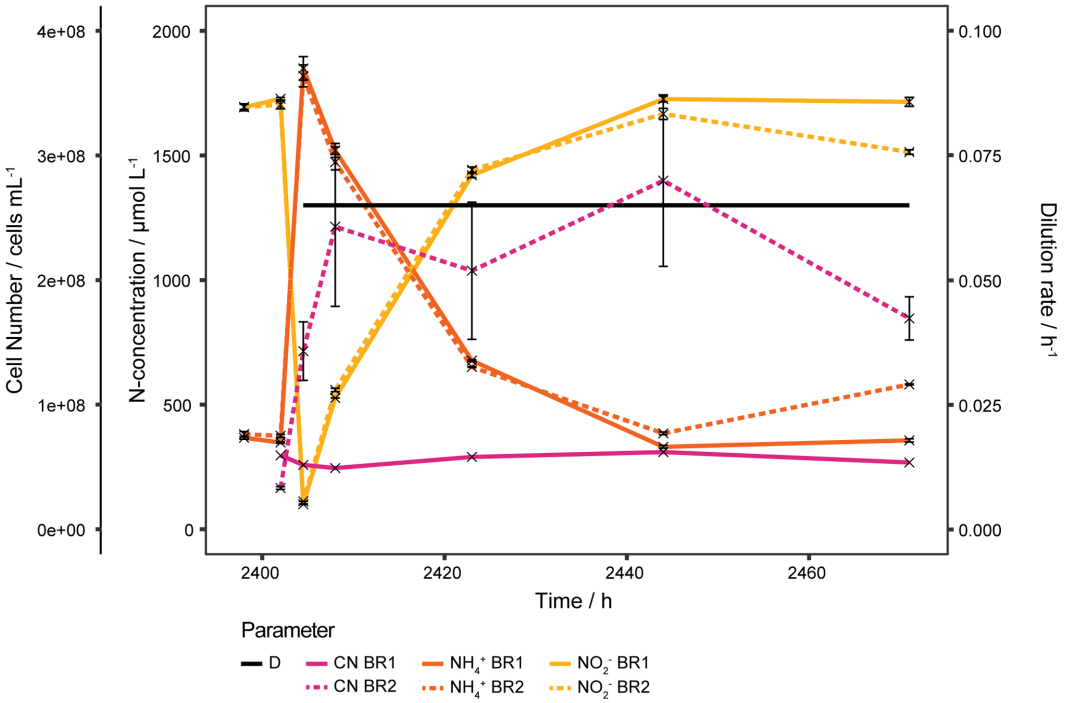

FIGURE 3
Ammonia oxidizing activity of biofilm. Bioreactors of continuous cultures grown at high *D* were washed, refilled with sterile medium and operated at *D* 0.065 h^{-1} to estimate the activity of the biofilm which had formed on the reactor walls due to the prolonged cultivation time. NH_3 oxidation started right away and within 2 days the same steady state as before the washing step was recovered in both reactors. Cell number in BR1 was almost unaffected by the washing step, indicating that most planktonic cells were seeded by the biofilm. The steep increase of the cell number in BR2 was due to biomass being scraped off from the reactor wall by precipitate that had formed at the inlet and was washed off during the washing step. Both reactors exhibited very comparable NH_3 oxidizing activities despite the fact that BR2 lost a considerable amount of its biofilm biomass as it was washed out with the effluent. NH_4^+, NO_2^-, and cell number of BR2 curves show mean values of technical triplicates and error bars represent the standard deviation of the mean. Points with small standard deviation may not have visible error bars.

similar amounts of biofilm, only about 14.67% of the cells in the biofilm would have been active.

This percentage should be taken as a conservative estimate as it would be lower if not all biofilm was removed from the reactor during this time period. Biofilm that was observed during takedown or BR2 would indicate this to be a possibility barring the production of new biofilm during the washout experiment.

Continuous culture experiments at low dilution rates

To get the full picture of how *D* effects *S*, a new continuous culture run was set up with 0.5 Vol.-% CO_2 enriched air to reduce the precipitation of CO_3^{2-} both at the inlets and in the medium. Initial *D* was set at 0.01 h^{-1} and all substrate was consumed. As shown in Figure 4 an increase in *D* to 0.020 h^{-1} resulted in a temporary increase of *S* to 11 and 44 µmol L^{-1} for BR3 and BR4 respectively, after which *S* returned to 0 µmol L^{-1}. Then CO_2 was increased to 2 Vol.-% at 96 h after *D* was increased, which surprisingly induced an increase of *S* in BR3 with a 55.5 h delay. *S* in BR3 slowly started to increase from 17 to finally 192 µmol L^{-1} whereas in BR4 *S* concentrations increased up to 95 µmol L^{-1} but only 216 h after the CO_2 was increased. The reduction of CO_2 to 0.5 Vol.-% caused an immediate consumption of all NH_4^+ in both reactors (553.5 to 577 h). Increasing *D* to 0.030 h^{-1} increased *S* in both reactors, but at this time BR4 showed higher *S* than BR3. A further increase of *D* to 0.040 h^{-1} induced an extended increase of *S* similar to the behavior seen at *D* 0.035 h^{-1}.

Cell concentrations remained rather stable over the whole run from *D* of 0.010 h^{-1} to 0.030 h^{-1} at $6.94 \cdot 10^7 \pm 1.02 \cdot 10^7$ cells mL^{-1}. Only one strong increase from $7.24 \cdot 10^7$ cells mL^{-1} to $1.23 \cdot 10^8$ cells mL^{-1} was observed in BR4 directly after decreasing the CO_2 concentration of the in-gas from 2 Vol.-% to 0.5 Vol.-%. However, the cell concentration decreased again to $7.77 \cdot 10^7$ cells mL^{-1} before increasing *D* from 0.020 h^{-1} to 0.030 h^{-1} (Figure 4). The amount of CO_2 in the gas phase seems to affect *S*. Depending on the CO_2 concentration of 0.5 Vol.-% and 2 Vol.-% in the gas phase *S* starts to accumulate at *D* of 0.030 h^{-1} or 0.020 h^{-1}, respectively.

Continuous cultures at high ammonia concentrations

Before starting a continuous culture with higher substrate concentrations, the inhibitory effect of NO_2^- was determined by batch cultures in 30 mL polystyrene tubes with varying NO_2^- starting concentrations of 0 to 19 mmol L^{-1} and 1 mmol L^{-1} NH_4^+. NO_2^- showed only a weak linear inhibitory effect on µ with 0.0342 to 0.0411 h^{-1} for 19 and 0 mmol L^{-1} NO_2^- starting concentrations, respectively (Supplementary Figure S6).

The bioreactor experiment commenced with a 2 mmol L^{-1} NH_4^+ batch, followed by a fed-batch to increase NO_2^- up to 10 mmol L^{-1} and then switching into continuous mode to see the effect of *D* on cell number and *S*. The NH_4^+ to pyruvate ratio was changed in the feed from 2 to 5 to avoid

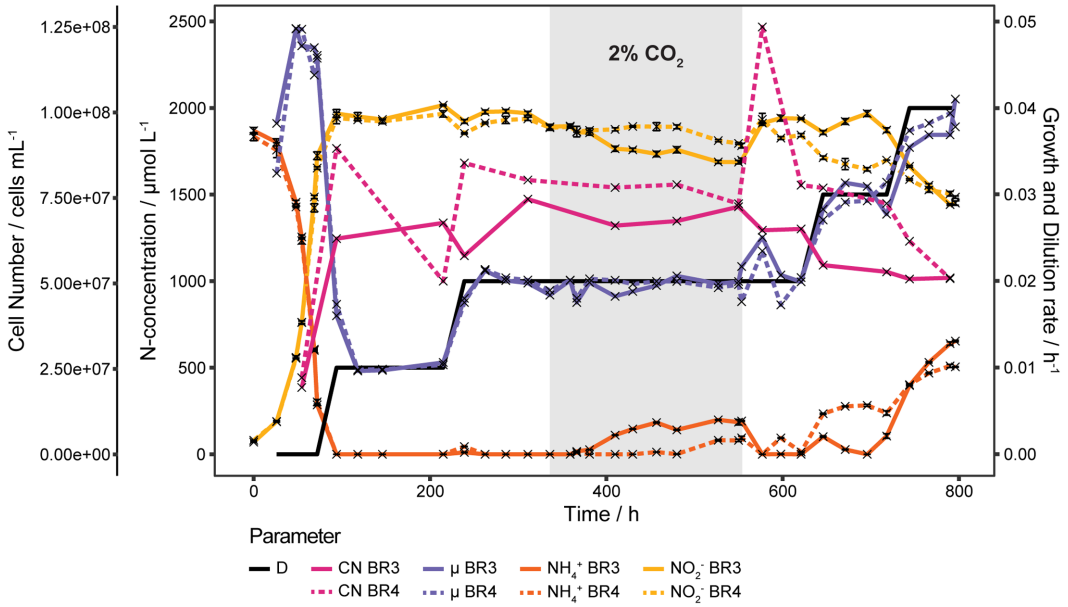

FIGURE 4
Continuous cultures of *N. viennensis* at low *D*. Two continuous cultures operated at *D* from 0.010 h^{-1} to 0.040 h^{-1} and the development of cell number (CN), NO_2^- derived µ, NH_4^+ and NO_2^- concentrations of the cultures grown in the corresponding reactors BR3 and BR4. Cultures were gassed with 2 sL L^{-1} h^{-1} 0.5% CO_2 enriched air, except for the gray area where CO_2 was increased to 2%. The elevated CO_2 concentration induced an increase of NH_4^+ with a delay of 55.5 h and 216 h in BR3 and BR4, respectively. NH_4^+ was consumed again right after decreasing CO_2 back to 0.5% which coincided with a temporary increase of the cell number in BR4. NH_4^+ and NO_2^- curves show mean values of technical triplicates and error bars represent the standard deviation of the mean. Points with small standard deviation may not have visible error bars.

excessive pyruvate concentrations that would promote bacterial growth in case of a contamination. For up to 6 mmol L^{-1} NO_2^- the cell number correlated very well with the NO_2^- concentration but then the cell number stagnated in both reactors even though NH_3 was still oxidized. Pyruvate was added to the reactors at the end of the fed-batch to increase the concentration from 2 mmol L^{-1} to 5 mmol L^{-1} and the feed media for the continuous cultures were also adjusted to 10 mmol L^{-1} NH_4Cl and 5 mmol L^{-1} pyruvate. Initial *D* was 0.006 h^{-1} to allow the cultures to recover but was further decreased to 0.005 h^{-1} to reduce the increase of *S*. In both cultures *S* appeared to be drifting, which means that µ (based on NO_2^- concentration) was always lower than *D* but still increased with increasing *D* (Figure 5). With such low *D* the residence time would have been far too long to wait for three volume exchanges to establish steady states (25 days at $D = 0.005\,h^{-1}$). *D* was increased incrementally after at least 200 h from 0.005 to 0.006, 0.008, 0.010 and 0.012 h^{-1}. *S* eventually stabilized around 5 mmol L^{-1} at $D = 0.01\,h^{-1}$ and an increase of *D* to 0.012 h^{-1} did not further increase *S*. The cell number increased in both reactors from $1.76{\cdot}10^8$ cells mL^{-1} and $1.88{\cdot}10^8$ cells mL^{-1} at the beginning of the continuous phase up to $3.22{\cdot}10^8$ cells mL^{-1} and $2.62{\cdot}10^8$ cells mL^{-1} for BR5 and BR6, respectively, after *D* was increased to 0.06 h^{-1} and from there gradually decreased to about $2.00{\cdot}10^8$ at $D = 0.01\,h^{-1}$ (Figure 5).

Even though very low *D* were used in this continuous culture experiments, surprisingly high NH_4^+ concentrations were measured. Once *S* stabilized, increases of *D* did not result in an increase of *S* as observed before with 2 mmol L^{-1} cultures. The NH_4Cl to pyruvate ratio should remain 2:1 to ensure ROS detoxification.

Quantitative physiological analysis of growth parameters

For the following analysis only steady states below $D = 0.050\,h^{-1}$ were considered, as we expect the results at and beyond this *D* to be heavily influenced by biofilm formation. Data points at $D = 0.0124\,h^{-1}$ and 0.0146 h^{-1} are from three different bioreactors that were used for lab scale biomass production (data not shown).

As shown in Figure 6A the cell number of *N. viennensis* increased slightly with *D* from $5.84{\cdot}10^7 \pm 1.19{\cdot}10^7$ cells mL^{-1} at $D = 0.010\,h^{-1}$ up to $7.67{\cdot}10^7 \pm 2.11{\cdot}10^7$ cells mL^{-1} at $D = 0.035\,h^{-1}$ from where it decreased linearly with *D* to $4.36{\cdot}10^7 \pm 2.18{\cdot}10^6$ cells mL^{-1} at $D = 0.046\,h^{-1}$.

NH_4^+ was completely consumed up to $D = 0.020\,h^{-1}$ by cultures gassed with 0.5 Vol.-% CO_2. For 2 Vol.-% CO_2 gassed cultures *S* started to accumulate at $D = 0.020\,h^{-1}$ to 138 ± 58.9 µmol L^{-1} and increased steeply up to 745.5 ± 27.6 µmol L^{-1} NH_4^+ at $D = 0.035\,h^{-1}$ where it began to stagnate and reach a maximum of 850.0 ± 11.6 µmol L^{-1} at $D = 0.046\,h^{-1}$. Despite the early onset of increasing *S*, the cell concentration remained surprisingly stable up to $D = 0.035\,h^{-1}$. Conversely, while the cell number was decreasing with *D* from 0.035 to 0.046 h^{-1}, *S* increased only marginally, thus changes in *S* appeared to be not reflected in the cell number and vice versa.

NO_2^- and cell productivities (P_{NO2}, P_C) are shown in Figure 6B. P_{NO2} increased logarithmically from *D* of 0.010 to 0.020 h^{-1} and from there on in a linear way up to 49.6 ± 0.3 µmol L^{-1} h^{-1} at $D = 0.046\,h^{-1}$. P_C increases linearly from $5.84{\cdot}10^5 \pm 1.19{\cdot}10^5$ cells mL^{-1} h^{-1} at $D = 0.010\,h^{-1}$ up to $2.69{\cdot}10^6 \pm 7.39{\cdot}10^5$ cells mL^{-1} h^{-1} at $D = 0.035\,h^{-1}$ from which point it started to decline to $2.00{\cdot}10^6 \pm 1.00{\cdot}10^5$ cells mL^{-1} h^{-1} at $D = 0.046\,h^{-1}$. As a result of a variable $Y_{(X/NH3)}$, P_{NO2} and P_C do not correlate in a fixed 1:1 ratio as would be expected. For comparison P_{NO2} and P_C of 10 mmol L^{-1} cultures at $D = 0.012\,h^{-1}$ are also shown in Figure 6C with 53.6 ± 0.9 µmol L^{-1} h^{-1} and $2.61{\cdot}10^6 \pm 2.30{\cdot}10^5$ cells mL^{-1} h^{-1}, respectively. The highest P_C was reached at $D = 0.035\,h^{-1}$ which is therefore the optimal *D* for biomass production for *N. viennensis*.

As shown in Figure 6C an average $Y_{(X/NH3)}$ of $3.36{\cdot}10^7 \pm 5.77{\cdot}10^6$ cells μmol^{-1} L^{-1} was determined from the batch cultures before changing into continuous mode. $Y_{(X/NH3)}$ from steady states at *D* of 0.010 to 0.030 h^{-1}

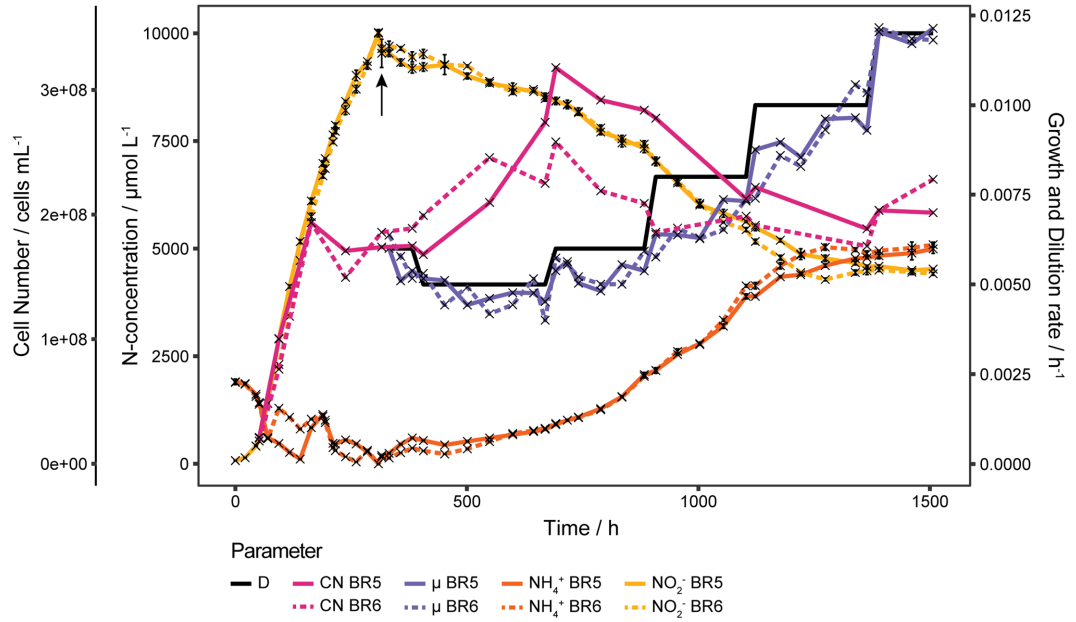

FIGURE 5
Continuous cultures of *N. viennensis* at high ammonia concentrations. Two continuous cultures gassed with 2 sL L^{-1} h^{-1} 0.5% CO_2 enriched air, operated at D = 0.005 h^{-1} to 0.012 h^{-1} and the development of cell number (CN), NO_2^- derived µ, NH_4^+ and NO_2^- concentrations of the cultures grown in the corresponding reactors BR5 and BR6. Batch cultures were grown with 2 mmol L^{-1} NH_4Cl and 1 mmol L^{-1} pyruvate and then fed with medium containing 32 mmol L^{-1} NH_4Cl and 4.75 mmol L^{-1} pyruvate to reach a final concentrations of 10 mmol L^{-1} NH_4Cl and 2 mmol L^{-1} pyruvate. The relative reduction of pyruvate to NH_4Cl caused a stagnation of the cell number, for which reason pyruvate was added to the cultures at the end of the feed phase (indicated by the arrow) to increase the concentration to 5 mmol L^{-1}. Cell number increased as a result of ROS detoxification by pyruvate, but started to decrease again as NH_4^+ increased. Once NH_4^+ stabilized at D = 0.010 h^{-1} increasing D further did not result in an increase of NH_4^+. NH_4^+ and NO_2^- curves show mean values of technical triplicates and error bars represent the standard deviation of the mean. Points with small standard deviation may not have visible error bars.

or 10 mmol L^{-1} NH_4Cl cultures (D from 0.005 to 0.012 h^{-1}) were well within this range, but from D = 0.035 h^{-1}, $Y_{(X/NH3)}$ were highly elevated with $6.12{\cdot}10^7 \pm 1.68{\cdot}10^7$ cells µmol^{-1} L^{-1} and decreased to $3.79{\cdot}10^7 \pm 1.90{\cdot}10^6$ cells µmol^{-1} L^{-1} at D = 0.046 h^{-1}. Cultures at D of 0.020 h^{-1} gassed with 0.5 Vol.-% and 2 Vol.-% CO_2 had very much the same $Y_{(X/NH3)}$ with $3.82{\cdot}10^7 \pm 1.96{\cdot}10^6$ cells µmol^{-1} L^{-1} and $3.86{\cdot}10^7 \pm 3.34{\cdot}10^5$ cells µmol^{-1} L^{-1}, respectively. While $Y_{(X/NH3)}$ of steady states at low D are comparable to batch cultures, at higher D, $Y_{(X/NH3)}$ increased up to 81.7% (D = 0.035 h^{-1}) compared to batch cultures.

Discussion

The substrate affinity, together with µ, are very important parameters for understanding the ecological strategy of an organism (*r*- and *k*-strategists). Due to their very high substrate affinity and low µ, AOA are regarded as typical k-strategists but the growth behavior of *N. viennensis* observed in this study can not sufficiently be described with Monod kinetics or more sophisticated models like the Briggs-Haldane model. The strong increase of S at D = 0.035 h^{-1} would indicate that D was already close to μ_{max}, but then S should have increased right after the start of the continuous culture and further increases of D should have resulted in even stronger increases of S. Instead S plateaued around 800 µmol L^{-1} NH_4^+ while the cell number decreased with D increasing up to 0.046 h^{-1}. An explanation for this behavior would be the formation of a biofilm that would retain cells in the reactor, but at the same time decrease planktonic cell concentrations. Thus, the activity of the whole system would increase while at the same time the measured cell concentrations would decrease, which describes the results. The stable S concentrations and sposntaneous but isochronal activity increases are difficult to integrate into this explanation. Only very strong increases of D like from 0.050 h^{-1} to 0.060 h^{-1} and further to 0.070 h^{-1} caused S to increase temporarily while cell concentrations remained surprisingly stable – considering a μ_{max} of 0.048 h^{-1} for *N. viennensis*. At $D > \mu_{max}$ cells should usually be washed out over time, but due to the seeding of cells by the biofilm this phenomenon was not observed. The linear decrease of S at D = 0.060 h^{-1} might be the result of an increase in active biofilm biomass, that reaches its limits at D = 0.070 h^{-1}. This would explain the very stable concentrations of S after the spontaneous activity increase. These increases of activity might be induced by quorum sensing and be dependent on cell density in the biofilm, which should gradually increase with time until a maximum is reached. This would provide a robust principle, which could explain the synchronistic nature of this very unusual physiological phenomenon. The mechanistic principle of how the cells are able to increase their substrate affinity abruptly could be explained by the expression of multiple *amo*C genes, of which the genome of *N. viennensis* contains six, which is likely to be the subunit that contains the catalytic center of the AMO protein complex. This assumption is based on recent findings of a bacterial particulate methane monooxygenase (Ross et al., 2019).

In addition, there seems to be another regulatory element in the growth behavior of *N. viennensis* that was observed with 2 mmol L^{-1} and 10 mmol L^{-1} NH_4^+ continuous cultures. At a certain D the organism consumes NH_3 at a slightly lower rate than provided, thus slowly increasing S until it finally stabilizes at roughly 50% of S_i. Once stabilized, S only marginally increases with D unless very strong changes are induced. This phenomenon appears to be linked to an increase in $Y_{(X/NH3)}$, which seems to be highly elevated at D > 0.030 h^{-1}. However,

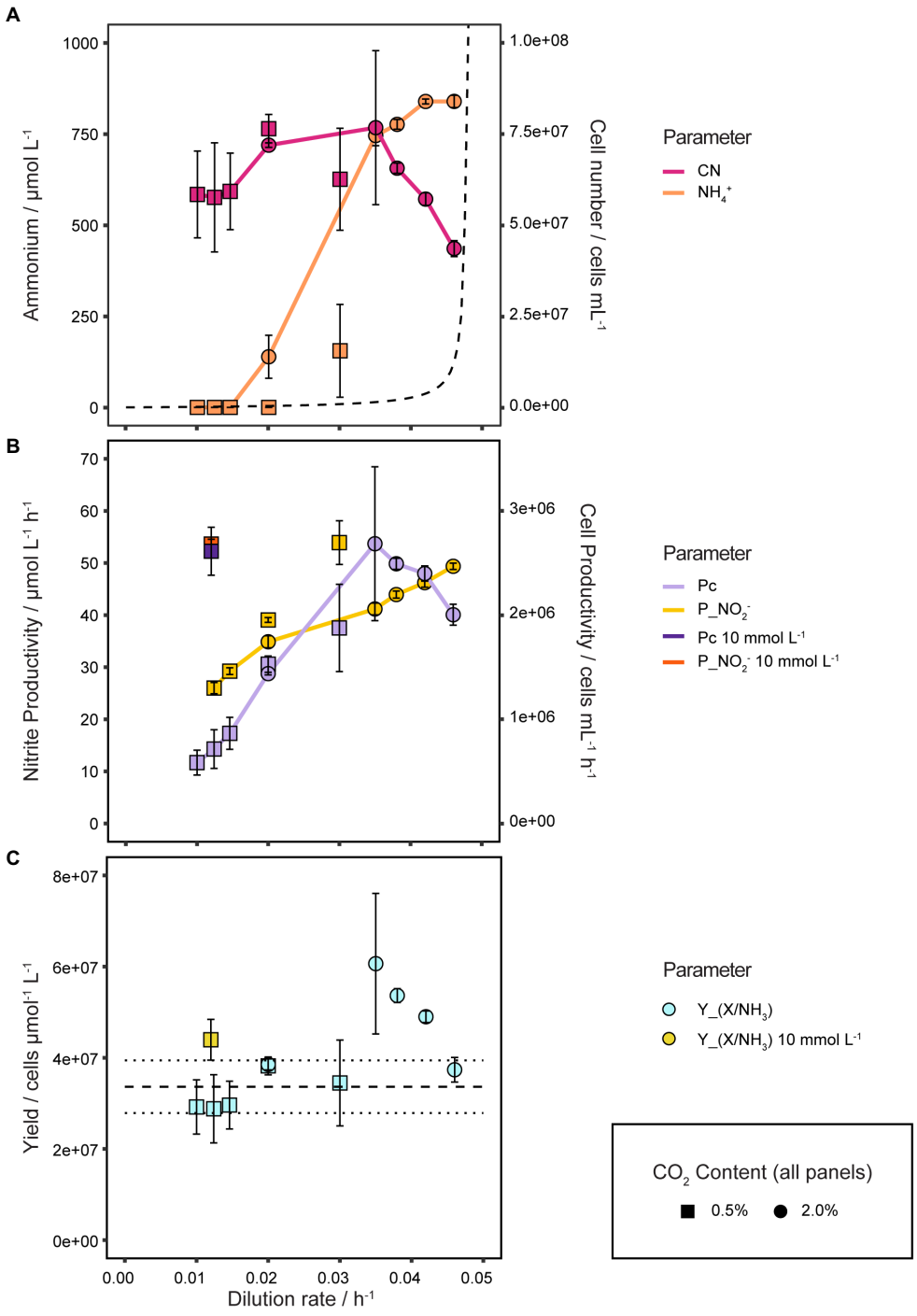

FIGURE 6
Quantitative analysis of physiological growth parameters. **(A)** Cell number and *S* in response to different *D* and CO_2 concentrations. The dashed line shows the theoretical development of *S* with increasing *D* assuming Monod kinetics, K_s equal to $K_{m(app)}$ of 5.4 µmol L^{-1} and μ_{max} of 0.048 h^{-1}, illustrating the difference to the observed growth behavior of *N. viennensis*. NH_4^+ and cell number curves show the mean values of biological duplicates, of which each NH_4^+ value consists of technical triplicates (samples taken at different time points), and error bars represent the standard deviation of the mean. **(B)** Nitrite (P_{NO2}) and cell productivity (P_C) of 2 and 10 mmol L^{-1} NH_4Cl continuous cultures at different *D* and CO_2 concentrations. P_{NO2} and P_C neither correlate in a fixed 1:1 ratio as would be expected for 0.5% nor 2% CO_2 gassed cultures, indicating a variable $Y_{(X/NH3)}$. P_{NO2} and P_C points show mean values of biological duplicates, triplicates for *D* of 0.0124 h^{-1} and 0.0146 h^{-1}, and error bars represent the standard deviation of the mean. **(C)** $Y_{(X/NH3)}$ in response to different *D* and CO_2 concentrations. $Y_{(X/NH3)}$ points show mean values of biological duplicates, triplicates for *D* = 0.0124 h^{-1} and 0.0146 h^{-1}, and error bars represent the standard deviation of the mean. Points with small standard deviation may not have visible error bars.

we must state that we analyze the biomass productivity in relation to the energy metabolism, assuming that energy is limiting the biomass formation and not carbon, which was provided in excess to *N. viennensis* during chemostat and biofilm formation experiments.

In a steady state $Y_{(X/NH3)}$ might be increased because the enzymatic machinery and metabolic networks can be fine tuned to a stable environmental condition. A batch culture needs to adapt constantly to the changing environment which requires energy. However, this

phenomenon occurs in every organism and can not describe the vast increase of $Y_{(X/NH3)}$ in continuous cultures of up to 81.7% compared to batch cultures. This might only be explained by taking into account the unique nature of archaeal ammonia oxidation, which produces significant amounts of ROS that can destroy the cells if not taken care of by the environment (e.g., by catalases, alpha keto-acids). Thus, there is a strong selection pressure on the organism to regulate its activity in accordance to its environment. Given the wide distribution of AOA, it seems that these organisms might have evolved elaborate metabolic regulations to enable them to thrive. The production of ROS by AOA might thus be key to understanding their ecological success, because it could also be used by the organisms to generate substrates from the environment by oxidative decarboxylation (Kim et al., 2016) or oxidative deamination (Akagawa et al., 2002) of organic matter. This would supply the organism with both CO_2 and NH_3 and could explain why some AOA, like the members of the Nitrosocosmicus clade, are highly abundant in very organic rich soils. However, the conditions in soil, the primary habitat of *Nitrososphaera* spp., are not close to the conditions inside a bioreactor that operates in continuous culture mode. Hence, biofilm formation might be a preferred form of life for soil AOA, or could confer some resistance to selection *via* μ. In addition, this kind of metabolism, however, requires a high degree of metabolic regulation which might be enabled by the transcription apparatus of archaea, which is usually summarized as a simplified version of the eukaryotic machinery, even though this observed simplicity is under constant revision as new insights are accumulated (Gehring et al., 2016). The unique nature of archaea and their gene regulation could therefore be responsible for this form of NH_3 oxidation. It appears that the guiding principle behind the growth dynamics of *N. viennensis*, and probably other AOA, is not substrate affinity but the maximization of $Y_{(X/NH3)}$ and therefore optimal utilization of a usually very limited substrate.

These insights into the regulation of the energy metabolism of *N. viennensis* have important implications for further bioprocess development to optimize biomass productivity. Due to the increase of $Y_{(X/NH3)}$ with higher D, biomass productivity also increases despite high S concentrations. CO_2 concentration in the in-gas plays a crucial role in the way that it does not effect $Y_{(X/NH3)}$ but μ_{max} and S. An optimal CO_2 concentration should not reduce μ_{max} but at the same time minimize S and therefore maximize the cell concentration at a given D and S_i. For higher concentrated feed medium it is probably worth in terms of biomass productivity to accept higher S concentrations as long as D positively affects $Y_{(X/NH3)}$ and biomass productivity. It is important to note that the NH_4Cl to pyruvate ratio should always be at least in a 2:1 to prevent self toxification by endogenously produced ROS. Depending on the scientific question, higher NH_4^+ concentrations might not be desirable as it certainty influences biomass composition and gene expression. For compounds of interest that cannot be recombinantly produced, higher substrate concentrations might very well be the method of choice as it looks promising to obtain good biomass productivities if further improved.

For the production of biomass, biofilm formation is not favorable as it reduces the amount of cells that can be harvested and thus the effective $Y_{(X/NH3)}$. Elevated temperatures are known to increase biofilm formation (Qureshi et al., 2005), therefore lowering the temperature might be a solution but at the cost of reducing μ_{max}. Reducing the CO_2 concentration will also likely reduce biofilm formation, because carbonate precipitate will be reduced and therefore also available surface that can induce biofilm formation. On the other hand, to understand the ecological function and behavior of *N. viennensis*, it would be very important to study the organism in biofilms, as this is more likely to be its prevalent form in soils. Gene abundances based on 16S rRNA or *amo*A are often used to infer NH_3 oxidizing activity of AOA in soils, but discrepancies with activity measurements of soil incubations are known. Estimates from this study show that only 14.67% of the cells in the biofilm would have been active at their maximum capacity. These results were obtained from two calculations with different assumptions in two different reactors in two different experiments. However, independent of the discrepancy of the results, this high ratio of inactive cells could also explain earlier findings of inactive cells that started the hypothesis of mixotrophic AOA together with the growth enhancing effect of alpha keto acids (Mußmann et al., 2011; Tourna et al., 2011). As biofilms have the potential for very complex cell interactions, it might also be that "inactive" cells simply perform different tasks in the biofilm beside NH_3 oxidation. Regardless, careful validation and/or correction of these results with future experiments would be needed to have a more accurate picture of the behavior of AOA biofilms.

Data availability statement

The raw data supporting the conclusions of this article will be made available by the authors, without undue reservation.

Author contributions

MM, CS, and SK-MRR: conceived and designed study. MM, MAM, and SK-MRR: performed research. MM and LH: analyzed the data. MM, LH, and SK-MRR: contributed new methods or models and wrote the paper. All authors read and approved the manuscript.

Funding

Open access funding by the University of Vienna.

Conflict of interest

SK-MRR was employed by the company Arkeon GmbH.

The remaining authors declare that the research was conducted in the absence of any commercial or financial relationships that could be construed as a potential conflict of interest.

Publisher's note

Supplementary material

The Supplementary material for this article can be found online at: https://www.frontiersin.org/articles/10.3389/fmicb.2023.1076342/full#supplementary-material

References

Abby, S. S., Melcher, M., Kerou, M., Krupovic, M., Stieglmeier, M., Rossel, C., et al. (2018). Candidatus Nitrosocaldus cavascurensis, an ammonia oxidizing, extremely Thermophilic Archaeon with a highly Mobile genome. *Front. Microbiol.* 9:28. doi: 10.3389/fmicb.2018.00028

Adair, K. L., and Schwartz, E. (2008). Evidence that ammonia-oxidizing archaea are more abundant than ammonia-oxidizing bacteria in semiarid soils of northern Arizona, USA. *Microb. Ecol.* 56, 420–426. doi: 10.1007/s00248-007-9360-9

Akagawa, M., Sasaki, T., and Suyama, K. (2002). Oxidative deamination of lysine residue in plasma protein of diabetic rats. Novel mechanism via the Maillard reaction. *Eur. J. Biochem.* 269, 5451–5458. doi: 10.1046/j.1432-1033.2002.03243.x

Alves, R. J. E., Kerou, M., Zappe, A., Bittner, R., Abby, S. S., Schmidt, H. A., et al. (2019). Ammonia oxidation by the Arctic terrestrial Thaumarchaeote Candidatus Nitrosocosmicus arcticus is stimulated by increasing temperatures. *Front. Microbiol.* 10:1571. doi: 10.3389/fmicb.2019.01571

Alves, R. J. E., Minh, B. Q., Urich, T., Haeseler, A., and von Schleper, C. (2018). Unifying the global phylogeny and environmental distribution of ammonia-oxidising archaea based on amoA genes. *Nat. Commun.* 9:1517. doi: 10.1038/s41467-018-03861-1

Bayer, B., Vojvoda, J., Reinthaler, T., Reyes, C., Pinto, M., and Herndl, G. J. (2019). Nitrosopumilus adriaticus sp. nov. and Nitrosopumilus piranensis sp. nov., two ammonia-oxidizing archaea from the Adriatic Sea and members of the class Nitrososphaeria. *Int. J. Syst. Evol. Microbiol.* 69, 1892–1902. doi: 10.1099/ijsem.0.003360

Blainey, P. C., Mosier, A. C., Potanina, A., Francis, C. A., and Quake, S. R. (2011). Genome of a low-salinity ammonia-oxidizing archaeon determined by single-cell and metagenomic analysis. *PLoS One* 6:e16626. doi: 10.1371/journal.pone.0016626

Bristow, L. A., Dalsgaard, T., Tiano, L., Mills, D. B., Bertagnolli, A. D., Wright, J. J., et al. (2016). Ammonium and nitrite oxidation at nanomolar oxygen concentrations in oxygen minimum zone waters. *Proc. Natl. Acad. Sci. U. S. A.* 113, 10601–10606. doi: 10.1073/pnas.1600359113

Caranto, J. D., and Lancaster, K. M. (2017). Nitric oxide is an obligate bacterial nitrification intermediate produced by hydroxylamine oxidoreductase. *PNAS* 114, 8217–8222. doi: 10.1073/pnas.1704504114

Daebeler, A., Herbold, C. W., Vierheilig, J., Sedlacek, C. J., Pjevac, P., Albertsen, M., et al. (2018). Cultivation and genomic analysis of "Candidatus Nitrosocaldus islandicus," an Obligately Thermophilic, ammonia-oxidizing Thaumarchaeon from a hot spring biofilm in Graendalur Valley, Iceland. *Front. Microbiol.* 9:193. doi: 10.3389/fmicb.2018.00193

Daims, H., Lebedeva, E. V., Pjevac, P., Han, P., Herbold, C., Albertsen, M., et al. (2015). Complete nitrification by Nitrospira bacteria. *Nature* 528, 504–509. doi: 10.1038/nature16461

De La Torre, J. R., Walker, C. B., Ingalls, A. E., Könneke, M., and Stahl, D. A. (2008). Cultivation of a thermophilic ammonia oxidizing archaeon synthesizing crenarchaeol. *Environ. Microbiol.* 10, 810–818. doi: 10.1111/j.1462-2920.2007.01506.x

Dodsworth, J. A., Hungate, B., de la Torre, J. R., Jiang, H., and Hedlund, B. P. (2011). Measuring nitrification, denitrification, and related biomarkers in terrestrial geothermal ecosystems. *Methods Enzymol.* 486, 171–203. doi: 10.1016/B978-0-12-381294-0.00008-0

Francis, C. A., Roberts, K. J., Beman, J. M., Santoro, A. E., and Oakley, B. B. (2005). Ubiquity and diversity of ammonia-oxidizing archaea in water columns and sediments of the ocean. *Proc. Natl. Acad. Sci. U. S. A.* 102, 14683–14688. doi: 10.1073/pnas.0506625102

French, E., Kozlowski, J. A., and Bollmann, A. (2021). Competition between ammonia-oxidizing Archaea and bacteria from freshwater environments. *Appl. Environ. Microbiol.* 87:e0103821. doi: 10.1128/AEM.01038-21

French, E., Kozlowski, J. A., Mukherjee, M., Bullerjahn, G., and Bollmann, A. (2012). Ecophysiological characterization of ammonia-oxidizing archaea and bacteria from freshwater. *Appl. Environ. Microbiol.* 78, 5773–5780. doi: 10.1128/AEM.00432-12

Gehring, A. M., Walker, J. E., and Santangelo, T. J. (2016). Transcription regulation in Archaea. *J. Bacteriol.* 198, 1906–1917. doi: 10.1128/JB.00255-16

Griffiths, R. I., Whiteley, A. S., O'Donnell, A. G., and Bailey, M. J. (2000). Rapid method for coextraction of DNA and RNA from natural environments for analysis of ribosomal DNA- and rRNA-based microbial community composition. *Appl. Environ. Microbiol.* 66, 5488–5491. doi: 10.1128/AEM.66.12.5488-5491.2000

Großkopf, R., Stubner, S., and Liesack, W. (1998). Novel Euryarchaeotal lineages detected on Rice roots and in the anoxic bulk soil of flooded Rice microcosms. *Appl. Environ. Microbiol.* 64, 4983–4989. doi: 10.1128/AEM.64.12.4983-4989.1998

Hanišáková, N., Vítězová, M., and Rittmann, S. K.-M. R. (2022). The historical development of cultivation techniques for methanogens and other strict anaerobes and their application in modern microbiology. *Microorganisms* 10:412. doi: 10.3390/microorganisms10020412

Herbert, D., Elsworth, R., and Telling, R. C. (1956). The continuous culture of bacteria; a theoretical and experimental study. *J. Gen. Microbiol.* 14, 601–622. doi: 10.1099/00221287-14-3-601

Hollibaugh, J. T., Gifford, S., Sharma, S., Bano, N., and Moran, M. A. (2011). Metatranscriptomic analysis of ammonia-oxidizing organisms in an estuarine bacterioplankton assemblage. *ISME J.* 5, 866–878. doi: 10.1038/ismej.2010.172

Hollocher, T. C., Tate, M. E., and Nicholas, D. J. (1981). Oxidation of ammonia by Nitrosomonas europaea. Definite 18O-tracer evidence that hydroxylamine formation involves a monooxygenase. *J. Biol. Chem.* 256, 10834–10836. doi: 10.1016/S0021-9258(19)68518-2

Hooper, A. B., and Terry, K. R. (1979). Hydroxylamine oxidoreductase of Nitrosomonas. Production of nitric oxide from hydroxylamine. *Biochim. Biophys. Acta* 571, 12–20. doi: 10.1016/0005-2744(79)90220-1

Hurley, S. J., Elling, F. J., Könneke, M., Buchwald, C., Wankel, S. D., Santoro, A. E., et al. (2016). Influence of ammonia oxidation rate on thaumarchaeal lipid composition and the TEX86 temperature proxy. *PNAS* 113, 7762–7767. doi: 10.1073/pnas.1518534113

Hyman, M. R., and Wood, P. M. (1985). Suicidal inactivation and labelling of ammonia mono-oxygenase by acetylene. *Biochem. J.* 227, 719–725. doi: 10.1042/bj2270719

Jackson, C. R., Langner, H. W., Donahoe-Christiansen, J., Inskeep, W. P., and McDermott, T. R. (2001). Molecular analysis of microbial community structure in an arsenite-oxidizing acidic thermal spring. *Environ. Microbiol.* 3, 532–542. doi: 10.1046/j.1462-2920.2001.00221.x

Jørgensen, S. L., and Zhao, R. (2016). Microbial inventory of deeply buried oceanic crust from a young ridge flank. *Front. Microbiol.* 7:820. doi: 10.3389/fmicb.2016.00820

Jung, M.-Y., Park, S.-J., Kim, S.-J., Kim, J.-G., Sinninghe Damsté, J. S., Jeon, C. O., et al. (2014). A mesophilic, autotrophic, ammonia-oxidizing archaeon of thaumarchaeal group I.1a cultivated from a deep oligotrophic soil horizon. *Appl. Environ. Microbiol.* 80, 3645–3655. doi: 10.1128/AEM.03730-13

Jung, M.-Y., Sedlacek, C. J., Kits, K. D., Mueller, A. J., Rhee, S.-K., Hink, L., et al. (2022). Ammonia-oxidizing archaea possess a wide range of cellular ammonia affinities. *ISME J.* 16, 272–283. doi: 10.1038/s41396-021-01064-z

Karner, M. B., DeLong, E. F., and Karl, D. M. (2001). Archaeal dominance in the mesopelagic zone of the Pacific Ocean. *Nature* 409, 507–510. doi: 10.1038/35054051

Kerou, M., Ponce-Toledo, R. I., Zhao, R., Abby, S. S., Hirai, M., Nomaki, H., et al. (2021). Genomes of Thaumarchaeota from deep sea sediments reveal specific adaptations of three independently evolved lineages. *ISME J.* 15, 2792–2808. doi: 10.1038/s41396-021-00962-6

Kim, J.-G., Park, S.-J., Damsté, J. S. S., Schouten, S., Rijpstra, W. I. C., Jung, M.-Y., et al. (2016). Hydrogen peroxide detoxification is a key mechanism for growth of ammonia-oxidizing archaea. *PNAS* 113, 7888–7893. doi: 10.1073/pnas.1605501113

Kits, K. D., Sedlacek, C. J., Lebedeva, E. V., Han, P., Bulaev, A., Pjevac, P., et al. (2017). Kinetic analysis of a complete nitrifier reveals an oligotrophic lifestyle. *Nature* 549, 269–272. doi: 10.1038/nature23679

Könneke, M., Bernhard, A. E., de la Torre, J. R., Walker, C. B., Waterbury, J. B., and Stahl, D. A. (2005). Isolation of an autotrophic ammonia-oxidizing marine archaeon. *Nature* 437, 543–546. doi: 10.1038/nature03911

Könneke, M., Schubert, D. M., Brown, P. C., Hügler, M., Standfest, S., Schwander, T., et al. (2014). Ammonia-oxidizing archaea use the most energy-efficient aerobic pathway for CO2 fixation. *PNAS* 111, 8239–8244. doi: 10.1073/pnas.1402028111

Kozlowski, J. A., Stieglmeier, M., Schleper, C., Klotz, M. G., and Stein, L. Y. (2016). Pathways and key intermediates required for obligate aerobic ammonia-dependent chemolithotrophy in bacteria and Thaumarchaeota. *ISME J.* 10, 1836–1845. doi: 10.1038/ismej.2016.2

Lancaster, K. M., Caranto, J. D., Majer, S. H., and Smith, M. A. (2018). Alternative bioenergy: updates to and challenges in nitrification Metalloenzymology. *Joule* 2, 421–441. doi: 10.1016/j.joule.2018.01.018

Lebedeva, E. V., Hatzenpichler, R., Pelletier, E., Schuster, N., Hauzmayer, S., Bulaev, A., et al. (2013). Enrichment and genome sequence of the group I.1a ammonia-oxidizing Archaeon "Ca. Nitrosotenuis uzonensis" representing a clade globally distributed in thermal habitats. *PLoS One* 8, 8:e80835. doi: 10.1371/journal.pone.0080835

Lehtovirta-Morley, L. E., Ross, J., Hink, L., Weber, E. B., Gubry-Rangin, C., Thion, C., et al. (2016). Isolation of "Candidatus Nitrosocosmicus franklandus", a novel ureolytic soil archaeal ammonia oxidiser with tolerance to high ammonia concentration. *FEMS Microbiol. Ecol.* 92:fiw057. doi: 10.1093/femsec/fiw057

Lehtovirta-Morley, L. E., Stoecker, K., Vilcinskas, A., Prosser, J. I., and Nicol, G. W. (2011). Cultivation of an obligate acidophilic ammonia oxidizer from a nitrifying acid soil. *Proc. Natl. Acad. Sci. U. S. A.* 108, 15892–15897. doi: 10.1073/pnas.1107196108

Leininger, S., Urich, T., Schloter, M., Schwark, L., Qi, J., Nicol, G. W., et al. (2006). Archaea predominate among ammonia-oxidizing prokaryotes in soils. *Nature* 442, 806–809. doi: 10.1038/nature04983

Luo, Z.-H., Narsing Rao, M. P., Chen, H., Hua, Z.-S., Li, Q., Hedlund, B. P., et al. (2020). Genomic insights of "Candidatus Nitrosocaldaceae" based on nine new Metagenome-assembled genomes, including "Candidatus Nitrosothermus" gen Nov. and two new species of "Candidatus Nitrosocaldus.". *Front. Microbiol.* 11:608832. doi: 10.3389/fmicb.2020.608832

Mauerhofer, L.-M., Pappenreiter, P., Paulik, C., Seifert, A. H., Bernacchi, S., and Rittmann, S. K.-M. R. (2019). Methods for quantification of growth and productivity in anaerobic microbiology and biotechnology. *Folia Microbiol.* 64, 321–360. doi: 10.1007/s12223-018-0658-4

Moissl-Eichinger, C., Probst, A. J., Birarda, G., Auerbach, A., Koskinen, K., Wolf, P., et al. (2017). Human age and skin physiology shape diversity and abundance of Archaea on skin. *Sci. Rep.* 7:4039. doi: 10.1038/s41598-017-04197-4

Mußmann, M., Brito, I., Pitcher, A., Sinninghe Damsté, J. S., Hatzenpichler, R., Richter, A., et al. (2011). Thaumarchaeotes abundant in refinery nitrifying sludges express amoA but are not obligate autotrophic ammonia oxidizers. *Proc. Natl. Acad. Sci. U. S. A.* 108, 16771–16776. doi: 10.1073/pnas.1106427108

Nakagawa, T., Koji, M., Hosoyama, A., Yamazoe, A., Tsuchiya, Y., Ueda, S., et al. (2021). Nitrosopumilus zosterae sp. nov., an autotrophic ammonia-oxidizing archaeon of phylum Thaumarchaeota isolated from coastal eelgrass sediments of Japan. *Int. J. Syst. Evol. Microbiol.* 71. doi: 10.1099/ijsem.0.004961

Nicol, G. W., Leininger, S., Schleper, C., and Prosser, J. I. (2008). The influence of soil pH on the diversity, abundance and transcriptional activity of ammonia oxidizing archaea and bacteria. *Environ. Microbiol.* 10, 2966–2978. doi: 10.1111/j.1462-2920.2008.01701.x

Nunoura, T., Chikaraishi, Y., Izaki, R., Suwa, T., Sato, T., Harada, T., et al. (2018). A primordial and reversible TCA cycle in a facultatively chemolithoautotrophic thermophile. *Science* 359, 559–563. doi: 10.1126/science.aao3407

Nunoura, T., Nishizawa, M., Kikuchi, T., Tsubouchi, T., Hirai, M., Koide, O., et al. (2013). Molecular biological and isotopic biogeochemical prognoses of the nitrification-driven dynamic microbial nitrogen cycle in hadopelagic sediments. *Environ. Microbiol.* 15, 3087–3107. doi: 10.1111/1462-2920.12152

Øvreås, L., Forney, L., Daae, F. L., and Torsvik, V. (1997). Distribution of bacterioplankton in meromictic Lake Saelenvannet, as determined by denaturing gradient gel electrophoresis of PCR-amplified gene fragments coding for 16S rRNA. *Appl. Environ. Microbiol.* 63, 3367–3373. doi: 10.1128/aem.63.9.3367-3373.1997

Pappenreiter, P. A., Zwirtmayr, S., Mauerhofer, L.-M., Rittmann, S. K.-M. R., and Paulik, C. (2019). Development of a simultaneous bioreactor system for characterization of gas production kinetics of methanogenic archaea at high pressure. *Eng. Life Sci.* 19, 537–544. doi: 10.1002/elsc.201900035

Park, S.-J., Park, B.-J., and Rhee, S.-K. (2008). Comparative analysis of archaeal 16S rRNA and amoA genes to estimate the abundance and diversity of ammonia-oxidizing archaea in marine sediments. *Extremophiles* 12, 605–615. doi: 10.1007/s00792-008-0165-7

Probst, A. J., Auerbach, A. K., and Moissl-Eichinger, C. (2013). Archaea on human skin. *PLoS One* 8:e65388. doi: 10.1371/journal.pone.0065388

Qin, W., Heal, K. R., Ramdasi, R., Kobelt, J. N., Martens-Habbena, W., Bertagnolli, A. D., et al. (2017). Nitrosopumilus maritimus gen. Nov., sp. nov., Nitrosopumilus cobalaminigenes sp. nov., Nitrosopumilus oxyclinae sp. nov., and Nitrosopumilus ureiphilus sp. nov., four marine ammonia-oxidizing archaea of the phylum Thaumarchaeota. *Int. J. Syst. Evol. Microbiol.* 67, 5067–5079. doi: 10.1099/ijsem.0.002416

Qureshi, N., Annous, B. A., Ezeji, T. C., Karcher, P., and Maddox, I. S. (2005). Biofilm reactors for industrial bioconversion processes: employing potential of enhanced reaction rates. *Microb. Cell Factories* 4:24. doi: 10.1186/1475-2859-4-24

Reigstad, L. J., Richter, A., Daims, H., Urich, T., Schwark, L., and Schleper, C. (2008). Nitrification in terrestrial hot springs of Iceland and Kamchatka. *FEMS Microbiol. Ecol.* 64, 167–174. doi: 10.1111/j.1574-6941.2008.00466.x

Rittmann, S., and Holubar, P. (2014). Rapid extraction of total RNA from an anaerobic sludge biocoenosis. *Folia Microbiol.* 59, 127–132. doi: 10.1007/s12223-013-0274-2

Rittmann, S. K.-M. R., Seifert, A. H., and Bernacchi, S. (2018). Kinetics, multivariate statistical modelling, and physiology of CO2-based biological methane production. *Appl. Energy* 216, 751–760. doi: 10.1016/j.apenergy.2018.01.075

Ross, M. O., MacMillan, F., Wang, J., Nisthal, A., Lawton, T. J., Olafson, B. D., et al. (2019). Particulate methane monooxygenase contains only mononuclear copper centers. *Science* 364, 566–570. doi: 10.1126/science.aav2572

Santoro, A. E. (2019). Crystal ball: the microbial map of the ocean. *Environ. Microbiol. Rep.* 11, 35–37. doi: 10.1111/1758-2229.12721

Santoro, A. E., Dupont, C. L., Richter, R. A., Craig, M. T., Carini, P., McIlvin, M. R., et al. (2015). Genomic and proteomic characterization of "Candidatus Nitrosopelagicus brevis": an ammonia-oxidizing archaeon from the open ocean. *Proc. Natl. Acad. Sci. U. S. A.* 112, 1173–1178. doi: 10.1073/pnas.1416223112

Sauder, L. A., Albertsen, M., Engel, K., Schwarz, J., Nielsen, P. H., Wagner, M., et al. (2017). Cultivation and characterization of Candidatus Nitrosocosmicus exaquare, an ammonia-oxidizing archaeon from a municipal wastewater treatment system. *ISME J.* 11, 1142–1157. doi: 10.1038/ismej.2016.192

Sauder, L. A., Engel, K., Lo, C.-C., Chain, P., and Neufeld, J. D. (2018). "Candidatus Nitrosotenuis aquarius," an ammonia-oxidizing Archaeon from a freshwater aquarium biofilter. *Appl. Environ. Microbiol.* 84, e01430–e01418. doi: 10.1128/AEM.01430-18

Sedlacek, C. J., Giguere, A. T., Dobie, M. D., Mellbye, B. L., Ferrell, R. V., Woebken, D., et al. (2020). Transcriptomic response of Nitrosomonas europaea transitioned from ammonia- to oxygen-limited steady-state growth. *mSystems* 5, e00562–e00519. doi: 10.1128/mSystems.00562-19

Stieglmeier, M., Klingl, A., Alves, R. J. E., Rittmann, S. K.-M. R., Melcher, M., Leisch, N., et al. (2014). Nitrososphaera viennensis sp. nov., an aerobic and mesophilic ammonia-oxidizing archaeon from soil and member of the archaeal phylum Thaumarchaeota. *Int. J. Syst. Evol. Microbiol.* 64, 2738–2752. doi: 10.1099/ijs.0.063172-0

Taubner, R.-S., and Rittmann, S. K.-M. R. (2016). Method for indirect quantification of CH4 production via H2O production using Hydrogenotrophic methanogens. *Front. Microbiol.* 7:532. doi: 10.3389/fmicb.2016.00532

Tourna, M., Stieglmeier, M., Spang, A., Könneke, M., Schintlmeister, A., Urich, T., et al. (2011). Nitrososphaera viennensis, an ammonia oxidizing archaeon from soil. *PNAS* 108, 8420–8425. doi: 10.1073/pnas.1013488108

Treusch, A. H., Leininger, S., Kletzin, A., Schuster, S. C., Klenk, H.-P., and Schleper, C. (2005). Novel genes for nitrite reductase and Amo-related proteins indicate a role of uncultivated mesophilic crenarchaeota in nitrogen cycling. *Environ. Microbiol.* 7, 1985–1995. doi: 10.1111/j.1462-2920.2005.00906.x

Vajrala, N., Martens-Habbena, W., Sayavedra-Soto, L. A., Schauer, A., Bottomley, P. J., Stahl, D. A., et al. (2013). Hydroxylamine as an intermediate in ammonia oxidation by globally abundant marine archaea. *Proc. Natl. Acad. Sci. U. S. A.* 110, 1006–1011. doi: 10.1073/pnas.1214272110

van Kessel, M. A. H. J., Speth, D. R., Albertsen, M., Nielsen, P. H., Op den Camp, H. J. M., Kartal, B., et al. (2015). Complete nitrification by a single microorganism. *Nature* 528, 555–559. doi: 10.1038/nature16459

Venter, J. C., Remington, K., Heidelberg, J. F., Halpern, A. L., Rusch, D., Eisen, J. A., et al. (2004). Environmental genome shotgun sequencing of the Sargasso Sea. *Science* 304, 66–74. doi: 10.1126/science.1093857

Vuillemin, A., Wankel, S. D., Coskun, Ö. K., Magritsch, T., Vargas, S., Estes, E. R., et al. (2019). Archaea dominate oxic subseafloor communities over multimillion-year time scales. *Sci. Adv.* 5:eaaw4108. doi: 10.1126/sciadv.aaw4108

Wang, X., Conway, W., Burns, R., McCann, N., and Maeder, M. (2010). Comprehensive study of the hydration and dehydration reactions of carbon dioxide in aqueous solution. *J. Phys. Chem. A* 114, 1734–1740. doi: 10.1021/jp909019u

Wrage-Mönnig, N., Horn, M. A., Well, R., Müller, C., Velthof, G., and Oenema, O. (2018). The role of nitrifier denitrification in the production of nitrous oxide revisited. *Soil Biol. Biochem.* 123, A3–A16. doi: 10.1016/j.soilbio.2018.03.020

Zhalnina, K. V., Dias, R., Leonard, M. T., Dorr de Quadros, P., Camargo, F. A. O., Drew, J. C., et al. (2014). Genome sequence of Candidatus Nitrososphaera evergladensis from group I.1b enriched from Everglades soil reveals novel genomic features of the ammonia-oxidizing Archaea. *PLoS One* 9:e101648. doi: 10.1371/journal.pone.0101648

Zhao, R., Hannisdal, B., Mogollon, J. M., and Jørgensen, S. L. (2019). Nitrifier abundance and diversity peak at deep redox transition zones. *Sci. Rep.* 9:8633. doi: 10.1038/s41598-019-44585-6

Zhao, R., Mogollón, J. M., Abby, S. S., Schleper, C., Biddle, J. F., Roerdink, D. L., et al. (2020). Geochemical transition zone powering microbial growth in subsurface sediments. *Proc. Natl. Acad. Sci. U. S. A.* 117, 32617–32626. doi: 10.1073/pnas.2005917117

Zhou, J., Bruns, M. A., and Tiedje, J. M. (1996). DNA recovery from soils of diverse composition. *Appl. Environ. Microbiol.* 62, 316–322. doi: 10.1128/aem.62.2.316-322.1996

frontiers | Frontiers in Microbiology

TYPE Original Research
PUBLISHED 13 March 2023
DOI 10.3389/fmicb.2023.1150353

OPEN ACCESS

EDITED BY
Haruyuki Atomi,
Kyoto University,
Japan

REVIEWED BY
Hiroya Tomita,
Osaka University,
Japan
Hisaaki Mihara,
Ritsumeikan University,
Japan

*CORRESPONDENCE
Hisashi Hemmi
✉ hhemmi@agr.nagoya-u.ac.jp

SPECIALTY SECTION
This article was submitted to Biology of Archaea, a section of the journal Frontiers in Microbiology

RECEIVED 24 January 2023
ACCEPTED 22 February 2023
PUBLISHED 13 March 2023

CITATION
Komeyama M, Kanno K, Mino H, Yasuno Y, Shinada T, Ito T and Hemmi H (2023) A [4Fe-4S] cluster resides at the active center of phosphomevalonate dehydratase, a key enzyme in the archaeal modified mevalonate pathway.
Front. Microbiol. 14:1150353.
doi: 10.3389/fmicb.2023.1150353

A [4Fe-4S] cluster resides at the active center of phosphomevalonate dehydratase, a key enzyme in the archaeal modified mevalonate pathway

Mutsumi Komeyama[1], Kohsuke Kanno[1], Hiroyuki Mino[2], Yoko Yasuno[3], Tetsuro Shinada[3], Tomokazu Ito[1] and Hisashi Hemmi[1]*

[1]Graduate School of Bioagricultural Sciences, Nagoya University, Nagoya, Aichi, Japan, [2]Graduate School of Science, Nagoya University, Nagoya, Aichi, Japan, [3]Graduate School of Science, Osaka Metropolitan University, Sugimoto, Osaka, Japan

The recent discovery of the archaeal modified mevalonate pathway revealed that the fundamental units for isoprenoid biosynthesis (isopentenyl diphosphate and dimethylallyl diphosphate) are biosynthesized *via* a specific intermediate, *trans*-anhydromevalonate phosphate. In this biosynthetic pathway, which is unique to archaea, the formation of *trans*-anhydromevalonate phosphate from (*R*)-mevalonate 5-phosphate is catalyzed by a key enzyme, phosphomevalonate dehydratase. This archaea-specific enzyme belongs to the aconitase X family within the aconitase superfamily, along with bacterial homologs involved in hydroxyproline metabolism. Although an iron–sulfur cluster is thought to exist in phosphomevalonate dehydratase and is believed to be responsible for the catalytic mechanism of the enzyme, the structure and role of this cluster have not been well characterized. Here, we reconstructed the iron–sulfur cluster of phosphomevalonate dehydratase from the hyperthermophilic archaeon *Aeropyrum pernix* to perform biochemical characterization and kinetic analysis of the enzyme. Electron paramagnetic resonance, iron quantification, and mutagenic studies of the enzyme demonstrated that three conserved cysteine residues coordinate a [4Fe-4S] cluster—as is typical in aconitase superfamily hydratases/dehydratases, in contrast to bacterial aconitase X-family enzymes, which have been reported to harbor a [2Fe-2S] cluster.

KEYWORDS

iron–sulfur cluster, archaea, mevalonate pathway, electron paramagnetic resonance, isoprenoid

1. Introduction

The archaeal mevalonate (MVA) pathway is a modified version of the eukaryotic MVA pathway (Hayakawa et al., 2018; Supplementary Figure 1). In this recently discovered pathway, (*R*)-mevalonate 5-phosphate (MVA5P) is converted into *trans*-anhydromevalonate phosphate (tAHMP), a specific intermediate of the pathway, by phosphomevalonate dehydratase (PMDh). tAHMP is then decarboxylated and phosphorylated to yield isopentenyl diphosphate, a common precursor for the biosynthesis of isoprenoids, such as archaeal membrane lipids. This pathway

is utilized by archaea, excluding some exceptions such as halophilic archaea of the class Halobacteria (Dellas et al., 2013; VanNice et al., 2014) and thermoacidophilic archaea of the orders Sulfolobales (Nishimura et al., 2013) and Thermoplasmatales (Azami et al., 2014; Vinokur et al., 2014, 2015, 2016; Rossoni et al., 2015; Aoki et al., 2022); therefore, it is considered the evolutionary prototype of the eukaryotic, haloarchaea, and *Thermoplasma*-type MVA pathways (Hayakawa et al., 2018; Aoki et al., 2022). The archaeal MVA pathway is also characterized by its lower ATP consumption compared to the other MVA pathways (Hayakawa et al., 2018). The energetically lower cost of the biosynthesis of isoprenoid precursors would be a critical factor in the metabolic engineering of microbial production of isoprenoids.

PMDh, a key enzyme in the archaeal MVA pathway, was first isolated from the hyperthermophilic archaeon *Aeropyrum pernix* (Hayakawa et al., 2018; Figure 1). *A. pernix* PMDh (ApPMDh) catalyzes the conversion of MVA5P into tAHMP, with equilibrium biased to MVA5P. Quantitative analysis of ApPMDh reactions showed that 87.7 ± 4.6% of tAHMP was converted into MVA5P in an equilibrium achieved by reverse reaction (Yasuno et al., 2021). Recombinant *A. pernix* PMDh (ApPMDh) exhibited a pale brown color immediately after purification from *E. coli* cells, but the color typically diminished after a few hours of air exposure. The decolorized recombinant protein lost most of its catalytic activity. The activity of PMDh from the methanogenic archaeon *Methanosarcina mazei* has also been confirmed by the successful reconstitution of a part of the archaeal MVA pathway in *Escherichia coli* cells, which was demonstrated visually by an increase in carotenoid production; however, an *in vitro* assay of the enzyme has not been performed (Yoshida et al., 2020).

PMDh belongs to the aconitase X (AcnX) enzyme family, which is part of the aconitase superfamily (Makarova and Koonin, 2003; Figure 2). Although the aconitase superfamily includes well-studied enzymes such as aconitase (see also Figure 1), homoaconitase (*cis*-homoaconitate dehydratase), and isopropylmalate dehydratase (Gruer et al., 1997), the AcnX family is a group of homologous enzymes whose functions have only recently been elucidated (Watanabe et al., 2016, 2017; Hayakawa et al., 2018). The AcnX family was discovered in a comparative genomic study (Makarova and Koonin, 2003), and comprises several subfamilies: type I, type IIa, type IIb, and type IIc-f (Watanabe et al., 2016, 2017, 2021). The type I AcnX subfamily contains *cis*-3-hydroxy-L-proline dehydratases (Figure 1) from bacteria, such as *Pseudomonas aeruginosa* and *Agrobacterium tumefaciens*, and fungi, such as *Trichoderma reesei* (Watanabe et al., 2016). The type IIa subfamily also contains bacterial *cis*-3-hydroxy-L-proline dehydratases (Watanabe et al., 2017), whereas the type IIb subfamily contains archaeal PMDhs (Hayakawa et al., 2018; Yoshida et al., 2020). The functions of bacterial enzymes belonging to other type II subfamilies (type IIc–IIf) remain unknown. Type I AcnX is encoded by a single gene, and its 4–1–2-3 domain organization resembles that of bacterial aconitase B (Figure 2A). Type II AcnX enzymes are composed of large (corresponding to domains 1–2-3 of aconitase) and small (corresponding to domain 4) subunits, like archaeal and bacterial homoaconitases and isopropylmalate dehydratases, and the subunits are usually encoded in tandemly aligned or neighboring genes. One [4Fe-4S] cluster is known to be contained in tightly packed domains 1–2-3 of most aconitase superfamily enzymes (Lauble et al., 1992; Gruer et al., 1997; Williams et al., 2002; Volz, 2008). The [4Fe-4S] cluster of most aconitase superfamily enzymes is coordinated with three conserved cysteine residues in domain 3 (at sites 1–3 in Figure 2B). Each cysteine residue binds to the iron of the cluster *via* its thiol group, and a vacant iron acts as a catalyst in dehydration/hydration reactions (Lauble et al., 1992).

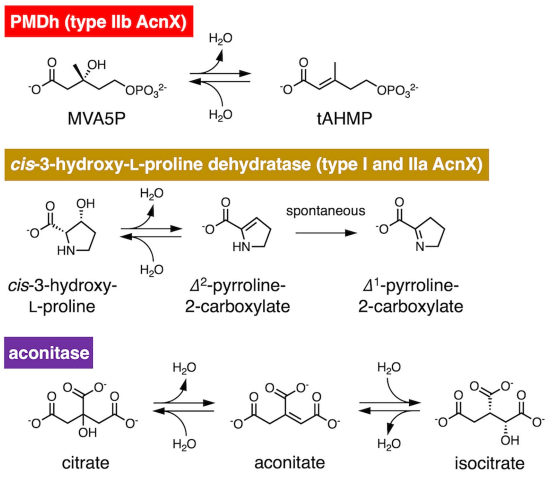

FIGURE 1
Reversible dehydration/hydration reaction catalyzed by phosphomevalonate dehydratase (PMDh), its bacterial homolog in the aconitase X (AcnX) family, and aconitase. PMDh assay in this study was performed *via* the hydration reaction from *trans*-anhydromevalonate phosphate (tAHMP) to (*R*)-mevalonate 5-phosphate (MVA5P).

However, a recent report by Watanabe et al. (2021) contradicts this common assumption. The authors determined the crystal structures of type I AcnX from *A. tumefaciens* (pdb#:7CNP and 7CNQ), which has *cis*-3-hydroxy-L-proline dehydratase activity, and those of type IIb AcnX from a hyperthermophilic archaeon *Thermococcus kodakarensis* (7CNR and 7CNS), although the enzymatic activity of the PMDh homolog was not confirmed. Surprisingly, the structures of *A. tumefaciens* type I AcnX had a [2Fe-2S] iron–sulfur cluster. The existence of the [2Fe-2S] cluster was also supported by electron paramagnetic resonance (EPR) analysis of the enzyme and its homolog from *Pseudomonas* sp. (Watanabe et al., 2021) In the substrate-free structure of *A. tumefaciens* type I AcnX (7CNP), the cluster is coordinated by three cysteine residues, Cys129, Cys508, and Cys510 (at sites A–C in Figure 2B), and a water molecule, which is replaced by the substrate *cis*-3-hydroxy-L-proline in the substrate-complex structure (7CNQ). All cysteine residues are conserved in type I AcnXs, but their positions are not completely identical to those of the conserved cysteines in the aconitase superfamily enzymes, as shown in Figure 2B. The cysteine residue at site A (Cys129 in *A. tumefaciens* AcnX) is not conserved in most aconitase superfamily enzymes, whereas those at site B (Cys508) and site C (Cys510) correspond well with the conserved cysteine residues at sites 2 and 3, respectively. In contrast, the crystal structures of the putative PMDh from *T. kodakarensis* (TkPMDh) contain a [3Fe-4S] cluster, and EPR analysis of the dithionite-reduced putative PMDh provided no evidence of the presence of a [4Fe-4S] cluster (Watanabe et al., 2021). However, it is suspected that the putative PMDh binding to the [3Fe-4S] cluster is in an inactive state, as no enzyme activity was shown. The sequences of type I and type IIb AcnXs also differed considerably. The cysteine residue at site C does not exist in PMDh

10.3389/fmicb.2023.1150353

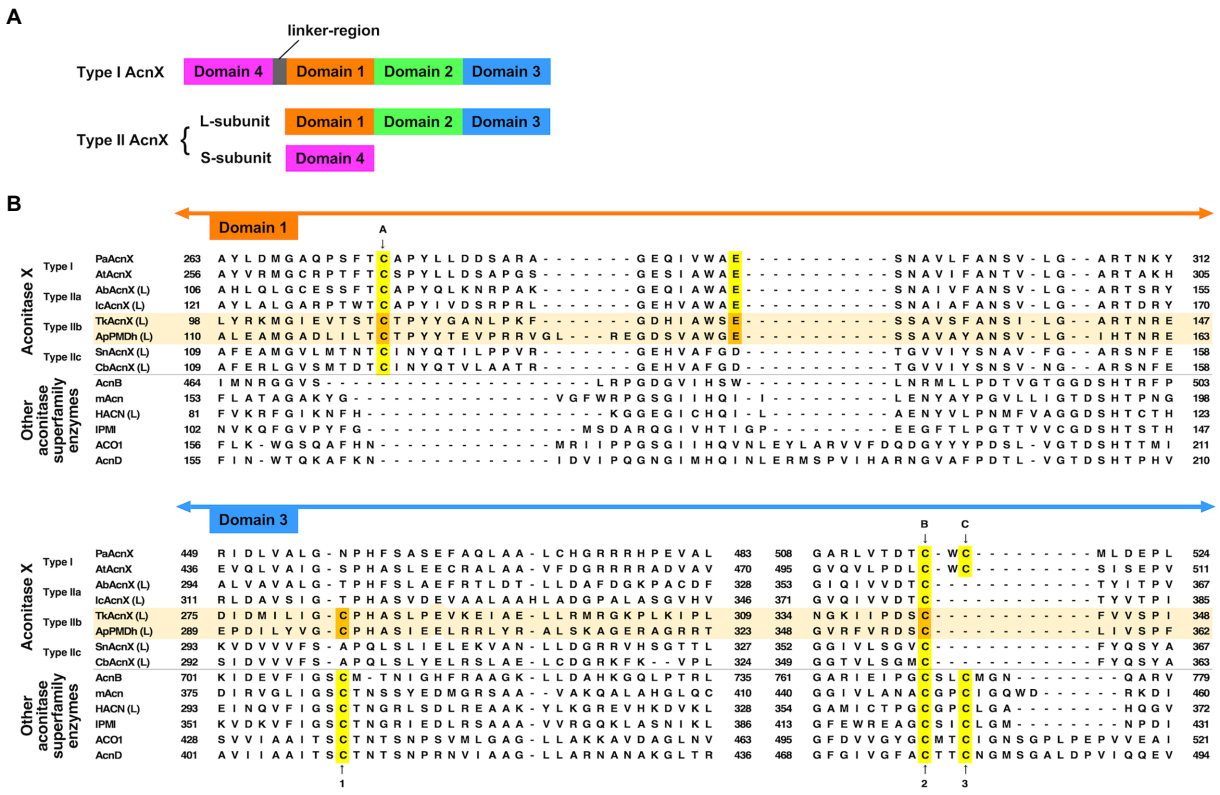

FIGURE 2
Characteristics of the primary structures of type IIb aconitase X (AcnX) enzymes and their homologs. **(A)** Domain structures of AcnX family enzymes. **(B)** Multiple sequence alignment of AcnX family and other aconitase superfamily enzymes. Sequence alignment was performed online using MAFFT with default parameters (https://mafft.cbrc.jp/alignment/server/; Katoh et al., 2019). The sequences of Type IIb AcnX are highlighted in pale orange. The conserved cysteine residues corresponding to those involved in iron–sulfur cluster binding in type I AcnX (cites A–C) and in aconitase superfamily enzymes (cites 1–3), as well as the conserved glutamate residues corresponding to that required for the activity of type I AcnX, are highlighted in yellow (or orange in the case of type IIb AcnX). The orange-colored residues in *Aeropyrum pernix* PMDh (ApPMDh), i.e., Cys122, Glu145, Cys297, and Cys356, were mutagenized in this study. PaAcnX, *cis*-3-hydroxy-L-proline dehydratase from *P. aeruginosa*; AtAcnX, *cis*-3-hydroxy-L-proline dehydratase from *Agrobacterium tumefaciens*; AbAcnX, *cis*-3-hydroxy-L-proline dehydratase from *Azospirillum brasiliense*; IcAcnX, putative *cis*-3-hydroxy-L-proline dehydratase from *Intrasporangium calvum*; TkAcnX, putative PMDh from *Thermococcus kodakarensis*; SnAcnX, AcnX family protein from *Starkeya novella* with unknown function; CbAcnX, AcnX family protein from *Cupriavidus basilensis* with unknown function; AcnB, *Escherichia coli* aconitase B; mAcn, mitochondrial aconitase from bovine; ACO1, cytosolic aconitase from human; AcnD, 2-methylcitrate dehydratase from *Shewanella oneidensis*; HACN (L), homoaconitase large subunit from *Methanocaldococcus jannaschii*; IPMI, isopropylmalate isomerase from *Saccharomyces cerevisiae*.

homologs, whereas those at sites A and B are well conserved (Figure 2B). Instead, PMDh homologs have another conserved cysteine residue at the position corresponding to that in aconitases at site 1. This confusing situation—in which different ion-sulfur clusters are formed in homologous enzymes—motivated us to identify the structure of the iron–sulfur cluster bound to active PMDh from *A. pernix*.

In the present study, we performed iron–sulfur cluster reconstruction to activate purified ApPMDh. The basic properties of ApPMDh, such as pH dependence, effects of divalent metal ions and inhibitors, temperature stability, and kinetic parameters, were determined for the first time *via* an enzyme coupling assay, wherein tAHMP prepared *via* stereoselective chemical synthesis (Yasuno et al., 2021) was employed as a substrate for the reverse reaction. Moreover, by using UV–visible spectrometry, EPR analysis, and iron quantification, we were able to demonstrate the existence of a [4Fe-4S] cluster in ApPMDh. The results from the mutagenetic study suggest three highly conserved cysteine residues as ligands for the [4Fe-4S] cluster and support the conclusion that PMDh exploits the cluster as a catalytic center, probably through a reaction mechanism similar to that proposed for aconitase superfamily enzymes.

2. Materials and methods

2.1. Materials

tAHMP was synthesized as previously described (Yasuno et al., 2021). Other reagents were purchased from Sigma-Aldrich (United States), Fujifilm Wako Pure Chemicals Co. (Osaka, Japan), or Kanto Chemical Co., Inc. (Tokyo, Japan).

2.2. Expression and purification of recombinant ApPMDh

The plasmid constructed in our previous study for the co-expression of the polyhistidine-tagged large subunit Ape_2087.1 and the untagged

small subunit Ape_2089 in *E. coli* cells (Yasuno et al., 2021) was mutagenized to replace the thrombin-recognition sequence LeuValProArgGlySer, which exists between an N-terminal polyhistidine tag and Ape_2087.1, with the HRV3C-recognition sequence LeuGluValLeuPheGlnGlyPro. Mutagenesis was performed using a QuikChange II site-directed mutagenesis kit (Agilent, United States) with the primers 5'-atcacagcagcggcCTGGAAGTTCTGTTCCAG GGCCCGcatatgatgtacctg-3′ and its complementary primers. The capitalized region encodes the HRV3C-recognition sequence, which replaces the thrombin recognition sequence coded in the nucleotide sequence CTGGTGCCGCGCGGCAGC. The mutagenized plasmid was named pET-HisApPMDh.

The expression system of untagged Ape_2089 was constructed using an NcoI/BamHI-digested pET15b vector and an Ape_2089 gene fragment amplified from pET-HisApPMDh using KOD-Plus-Neo DNA polymerase and a pair of primers:5′-gaagtccatggaggtc ctcaggtacaggtcc-3′ and 5′-gaagtggatcctttagggctggccagggcctagg-3.' The underlined sequences of the primers are the recognition sites for NcoI and BamHI, respectively. The amplified fragment was inserted into the vector using Ligation High (TOYOBO, Osaka, Japan) to yield the plasmid pET-ApPMDh-S.

A strain of *E. coli*, Rosetta2 (DE3), was transformed with pET-HisApPMDh. The transformants were cultivated in 1 l Auto Induction medium supplemented with 100 μg/ml ampicillin and 30 μg/ml chloramphenicol at 37°C for 18 h. After harvesting by centrifugation, the cells were placed in an anaerobic glovebox, YUL-800A (UNICO, Tokyo, Japan), equipped with an OTE-70 deoxidizing catalyst unit. All manipulations for enzyme purification were performed anaerobically under 100% N_2 gas using deoxygenated reagents. The cells were dissolved in a Histrap binding buffer containing 20 mM sodium phosphate (pH 7.4), 500 mM NaCl, and 20 mM imidazole and then disrupted using an ultrasonic homogenizer, THU-80 (AS ONE, Osaka, Japan), for six 1-min sessions of sonication. After centrifugation at 12,000 × *g* for 20 min, the supernatant was heat-treated at 60°C for 30 min. After centrifugation at 12,000 × *g* for 20 min, the supernatant was recovered and filtered using a syringe filter (0.45 μm pore size). The filtrate was applied to a 1-mL Histrap FF column (GE Healthcare, United States) equilibrated with Histrap binding buffer. After washing the column with 10 ml Histrap binding buffer, proteins bound to the column were eluted with Histrap elution buffer containing 20 mM sodium phosphate (pH 7.4), 500 mM NaCl, and 150 mM imidazole. The eluted protein was used as the purified ApPMDh. To estimate the ratio of untagged Ape_2089, the small subunit of ApPMDh co-purified with the tagged large subunit Ape_2087.1, the cells of *E. coli* Rosetta2 (DE3) transformed with pET-ApPMDh-S were cultivated and harvested in a manner similar to that of pET-HisApPMDh. Approximately equal amounts of the two cell types were mixed and subjected to the same affinity purification process as described above. The purification and subunit ratios of purified ApPMDh were checked using 15% SDS-PAGE and ImageJ software (Schneider et al., 2012).

2.3. Reconstruction of ApPMDh

Under anaerobic conditions, purified ApPMDh was incubated overnight at RT with 5 mM dithiothreitol. Subsequently, a 10-fold molar excess of $FeCl_3$ was added to the enzyme solution. After 5 min, a molar amount of Na_2S, equal to that of $FeCl_3$ was added. After 2 h of incubation, unbound ions were removed from the ApPMDh using a PD-10 desalting column (GE Healthcare). ApPMDh was recovered from the column and used for analyses as reconstructed ApPMDh within 12 h after reconstruction. The UV–visible spectra of purified ApPMDh and reconstructed ApPMDh were measured anaerobically using a UV-2450 spectrophotometer (Shimadzu, Kyoto, Japan) and a quartz cuvette that could be tightly sealed with a rubber cap (Hellma Analytics, Müllheim, Germany). The UV–visible spectrum of oxidized ApPMDh, obtained by overnight exposure of the reconstructed ApPMDh to air, was also measured.

2.4. Enzyme-coupling PMDh assay

The activity of ApPMDh was quantitatively measured for the reverse reaction of tAHMP to MVA5P as described in our previous study (Yasuno et al., 2021), excepting that anaerobic PMDh reaction was carried out, in a 100-μL volume, at 70°C for 20 min (30 min for assay with inhibitors) in 70 mM Tris–HCl buffer, pH 7.0. The concentration of ApPMDh was controlled; for example, to 17 nM for purified ApPMDh or 5 nM for reconstructed ApPMDh, to match the initial rate wherein less than 10% of the substrate reacted. To elucidate the thermostability of ApPMDh, 5 μM of a reconstructed ApPMDh solution was treated for 30 min at 60, 70, 80, 90, or 100°C and used for the reaction. To investigate the effects of divalent cations or inhibitors, final 1 mM of a divalent cation (Mg^{2+}, Mn^{2+}, or Zn^{2+}) or an inhibitor (iodoacetamide, H_2O_2, or EDTA) was added to the reaction mixture. To determine the pH dependence of ApPMDh, 70 mM PIPES-NaOH (pH 6.1–7.0), Tris–HCl (pH7.0–8.6), or CHES-NaOH (pH 8.5–9.6) was used instead of a buffer.

For the kinetic assay, we used a different method (Supplementary Figure 2). The anaerobically prepared reaction mixture of a 300 μL volume contained 0, 10, 15, 20, 30, or 50 μM tAHMP, 70 mM Tris–HCl buffer (pH 7.0 at 70°C), and 0.22 nM reconstructed ApPMDh, which was reconstructed on the same day. After incubation at 70°C for 20 min, the PMDh reaction was stopped on ice and removed from the anaerobic chamber. The enzyme was removed using a 0.5-mL AMICON ULTRA filter (10 kDa cutoff, Merck Millipore). In each well of a 96-well microtiter plate, 50 μL of the ultrafiltrate or standard MVA5P solution containing 0, 1.2, 2.0, 4.0, 16, or 32 μM of (*R,S*)-MVA5P (Sigma Aldrich) was mixed with 48 μL of a coupling enzyme solution, which contained 290 mM sodium phosphate, pH 7.5, 10 mM $MgCl_2$, 420 μM Amplite™ ADHP (10-acetyl-3,7-dihydroxyphenoxazine, COSMO BIO Co., Ltd., Tokyo, Japan), 2.1 mM phosphoenolpyruvate, 1 unit of pyruvate kinase from rabbit muscle (Fujifilm Wako Pure Chemicals), 0.4 units of pyruvate oxidase from microorganism (TOYOBO), 1 unit of horse radish peroxidase (Oriental Yeast), and 3.7 μM of phosphomevalonate kinase from *Saccharolobus solfataricus*, which was prepared as described in our previous study (Nishimura et al., 2013) and confirmed not to react with tAHMP. After preheating at 37°C, the reaction was initiated by the addition of a 2-μL solution of 10 mM ATP. During the reaction at 37°C, the absorbance at 571 nm was monitored every minute, after 3 s of shaking, using an Infinite 200 PRO microplate spectrophotometer (TECAN, Männedorf, Switzerland). Spectrometric analysis of each sample was performed in quadruplicate. The amount of (*R*)-MVA5P in the ultrafiltate samples was quantified using a standard curve based

on the data from the standard solutions. Kinetic parameters were determined by Michaelis–Menten curve fitting to the substrate concentration vs. initial velocity plot using GraphPad Prism 9 (GraphPad Software, United States).

2.5. Site-directed mutagenesis of ApPMDh

Plasmids for the expression of mutated enzymes were constructed using the QuikChange II site-directed mutagenesis kit (Agilent) using the plasmids pET-HisApPMDh, KOD-Plus-Neo DNA polymerase (TOYOBO) and the primers listed below (one of the complementary primer pairs is shown): for C122A, 5'-gacttgatactgacgGCca cgccctactacacc-3′; for E145A, 5'-gtggcctggggcgCgtccagcgcagtg-3′; for C297A, 5'-cctctacgttggcGCcccccacgccagcatag-3′; and for C356A, 5'-cgtgagggactccGCcctcatagtcagcccc-3.' Capitalized letters indicate mismatched nucleotides. Recombinant expression, purification, UV–visible spectrum measurement, and assays of mutated enzymes were performed using the same procedures as those described above for wild-type ApPMDh.

2.6. EPR analysis of ApPMDh

Under anaerobic conditions, the buffer of the purified ApPMDh solution was exchanged with HRV3C protease buffer containing 20 mM Tris–HCl (pH 7.9), 150 mM NaCl, and 10% glycerol. The polyhistidine tag fused with purified ApPMDh was then cleaved by adding 10 units of HRV3C protease (Funakoshi, Tokyo, Japan) per 1 mg purified ApPMDh, followed by incubation with shaking at 4°C for 24 h. The reaction mixture was loaded into a 1-mL Histrap FF column (GE Healthcare) equilibrated with HRV3C protease buffer, and the flow-through fraction was recovered. The fraction contained tag-free ApPMDh, from which the polyhistidine tag was removed. The enzyme was reconstructed with $FeCl_3$ and Na_2S, as described above, with the exception of 100 mM glycine-KOH buffer (pH 10.0) containing 20 mM imidazole and 20% glycerol in the desalting treatment of the enzyme in a PD-10 column. The tag-free ApPMDh was concentrated using a 0.5-mL AMICON ULTRA filter (10 kDa cutoff, Merck Millipore) until its concentration exceeded 10 mg/ml (180 μM). A 50-fold molar excess of $Na_2S_2O_4$ was then added to the enzyme solution, followed by incubation at 40°C for 30 min to prepare reduced ApPMDh. A nonreduced ApPMDh sample was prepared using the same method, without $Na_2S_2O_4$. A substrate-binding ApPMDh sample was prepared by adding a three-fold molar excess of (*R,S*)-MVA5P to the reduced ApPMDh sample.

In the anaerobic chamber, 150 μL of each sample was placed into a Suprasil quartz EPR tube (5 mm OD) and frozen in liquid nitrogen. The frozen sample tube was sealed, removed from the chamber, and analyzed using an E580 EPR spectrometer (Bruker, United States) equipped with an ER 4122SHQ cavity and ESR 910 cryostat (Oxford Instruments, Abingdon-on-Thames, GB). The measurement conditions were as follows: microwave frequency, 9.48 GHz; microwave power, 10 mW; center field, 3,456 G; modulation amplitude, 18 G; modulation frequency, 100 kHz; time constant, 163 ms; sweep time, 167 s.

Data fitting of the micropower dependence of the EPR signal intensity was performed following Equation 1 (Rupp et al., 1978), where P and b represent microwave power and inhomogeneous parameters, respectively.

$$Intensity \propto \frac{P^{0.5}}{\left[1 + P / P_{1/2}\right]^{0.5b}} \qquad \text{(Equation 1)}$$

2.7. Iron assay of ApPMDh

The reconstruction of tag-free ApPMDh was performed as described above, except that Li_2S, which is less hygroscopic than Na_2S (Freibert et al., 2018), was used in the Fe-S cluster reconstruction process. The protein concentration in the enzyme solution was measured using the Bradford method with a Protein Assay CBB Solution (Nacalai Tesque, Inc., Kyoto, Japan). The enzyme solution was diluted 10 times with deionized water, after which HCl was mixed to a final concentration of 0.06 M. The concentration of iron in the sample solution was measured based on the absorbance of chelating complex of Fe^{2+} and 2-nitroso-5-[*N*-n-propyl-*N*-(3-sulfopropyl) amino]phenol using an iron assay kit LS (Metallogenics Co., Ltd., Chiba, Japan) and compared with standard iron solutions. Absorbance at 560 nm was measured using an Infinite 200 PRO microplate spectrophotometer (TECAN).

2.8. Construction of ApPMDh model structure

The structural model of apo-ApPMDh, which consists of only the large and small subunit proteins, was constructed with Colabfold2 (Mirdita et al., 2022) working on Google Colaboratory, and the [4Fe-4S] cluster and MVA5P were manually added based on the aligned structure of putative TkPMDh (pdb#:7CNS). The holo-ApPMDh model was optimized by simplified molecular dynamics calculations (without solvation) using Molby (Nagata, 2014), which integrated AmberTools (Case et al., 2005). Visualization, editing, and figure construction of structural data were performed using Open-source Pymol (Schrödenger, LLC, United States).

3. Results

3.1. Reconstituting the catalytic center of ApPMDh

Recombinant ApPMDh was expressed in *E. coli* cells for characterization. The large subunit, Ape_2087.1, of ApPMDh fused with an N-terminal polyhistidine tag was co-expressed with the small subunit Ape_2089 with no affinity tag sequence in the same bacterial cells. Applying affinity chromatography with a polyhistidine tag enabled the purification of both the large and small subunits, revealing the formation of a heteromeric complex. Based on the protein bands detected by SDS-PAGE analysis, the ratio of the subunits appeared to be 1:1 (Figure 3A). For confirmation, ApPMDh was purified in a similar manner from a mixture of cells expressing both polyhistidine-tagged Ape_2087.1 and tag-free Ape_2089, and those expressing only

tag-free Ape_2089 (Supplementary Figure 3A). An intense band for tag-free Ape_2089 was observed in the cell-free protein sample that was used for affinity purification, indicating that an excess amount of the tag-free small subunit was supplied. However, after purification, the ratio of the subunits remained approximately 1:1, and most of the Ape_2089 had become part of the flow-through fraction. Based on these observations, we conclude that ApPMDh is a heteromultimeric protein composed of the same number of large and small subunits, similar to other members of the aconitase superfamily.

Biochemical characterization was performed using purified ApPMDh. Because the brown color of ApPMDh purified from aerobically grown *E. coli* cells was sometimes very pale and diminished after oxidation, we assumed that most of the purified enzyme could be in the apo state, lacking the cofactor in its catalytic center, but the nature of the colored cofactor was unclear at that time. This is in contrast to the homolog from *T. kodakarensis*, which was reported to have a brown color even after crystallization (Watanabe et al., 2021). Thus, we attempted to reconstruct the catalytic center using a standard protocol for iron–sulfur cluster reconstruction. Anaerobic treatment of purified ApPMDh with excess $FeCl_3$ and then with Na_2S, followed by desalting, yielded an enzyme solution with a deeper brown color. The UV–visible spectrum of the reconstructed ApPMDh showed an absorption maximum at 410 nm, which could be attributed to the existence of an unidentified cofactor (Figure 3B). Before and after the reconstruction process, the ratio of absorbance at 410 and 280 nm (A_{410}/A_{280}) for purified ApPMDh was 9.5 and 23.8%, respectively. After overnight air exposure of the reconstructed ApPMDh solution, the solution turned colorless and A_{410}/A_{280} decreased to 6.3%. Based on the supposition that the reconstructed ApPMDh was in a complete holo-state and the air-oxidized ApPMDh was in a complete apo-state, calculations suggested that only approximately 18% of the purified ApPMDh was bound to the colored cofactor.

Subsequently, we measured the activity of purified, reconstructed, and air-oxidized enzymes using a recently developed enzyme-coupling PMDh assay method (Yasuno et al., 2021). In this assay, synthetic tAHMP was used as a substrate for the reverse reaction of PMDh performed anaerobically at 70°C. Then MVA5P formed by the reaction was measured by coupling with the oxidation of NADH. Using this method, the specific activities of the purified and reconstructed ApPMDh were determined to be 2.86 ± 0.3 and 14.8 ± 2.2 μmol/min/mg, respectively, and the air-oxidized ApPMDh was completely inactive. This indicated that the enzyme was activated by the reconstruction process. The activity of the reconstructed ApPMDh was five times higher than that of the purified enzyme, which is in good agreement with the above-calculated percentage of holo-enzyme in the purified ApPMDh.

3.2. Biochemical characterization of ApPMDh

The enzymatic properties, such as pH dependence, effects of metal ions, thermostability, and tolerance against chemical inhibitors, of the reconstructed ApPMDh were analyzed to compare the enzyme with other known aconitase superfamily members. The optimal pH for ApPMDh was 7.0, as shown in Figure 4A. Neither the addition of 1 mM Mg^{2+} nor 1 mM Mn^{2+} had a significant effect on the enzyme activity, whereas Zn^{2+} had an inhibitory effect on the ApPMDh reaction, causing almost complete inactivation (Figure 4B). Notably, inhibition by Zn^{2+} has been reported for both bacterial type I AcnX and mammalian mitochondrial aconitase (Costello et al., 1997; Watanabe et al., 2016), although we cannot exclude the possibility that Zn^{2+} inhibits the other enzymes utilized in the coupling assay. Thermostability of ApPMDh was analyzed by applying 30 min of heat treatment to an enzyme solution at temperatures ranging from 60 to 100°C, followed by enzyme assay at 70°C. After treatment at 60–80°C, the activity of ApPMDh was reduced, but not at a significant level compared with that of the enzyme without heat treatment. Treatment at 90°C, however, caused a loss of most enzyme activity, and treatment at 100°C resulted in complete inactivation (Figure 4C). Considering the optimal growth temperature of *A. pernix* at 90–95°C, the observed thermostability of ApPMDh seemed somewhat lower, although this was likely because of the *in vitro* conditions of the heat treatment. The enzyme assay, in the presence of potential chemical inhibitors,

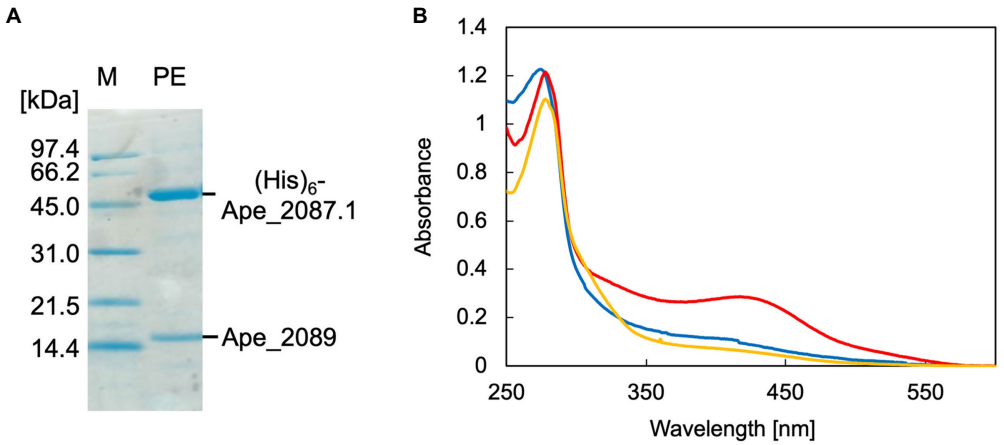

FIGURE 3
SDS-PAGE and UV–visible spectra of *Aeropyrum pernix* phosphomevalonate dehydratase (ApPMDh). **(A)** SDS-PAGE of purified ApPMDh containing a polyhistidine-tagged large subunit, $(His)_6$-Ape2087.1, and a small subunit without tag, Ape_2089. M, molecular marker proteins; PE, purified enzyme. **(B)** UV–visible spectra of ApPMDh before (blue) and after reconstruction (red) or after air-oxidation (yellow).

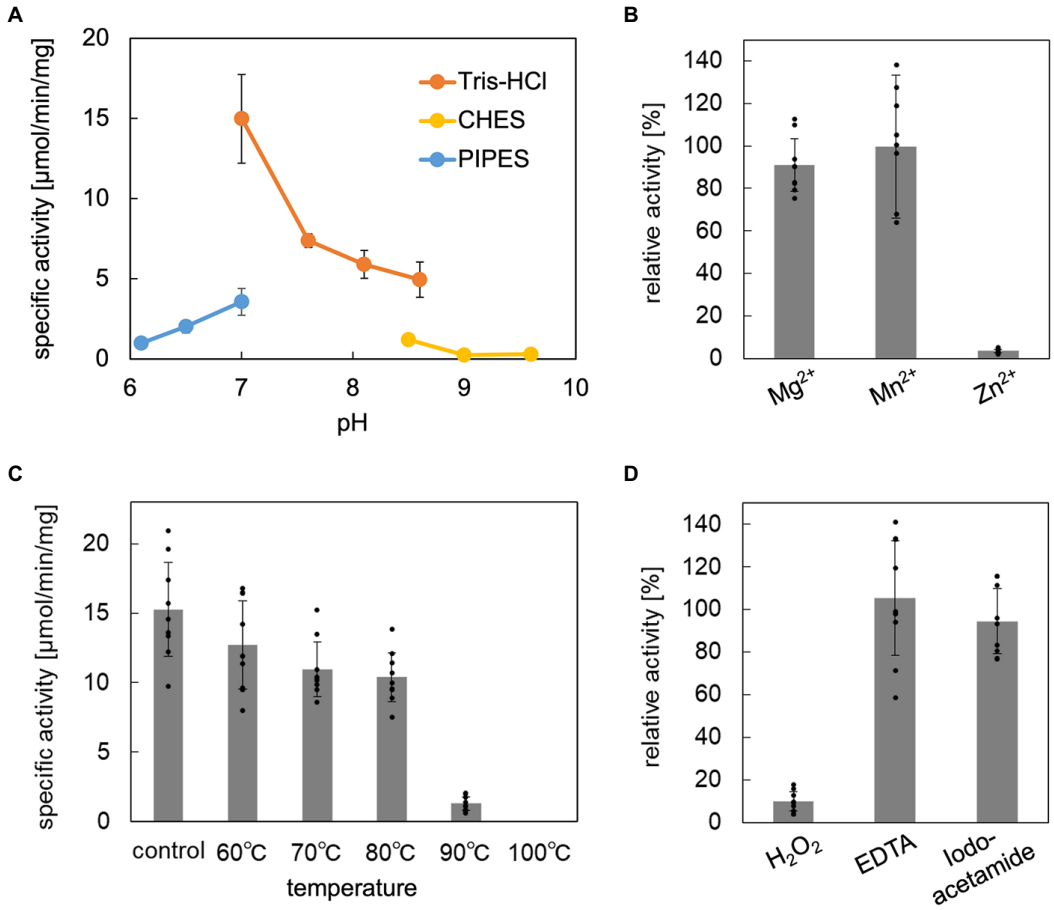

FIGURE 4
Biochemical properties of *Aeropyrum pernix* phosphomevalonate dehydratase (ApPMDh). **(A)** pH dependence. **(B)** Effect of metal ion at 1mM each. **(C)** Thermostability after 30min of heat treatment. **(D)** Effects with 1mM additives. ApPMDh reaction using *trans*-anhydromevalonate phosphate (tAHMP) as a substrate was conducted anaerobically at 70°C for 20min for **(A–C)** and 30min for **(D)**. All reactions were performed in triplicate. The amount of produced MVA5P in each reaction mixture, from which ApPMDh had been removed by ultrafiltration, was colorimetrically analyzed in triplicate through the coupling reactions of phosphomevalonate decarboxylase, pyruvate kinase, and lactate dehydrogenase, which caused a commensurate decrease in NADH, as measured by absorbance at 340nm. The amount of (*R*)-mevalonate 5-phosphate (MVA5P) was quantified based on a standard curve. Error bars indicate standard deviations. For **(B,D)**, the activity without additive was set at 100%.

demonstrated that ApPMDh was strongly inhibited by H_2O_2, which agrees with the reported sensitivity of aconitase toward reactive species (Castro et al., 2019; Figure 4D). In contrast, neither EDTA nor iodoacetamide showed significant inhibitory effects. The insensitivity toward the chelating agent EDTA is in good agreement with the finding described above, wherein the addition of Mg^{2+} or Mn^{2+} did not enhance ApPMDh activity, suggesting that ApPMDh does not require divalent cations to bind its phosphorylated substrates, MVA5P and tAHMP, and to catalyze dehydration/hydration. Although the insensitivity toward the thiol modification agent iodoacetamide appears to contradict the expected catalytic importance of conserved cysteine residues in PMDh, mitochondrial aconitase has also been reported to only be slightly inhibited by EDTA and iodoacetamide, probably suggesting the tolerance of its [4Fe-4S] cluster to such reagents (Kennedy et al., 1983, 1988).

To perform a kinetic study of ApPMDh, we developed a different enzyme-coupling assay method that enabled high sensitivity and low background detection of the PMDh reaction with a lower concentration of tAHMP. In this method, the concentration of MVA5P formed from tAHMP by the anaerobic PMDh reaction at 70°C was measured afterwards by the formation of a dye, resorufin, from anaerobic enzyme-coupling reactions of phosphomevalonate kinase, pyruvate kinase, pyruvate oxidase, and peroxidase (Supplementary Figure 2). Using the new assay method, we found the K_m and k_{cat} of the reconstructed ApPMDh to be 18.3 μM and 15.2 s^{-1}, respectively (Supplementary Figure 4). The k_{cat}/K_m value, 8.28×10^5 M^{-1}·sec^{-1}, was larger than that of type I AcnX from *A. tumefaciens* in the reaction with *cis*-3-hydroxy-L-proline (2.87×10^4 M^{-1}· sec^{-1}; Watanabe et al., 2021), whereas the activity of PMDh was measured with the reverse reaction from tAHMP to MVA5P. It should be also noted that ApPMDh assay was performed at the temperature that was unlikely optimal for the enzyme from the hyperthermophilic archaeon.

3.3. Effect of mutagenesis on the catalytic center of ApPMDh

Site-directed mutagenesis was performed on the conserved residues that are supposedly involved in cofactor binding at the

catalytic center of ApPMDh: Cys122 corresponds to site A of the AcnX family enzymes; Cys297 corresponds to site 1 of most aconitase superfamily enzymes; and Cys356 corresponds to site B of the AcnX family proteins and site 2 of most aconitase superfamily enzymes (Figure 2). Additionally, Glu145, which is highly conserved among all AcnX family enzymes, was selected for mutagenesis, given that alanine replacement of the corresponding residue was reported to cause complete inactivation of *P. aeruginosa* type I AcnX (Watanabe et al., 2016). Indeed, the corresponding glutamate residue interacts with the water molecule coordinated to the [2Fe-2S] cluster in the crystal structure of *A. tumefaciens* type-I AcnX (pdb#:7CNP). Alanine replacement of each residue was performed to construct the mutant enzymes C122A, E145A, C297A, and C356A (Figure 2). Affinity purification of the mutants yielded purified proteins with similar levels of purity, except for C297A, which contained faint but not negligible bands of smaller (<14.4 kDa) proteins that were likely derived from its partial degradation (Supplementary Figure 3B). However, reconstruction of the mutants resulted in different A_{410}/A_{280} ratios (Supplementary Figure 5A). The A_{410}/A_{280} ratios of C122A, C297A, and C356A (7.5, 8.1, and 10.7%, respectively) were much lower than those of the reconstructed wild-type ApPMDh (23.8%) and more closely approximated that of the air-oxidized ApPMDh (6.3%). An enzyme-coupled assay of the mutants demonstrated that the A_{410}/A_{280} ratio was in good agreement with the PMDh activity. The E145A mutant retained 76% of the activity of the wild-type ApPMDh, whereas the activity of the other mutants was less than 4% of that of the wild type (Supplementary Figure 5B). These results suggest that the three conserved cysteine residues of ApPMDh (Cys122, Cys297, and Cys356) are involved in the formation of one iron–sulfur cluster in the enzyme, whereas Glu145 probably has no direct role in cofactor formation. Although our mutagenic study was performed before the publication of the crystal structures of TkPMDh (pdb#:7CNR and 7CNS; Watanabe et al., 2021), the structure demonstrated that in the putative PMDh, the corresponding three cysteine residues actually coordinate a [3Fe-4S] cluster. However, the [3Fe-4S] cluster does not fit well with the dehydration/hydration-catalyzing activity of PMDh, as also suggested by the authors. Similar to ordinary aconitase superfamily enzymes, a [4Fe-4S] cluster, which can provide vacant iron for catalysis, appears to be a more appropriate cofactor of PMDh.

3.4. EPR analysis of ApPMDh

EPR analysis was performed to identify the type and structure of the catalytic center of active ApPMDh. To exclude the possibility of artifactual metal ion binding, the polyhistidine tag was removed from purified ApPMDh (Supplementary Figure 3B). Tag-free ApPMDh was subjected for iron–sulfur cluster reconstruction in glycine-KOH buffer, pH10. UV–visible spectrum of the reconstructed tag-free ApPMDh had the value of A_{410}/A_{280} with 25.5%, suggesting the formation of the same iron–sulfur cluster with that in the reconstructed tagged-ApPMDh (Supplementary Figure 6). After concentration, the enzyme was treated with or without excess sodium dithionite and analyzed by EPR spectroscopy. We confirmed that reconstructed tag-free ApPMDh had activity of 1.00 ± 0.17 μmol/min/mg at pH10, which was comparable with 0.30 ± 0.17 μmol/min/mg of the reconstructed tagged ApPMDh in CHES buffer, pH9.6 (Figure 4A). In Figure 5A, we present the observed EPR spectra of dithionite-treated (top) and untreated (bottom) ApPMDh. The spectrum of dithionite-treated ApPMDh had clear rhombic-type EPR signals with $g_Z = 2.04$, $g_Y = 1.94$, and $g_X = 1.91$, whereas the untreated enzyme was almost EPR-silent and gave only a faint signal at $g = \sim 2.0$. The shape of the spectrum of dithionite-treated ApPMDh was similar to that reported for bovine mitochondrial aconitase (Emptage et al., 1983). The signals of dithionite-treated ApPMDh were detectable only at extremely low temperatures, ranging from 10 to 50 K, with the maximum strength obtained at approximately 25 K (Figure 5B). These properties of the spectrum, that is, its rhombic shape, appearance only after dithionite reduction, and dependence on extremely low temperatures, strongly suggest that ApPMDh has a [4Fe-4S]-type iron–sulfur cluster, rather than a [3Fe-4S] or [2Fe-2S] cluster (Lancaster et al., 1979; Beinert et al., 1996). Indeed, the EPR spectrum of dithionite-treated ApPMDh, which was presumably derived from an S = 1/2 ground spin state $[4Fe\text{-}4S]^{1+}$, was distinct from the reported EPR signal of dithionite-treated *cis*-3-hydroxy-L-proline dehydratase (type I AcnX) from *A. tumefaciens*, which had *g*-values of 2.02, 1.94, and 1.86, attributed to the [2Fe-2S] cluster (Watanabe et al., 2021).

The EPR spectrum of dithionite-treated bovine mitochondrial aconitase was reported to change in shape when citrate, a substrate of the enzyme, was added (Emptage et al., 1983). The *g*-values without the substrate were 2.06, 1.93, and 1.86, but when 0.1 mM citrate was added, the *g*-values shifted to 2.04, 1.85, and 1.78, respectively. This change in the EPR signal shape, along with data from other spectroscopic observations, such as Mössbauer and ENDOR, was attributed to the coordination of the substrate to the [4Fe-4S] cluster (Beinert et al., 1996). The coordination of a substrate, isocitrate or citrate, to a vacant iron in the [4Fe-4S] cluster of aconitase was clearly demonstrated by the crystal structures of mitochondrial aconitases from porcine and bovine sources (pdb#:7ACN, 1C96, and 1C97), in which the other three irons of the cluster were coordinated to three conserved Cys residues (Lauble et al., 1992; Beinert et al., 1996). Thus, we added approximately 0.5 mM of (*R,S*)-MVA5P, a substrate of ApPMDh, to an enzyme solution prepared as described above and performed EPR analysis after dithionite treatment. However, the observed EPR spectrum (Figure 5A, middle) was almost identical to that observed in the absence of the substrate (upper). This phenomenon implies that MVA5P might not bind to the catalytic center of ApPMDh when the iron–sulfur cluster is reduced to $[4Fe\text{-}4S]^{1+}$, possibly because $[4Fe\text{-}4S]^{2+}$ is the catalytically active species. However, the temperature dependence of the EPR spectrum differed in the absence and presence of the substrate (Figure 5B). The maximum EPR signal intensity was obtained at approximately 25 K in the absence of MVA5P, and the temperature of the maximum intensity decreased to 17.5 K when the substrate was added. The microwave power dependence of the EPR signal intensity also changed between dithionite-treated ApPMDh with and without MVA5P (Figure 5C). The $P_{1/2}$ value decreased from 130 mW to 65 mW, with the inhomogeneous parameter *b* of 1, with the addition of the substrate. These differences are likely indicative of the binding of the substrate near the cluster, but the similarity of the EPR spectra shapes suggests that the binding mode of MVA5P in ApPMDh could be different from that of citrate in aconitase and, therefore, would not significantly affect the structure and/or charge distribution of the [4Fe-4S] cluster.

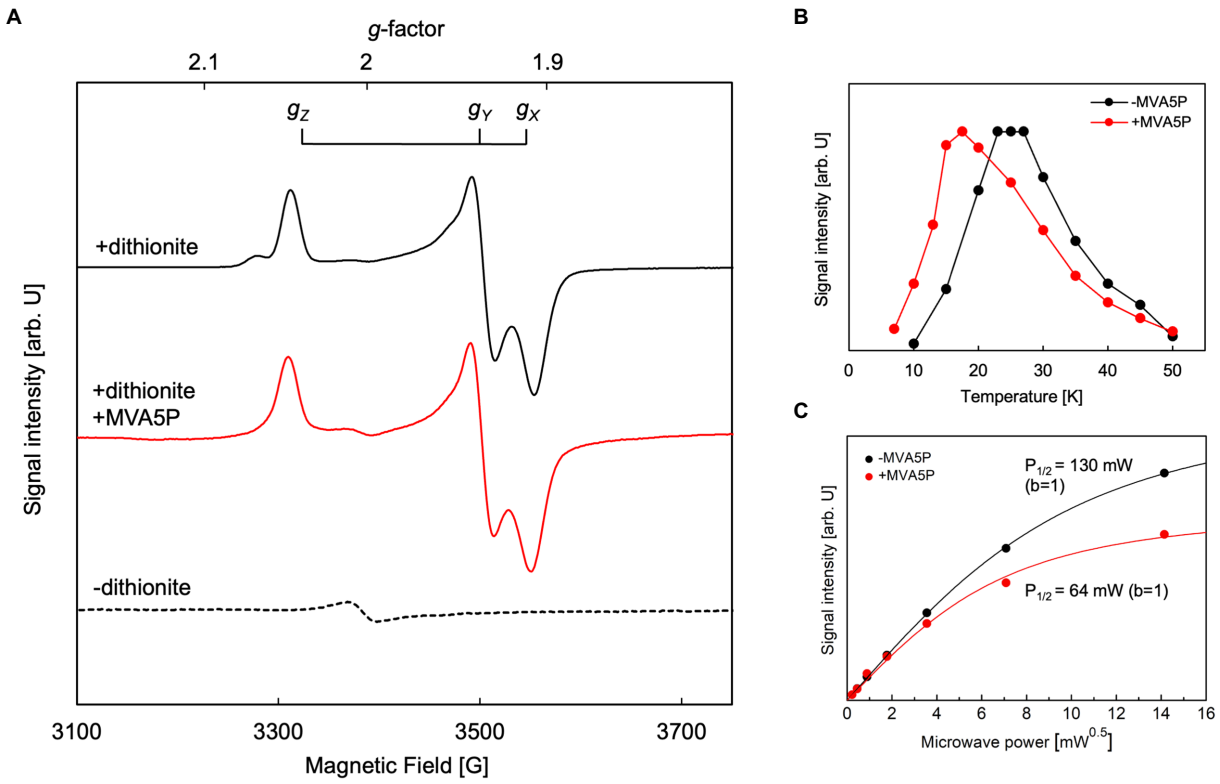

FIGURE 5
Electron paramagnetic resonance (EPR) analysis of *Aeropyrum pernix* phosphomevalonate dehydratase (ApPMDh). **(A)** EPR spectra of untreated ApPMDh at 25K (broken line), dithionite-treated ApPMDh at 19K (black line), and dithionite-treated ApPMDh in the presence of MVA5P at 17.5K (red line). Measurements were performed at microwave frequency of 9.48GHz. **(B)** Temperature dependence and **(C)** microwave power dependence at 25K of the EPR signal intensity of dithionite-treated ApPMDh. Data in the presence and absence of (*R*)-mevalonate 5-phosphate (MVA5P) are shown in red and black, respectively. Lines in **(C)** are the fitting curves based on Equation 1 in the Materials and Methods section.

3.5. Quantification of iron in ApPMDh

The enzyme was desalted and concentrated in an anaerobic chamber immediately after reconstruction of the iron–sulfur cluster of tag-free ApPMDh. The protein concentration of the enzyme solution was found to be 21.1 ± 1.6 μM. The solution was diluted and acidified with HCl, and the Fe^{2+} concentration was measured based on the formation of a colorimetric chelating complex after the reduction of iron ions. The iron concentration in the ApPMDh solution before dilution was determined to be 86.8 ± 2.6 μM. Therefore, the number of iron atoms contained in an ApPMDh molecule (the complex of the large and small subunits) was calculated to be 4.11. From both the results and EPR data, we concluded that a [4Fe-4S]-type iron–sulfur cluster exists in ApPMDh.

4. Discussion

In the present study, we revealed the enzymatic properties of an archaeal AcnX family enzyme, ApPMDh, which plays a key role in the recently discovered archaeal MVA pathway. Our results demonstrate that ApPMDh harbors a [4Fe-4S] cluster, similar to most hydratases/dehydratases belonging to the aconitase superfamily, whereas the previously reported crystal structures of TkPMDh contain a [3Fe-4S] cluster (Watanabe et al., 2021). Considering the fact that the [4Fe-4S] cluster of mitochondrial aconitase is known to be converted into a [3Fe-4S] cluster through oxidation (Lauble et al., 1992; Beinert et al., 1996), the [3Fe-4S] cluster observed *via* structural analysis of TkPMDh might also be derived from its original active form, the [4Fe-4S] cluster, as speculated by Watanabe et al. (2021). The existence of the [4Fe-4S] cluster is consistent with the oxygen- and H_2O_2-sensitivity of ApPMDh, which is distinct from the reported oxygen tolerance of the bacterial homolog and similar to the oxygen sensitivity of the usual aconitase-superfamily hydratases/dehydratases. The tolerance of ApPMDh to EDTA and iodoacetamide also resembles the reported insensitivity of aconitase toward these agents (Kennedy et al., 1983, 1988). Based on our finding that the [4Fe-4S] cluster is required for enzyme activity, the catalytic role of the iron–sulfur cluster in ApPMDh is thought to be similar to that of aconitase. If so, the vacant iron of the cluster, which is not bound to conserved cysteine residues unlike the other irons in the cluster, is thought to be coordinated to the tertiary hydroxyl group of MVA5P in the enzyme-substrate complex to catalyze its elimination or to a water molecule as a second substrate to catalyze the transfer of a hydroxyl group to tAHMP in the reverse reaction. Indeed, the MVA5P-complex structure of TkPMDh (pdb#:7CNS) recently reported by Watanabe et al. (2021) suggests that the substrate is bound in the proximity of the [3Fe-4S] cluster with an appropriate conformation to undergo dehydration if additional iron exists (Figure 6A). The EPR spectra of ApPMDh, however, did not change with the addition of the substrate MVA5P, unlike the spectra

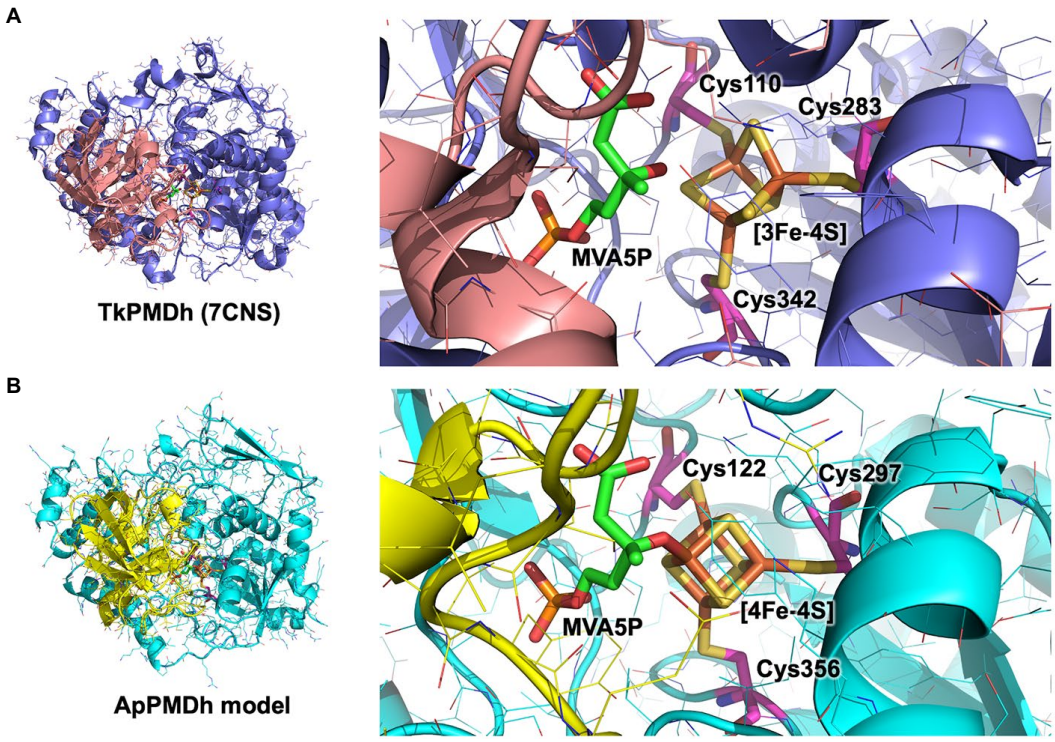

FIGURE 6
Putative catalytic center structure of *Aeropyrum pernix* phosphomevalonate dehydratase (ApPMDh). The structures of the overall protein complex (left) and the catalytic center containing an iron–sulfur cluster (right) of *Thermococcus kodakarensis* phosphomevalonate dehydratase (TkPMDh) [**(A)**, pdb#: 7CNS] are shown, along with those of modeled ApPMDh **(B)**. The large and small subunits of TkPMDh are colored in dark blue and orange, and those of ApPMDh are in cyan and yellow, respectively. (*R*)-mevalonate 5-phosphate (MVA5P) and cysteine residues coordinating the iron–sulfur cluster are represented in stick models in green and magenta, respectively. The structure model of apo-ApPMDh was constructed using Colabfold (Mirdita et al., 2022), after which the [4Fe-4S] cluster and MVA5P were manually added based on the aligned structure of putative TkPMDh (pdb#: 7CNS). The model of holo-ApPMDh was optimized *via* simplified molecular dynamics using Molby (Nagata, 2014).

of mitochondrial aconitase, which were largely affected by the addition of citrate (Emptage et al., 1983). This indicates that the electronic structure of the substrate-coordinating cluster in ApPMDh is similar to that of the substrate-free cluster, which is likely coordinated by a water molecule at the vacant iron. The MVA5P-complex structure of TkPMDh may explain this phenomenon. In the structure, neither the carboxyl group nor the phosphate group of MVA5P faces the [3Fe-4S] cluster because they are in contact with the surrounding residues, that is, Thr63, Ser130, and Lys361 for the carboxyl group and Gly48, Val49, Ser50, Asn53, Asn79, and Pro80 for the phosphate group. Thus, these ionized groups are unlikely to coordinate directly to the [4Fe-4S] cluster in the putative active form of the enzyme. In contrast, in both the citrate complex and isocitrate-complex structures of mammalian mitochondrial aconitase, a carboxyl group of the substrates was reported to interact with the vacant iron of the [4Fe-4S] cluster, as well as the hydroxyl group that would be eliminated (Lauble et al., 1992; Beinert et al., 1996). The interaction of the carboxyl group probably affects the electronic structure of the cluster, which would result in a significant change in the EPR spectra (Emptage et al., 1983). Based on these structural insights, we constructed a structural model of ApPMDh, whose large and small subunits have 38 and 44% sequence identities with those of TkPMDh, respectively (Figure 6B). In the modeled structure, three irons in the [4Fe-4S] cluster were coordinated by three cysteine residues, Cys122, Cys 297, and Cys356, and only the 3-hydroxyl group, not the carboxyl or phosphate group, of MVA5P was coordinated to the remaining iron.

Because ApPMDh, a type IIb AcnX, has a [4Fe-4S] cluster similar to other aconitase superfamily enzymes, it is surprising that its bacterial homolog, type I AcnX, uses a [2Fe-2S] cluster for the catalysis of hydroxyproline dehydration. Bacterial type I AcnX enzymes have been reported to be tolerant to oxidation (Watanabe et al., 2016), and this property might be attributed to the presence of the unusual [2Fe-2S] cluster. It remains unclear which type of iron–sulfur cluster exists in members of the other AcnX subfamilies. If a PMDh that utilizes a [2Fe-2S] cluster for catalysis is discovered or synthesized, it might be used for the bioproduction of isoprenoids through the ATP-saving archaeal MVA pathway (Hayakawa et al., 2018), as the existing archaeal MVA pathway is functional only under nearly anaerobic conditions when reconstructed in bacterial cells (Yoshida et al., 2020).

Data availability statement

The raw data supporting the conclusions of this article will be made available by the authors, without undue reservation.

Author contributions

MK and HH were involved in the study design, data analysis, and drafting of the article. MK, KK, HM, TI, and HH were involved in data acquisition. YY and TS provided reagents. All authors revised the

manuscript, approved the manuscript for publication, and agreed to be accountable for all aspects of the work in ensuring that questions related to the accuracy or integrity of any part of the work are appropriately investigated and resolved.

Funding

This work was supported by JSPS KAKENHI Grant Numbers 18 K19170, 19H04651 and 20H02899, and by grants-in-aid from the Institute for Fermentation, Osaka, the Noda Institute for Scientific Research, and the Nagase Scientific Technology Foundation for HH.

Acknowledgments

We are grateful to Michio M. Matsushita, Graduate School of Science, Nagoya University, for the preliminary EPR analysis and helpful suggestions. We thank Tohru Yoshimura, Graduate School of Bioagricultural Sciences, Nagoya University, for the helpful discussions.

Conflict of interest

The authors declare that the research was conducted in the absence of any commercial or financial relationships that could be construed as a potential conflict of interest.

Publisher's note

All claims expressed in this article are solely those of the authors and do not necessarily represent those of their affiliated organizations, or those of the publisher, the editors and the reviewers. Any product that may be evaluated in this article, or claim that may be made by its manufacturer, is not guaranteed or endorsed by the publisher.

Supplementary material

The Supplementary material for this article can be found online at: https://www.frontiersin.org/articles/10.3389/fmicb.2023.1150353/full#supplementary-material

References

Aoki, M., Vinokur, J., Motoyama, K., Ishikawa, R., Collazo, M., Cascio, D., et al. (2022). Crystal structure of mevalonate 3,5-bisphosphate decarboxylase reveals insight into the evolution of decarboxylases in the mevalonate metabolic pathways. *J. Biol. Chem.* 298:102111. doi: 10.1016/j.jbc.2022.102111

Azami, Y., Hattori, A., Nishimura, H., Kawaide, H., Yoshimura, T., and Hemmi, H. (2014). (R)-mevalonate 3-phosphate is an intermediate of the mevalonate pathway in Thermoplasma acidophilum. *J. Biol. Chem.* 289, 15957–15967. doi: 10.1074/jbc.M114.562686

Beinert, H., Kennedy, M. C., and Stout, C. D. (1996). Aconitase as iron-sulfur protein, enzyme, and iron-regulatory protein. *Chem. Rev.* 96, 2335–2374. doi: 10.1021/cr950040z

Case, D. A., Cheatham, T. E., Darden, T., Gohlke, H., Luo, R., Merz, K. M., et al. (2005). The Amber biomolecular simulation programs. *J. Comput. Chem.* 26, 1668–1688. doi: 10.1002/jcc.20290

Castro, L., Tortora, V., Mansilla, S., and Radi, R. (2019). Aconitases: non-redox iron-sulfur proteins sensitive to reactive species. *Acc. Chem. Res.* 52, 2609–2619. doi: 10.1021/acs.accounts.9b00150

Costello, L. C., Liu, Y. Y., Franklin, R. B., and Kennedy, M. C. (1997). Zinc inhibition of mitochondrial aconitase and its importance in citrate metabolism of prostate epithelial cells. *J. Biol. Chem.* 272, 28875–28881. doi: 10.1074/jbc.272.46.28875

Dellas, N., Thomas, S. T., Manning, G., and Noel, J. P. (2013). Discovery of a metabolic alternative to the classical mevalonate pathway. *elife* 2:e00672. doi: 10.7554/eLife.00672

Emptage, M. H., Dreyer, J. L., Kennedy, M. C., and Beinert, H. (1983). Optical and electron-paramagnetic-res characterization of different species of active and inactive Aconitase. *J. Biol. Chem.* 258, 11106–11111. doi: 10.1016/S0021-9258(17)44391-2

Freibert, S. A., Weiler, B. D., Bill, E., Pierik, A. J., Muhlenhoff, U., and Lill, R. (2018). Biochemical reconstitution and spectroscopic analysis of iron-sulfur proteins. *Fe-S Clust. Enzym.* 599, 197–226. doi: 10.1016/bs.mie.2017.11.034

Gruer, M. J., Artymiuk, P. J., and Guest, J. R. (1997). The aconitase family: three structural variations on a common theme. *Trends Biochem. Sci.* 22, 3–6. doi: 10.1016/S0968-0004(96)10069-4

Hayakawa, H., Motoyama, K., Sobue, F., Ito, T., Kawaide, H., Yoshimura, T., et al. (2018). Modified mevalonate pathway of the archaeon Aeropyrum pernix proceeds via trans-anhydromevalonate 5-phosphate. *Proc. Natl. Acad. Sci. U. S. A.* 115, 10034–10039. doi: 10.1073/pnas.1809154115

Katoh, K., Rozewicki, J., and Yamada, K. D. (2019). MAFFT online service: multiple sequence alignment, interactive sequence choice and visualization. *Brief. Bioinform.* 20, 1160–1166. doi: 10.1093/bib/bbx108

Kennedy, M. C., Emptage, M. H., Dreyer, J. L., and Beinert, H. (1983). The role of iron in the activation-inactivation of Aconitase. *J. Biol. Chem.* 258, 11098–11105. doi: 10.1016/S0021-9258(17)44390-0

Kennedy, M. C., Spoto, G., Emptage, M. H., and Beinert, H. (1988). The active-site sulfhydryl of Aconitase is not required for catalytic activity. *J. Biol. Chem.* 263, 8190–8193. doi: 10.1016/S0021-9258(18)68460-1

Lancaster, J. R., Vega, J. M., Kamin, H., Orme-Johnson, N. R., Orme-Johnson, W. H., Krueger, R. J., et al. (1979). Identification of the iron-sulfur center of spinach ferredoxin-nitrite reductase as a tetranuclear center, and preliminary EPR studies of mechanism. *J. Biol. Chem.* 254, 1268–1272. doi: 10.1016/S0021-9258(17)34197-2

Lauble, H., Kennedy, M. C., Beinert, H., and Stout, C. D. (1992). Crystal-structures of Aconitase with Isocitrate and Nitroisocitrate bound. *Biochemistry* 31, 2735–2748. doi: 10.1021/bi00125a014

Makarova, K. S., and Koonin, E. V. (2003). Filling a gap in the central metabolism of archaea: prediction of a novel aconitase by comparative-genomic analysis. *FEMS Microbiol. Lett.* 227, 17–23. doi: 10.1016/S0378-1097(03)00596-2

Mirdita, M., Schutze, K., Moriwaki, Y., Heo, L., Ovchinnikov, S., and Steinegger, M. (2022). ColabFold: making protein folding accessible to all. *Nat. Methods* 19, 679–682. doi: 10.1038/s41592-022-01488-1

Nagata, T. (2014). Molby: graphical molecular modeling software with integrated ruby interpreter. *Biol. Chem. Soc. Jpn.* 87, 902–904. doi: 10.1246/bcsj.20140093

Nishimura, H., Azami, Y., Miyagawa, M., Hashimoto, C., Yoshimura, T., and Hemmi, H. (2013). Biochemical evidence supporting the presence of the classical mevalonate pathway in the thermoacidophilic archaeon Sulfolobus solfataricus. *J. Biochem.* 153, 415–420. doi: 10.1093/jb/mvt006

Rossoni, L., Hall, S. J., Eastham, G., Licence, P., and Stephens, G. (2015). The putative mevalonate diphosphate decarboxylase from Picrophilus torridus is in reality a mevalonate-3-kinase with high potential for bioproduction of isobutene. *Appl. Environ. Microbiol.* 81, 2625–2634. doi: 10.1128/AEM.04033-14

Rupp, H., Rao, K. K., Hall, D. O., and Cammack, R. (1978). Electron spin relaxation of iron-Sulphur proteins studied by microwave power saturation. *Biochim. Biophys. Acta* 537, 255–269. doi: 10.1016/0005-2795(78)90509-3

Schneider, C. A., Rasband, W. S., and Eliceiri, K. W. (2012). NIH image to ImageJ: 25 years of image analysis. *Nat. Methods* 9, 671–675. doi: 10.1038/nmeth.2089

VanNice, J. C., Skaff, D. A., Keightley, A., Addo, J., Wyckoff, G. J., and Miziorko, H. M. (2014). Identification in Haloferax volcanii of Phosphomevalonate decarboxylase and Isopentenyl phosphate kinase as catalysts of the terminal enzymatic reactions in an Archaeal alternate Mevalonate pathway. *J. Bacteriol.* 196, 1055–1063. doi: 10.1128/JB.01230-13

Vinokur, J. M., Cummins, M. C., Korman, T. P., and Bowie, J. U. (2016). An adaptation to life in acid through a novel Mevalonate pathway. *Sci. Rep.* 6:39737. doi: 10.1038/srep39737

Vinokur, J. M., Korman, T. P., Cao, Z., and Bowie, J. U. (2014). Evidence of a novel mevalonate pathway in archaea. *Biochemistry* 53, 4161–4168. doi: 10.1021/bi500566q

Vinokur, J. M., Korman, T. P., Sawaya, M. R., Collazo, M., Cascio, D., and Bowie, J. U. (2015). Structural analysis of mevalonate-3-kinase provides insight into the mechanisms of isoprenoid pathway decarboxylases. *Protein Sci.* 24, 212–220. doi: 10.1002/pro.2607

Volz, K. (2008). The functional duality of iron regulatory protein 1. *Curr. Opin. Struc. Biol.* 18, 106–111. doi: 10.1016/j.sbi.2007.12.010

Watanabe, S., Fukumori, F., Miyazaki, M., Tagami, S., and Watanabe, Y. (2017). Characterization of a novel cis-3-Hydroxy-l-Proline dehydratase and a trans-3-Hydroxy-l-Proline dehydratase from bacteria. *J. Bacteriol.* 199, e00255–e00217. doi: 10.1128/JB.00255-17

Watanabe, S., Murase, Y., Watanabe, Y., Sakurai, Y., and Tajima, K. (2021). Crystal structures of aconitase X enzymes from bacteria and archaea provide insights into the molecular evolution of the aconitase superfamily. *Commun. Biol.* 4:687. doi: 10.1038/s42003-021-02147-5

Watanabe, S., Tajima, K., Fujii, S., Fukumori, F., Hara, R., Fukuda, R., et al. (2016). Functional characterization of aconitase X as a cis-3-hydroxy-L-proline dehydratase. *Sci. Rep.* 6:38720. doi: 10.1038/srep38720

Williams, C. H., Stillman, T. J., Barynin, V. V., Sedelnikova, S. E., Tang, Y., Green, J., et al. (2002). E-coli aconitase B structure reveals a HEAT-like domain with implications for protein-protein recognition. *Nat. Struct. Biol.* 9, 447–452. doi: 10.1038/nsb801

Yasuno, Y., Nakayama, A., Saito, K., Kitsuwa, K., Okamura, H., Komeyama, M., et al. (2021). Total synthesis and structure confirmation of trans-Anhydromevalonate-5-phosphate, a key biosynthetic intermediate of the Archaeal Mevalonate pathway. *J. Nat. Prod.* 84, 2749–2754. doi: 10.1021/acs.jnatprod.1c00615

Yoshida, R., Yoshimura, T., and Hemmi, H. (2020). Reconstruction of the "Archaeal" Mevalonate pathway from the Methanogenic archaeon *Methanosarcina mazei* in *Escherichia coli* cells. *Appl. Environ. Microbiol.* 86, e02889–e02819. doi: 10.1128/AEM.02889-19

frontiers | Frontiers in Microbiology

TYPE Original Research
PUBLISHED 13 December 2023
DOI 10.3389/fmicb.2023.1273211

OPEN ACCESS

EDITED BY
Long Jin,
Nanjing Forestry University, China

REVIEWED BY
Xuesong Luo,
Huazhong Agricultural University, China
Yantao Liang,
Ocean University of China, China

*CORRESPONDENCE
Qian Liu
✉ liuqian@sio.org.cn

†These authors have contributed equally to this work and share first authorship

RECEIVED 05 August 2023
ACCEPTED 09 November 2023
PUBLISHED 13 December 2023

CITATION
Liu Q, Chen Y and Xu X-W (2023) Genomic insight into strategy, interaction and evolution of nitrifiers in metabolizing key labile-dissolved organic nitrogen in different environmental niches.
Front. Microbiol. 14:1273211.
doi: 10.3389/fmicb.2023.1273211

Genomic insight into strategy, interaction and evolution of nitrifiers in metabolizing key labile-dissolved organic nitrogen in different environmental niches

Qian Liu[1,2,3*†], Yuhao Chen[2,4†] and Xue-Wei Xu[2,3,4]

[1]Donghai Laboratory, Zhoushan, Zhejiang, China, [2]Key Laboratory of Marine Ecosystem Dynamics, Second Institute of Oceanography, Ministry of Natural Resources, Hangzhou, Zhejiang, China, [3]Ocean College, Zhejiang University, Hangzhou, Zhejiang, China, [4]School of Oceanography, Shanghai Jiao Tong University, Shanghai, China

Ammonia-oxidizing archaea (AOA) and bacteria (AOB), nitrite-oxidizing bacteria (NOB), and complete ammonia oxidizers (comammox) are responsible for nitrification in nature; however, some groups have been reported to utilize labile-dissolved organic nitrogen (LDON) for satisfying nitrogen demands. To understand the universality of their capacity of LDON metabolism, we collected 70 complete genomes of AOA, AOB, NOB, and comammox from typical environments for exploring their potentials in the metabolism of representative LDON (urea, polyamines, cyanate, taurine, glycine betaine, and methylamine). Genomic analyses showed that urea was the most popular LDON used by nitrifiers. Each group harbored unique urea transporter genes (AOA: *dur3* and *utp*, AOB: *utp*, and NOB and comammox: *urtABCDE* and *utp*) accompanied by urease genes *ureABC*. The differentiation in the substrate affinity of these transporters implied the divergence of urea utilization efficiency in nitrifiers, potentially driving them into different niches. The cyanate transporter (*cynABD* and *focA/nirC*) and degradation (*cynS*) genes were detected mostly in NOB, indicating their preference for a wide range of nitrogen substrates to satisfy high nitrogen demands. The lack of genes involved in the metabolism of polyamines, taurine, glycine betaine, and methylamines in most of nitrifiers suggested that they were not able to serve as a source of ammonium, only if they were degraded or oxidized extracellularly as previously reported. The phylogenetic analyses assisted with comparisons of GC% and the Codon Adaptation Index between target genes and whole genomes of nitrifiers implied that urea metabolic genes *dur3* and *ureC* in AOA evolved independently from bacteria during the transition from *Thaumarchaeota* to AOA, while *utp* in terrestrial AOA was acquired from bacteria via lateral gene transfer (LGT). Cyanate transporter genes *cynS* and *focA*/*nirC* detected only in a terrestrial AOA *Candidadus* Nitrsosphaera gargensis Ga9.2 could be gained synchronously with *Nitrospira* of NOB by an ancient LGT. Our results indicated that LDON utilization was a common feature in nitrifiers, but metabolic potentials were different among nitrifiers, possibly being intensely interacted with their niches, survival strategies, and evolutions.

KEYWORDS

ammonia-oxidizing archaea, ammonia-oxidizing bacteria, nitrite-oxidizing bacteria, comammox, dissolved organic nitrogen, urea, polyamine, cyanate

1 Introduction

Labile-dissolved organic nitrogen (LDON) compounds are the groups with low-molecule weights and rapid turnover rates in the environments (Sipler et al., 2013). They are generally produced from the degradation of proteins or released from primary producers (e.g., phytoplankton in the ocean), and preferentially taken up by heterotrophic bacteria as nitrogen sources (e.g., Liu et al., 2016, 2022b; Damashek et al., 2019). LDON compounds generally include dissolved free amino acids, urea, polyamines, methylamines, taurine, cyanate, and glycine betaine. Their uptake contributes significantly to bacterial nitrogen demands and enhances nitrogen cycling (e.g., Jørgensen, 2006; Liu et al., 2015, 2022a; Clifford et al., 2019). In addition, photoautotrophic phytoplankton in the ocean can also assimilate or oxidize LDON for acquiring nitrogen and energy, especially in N-limiting environments (Glibert et al., 2016). In recent years, more studies reveal that the chemoautotrophic prokaryotes involved in nitrification (e.g., *Nitrospinae* and *Thaumarchaeota*) may be capable of utilizing LDON for enhancing or sustaining the growth as well (Koch et al., 2015; Qin et al., 2017; Kitzinger et al., 2019, 2020).

The nitrification process is one of the most important steps in the nitrogen cycle driven by a complex microbial consortium (Voss et al., 2013), including ammonia-oxidizing archaea (AOA) and bacteria (AOB), nitrite-oxidizing bacteria (NOB), and complete ammonia oxidizer (comammox; He et al., 2018). They are key players in global nitrogen and carbon cycles (Bayer et al., 2019). AOA and AOB perform ammonia oxidation, the first and rate-limiting step of nitrification (Könneke et al., 2005), and NOB catalyze the second step of nitrification by oxidizing nitrite to nitrate (Daims et al., 2016). Comammox are capable of converting ammonia to nitrate in one step (Hu and He, 2017). AOA usually outcompete AOB for ammonia and play a major role in controlling ammonia oxidation in most environments due to their relatively higher affinity for ammonia (Stahl and de la Torre, 2012). They are mainly categorized into four phylogenetic lineages, namely, *Nitrosopumilales* (Group I.1a), "*Ca*. Nitrosotaleales" (Group I.1a-associated), *Nitrososphaerales* (Group I.1b), and "*Ca*. Nitrosocaldales" (Jung et al., 2022). AOB are commonly detected in ammonia-rich environments, such as sewage treatment plants, eutrophic freshwater, coastal waters, and soil (Soliman and Eldyasti, 2018). A total of five genera have been identified as AOB, in which *Nitrosomonas*, *Nitrosospira*, *Nitrosovibrio*, and *Nitrosolobus* belong to the subclass β-Proteobacteria and *Nitrosococcus* to the subclass γ-Proteobacteria. Among all known NOB, the genus *Nitrospira* appears to be most widespread and phylogenetically diverse in different habitats (Koch et al., 2015). *Nitrospira* strains are well adapted to low nitrite concentrations and form at least six phylogenetic lineages that are globally distributed in soils, oceans, freshwater, hot springs, etc. (Koch et al., 2015). *Nitrospinae* are the dominant marine NOB and can reach high abundances (up to ~10% of the microbial community) in mesopelagic zones, oxygen minimum zones (OMZs), deep-sea waters, and sediments (Daims et al., 2016). The comammox *Nitrospira* are abundant in natural and engineered habitats. It is reported that comammox may functionally outcompete other canonical nitrifiers under highly oligotrophic conditions (Hu and He, 2017).

The capability of utilizing extracellular LDON may increase nitrogen assimilation and be beneficial for the production of energy and biomass of nitrifiers (Kitzinger et al., 2019). Ammonia oxidizers (AOM) have been suggested to utilize extracellular LDON as an alternative source of ammonia under the situation of ammonia limitation (Sliekers et al., 2004; Qin et al., 2017), while NOB use them for reciprocal feeding with AOM (Palatinszky et al., 2015). The urea utilization has been detected in verified experiments for AOA strains *Ca*. Nitrososphaera gargensis Ga9.2, *N. viennensis* EN76, and *Nitrosopumilus ureiphilus* PS0 (Wetzel et al., 2011; Qin et al., 2014; Damashek et al., 2019), AOB strains *Nitrosomonas oligotropha* and *N. ureae* (Tourna et al., 2011; Spang et al., 2012; Qin et al., 2014), and NOB *Nitrospira moscoviensis* (Sliekers et al., 2004). The field samples collected from marine environments also reveal that AOA and *Nitrospinae* of NOB can incorporate urea-and cyanate-derived nitrogen at significantly higher rates than other microorganisms (Kitzinger et al., 2018, 2020). A recent study in the Gulf of Mexico found that AOA mainly used ammonium, while most of the cellular nitrogen-demand of *Nitrospinae* was met by the assimilation of urea and cyanate (Kitzinger et al., 2020). The alternative utilization of LDON for avoiding the competition with ammonia-oxidizing microbes may be a key factor for ecological success of NOB (Kitzinger et al., 2020). Moreover, the metagenome-assembled genomes (MAGs) of *Nitrospinae* encode ABC-type transporter of spermidine, amino acids, and peptides, an indication for their additional nitrogen sources for growth (Kitzinger et al., 2020). Therefore, the potential of nitrifiers in utilizing LDON could be related to their survival strategies.

Although a few studies have showed that nitrifying microbes are capable of utilizing LDON based on both laboratory experiments or genomic analysis (Tourna et al., 2011; Palatinszky et al., 2015; Qin et al., 2017), as more strains are identified from different habitats, little has been done to systematically catalog the metabolic potential of LDON of these nitrifiers from different environments for understanding their utilization mechanisms and strategies. Whether it is a common metabolic process or only occurs in certain environments needs more investigation. Moreover, since the availability of LDON increases rapidly as a consequence of anthropogenic impact, especially in estuary and coastal waters (Seitzinger et al., 2002), assessing the potentials of nitrifiers in the utilization of LDON can further explore the ecological role of LDON in the ecosystem. To fill this gap, we compared metabolic potentials of LDON among AOA, AOB, NOB, and comammox, and between marine and terrestrial taxa based on genomic analyses, to discuss mechanisms and strategies of LDON utilization by nitrifiers in different environments.

2 Materials and methods

2.1 Genomic information collection

The complete genome sequences of representative AOA ($n = 46$), AOB ($n = 10$), NOB ($n = 12$), and comammox ($n = 2$) strains were collected from National Center for Biotechnology Information (NCBI; https://www.ncbi.nlm.nih.gov/), Joint Genome Institute (JGI; https://jgi.doe.gov/), or Beijing Institute of Genomics Data Center (BIGD; https://ngdc.cncb.ac.cn/) according to the accession number (Supplementary Table S1). The dataset included all available genomes from isolated and enriched AOA strains, representatives of available genomes of AOB and NOB, and selected metagenomic-assembled genomes (MAGs, completeness >70%, low completeness could result

in non-detection of target genes) of nitrifiers from extreme marine environments (Supplementary Table S1). Diverse habitats from both marine (e.g., sediment, estuary, coastal seawater, and deep-sea) and terrestrial (e.g., soil, freshwater, and wastewater treatment plant) environments were covered for the subsequent analysis and comparison (Supplementary Table S1).

2.2 Cell volume estimation

We recorded the shape, width, and length of cells for collected AOA, AOB, NOB, and comammox according to the description in the literature (Supplementary Table S2). The ratio of surface area and cell volume (SA/V) was estimated assuming a spherical cell based on equation (1) (Pachiadaki et al., 2017). The SA/V ratio of a rod-shaped cell was calculated with equation (2) (Boyde and Williams, 1971). Cell widths and lengths used in the formula were means of values in corresponding references (Supplementary Table S2).

$$\frac{S}{V}=\frac{\pi\times \mathrm{d}^2}{\frac{4}{3}\times\pi\times\left(\frac{d}{2}\right)^3} \quad (1)$$

$$\frac{SA}{V}=\frac{\pi\times \mathrm{d}\times \mathrm{h}+2\times\pi\times\left(\frac{d}{2}\right)^2}{\pi\times\left(\frac{d}{2}\right)^2\times h} \quad (2)$$

where V is the cell volume, d is the cell diameter, h is the cell length, and SA is the surface area.

2.3 Gene collection and genome annotation

Amino acid sequences of key functional genes related to ammonia oxidation, and transport, biosynthesis, and degradation of selected LDON compounds (urea, polyamines, cyanate, taurine, glycine betaine, and methylamines) were collected from the NCBI (Figure 1; Supplementary Table S3) for the subsequent alignment with genomes of AOA, AOB, NOB, and comammox strains. They included genes encoding ammonia monooxygenase (*amoABC*, K10944-K10946; Zhang et al., 2023), bacteria-type urea ABC transporter (*urtABCDE*, K11959-K11963; Veaudor et al., 2019), a prokaryote-origin mammalian urea transporter (*utp*, K08717; Minocha et al., 2003; Levin et al., 2009; Spang et al., 2012), urea active transporter (*dur3*, K20989) generally detected in marine unicellular photosynthetic eukaryotes (Solomon et al., 2010), urease (*ureABC*, K01428-K01430; *ureDFG*, K03188-K03190; *ureE*, K03187; Veaudor et al., 2019), polyamine ABC transporter (spermidine-preferential ABC transporter, *potABCD*, K11069-K11072; putrescine ABC transporter, *potFGHI*, K11073-K11076; Mou et al., 2010), cyanate ABC transporter (*cynABD*, K15576, K15577, and K15579; Maeda and Omata, 2009), a formate–nitrite transporter (FNT, *focA*/*nirC*, K21990) functioning in cyanate assimilation in cyanobacteria (Maeda and Omata, 2009), cyanase (*cynS*, K01725; Taubert et al., 2017), taurine ABC transporter (*tauACB*, K15551, K15552, and K10831; Cook and Denger, 2006; Rohwerder, 2020), glycine betaine transporter (*opuD*, K05020; Wetzel et al., 2011; Boysen et al., 2022), trimethylamine (TMA) monooxygenase (*tmm*, K18277), glutamate-methylamine (GMA) synthetase (*gmaS*, K01949), N-Methyl-L-glutamate (NMG) synthase (*mgsABC*, K22081-K22083), NMG dehydrogenase (*mgdABCD*, K22084-K22087), methylamine dehydrogenase (*mauAB*, K15228, K15229) in methylamines metabolism (Chen, 2012; Taubert et al., 2017), and enzymes involved in polyamine biosynthesis (*speA*, K01585; *speB*, K01480; *speC*, K01581; *speE*, K00797; *aguA*, K10536; *aguB*, K12251) and catabolism (*puuA*, K09470; *spuC*, K12256; *kauB*, K12254; *gabT*, K07250; *spdH*, K00316; Mou et al., 2010, 2011), taurine degradation (*tauD*, K03119; *tpa*, K03851; *xsc*, K03852; *pta*, K13788; *tauXY*, K07255 and K07256; Cook and Denger, 2006; Rohwerder, 2020), glycine betaine synthesis (*betAB*, K00108, and K00130), and catabolism (*gbcAB*, K00479, and K21832; *bhmt*, K00544; *grdHI*, K21579, and K21578; *cdh*, K17735; Wetzel et al., 2011; Boysen et al., 2022). The genome-wide gene annotation was carried out through the website of Rapid Annotation using Subsystem Technology (RAST, https://rast.nmpdr.org/) with all collected genomes of AOA, AOB, NOB, and comammox. RAST annotation results and the NCBI database were used to identify homologs of targeted genes (Supplementary Table S3). All functional gene sequences were subjected to BLASTp. The amino acid sequence with a percent identity to the reference gene (Supplementary Table S3) greater than 40% was considered to be the homolog of the target gene (Pearson, 2013).

2.4 Phylogenetic analysis of key functional genes

To demonstrate the evolution of functional genes involved in LDON metabolism, phylogenetic trees were constructed with amino acid sequences for key genes by maximum likelihood based on the model of Le and Gascuel (2008) with 1,000 bootstrap replications using the software MEGA 7.0 (Kumar et al., 2016). The amino acid sequences were aligned using Clustal W (Thompson et al., 1994). The best model was used after the alignment (Hall, 2013). Models with the lowest Bayesian information criterion (BIC) score were considered to best describe the substitution pattern (Bast, 2013). A discrete gamma distribution was used to model differences of evolutionary rates among sites [five categories (+G)]. For *utp* and *focA*/*nirC*, the rate variation model allowed for some sites to be evolutionarily invariable ([+I]). All phylogenetic trees were drawn to scale with branch lengths measured in the number of substitutions per site.

The GC contents of key genes of selected AOA, AOB, NOB, and comammox, and outgroup species in phylogenetic analyses were calculated using GC Content Calculator,[1] while those of whole genomes were obtained from the NCBI database.[2] The values of the Codon Adaptation Index (CAI) of the same group of genes and whole genomes of selected nitrifiers and outgroup species were calculated using an online CAI calculator.[3]

1 https://www.biologicscorp.com/tools/GCContent/

2 http://www.ncbi.nlm.nih.gov

3 https://www.biologicscorp.com/tools/CAICalculator

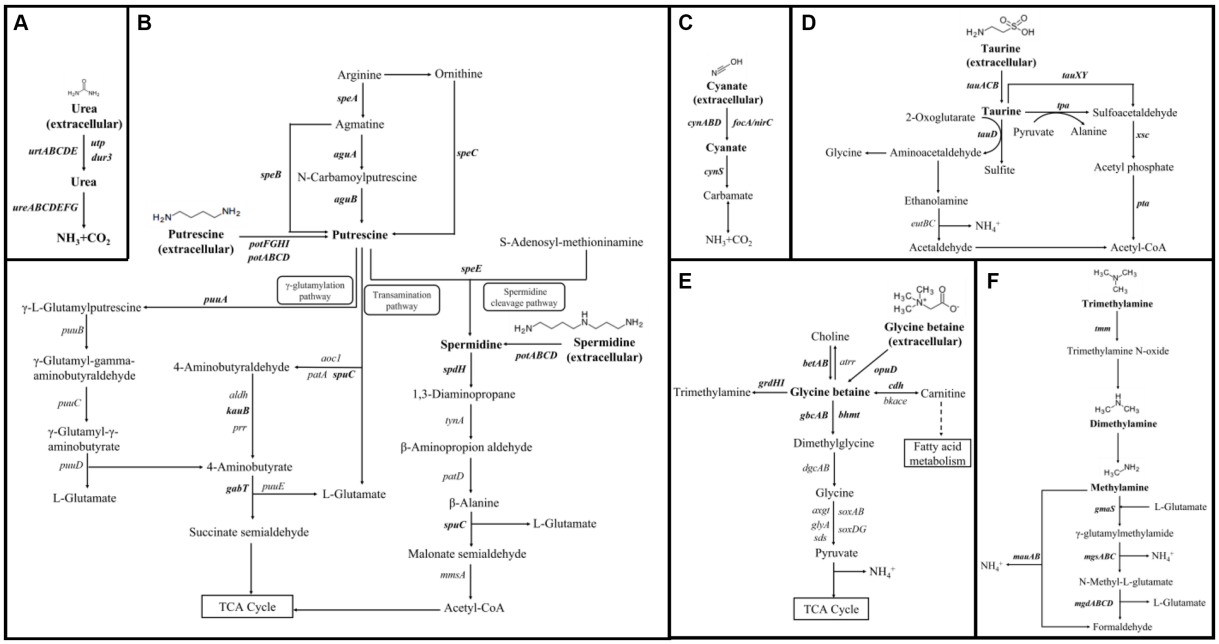

FIGURE 1
Metabolic pathways and products of representative labile-dissolved organic nitrogen (LDON), including **(A)** urea (Spang et al., 2012; Veaudor et al., 2019), **(B)** polyamines (Igarashi and Kashiwagi, 2010; Mou et al., 2011), **(C)** cyanate (Maeda and Omata, 2009; Palatinszky et al., 2015), **(D)** taurine (Cook and Denger, 2006; Engelberts et al., 2020; Rohwerder, 2020), **(E)** glycine betaine (Li et al., 2021; Boysen et al., 2022), and **(F)** methylamine (Chen, 2012; Taubert et al., 2017). Gene involved in metabolic processes are listed in italics. The LDON compounds and genes investigated in this study are highlighted in bold. Black dotted arrows represent the potential fates of molecules.

2.5 Data and material availability

Genome sequence data are available in NCBI, JGI, or BIGD databases, and their accession numbers are listed in Supplementary Table S1. All other data products associated with this study are available from the corresponding authors upon request.

3 Results

3.1 Genomic and phenotypic characteristics of collected nitrifiers

Collected strains of AOA belonging to the genera *Nitrosopumilus*, *Nitrosopelagicus*, *Nitrosomarinus*, and *Cenarchaeum* were all of marine origin ($n = 26$). The genera *Nitrosarchaeum*, *Nitrosotenuis*, *Nitrosotalea*, *Nitrososphaera*, *Nitrosocosmicus*, and *Nitrosocaldus* were mostly from terrestrial environments, including hot springs, lakes, and soil ($n = 20$; Supplementary Table S1). Only strains *Ca*. Nitrosarchaeum limnium SFB1 and BG20 were enriched from marine environments (Supplementary Table S1). In AOB, all three *Nitrosococcus* strains were enriched from marine environments, and *Nitrosomonas* strains and *Ca*. Nitrosacidococcus tergens sp. RJ19 were terrestrial (Supplementary Table S1). *Nitrospina gracilis*, *Nitrospira marina* Nb-295, *Ca*. Nitrohelix vancouverensis, and *Ca*. Nitronauta litoralis of NOB were inhabited in marine environments, and two *Nitrobacter* strains, *Ca*. Nitrotoga arctica, and the rest of *Nitrospira* species including two comammox *Ca*. N. inopinata and *Ca*. N. kreftii were terrestrial origin (Supplementary Table S1).

Since functional and genomic characteristics of the comammox were similar to NOB, we grouped them into NOB for the subsequent analysis. The total genome length of AOB (1.81–4.08 Mb, median: 3.16 Mb, $n = 10$) was smaller than NOB (3.08–4.69 Mb, median: 3.91 Mb, $n = 14$; one-way ANOVA and Dunn's method, $p < 0.01$) but larger than AOA (1.05–3.43 Mb, median: 1.85 Mb, $n = 46$; $p < 0.01$; Figure 2A; Supplementary Table S1). The GC contents of NOB ranging from 47.2 to 62.0% (median: 56.1%, $n = 14$) were greater than AOB ranging from 37.0 to 51.6% (47.1%, $n = 10$; one-way ANOVA and Dunn's method, $p < 0.01$), and they were both greater than those of AOA (31.4–57.4%, 36.7%, $n = 46$; $p < 0.01$). Only the GC contents of marine AOA *Cenarchaeum symbiosum* A and two terrestrial species *Nitrososphaera viennensis* EN76 and *Ca*. N. evergladensis SR1 were over 50%. Marine AOA exhibited significantly smaller total genome lengths and GC contents than terrestrial ones ($p < 0.05$, Student's *t*-test), but there was no difference observed between marine and terrestrial AOB or NOB ($p > 0.05$). In addition, it showed that bacterial or archaeal strains of the same genus had similar GC contents and total genome lengths (Figure 2A; Supplementary Table S1). The SA/V ratios of AOA (4.62–23.4 μm^{-1}, 13.8 μm^{-1}, $n = 26$) were larger than those of AOB (2.79–24.0 μm^{-1}, 8.30 μm^{-1}, $n = 8$; one-way ANOVA and Dunn's method, $p < 0.05$), but the ratios of NOB (0.93–24.2 μm^{-1}, 12.9 μm^{-1}, $n = 10$) were not significantly different from those of AOA and AOB ($p > 0.05$; Figure 2B). The SA/V ratios of collected marine AOA (15.4–23.4 μm^{-1}, 19.6 μm^{-1}, $n = 10$) were larger than those of terrestrial ones (4.62–22.9 μm^{-1}, 10.13 μm^{-1}, $n = 16$; one-way ANOVA and Dunn's method, $p < 0.01$), but the ratios of AOB and NOB did not show the same trend ($p > 0.05$; Figure 2B). The GC content and the SA/V ratio were positively ($R = 0.783$) and negatively ($R = 0.326$)

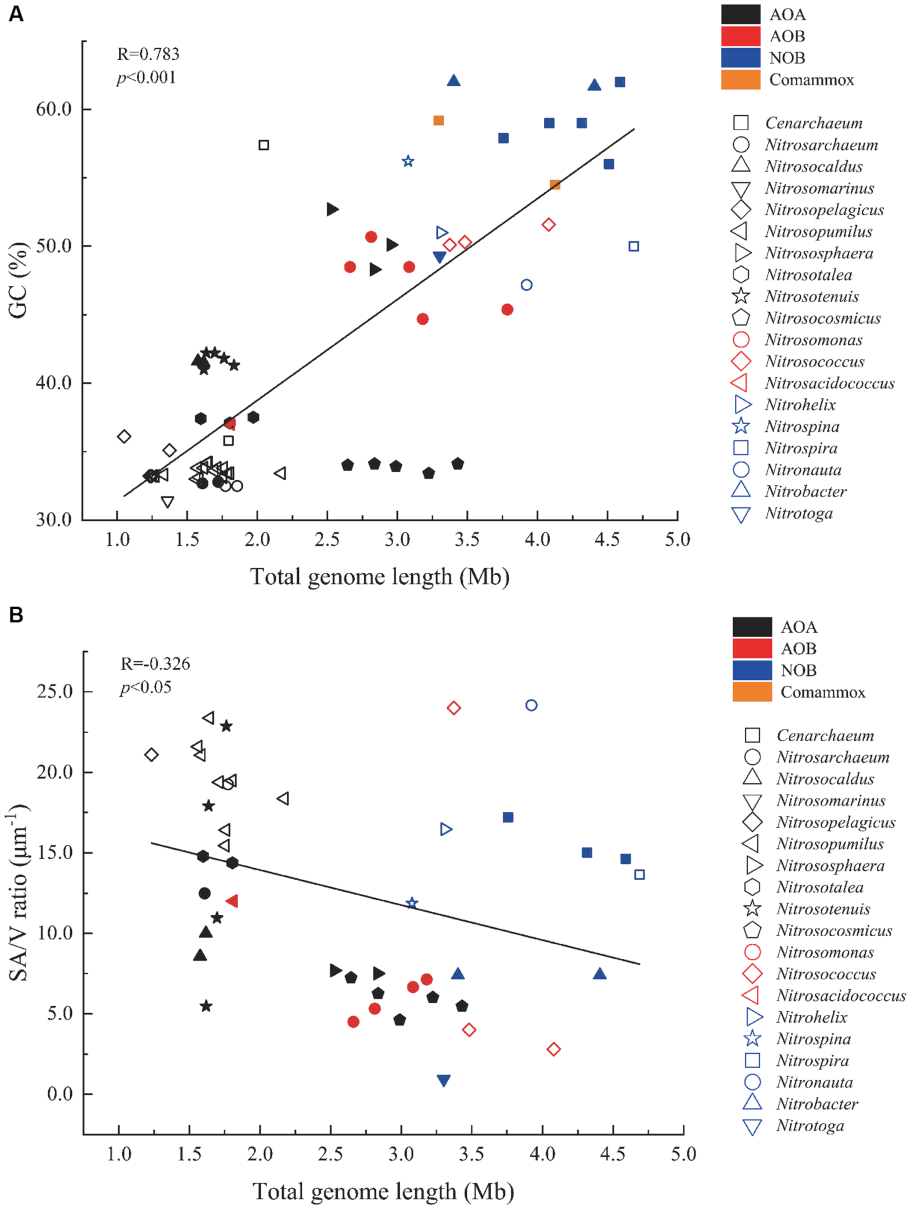

FIGURE 2
Scatter plots of correlations between **(A)** GC content (%) and total genome length (Mb) and between **(B)** SA/V ratio (μm^{-1}) and total genome length (Mb) of selected nitrifiers. The Pearson correlation coefficient (R) of each plot is listed. Filled and open symbols represent strains from terrestrial and marine environments, representatively. AOA, Ammonia-oxidizing archaea; AOB, Ammonia-oxidizing bacteria; NOB, Nitrite-oxidizing bacteria; and Comammox, Complete ammonia oxidizers.

correlated with the genome length, respectively (Pearson's correlation, $p < 0.05$; Figure 2).

3.2 Distributions of *amo* and metabolic genes of representative LDON in genomes of nitrifiers

In AOA, *Ca*. Nitrosotalea okcheonensis CS and *Nitrosopumilus piranensis* D3C had two copies of *amoA* and *amoB*, respectively, and *Nitrosopumilus ureiphilus* PS0, *Ca*. Nitrosotenuis uzonensis N4, *Ca*. Nitrososphaera gargensis Ga9.2, and *Ca*. Nitrosocosmicus agrestis SS contained two copies of *amoC*. Two terrestrial AOA, namely, *Nitrososphaera viennensis* EN76 and *Ca*. N. evergladensis SR1, had six and seven copies of *amoC* gene, respectively (Figure 3). In AOB, all strains in genus *Nitrosococcus* ($n = 3$) and *Ca*. *Nitrosacidococcus tergens* sp. RJ19 only contained one copy of *amoABC*, in contrary to multiple ones in the genus *Nitrosomonas* (Figure 3). Two *Nitrospira* strains of the comammox contained one copy of *amoABC* as well.

In AOA, none of the collected genomes contains bacteria-type urea ABC transporter genes *urtABCDE*. Instead, most harbored the gene *dur3* accompanied by urease-encoding genes *ureABC* and *ureDEFG* (Figure 3). In addition, the genomes of terrestrial genera *Nitrososphaera*, *Nitrosocosmicus*, and *Nitrosocaldus* also contained the

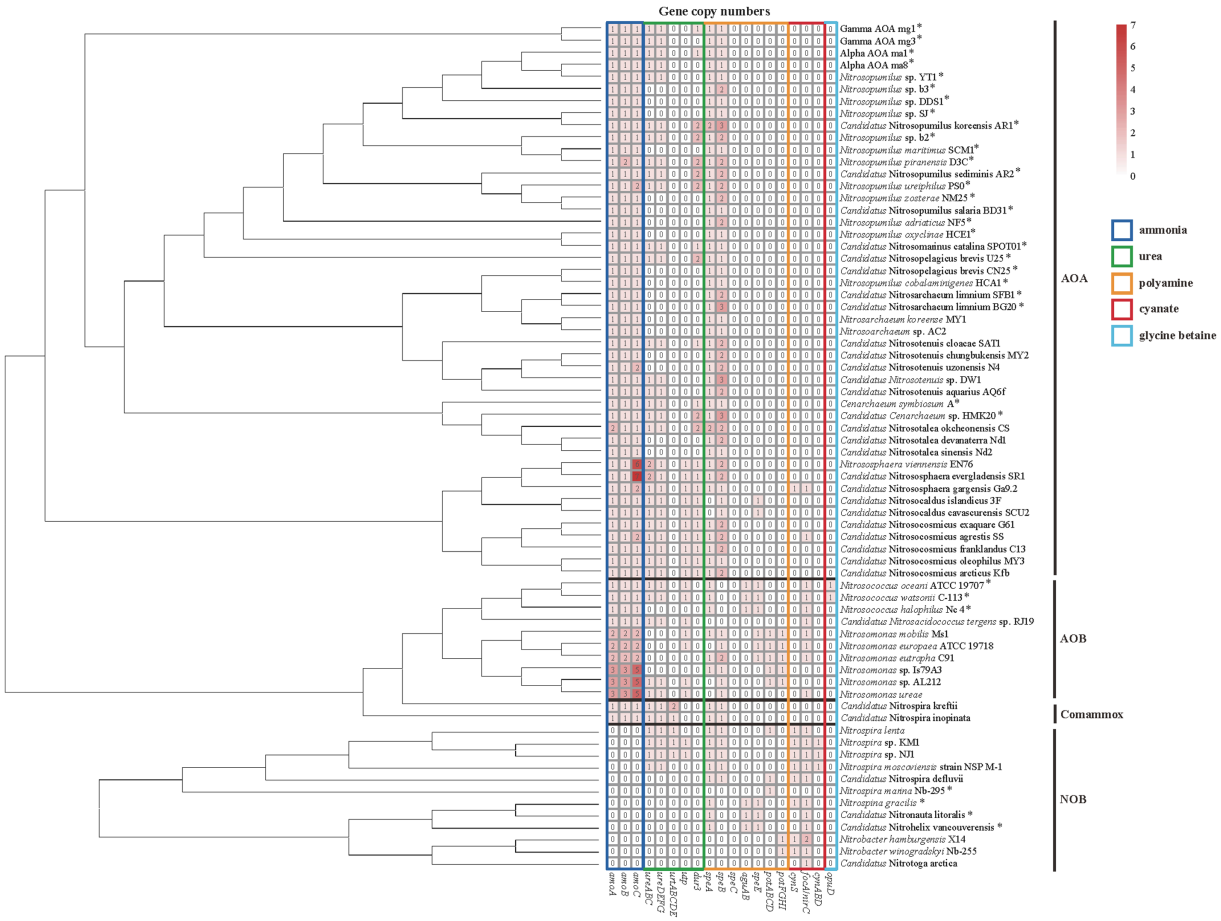

FIGURE 3
Heatmap of copy numbers of metabolic genes of ammonia (dark blue box), urea (green box), polyamine (orange box), cyanate (red box), and glycine betaine (GBT; light blue box). The strain with an asterisk represents the marine origin. The phylogenetic tree of amino acid sequences of *amoA* is used for the classification of ammonia-oxidizing archaea (AOA), ammonia-oxidizing bacteria (AOB), and complete ammonia oxidizers (Comammox) and that of 16S rRNA gene is used for the classification of nitrite-oxidizing bacteria (NOB).

gene *utp* (Figure 3). The marine AOA including *Nitrosopumilus* strains which contained the gene *dur3*, *Ca.* Nitrosopelagicus brevis U25 and *Ca. Cenarchaeum* sp. HMK 20, and the terrestrial one *Ca.* Nitrosotalea okcheonensis CS had two copies of *dur3*. Two *Nitrososphaera* strains, namely, *Ca.* N. evergladensis SR1 and *N. viennensis* EN76, harbored two copies of *ureABC* (Figure 3). The genomes of *Nitrosopumilus* sp. YT1, Alpha AOA ma8, Gamma AOA mg3, *Ca. Nitrosotenuis* sp. DW1, and *Ca.* N. aquarius AQ6f harbored urease genes but were not detected with any type of urea transporter genes (Figure 3). All collected strains in the genus *Nitrosarchaeum* did not contain genes related to urea utilization (Figure 3). The ordering of *ureABC* and *ureEFGD* in AOA was contiguous or spaced by a small number of genes (Figure 4A). Except Alpha AOA ma1, Gamma AOA mg1, and *Ca.* Nitrosotenuis cloacae SAT1, the genes *utp* and *dur3* were in close proximity to *ure* in AOA, and *utp* was closer to *ure* than *dur3* when both genes were present (Figure 4A). In AOB, genomes of two *Nitrosococcus* strains, *N. oceani* ATCC 19707 and *N. watsonii* C-113, four *Nitrosomonas* strains, *N. mobilis* Ms1, *N. europaea* ATCC 19718, *Nitrosomonas* sp. AL212 and *N. ureae*, and *Ca. Nitrosacidococcus tergens* sp. RJ19 harbored the gene *utp*, but *N. mobilis* Ms1 and *N. europaea* ATCC 19718 did not carry *ure* genes (Figure 3). The gene *ureD* was divided from *ureEFG* by *ureABC*, and *utp* was adjacent to *ureD* or *ureG* (Figure 4A). The complete set of urea transporter genes *urtABCDE* was only found in genomes of two comammox, and *Nitrospira* sp. KM1, *Nitrospira* sp. NJ1, and *N. lenta* of NOB in the neighbor of *ureABC* and *ureDFG*. The comammox *Ca.* Nitrospira kreftii contained a second copy of *urtABCDE* that was distantly away from *ure* (2236 interval open reading frames; Figures 3, 4A). The gene *utp* was present close to *ureA* in genomes of *Nitrospira* sp. KM1 and *Nitrospira* sp. NJ1 (Figures 3, 4A). The gene *ureE* was absent in genomes of NOB and comammox except in that of *Nitrospira* sp. NJ1 (Figure 4A).

None of the collected AOA and comammox genomes harbored polyamine transporter genes (*potABCD* and *potFGHI*; Figure 3). *Nitrosomonas* strains of AOB contained *potABCD* and *potFGHI* except *N. ureae*. *Nitrospira lenta*, *Ca.* N. defluvii, and *N. marina* Nb-295 of NOB harbored *potABCD*, while two *Nitrobacter* strains owned *potFGHI* (Figure 3). Genes encoding enzymes for complete pathways of putrescine catabolism were absent in all genomes of collected nitrifiers (Figures 1B, 3). The genomic evidence showed that all AOA, *Nitrosomonas* of AOB, and most *Nitrospira* of NOB and comammox might be capable of synthesizing polyamines intracellularly by arginine

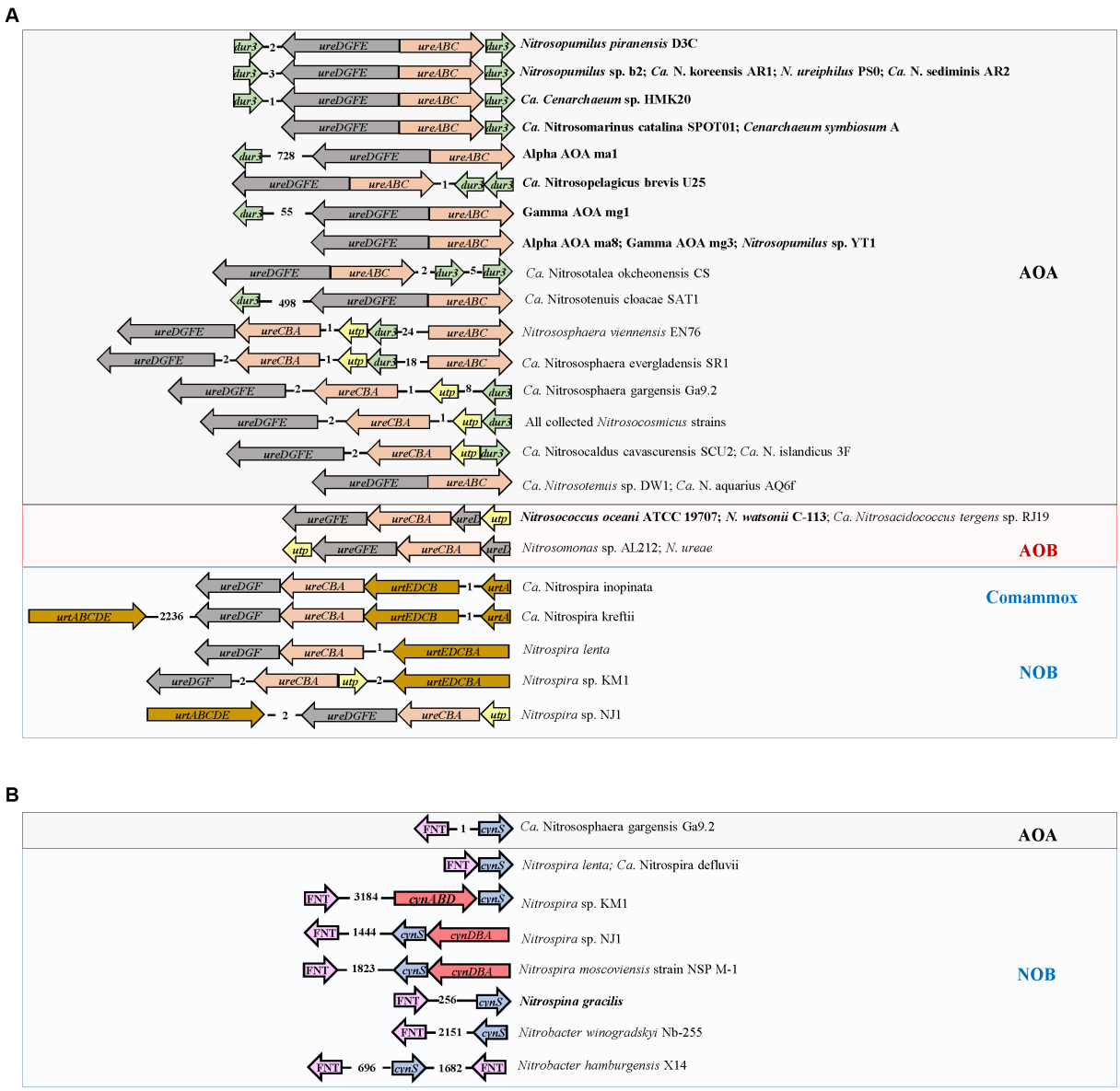

FIGURE 4
Organization of **(A)** genes encoding urease (*ure*) and urea transporter (*utp*, *dur3*, and *urt*) in genomes of ammonia-oxidizing archaea (AOA) and bacteria (AOB), nitrite-oxidizing bacteria (NOB), and complete ammonia oxidizers (Comammox), and **(B)** genes encoding cyanase (*cynS*), the FNT family (*focA/nirC*), and cyanate ABC transporter (*cynABD*) in genomes of AOA and NOB. The numbers between two genes indicate the number of interval open reading frames (ORFs). The strains highlighted in bold represent marine origin.

decarboxylase [EC: 4.1.1.19] and agmatinase [EC: 3.5.5.11] encoded by *speA* and *speB*, respectively (Figures 1B, 3). Most of AOA contained 2–3 copies of *speB* (Figures 1B, 3). *Nitrosococcus* of AOB, and NOB strains *Nitrospina gracilis*, *Ca.* Nitrohelix vancouverensis, and *Ca.* Nitronauta litoralis were lack of *speB* but owned *aguAB* encoding agmatine deiminase [EC: 3.5.3.12] and N-carbamoylputrescine amidase [EC: 3.5.1.53] for an alternative pathway to synthesize putrescine from agmatine (Figures 1B, 3). The gene *speC* encoding ornithine decarboxylase which could convert ornithine to putrescine was not found in these bacteria and archaea (Figures 1B, 3).

The cyanate ABC-type transporter encoding genes *cynABD* were only detected in *Nitrospira moscoviensis* strain NSP M-1, *Nitrospira* sp. KM1, and *Nitrospira* sp. NJ1 of NOB, accompanied by the gene *cynS* encoding cyanase (Figure 3). The genes *cynABD* were in the neighbor of *cynS* (Figure 4B). In addition, the gene *cynS* was also present in *Ca.* Nitrososphaera gargensis Ga9.2 of AOA, and *Nitrospira lenta*, *Ca.* N. defluvii, *Nitrobacter hamburgensis* X14, and *N. winogradskyi* Nb-255 of NOB (Figure 3), but they only contained the FNT family gene *focA/nirC*, which were more common in AOB and NOB (Figure 3). Among the nine strains possessing *cynS*, the gene *focA/nirC* was adjacent to *cynS in Ca.* N. gargensis Ga9.2, *N. lenta*, and *Ca.* N. defluvii (Figure 4B) but was distantly away from *cynS* (over 256 interval open reading frames) in remaining genomes of NOB (Figure 4B).

The GBT transporter gene *opuD* was only detected in genomes of two AOB strains *Nitrosococcus oceani* ATCC 19707 and *N. watsonii* C-113 (Figure 3), but genes functioning in GBT synthesis and degradation, such as *betAB*, *gbcAB*, *bhmt*, *grdHI*, and *cdh* (Figure 1E), were absent in all genomes of collected nitrifiers. In additions, genes encoding enzymes involved in the utilization of taurine (*tauACB*, *tauD*, *tpa*, *tauXY*, *xsc*, and *pta*) and methylamine (*tmm*, *mauAB*, *gmaS*, *mgsABC*, and *mgdABCD*; Figures 1D,F) were not found in any genome of collected nitrifiers.

3.3 Phylogenetic relationships of key genes involved in urea and cyanate utilization

Thirty-one amino acid sequences of *dur3* from AOA strains were analyzed for phylogenetic relationship (Figure 5A). The sequence of *dur3* in the genome of *Micromonas commoda* was selected as the out-group because *dur3* was originally detected in eukaryotic organisms (Coimbra, 2022). In AOA with two copies of *dur3*, we considered the copy closer to *ure* genes as Copy 1 and the other as Copy 2 for subsequential phylogenetic analysis (Figures 4A, 5A). Basically, the sequences from terrestrial and marine AOA were well divided into two clusters except that Copy 2 of *dur3* from marine AOA strains formed a close relationship with those from terrestrial genera *Nitrososphaera* and *Nitrosocaldus* (Figure 5A; Supplementary Table S4). The Copy 1 sequences of *dur3* from marine AOA genus were homogeneous to that of *M. commoda*, which also included Copy 2 of *dur3* from a terrestrial strain *Ca.* Nitrosotalea okcheonensis CS (Figure 5A). The phylogenetic analysis grouped 10 amino acid sequences of the gene *utp* from AOAs, 7 from AOBs, and 2 from NOBs. The sequence of *utp* of Deltaproteobacteria *Desulfovibrio vulgaris* DP4 was used as an out-group because it possessed a homologous urea transporter gene (*utp*) found in mammals (Levin et al., 2009; Figure 5B). The sequences of *utp* from NOB and AOB were homologous to that of *D. vulgaris* DP4 and distinguished from the cluster of AOA (Figure 5B). The amino acid sequence of *ureC* from a marine α-proteobacterium *Ruegeria pomeroyi* DSS-3 was used as an out-group for constructing a phylogenetic tree of *ureC* (Figure 5C). *Ruegeria pomeroyi* DSS-3 is a heterotrophic bacterium ubiquitous in marine environments and is capable of degrading urea with urease (Ferrer-González et al., 2023). Similarly, the sequences of *ureC* from archaea and bacteria were distinctively divided into two groups (Figure 5C). In AOA, the sequences from genera *Nitrosocosmicus* and *Nitrososphaera* belonging to the order of *Nitrososphaerales* (Group I.1b) were clustered with *Nitrosocaldus* of the order *Ca.* Nitrosocaldales except for the second copies of *ureC* in genomes of *Nitrososphaera viennensis* EN76 and *Ca.* N. evergladensis SR1. They were more phylogenetically close to sequences from the genus *Nitrosotalea* belonging to the order *Ca.* Nitrosotaleales (Group I.1a-associated) and the order *Nitrosopumilales* mostly comprised of marine AOA (Figure 5C). The amino acid sequences of *ureC* from AOB, NOB, and comammox were tightly clustered and homologous to that of *R. pomeroyi* DSS-3 (Figure 5C).

Amino acid sequences of *cynS* and the FNT family gene *focA*/*nirC* from *Ca.* Nitrososphaera gargensis Ga9.2 and NOB strains were individually analyzed for the phylogenetic relationship with corresponding sequences from the out-group *Prochlorococcus marinus* since the genes were mostly found in marine cyanobacterial strains and their functions had been verified (Maeda and Omata, 2009; Maeda et al., 2015; Figure 6). The *cynS* sequence of *Ca.* N. gargensis Ga9.2 was clustered with those of *Nitrospira* and distinguished from two *Nitrobacter* strains and the marine AOB *Nitrospina gracilis*, which were phylogenetically close to *P. marinus* (Figure 6A). Differently, in the phylogenetic tree of the gene *focA*/*nirC*, in addition to three *Nitrospira* strains, *Nitrospira* sp. NJ1, *Nitrospira* sp. KM1, and *N. Moscoviensis* strain NSP M-1, the sequence of *Ca.* N. gargensis Ga9.2 was also clustered with those of two Nitrobacter strains, which were closely related to that of *P. marinus* (Figure 6B). The gene *focA*/*nirC* of the marine AOB *N. gracilis* grouped with those from *Nitrospira lenta* and *Ca.* N. defluvii and the second copy of *focA*/*nirC* in *Nitrobacter hamburgensis* X14 (Figure 6B).

4 Discussion

4.1 Genomic and phenotypic characteristics of nitrifiers reflecting nitrogen availability and affinity of nitrifiers

Although we did not collect genomes of all nitrifiers, such as those identified by MAG and single-cell sequencing, the genomes of isolated and enriched nitrifier strains as well as several MAGs from extreme environments could act as representatives of typical habitats (Supplementary Table S1). The genomic analysis and comparison were believed to be vigorous to gain insights into differences in physiological and metabolic characteristics among AOA, AOB, NOB, and comammox.

Generally, AOA have smaller genome lengths and lower GC contents than AOB and NOB (Figure 2A; Supplementary Table S1). The environmental differences in ecological niches may lead to this differentiation, in line with survival strategy and nitrogen metabolic capacity (Kitzinger et al., 2020). Previous studies on bacteria showed that those with large chromosomes usually had higher GC contents (Guo et al., 2009). Genomes lacking GC may be beneficial to the survival in nitrogen-limiting environments because AT pairs use one less nitrogen than GC pairs (Luo et al., 2015). Thus, low GC contents in AOA indicated nitrogen limitation in their niches, especially those in marine environments. The limited capacity of using LDON may also prohibit the access of nitrogen to AOA (Figure 3). However, great SA/V ratios of marine AOA suggested a high affinity of ammonia for compensating low concentrations in marine environments. More copies of urea transporter gene *dur3* corresponding to higher SA/V ratios might be a strategy for conquering nitrogen limitation as well ($R = 0.754$, $p = 0.003$, Spearman rank correlation; Supplementary Figure S1). The group *Nitrosocosmicus* had a large genome size (2.64–3.63 Mb) but a low GC content (33.4–34.1%; Figure 2A; Supplementary Table S1) probably due to its extreme low affinity of NH_3 plus NH_4^+ (Jung et al., 2022), although the surrounding environment might not be limited by nitrogen (e.g., waste water plant treatment; Sauder et al., 2017). NOB generally had larger GC contents in response to greater genome lengths (Figure 2A), suggesting either nitrogen sufficiency in their habitats or their great efficiency to absorb substrates from the environment. The larger SA/V ratio of most collected NOB (e.g., *Nitronauta*, *Nitrohelix*, and *Nitrospira*) implied the latter circumstance, but the potential of using diverse nitrogen sources (e.g., urea and cyanate; Figure 3) might enhance their

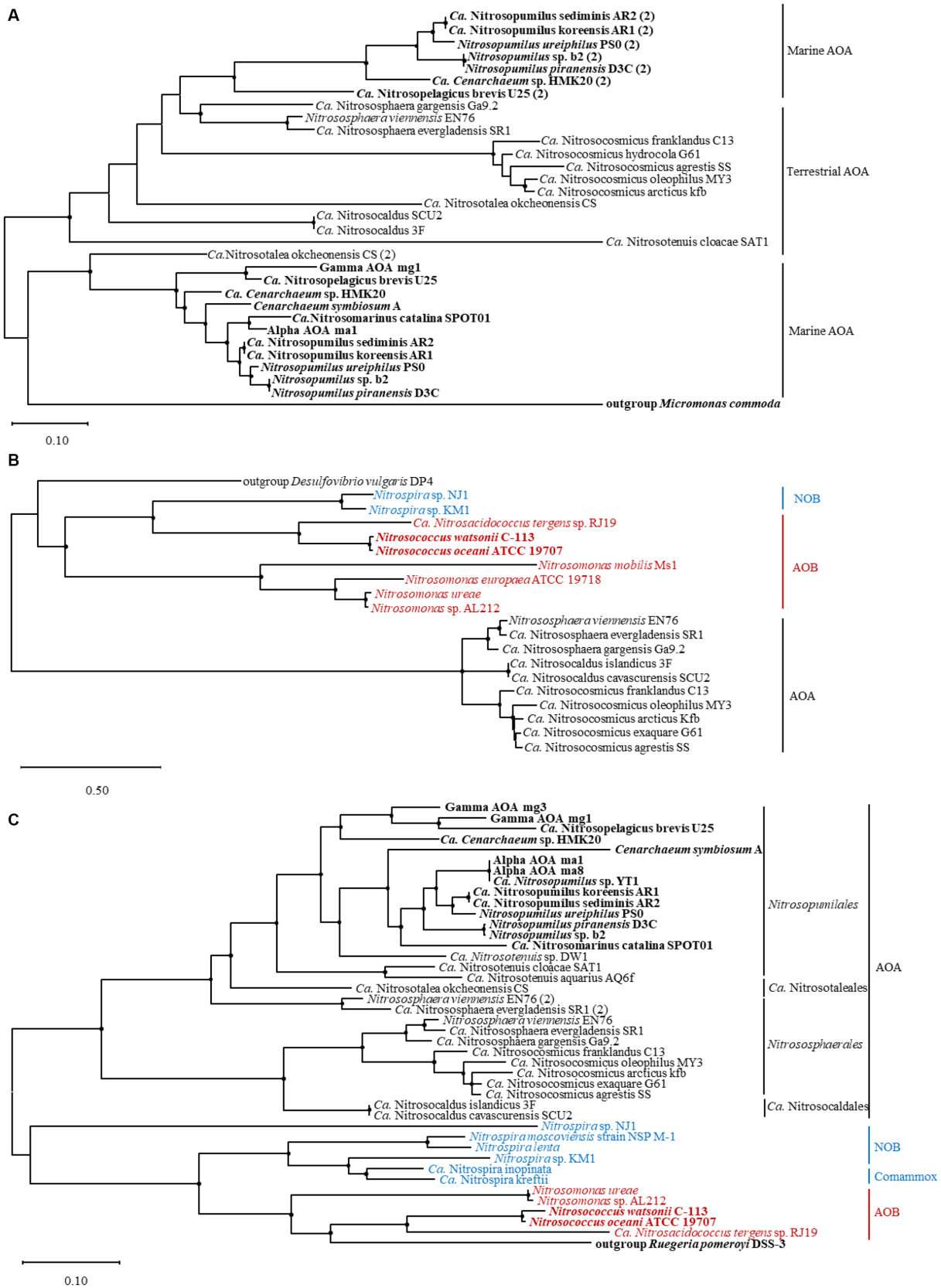

Figure 5

FIGURE 5
Phylogenetic trees of amino acid fragments of **(A)** *dur3*, **(B)** *utp*, and **(C)** *ureC* identified from ammonia-oxidizing archaea (AOA) and bacteria (AOB), nitrite-oxidizing bacteria (NOB) and complete ammonia oxidizers (Comammox). The trees are constructed with the maximum likelihood method. Bootstrap values based on 1,000 replicates are indicated for the major branches, and the values >50 are shown as black dots. The numbers in brackets indicate the second copy of *dur3* or *ureC* from the same strain. The strains highlighted in bold represent marine origin.

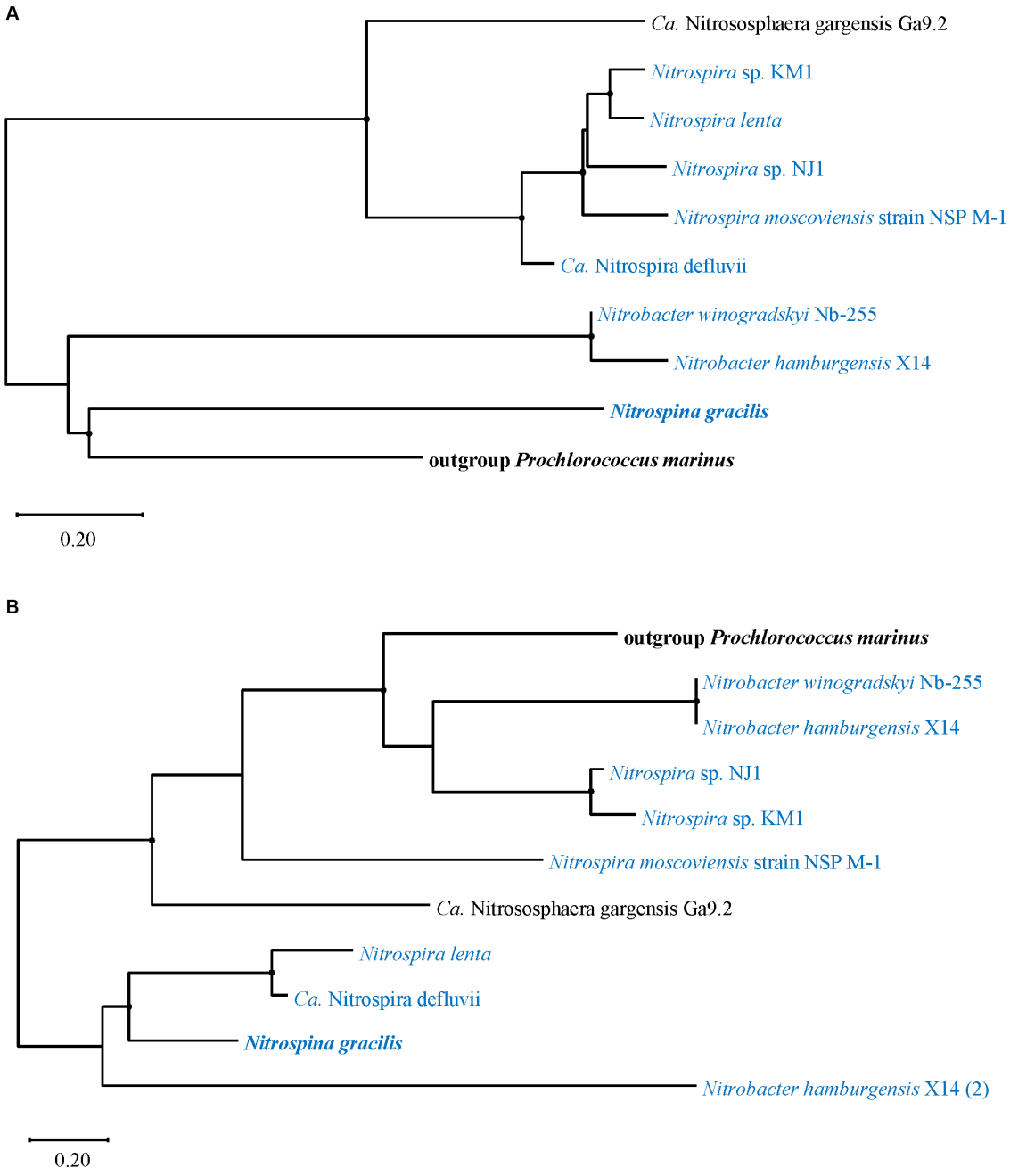

FIGURE 6
Phylogenetic trees of amino acid fragments of **(A)** *cynS* and **(B)** the FNT family gene *focA/nirC* identified from ammonia-oxidizing archaea (AOA) and nitrite-oxidizing bacteria (NOB). The strains shown in panel **(B)** are selected as ones which also contain *cynS*. The trees are constructed with the maximum likelihood method. Bootstrap values based on 1,000 replicates are indicated for the major branches, and the values >50 are shown as black dots. The numbers in brackets indicate the second copy of *focA/nirC* from the same strain. The strains highlighted in bold represent marine origin.

versatility of acquiring nitrogen from the environment, resulting in increased GC content and genome length. The relatively greater GC contents but lower SA/V ratios of AOB compared to AOA could be the consequence of AOB survival in substrate-rich environments with increased nitrogen availability (Soliman and Eldyasti, 2018). Thus, the genomic (e.g., GC%) and phenotypic characteristics (e.g., SA/V) of nitrifiers might reveal their niche partitioning as the basis of their capability and efficiency of nitrogen utilization for environmental adaptation.

4.2 Strategy of urea and cyanate utilization being intensely to characteristics of environmental niches and nitrogen demand of nitrifiers

Most of the collected AOA harbor urease genes (*ureABC* and *ureDEFG*; Figure 3); however, urea ABC transporter genes *urtABCDE* commonly detected in bacterial genomes (Veaudor et al., 2019) were not found in any collected AOA. Instead, two types of urea transporter

genes *dur3* (Solomon et al., 2010) and *utp* (Bossé et al., 2001) were present in AOA harboring *ure* genes except *Ca*. *Nitrosotenuis* sp. DW1, *Ca*. N. aquarius AQ6f, *Nitrosopumilus* sp. YT1, Alpha AOA ma8, and Gamma AOA mg3 (Figure 3). Since nitrite production has been detected in the enrichment culture of *Ca*. N. aquarius AQ6f with urea (Sauder et al., 2018), it suggests that these five strains may contain unknown urea transporter proteins, or urea could diffuse across the cell membrane without active transports (Sauder et al., 2018). The genes *utp* and *dur3* are both present in genera belonging to Group I.1b (*Nitrososphaera and Nitrososcosmicus*) and *Nitrosocaldus*, while *dur3* is the only urea-transporter gene in genomes of Group I.1a (*Nitrosopumilus*, *Nitrosopelagicus*, and *Nitrosotenuis*) and Group I.1a-associated (*Nitrosotalea*) strains (Figures 3, 4A). The verified growth of two *Nitrososphaera* strains and *Nitrosopumilus ureiphilus* PS0 in media added with urea suggests that the urea transporter encoded by *dur3* is functional; however, whether *dur3* is functional requires further experimental validation because some AOA lacking *dur3* or *utp* can also hydrolyze urea without the known transporters (Sauder et al., 2018). In addition, the presence of two copies of *dur3* in the genus *Nitrosopumilus* except *Nitrosopumilus* sp. YT1, and *Ca*. Nitrosopelagicus brevis U25 from marine environments (Figure 3) could be the result of the low availability of urea, which triggers marine AOA to produce more transporter proteins for efficiently utilizing urea (Offre et al., 2014). The protein Dur3 has been demonstrated to encode a high-affinity urea active transporter in marine unicellular photosynthetic eukaryotes (Solomon et al., 2010). Thus, AOA may be advantageous in urea uptake, corresponding to their higher urea uptake rates in several marine ecosystem (e.g., polar waters, the Gulf of Mexico, and coastal Georgia; Alonso-Sáez et al., 2012; Tolar et al., 2016; Kitzinger et al., 2019). The homogeneity of Copy 2 of *dur3* in marine AOA to those in genomes of terrestrial ones indicates lateral gene transfer (LGT) of genes from terrestrial AOA (Figure 5A). The gene *utp* identified in genomes of some terrestrial AOA appears simultaneously with *dur3* (Figures 3, 4A). Since the protein Utp has been considered as a low-affinity urea transporter (Bossé et al., 2001; Raunser et al., 2009), the presence of *utp* in terrestrial AOA could be due to the complex terrestrial environments (wastewater treatment plant, agricultural soils, mud, etc.) with the detection of high urea concentrations (Rittstieg et al., 2001; Wang et al., 2012); however, whether the urea transporter protein encoded by *utp* functions in AOA as an alternative way of urea transport by Dur3 still needs further experimental verification.

The urea transporter encoding gene *dur3* was not detected in genomes of selected AOB and NOB, but instead it was replaced by *utp* and *urt*, respectively (Figures 3, 4A). Genomes of *Nitrosococcus oceani* ATCC 19707, *N. watsonii* C-113, *Nitrosomonas* sp. AL212, *N. ureae* and *Ca*. *Nitrosacidococcus tergens* sp. RJ19 of AOB processed both *utp* and *ure*, while terrestrial AOB *Nitrosomonas mobilis* Ms1 and *N. europaea* ATCC 19718 only possessed a copy of *utp* (Figure 3). Nitrite has been found rapidly produced from *N. oceani* ATCC19707 cultured in the medium with urea replacing ammonia (Koper et al., 2004), suggesting that *utp* functions as a urea transporter. Assimilated urea could be efficiently degraded and used as a source of NH_4^+ by AOB. *Nitrosococcus oceani* is an AOB species distributed ubiquitously in the oceanic environment and is an important nitrifier in the OMZ (Lam et al., 2009). It incorporates with anammox bacteria and is responsible for nitrogen loss (Woebken et al., 2008). Thus, *N. oceani* may be responsible for urea hydrolyzation and subsequential oxidization of ammonia in the OMZ. Urease activity in *N. europaea* ATCC 19718 has been experimentally proven absent (de Boer and Laanbroek, 1989; Sliekers et al., 2004), consistent with the genomic evidence (Figure 3). The presence of *utp* without the co-occurrence of urease genes is probably due to its non-specificity for urea. It may also facilitate the diffusion of urea analogs along their concentration gradients (Levin et al., 2009). The detection of *utp* only in AOB implies the advantage of AOA with both *utp* and *dur3* in utilizing urea in different environments because they may alternate the urea transporter depending on urea concentrations.

Genomes of collected NOB and comammox have a full set of *urt* and *ure* genes (Figures 3, 4A), indicating that they are capable of urea utilization. The ureolytic activity has been observed in the culture of *Nitrospira moscoviensis*, *Ca*. N. nitrosa, and *Ca*. N. nitrificans with urea-containing media (Koch et al., 2015; Van Kessel et al., 2015; Vijayan et al., 2021). The gene cluster *urt* is a high-affinity urea transporter (Valladares et al., 2002), suggesting that *Nitrospira* has a competitive advantage in urea uptake in environments with low urea concentrations. Since *Nitrospira* occur ubiquitously in different terrestrial and aquatic habitats (Latocheski et al., 2022), it is tempting to speculate that reciprocal feeding between *Nitrospira* and AOM could be a common phenomenon in nature, but their contribution to total nitrification in different ecosystems remains to be determined. The marine NOB (*Nitrospira marina* Nb-295, *Ca*. Nitronauta litoralis, *Ca*. Nitrohelix vancouverensis, and *Nitrospina gracilis*) do not contain any urea-related gene (Figure 3); however, although the genome of the type strain *N. gracilis* of the genus *Nitrospinae* does not contain ureases genes, other clades of *Nitrospinae* (e.g., *Nitrospinae* Clade 2 in the Gulf of Mexico, Kitzinger et al., 2020) representing the major groups of NOB in marine environments commonly contain complete sets of urea transporter and urease genes, and form an intense relationship of reciprocal feeding with AOM (Koch et al., 2015; Pachiadaki et al., 2017). In addition, in NOB, only *Nitrospira* sp. KM1 and *Nitrospira* sp. NJ1 own *utp* (Figures 3, 4A). The reason that both AOB and NOB lack the gene *dur3* could be due to the fact that *dur3* of AOA was derived from the same ancestor as that of eukaryotes (Figure 5A; Levin et al., 2009; Spang et al., 2012). The gene *utp* of terrestrial AOA may evolve from bacteria through LGT (Figure 5B). Overall, the genes *dur3* and *utp* may be functional and encode proteins for urea transport from extracellular environments; however, as evidence shows that AOM harboring these two genes have a lower urea uptake rate than those with *urt*, such as *Nitrospira* or other heterotrophic bacteria (Vijayan et al., 2021), it suggests that urea may be the alternative energy and nitrogen source of AOM, which still use ammonia or ammonium as their major substrate (Kitzinger et al., 2020). It is noted that most of *Nitrospira* genomes lack *ureE* that serves as a bridge to acquire nickel from hydrogenase maturation factor HypA, which is subsequently donated to UreG. HypA is a metallochaperone and selectively delivers the nickel to the active site (Xiong et al., 2023). The absence of *ureE* may result in low urease activity in NOB (Carter et al., 2009; Fujitani et al., 2020).

The cyanate degradation gene *cynS* was only detected in NOB and one AOA strain *Ca*. Nitrososphaera gargensis Ga9.2 (Figure 3). Although both comammox strains do not contain *cynS* in this study, it has been found that a comammox MAG LK70 owns *cynS* (Yang et al., 2020). The genes *cynABD* encoding a high-affinity cyanate ABC transporter (Maeda and Omata, 2009) were only detected in *Nitrospira* sp. KM1, *Nitrospira* sp. NJ1, and *N. moscoviensis* strain NSP M-1 of

NOB (Figures 3, 4B), and *N. moscoviensis* was proven to use cyanate (Palatinszky et al., 2015). The remaining strains with *cynS* without *cynABD* contained the FNT family encoded by *focA*/*nirC* (Figures 3, 4B), which was hypothesized as the low-affinity cyanate transporter (Rycovska et al., 2012; Spang et al., 2012; Palatinszky et al., 2015). FNT proteins are found in most phyla of bacteria, archaea, and lower eukaryotes (Falke et al., 2010) and are key regulators of the metabolic flow in microorganisms (Wiechert and Beitz, 2017). The formate transporter (FocA) fuels the energy-generating formate hydrogen lyase reaction. Nitrite derived from chemical reduction of nitrate or oxidation of nitrogen monoxide is transported via NirC (Wiechert and Beitz, 2017). Formate/nitrite transporter is also presumed to be permeable for cyanate due to the proximity of genes for transporter and enzymatic degradation (Spang et al., 2012). Thus, the adjacent relationship between *cynS* and *focA*/*nirC* in genomes of *Ca.* Nitrososphaera gargensis Ga9.2, *Nitrospira lenta*, *Ca.* N. defluvii, *Nitrobacter hamburgensis* X14, and *N. winogradskyi* Nb-255 (Figure 4B) may suggest the involvement of FNT family gene encoding protein in cyanate transport. However, there is no experimental evidence that those five nitrifiers can use cyanate. The role of FNT family gene as the cyanate transporter is still uncertain with only genomic evidence (Spang et al., 2012). Although it is lack of evidence that the AOM can assimilate and break down cyanate from the environment, a previous study has shown that the pure culture of *Nitrosopumilus maritimus* SCM1 added with ^{15}N-cyanate produces ^{15}N-ammonium and ^{15}N-nitrite, which suggests a process of extracellular breakdown of cyanate by AOM (Kitzinger et al., 2019). It is also reported that NOB supply cyanase-lacking AOM with ammonium from cyanate. The ammonium can be fully nitrified by this microbial consortium through reciprocal feeding in co-culture experiments (Palatinszky et al., 2015). If the FNT family was a cyanate transporter, NOB could be the dominant nitrifier in cyanate utilization and play a key role in reciprocal feeding in nature. Thus, NOB that have high GC contents and SA/V ratios may have more versatility to utilize different extracellular nitrogen to satisfy their nitrogen demands.

4.3 Metabolic potentials of other LDON compounds

Polyamines are the primary amines consisting of two or more amine substitutions (Liu et al., 2015; Damashek et al., 2019). They are ubiquitous in cells of all lives and are essential for integral cellular processes, such as nucleic acid synthesis and stabilization, cellular growth, protein synthesis, biofilm formation, and siderophore production (Michael, 2018). They are *de novo* synthesized intracellularly (Figure 1B) and can be directly released from living and dead cells or from protein degradation into environments (Liu et al., 2016; Michael, 2016). Eukaryotic phytoplankton and heterotrophic bacteria (e.g., *Roseobacter* and SAR11) have been detected to utilize extracellular polyamines (Mou et al., 2010; Liu et al., 2016; Noell et al., 2021). Polyamines can be used by bacterioplankton as a nitrogen source (Figure 1B) and contribute to over 4% of bacterial nitrogen demand in aquatic environments (Liu et al., 2015; Krempaska et al., 2018; Madhuri et al., 2019; Liu et al., 2022a). Previous studies observed that putrescine-N could be oxidized and contribute to a significant fraction of total nitrification in coastal waters, and putrescine-N oxidation rate even exceeded that of urea (Damashek et al., 2019). Moreover, the faster polyamine-N oxidation rate than its uptake rate in the same water region as well as the production of ^{15}N-NO_2^- in pure cultures of some AOA with ^{15}N-putrescine suggest that AOM directly oxidize amine groups of polyamines resembling the pathway of ammonia oxidation (Liu et al., 2015; Damashek et al., 2021) since ammonia monooxygenase can co-metabolize a variety of organic compounds (Rasche et al., 1991; Wright et al., 2020). Thus, it is reasonable that genes homologous to *pot*-encoding polyamine transporters are not detected in selected AOA strains. The protein Dur3 has been found to be capable of transporting polyamines along with urea (Uemura et al., 2007), raising the potential that AOA may also assimilate polyamines; however, since all AOA, *Nitrosomonas* of AOB, and *Nitrospira lenta*, *Ca.* N. defluvii, *N. marina* Nb-295, *Nitrobacter hamburgensis* X14, and *N. winogradskyi* Nb-255 of NOB, which harbor *pot* genes, lack genes involved in polyamine catabolism (Figures 1B, 3), polyamines may not be degraded into ammonium intracellularly for the following oxidation processes. Instead, assimilated polyamines may serve for other physiological purposes as mentioned above (Kim et al., 2016).

In this study, all selected nitrifiers have the potential to synthesize putrescine either from arginine or agmatine except *Ca. Nitrosacidococcus tergens* sp. RJ19 of AOB and *Nitrospira marina* Nb-295, *Nitrobacter hamburgensis* X14, *N. winogradskyi* Nb-255, and *Ca.* Nitrotoga arctica of NOB (Figures 1B, 3). Archaea have been mentioned to form branched or long-chain polyamines and induce structural changes to DNA that can facilitate growth in extreme environments (Michael, 2018), or polyamines could be used as a donation of aminobutyl group for the growth of some archaeal halophiles and some methanogens (Michael, 2018). Polyamine synthesis and excretion are significantly up-regulated in AOA grown in environments with high levels of ammonia, which is thought to be one of the reasons for the ammonia tolerance of AOA in terrestrial environments (Liu et al., 2021). AOA may also use polyamines for detoxification (e.g., H_2O_2) or form biofilm for substrate uptake (Michael, 2018). More copies of *speB* detected in AOA may be the evolutionary consequence for polyamine synthesis (Magadum et al., 2013). Thus, instead of utilizing polyamine-N as an energy source, AOA might be a significant source of polyamines and contribute to polyamine cycling in different environments.

Taurine dissimilation could be an important source of nitrogen (Denger et al., 2004). *Thaumarchaeota* and *Euryarchaeota* have been reported to assimilate taurine in the upper water column of the northern Adriatic Sea identified by MICRO-CARD-FISH, and the uptake by *Thaumarchaeota* is even beyond that of SAR11 and *Roseobacter* clade in fall when the release of taurine is enhanced by zooplankton (Clifford et al., 2019); however, in this study, none of collected nitrifiers possesses taurine transporter genes *tauACB* and catabolic genes (Figure 1D), suggesting that nitrifiers either assimilate taurine using other transporters (e.g., those for amino acids) or directly break down taurine extracellularly (Damashek et al., 2019, 2021). In this study, only two marine AOB strains *Nitrosococcus oceani* ATCC 19707 and *N. watsonii* C-113 own glycine betaine (GBT) transport gene *opuD*. GBT has been found common in bacteria as osmotic molecules (Shakhman and Harries, 2021). A variety of soil and aquatic bacteria have catabolic pathways that convert choline to glycine in multiple steps via GBT (Figure 1E), using both choline and GBT as the sole carbon and nitrogen sources (Wargo, 2013). In addition, bacteria and methanogenic archaea in the cold spring are

able to synergistically convert GBT to methane (Li et al., 2021). The lack of GBT transport, synthesis, and degradation genes in most of selected nitrifiers suggests that GBT is not a nitrogen source to nitrifiers but may function in regulating osmotic pressure (Csonka, 1989). Similarly, methylamines which have been considered as important nitrogen and energy sources for heterotrophic bacteria in natural environments (Chen, 2012) may not be utilized by nitrifiers due to the lack of functional genes.

4.4 Evolution of LDON metabolism in nitrifiers

It is reported that archaeal ammonia monooxygenases share a more recent evolutionary history with actinobacterial monooxygenases than with those of AOB or comammox (Alves et al., 2018). The *amoA* of the comammox *Nitrospira* was transferred to AOB or that of both bacteria was derived from an unknown third donor (Palomo et al., 2018). The *ureC* gene of these bacteria and archaea probably evolved independently after an early gene duplication event, as did cyanobacteria and eukaryotes (Glass et al., 2009). The acquisition of urease genes may coincide with the gain of ammonia monooxygenase genes during the transition from *Thaumarchaeota* to AOA (Sheridan et al., 2020). Therefore, the potential LGT between bacteria and archaea may not exist in the evolutions of *amoA* and *ureC* (Figures 3, 5C). However, a previous study suggested that a certain amount of thaumarchaeotal gene clusters were recruited from bacteria for overcoming stresses and facilitating the environmental adaptation of *Thaumarchaeota* (Ren et al., 2019). According to the phylogenetic relationships of *utp* (Figure 5B), and two cyanate metabolic genes *cynS* and *focA*/*nirC* (Figure 6) between nitrifiers, it seems that LGT affects these genes and mostly happens between terrestrial AOA and bacteria (Figures 5B, 6). It has been proposed that the UT family is prokaryotic origin, and the encoding gene *utp* in groups of terrestrial AOA (*Nitrososphaerales* and *Ca*. Nitrosocaldales) is probably either transmitted vertically or horizontally acquired from a bacterium (Figure 5B; Minocha et al., 2003). Since the GC content of a newly acquired gene differs from that of the whole genome, a significant difference in the GC content between the gene *utp* (41.6–57.0%, median: 43.5%) and whole genomes of terrestrial AOA (33.4–52.7, 37.8%; $p = 0.04$, Mann–Whitney rank sum test; Supplementary Table S5) indicates a LGT event of *utp* (Lal and Lal, 2010). The adaptation of bacterial *utp* to their respective genomes as depicted by GC contents (*utp*: 35.0–59.0, 48.1%, genome: 37.0–59.0, 50.1%; $p > 0.05$; Supplementary Table S5) suggests that *utp* is bacterial origin and acquired by terrestrial AOA via LGT. GC contents of *cynS* (53.5–59.9, 56.3%) and *focA*/*nirC* (59.4–66.6, 60.3%) in bacteria which contain both genes did not show significant differences from those of whole genomes (56.0–62.0, 59.0%; $p < 0.05$). Similarly, GC contents of the two genes of *Ca*. Nitrososphaera gargensis Ga9.2 follow the same pattern as *Nitrospira* with a relatively lower and higher GC content of *cynS* and *focA*/*nirC* than that of the whole genome, respectively (Supplementary Table S5). It implies that *Nitrososphaera* and *Nitrospira* may acquire them via an ancient LGT event, which was also supported by good bootstrap values (Figure 6). The significantly greater CAI values of *cynS* (0.65–0.75, 0.66) and *focA*/*nirC* (0.65–0.76, 0.70) than those of bacterial whole genomes (0.51–0.62, 0.56; $p < 0.05$) further support the idea of LGT and indicate high gene expression in bacteria (Supplementary Table S6). A synchronous acquisition of genes via LGT by *Nitrospira* and terrestrial AOA genera *Nitrsosphaera* could also be verified by *speA* (Supplementary Figure S2) that is involved in the key process of putrescine synthesis (Figure 1B).

It is reported that the emerged AOA progress through an adaptive pathway from terrestrial hot springs to mesophilic soil (~652 Ma) and then to shallow and deep oceans (~509 Ma; Yang et al., 2021). The glaciation triggers the evolution of AOA diverging into two groups, one having the mesophilic terrestrial AOA group (genera *Nitrosocosmicus* and *Nitrososphaera*) and the other including marine AOA and acidic soil AOA group (genus *Nitrosotalea*; Yang et al., 2021). The driver for the evolutionary divergence of marine AOA from acidic soil AOA is oxygenation (Yang et al., 2021). The cluster of amino acid sequences of *amoA*, *dur3*, or *ureC* of marine AOA (Figures 3, 5B,C) confirms that marine AOA evolve intimately. However, *dur3* in genomes of AOA, on the other hand, differs from other genes in that the two copies of marine AOA are of different origins according to both phylogenetic relationships and GC contents (Figures 4A, 5A; Supplementary Table S5). It is observed that both copies of *dur3* of marine AOA exhibit higher GC contents (Copy 1: 40.1–43.9, 40.6%; Copy 2: 36.3–40.6, 37.5%) than those of whole genomes (33.2–35.8, 33.6%; calculations only count marine AOA with both copies of *dur3*; $p < 0.05$; Supplementary Table S5), while GC contents of *dur3* of terrestrial AOA (36.3–56.4, 38.9%) are in the same range to those of respective genomes (33.4–52.7, 39.3%; $p > 0.05$). It suggests that *dur3* may originate around the same period of time of *ure* acquisition during the transition from *Thaumarchaeota* to AOA and then diverge into two groups during glaciation events (Yang et al., 2021). The close clustering of Copy 1 of *dur3* of marine AOA and Copy 2 of *Nitrosotalea* verifies this evolutionary process (Figure 5A). Copy 1 of *dur3* of *Nitrosotalea* and Copy 2 of marine AOA are apparently not gained from gene duplication; instead, it could be transferred from terrestrial AOA through LGT. Dur3 orthologues have been detected in higher plants, algae, and fungi (Solomon et al., 2010). The lack of *dur3* in genomes of bacterial nitrifiers, and the clustering of *dur3* sequences of marine AOA and a marine alga *M. commoda* (Figure 5A) imply that *dur3* in eukaryotic may evolve from AOA.

5 Conclusion

The analysis of diversities and phylogenetic relationships of genes involved in LDON metabolisms in genomes of representative AOA, AOB, NOB, and comammox develops a more holistic understanding of the potentials of LDON metabolism by nitrifiers and sheds light on evolutionary relationships of functional genes involved in these processes. Our data suggest that GC contents, genome sizes, and SA/V ratios of nitrifiers may reflect the availability of nitrogen in their environmental niches and their capability of nitrogen assimilation for environmental adaptation. Our finding reinforces that nitrifiers tend to assimilate and degrade LDON for acquiring nitrogen or reciprocal feeding (e.g., urea and cyanate). They may also directly oxidize amine groups in LDON (e.g., polyamines and taurine) extracellularly to increase their competitive advantage when facing the substrate limitation. They could acquire this capability from early genetic evolution or LGT. Within different groups of nitrifiers, NOB are more advantageous and versatile in nitrogen assimilation than AOM due to their high affinity of ammonia and urea, and potentials in cyanate

utilization. They may share similar environmental niches with AOA and form intense reciprocal feeding relationships. In marine environments, AOA could be more efficient in using urea than AOB, which only dominate in environments with high urea concentration. In terrestrial environments, AOA may adjust the protein expression of the urea transporter (Utp or Dur3) to adapt to different urea concentrations, but again AOB only use urea at high concentrations. Our comparative analysis of LDON metabolic genes in different nitrifiers will guide future studies on the isolation and culture of new strains, providing a theoretical basis for their survival strategies in diverse environments. Moreover, it will contribute to model systems to study reciprocal or competitive interactions, which can severely affect matter and energy flows of ecosystems.

Data availability statement

The original contributions presented in the study are included in the article/Supplementary material, further inquiries can be directed to the corresponding author.

Author contributions

QL: Conceptualization, Data curation, Funding acquisition, Investigation, Methodology, Project administration, Supervision, Validation, Visualization, Writing – original draft, Writing – review & editing. YC: Data curation, Formal analysis, Investigation, Methodology, Resources, Software, Validation, Visualization, Writing – original draft, Writing – review & editing. X-WX: Project administration, Writing – review & editing.

Funding

The author(s) declare financial support was received for the research, authorship, and/or publication of this article. This research was funded by the National Natural Science Foundation of China (no. 42176038), Scientific Research Fund of the Second Institute of Oceanography, MNR (no. HYGG1901), the Project of State Key Laboratory of Satellite Ocean Environment Dynamics, Second Institute of Oceanography (no. SOEDZZ2204), and Science Foundation of Donghai Laboratory (no. DH-2022KF0211).

Acknowledgments

We thank Dr. Hong Chen and Dr. Yue-Hong Wu from the Second Institute of Oceanography, MNR China for providing hardware facilities.

Conflict of interest

The authors declare that the research was conducted in the absence of any commercial or financial relationships that could be construed as a potential conflict of interest.

Publisher's note

Supplementary material

The Supplementary material for this article can be found online at: https://www.frontiersin.org/articles/10.3389/fmicb.2023.1273211/full#supplementary-material

References

Alonso-Sáez, L., Waller, A. S., Mende, D. R., Bakker, K., Farnelid, H., Yager, P. L., et al. (2012). Role for urea in nitrification by polar marine Archaea. *Proc. Natl. Acad. Sci.* 109, 17989–17994. doi: 10.1073/pnas.1201914109

Alves, R. J. E., Minh, B. Q., Urich, T., von Haeseler, A., and Schleper, C. (2018). Unifying the global phylogeny and environmental distribution of ammonia-oxidizing archaea based on amoA genes. *Nat. Commun.* 9, 1–17. doi: 10.1038/s41467-018-03861-1

Bast, F. (2013). Sequence similarity search, multiple sequence alignment, model selection, distance matrix and phylogeny reconstruction. *Nat Protoc Exchang*. doi: 10.1038/protex.2013.065

Bayer, B., Vojvoda, J., Reinthaler, T., Reyes, C., Pinto, M., and Herndl, G. J. (2019). Nitrosopumilus adriaticus sp. nov. and Nitrosopumilus piranensis sp. nov., two ammonia-oxidizing archaea from the Adriatic Sea and members of the class Nitrososphaeria. *Int. J. Syst. Evol. Microbiol.* 69, 1892–1902. doi: 10.1099/ijsem.0.003360

Bossé, J. T., Gilmour, H. D., and MacInnes, J. I. (2001). Novel genes affecting urease activity in *Actinobacillus pleuropneumoniae*. *J. Bacteriol.* 183, 1242–1247. doi: 10.1128/JB.183.4.1242-1247.2001

Boyde, A., and Williams, R. (1971). Estimation of the volumes of bacterial cells by scanning electron microscopy. *Arch. Oral Biol.* 16, 259–267. doi: 10.1016/0003-9969(71)90019-7

Boysen, A. K., Durham, B. P., Kumler, W., Key, R. S., Heal, K. R., Carlson, L., et al. (2022). Glycine betaine uptake and metabolism in marine microbial communities. *Environ. Microbiol.* 24, 2380–2403. doi: 10.1111/1462-2920.16020

Carter, E. L., Flugga, N., Boer, J. L., Mulrooney, S. B., and Hausinger, R. P. (2009). Interplay of metal ions and urease. *Metallomics* 1, 207–221. doi: 10.1039/b903311d

Chen, Y. (2012). Comparative genomics of methylated amine utilization by marine Roseobacter clade bacteria and development of functional gene markers (tmm, gmaS). *Environ. Microbiol.* 14, 2308–2322. doi: 10.1111/j.1462-2920.2012.02765.x

Clifford, E. L., Varela, M. M., Corte, D. D., Bode, A., Ortiz, V., Herndl, G. J., et al. (2019). Taurine is a major carbon and energy source for marine prokaryotes in the North Atlantic Ocean off the Iberian Peninsula. *Microb. Ecol.* 78, 299–312. doi: 10.1007/s00248-019-01320-y

Coimbra, T.A.V.P. (2022). Bioinformatic strategies to explore iodine transport in plants and its potential application in biofortification. Master's thesis. University of Minho, Braga (MP).

Cook, A. M., and Denger, K. (2006). Metabolism of taurine in microorganisms. *Taurine* 583, 3–13. doi: 10.1007/978-0-387-33504-9_1

Csonka, L. N. (1989). Physiological and genetic responses of bacteria to osmotic stress. *Microbiol. Rev.* 53, 121–147. doi: 10.1128/mr.53.1.121-147.1989

Daims, H., Lücker, S., and Wagner, M. (2016). A new perspective on microbes formerly known as nitrite-oxidizing bacteria. *Trends Microbiol.* 24, 699–712. doi: 10.1016/j.tim.2016.05.004

Damashek, J., Bayer, B., Herndl, G.J., Wallsgrove, N.J., Allen, T., Popp, B.N., et al. (2021). Limited accessibility of nitrogen supplied as amino acids, amides, and amines as energy sources for marine Thaumarchaeota. bioRxiv. doi: 10.1101/2021.07.22.453390

Damashek, J., Tolar, B. B., Liu, Q., Okotie-Oyekan, A. O., Wallsgrove, N. J., Popp, B. N., et al. (2019). Microbial oxidation of nitrogen supplied as selected organic nitrogen compounds in the South Atlantic bight. *Limnol. Oceanogr.* 64, 982–995. doi: 10.1002/lno.11089

de Boer, W., and Laanbroek, H. J. (1989). Ureolytic nitrification at low pH by Nitrosospira spec. *Arch. Microbiol.* 152, 178–181. doi: 10.1007/BF00456098

Denger, K., Weinitschke, S., Hollemeyer, K., and Cook, A. M. (2004). Sulfoacetate generated by *Rhodopseudomonas palustris* from taurine. *Arch. Microbiol.* 182, 254–258. doi: 10.1007/s00203-004-0678-0

Engelberts, J. P., Robbins, S. J., de Goeij, J. M., Aranda, M., Bell, S. C., and Webster, N. S. (2020). Characterization of a sponge microbiome using an integrative genome-centric approach. *ISME J.* 14, 1100–1110. doi: 10.1038/s41396-020-0591-9

Falke, D., Schulz, K., Doberenz, C., Beyer, L., Lilie, H., Thiemer, B., et al. (2010). Unexpected oligomeric structure of the FocA formate channel of *Escherichia coli*: a paradigm for the formate–nitrite transporter family of integral membrane proteins. *FEMS Microbiol. Lett.* 303, 69–75. doi: 10.1111/j.1574-6968.2009.01862.x

Ferrer-González, F. X., Hamilton, M., Smith, C. B., Schreier, J. E., Olofsson, M., and Moran, M. A. (2023). Bacterial transcriptional response to labile exometabolites from photosynthetic picoeukaryote Micromonas commoda. *ISME Commun.* 3:5. doi: 10.1038/s43705-023-00212-0

Fujitani, H., Momiuchi, K., Ishii, K., Nomachi, M., Kikuchi, S., Ushiki, N., et al. (2020). Genomic and physiological characteristics of a novel nitrite-oxidizing Nitrospira strain isolated from a drinking water treatment plant. *Front. Microbiol.* 11:545190. doi: 10.3389/fmicb.2020.545190

Glass, J. B., Wolfe-Simon, F., and Anbar, A. (2009). Coevolution of metal availability and nitrogen assimilation in cyanobacteria and algae. *Geobiology* 7, 100–123. doi: 10.1111/j.1472-4669.2009.00190.x

Glibert, P. M., Wilkerson, F. P., Dugdale, R. C., Raven, J. A., Dupont, C. L., Leavitt, P. R., et al. (2016). Pluses and minuses of ammonium and nitrate uptake and assimilation by phytoplankton and implications for productivity and community composition, with emphasis on nitrogen-enriched conditions. *Limnol. Oceanogr.* 61, 165–197. doi: 10.1002/lno.10203

Guo, F.-B., Lin, H., and Huang, J. (2009). A plot of G+ C content against sequence length of 640 bacterial chromosomes shows the points are widely scattered in the upper triangular area. *Chromosom. Res.* 17, 359–364. doi: 10.1007/s10577-009-9024-3

Hall, B. G. (2013). Building phylogenetic trees from molecular data with MEGA. *Mol. Biol. Evol.* 30, 1229–1235. doi: 10.1093/molbev/mst012

He, H., Zhen, Y., Mi, T., Fu, L., and Yu, Z. (2018). Ammonia-oxidizing Archaea and Bacteria differentially contribute to ammonia oxidation in sediments from adjacent waters of Rushan Bay, China. *Front. Microbiol.* 9:116. doi: 10.3389/fmicb.2018.00116

Hu, H.-W., and He, J.-Z. (2017). Comammox—a newly discovered nitrification process in the terrestrial nitrogen cycle. *J. Soils Sediments* 17, 2709–2717. doi: 10.1007/s11368-017-1851-9

Igarashi, K., and Kashiwagi, K. (2010). Characteristics of cellular polyamine transport in prokaryotes and eukaryotes. *Plant Physiol. Biochem.* 48, 506–512. doi: 10.1016/j.plaphy.2010.01.017

Jørgensen, N. O. G. (2006). Uptake of urea by estuarine bacteria. *Aquat. Microb. Ecol.* 42, 227–242. doi: 10.3354/ame042227

Jung, M.-Y., Sedlacek, C. J., Kits, K. D., Mueller, A. J., Rhee, S.-K., Hink, L., et al. (2022). Ammonia-oxidizing archaea possess a wide range of cellular ammonia affinities. *ISME J.* 16, 272–283. doi: 10.1038/s41396-021-01064-z

Kim, J.-G., Park, S.-J., Sinninghe Damsté, J. S., Schouten, S., Rijpstra, W. I. C., Jung, M.-Y., et al. (2016). Hydrogen peroxide detoxification is a key mechanism for growth of ammonia-oxidizing archaea. *Proc. Natl. Acad. Sci.* 113, 7888–7893. doi: 10.1073/pnas.1605501113

Kitzinger, K., Koch, H., Lücker, S., Sedlacek, C. J., Herbold, C., Schwarz, J., et al. (2018). Characterization of the first "Candidatus Nitrotoga" isolate reveals metabolic versatility and separate evolution of widespread nitrite-oxidizing bacteria. *MBio* 9:e01186. doi: 10.1128/mBio.01186-18

Kitzinger, K., Marchant, H. K., Bristow, L. A., Herbold, C. W., Padilla, C. C., Kidane, A. T., et al. (2020). Single cell analyses reveal contrasting life strategies of the two main nitrifiers in the ocean. *Nat. Commun.* 11, 1–12. doi: 10.1038/s41467-020-14542-3

Kitzinger, K., Padilla, C. C., Marchant, H. K., Hach, P. F., Herbold, C. W., Kidane, A. T., et al. (2019). Cyanate and urea are substrates for nitrification by Thaumarchaeota in the marine environment. *Nat. Microbiol.* 4, 234–243. doi: 10.1038/s41564-018-0316-2

Koch, H., Lücker, S., Albertsen, M., Kitzinger, K., Herbold, C., Spieck, E., et al. (2015). Expanded metabolic versatility of ubiquitous nitrite-oxidizing bacteria from the genus Nitrospira. *Proc. Natl. Acad. Sci.* 112, 11371–11376. doi: 10.1073/pnas.1506533112

Könneke, M., Bernhard, A. E., de La Torre, J. R., Walker, C. B., Waterbury, J. B., and Stahl, D. A. (2005). Isolation of an autotrophic ammonia-oxidizing marine archaeon. *Nature* 437, 543–546. doi: 10.1038/nature03911

Koper, T. E., El-Sheikh, A. F., Norton, J. M., and Klotz, M. G. (2004). Urease-encoding genes in ammonia-oxidizing bacteria. *Appl. Environ. Microbiol.* 70, 2342–2348. doi: 10.1128/AEM.70.4.2342-2348.2004

Krempaska, N., Horňák, K., and Pernthaler, J. (2018). Spatiotemporal distribution and microbial assimilation of polyamines in a mesotrophic lake. *Limnol. Oceanogr.* 63, 816–832. doi: 10.1002/lno.10672

Kumar, S., Stecher, G., and Tamura, K. (2016). MEGA7: molecular evolutionary genetics analysis version 7.0 for bigger datasets. *Mol. Biol. Evol.* 33, 1870–1874. doi: 10.1093/molbev/msw054

Lal, D., and Lal, R. (2010). Evolution of mercuric reductase (merA) gene: a case of horizontal gene transfer. *Microbiology* 79, 500–508. doi: 10.1134/S0026261710040120

Lam, P., Lavik, G., Jensen, M. M., van de Vossenberg, J., Schmid, M., Woebken, D., et al. (2009). Revising the nitrogen cycle in the Peruvian oxygen minimum zone. *Proc. Natl. Acad. Sci.* 106, 4752–4757. doi: 10.1073/pnas.0812444106

Latocheski, E. C., da Rocha, M. C. V., and Braga, M. C. B. (2022). Nitrospira in wastewater treatment: applications, opportunities and research gaps. *Rev. Environ. Sci. Biotechnol.* 21, 905–930. doi: 10.1007/s11157-022-09634-z

Le, S. Q., and Gascuel, O. (2008). An improved general amino acid replacement matrix. *Mol. Biol. Evol.* 25, 1307–1320. doi: 10.1093/molbev/msn067

Levin, E. J., Quick, M., and Zhou, M. (2009). Crystal structure of a bacterial homologue of the kidney urea transporter. *Nature* 462, 757–761. doi: 10.1038/nature08558

Li, L., Zhang, W., Zhang, S., Song, L., Sun, Q., Zhang, H., et al. (2021). Bacteria and archaea synergistically convert glycine betaine to biogenic methane in the Formosa cold seep of the South China Sea. *Msystems* 6, e00703–e00721. doi: 10.1128/mSystems.00703-21

Liu, L., Liu, M., Jiang, Y., Lin, W., and Luo, J. (2021). Production and excretion of polyamines to tolerate high ammonia, a case study on soil ammonia-oxidizing archaeon "Candidatus Nitrosocosmicus agrestis". *Msystems* 6, e01003–e01020. doi: 10.1128/mSystems.01003-20

Liu, Q., Lu, X., Tolar, B. B., Mou, X., and Hollibaugh, J. T. (2015). Concentrations, turnover rates and fluxes of polyamines in coastal waters of the South Atlantic bight. *Biogeochemistry* 123, 117–133. doi: 10.1007/s10533-014-0056-1

Liu, Q., Lu, Y., Xu, J., Zhu, Z.-Y., Yuan, Y., Ma, W.-C., et al. (2022a). Dissolved free amino acids and polyamines are two major dissolved organic nitrogen sources for marine bacterioplankton in the northern slope of the South China Sea. *Biogeochemistry* 157, 109–126. doi: 10.1007/s10533-021-00860-1

Liu, Q., Nishibori, N., and Hollibaugh, J. T. (2022b). Sources of polyamines in coastal waters and their links to phytoplankton. *Mar. Chem.* 242:104121. doi: 10.1016/j.marchem.2022.104121

Liu, Q., Nishibori, N., Imai, I., and Hollibaugh, J. T. (2016). Response of polyamine pools in marine phytoplankton to nutrient limitation and variation in temperature and salinity. *Mar. Ecol. Prog. Ser.* 544, 93–105. doi: 10.3354/meps11583

Luo, H., Thompson, L. R., Stingl, U., and Hughes, A. L. (2015). Selection maintains low genomic GC content in marine SAR11 lineages. *Mol. Biol. Evol.* 32, 2738–2748. doi: 10.1093/molbev/msv149

Madhuri, S., Wang, K., Bade, D., and Mou, X. (2019). Concentration and turnover of dissolved free polyamines on the south coast of Lake Erie. *Limnol. Oceanogr.* 64, 1641–1650. doi: 10.1002/lno.11141

Maeda, S. I., Murakami, A., Ito, H., Tanaka, A., and Omata, T. (2015). Functional characterization of the FNT family nitrite transporter of marine picocyanobacteria. *Lifestyles* 5, 432–446. doi: 10.3390/life5010432

Maeda, S.-I., and Omata, T. (2009). Nitrite transport activity of the ABC-type cyanate transporter of the cyanobacterium *Synechococcus elongatus*. *J. Bacteriol.* 191, 3265–3272. doi: 10.1128/JB.00013-09

Magadum, S., Banerjee, U., Murugan, P., Gangapur, D., and Ravikesavan, R. (2013). Gene duplication as a major force in evolution. *J. Genet.* 92, 155–161. doi: 10.1007/s12041-013-0212-8

Michael, A. J. (2016). Biosynthesis of polyamines and polyamine-containing molecules. *Biochem. J.* 473, 2315–2329. doi: 10.1042/BCJ20160185

Michael, A. J. (2018). Polyamine function in archaea and bacteria. *J. Biol. Chem.* 293, 18693–18701. doi: 10.1074/jbc.TM118.005670

Minocha, R., Studley, K., Saier, J., and Milton, H. (2003). The urea transporter (UT) family: bioinformatic analyses leading to structural, functional, and evolutionary predictions. *Recept. Channels* 9, 345–352. doi: 10.3109/714041015

Mou, X., Sun, S., Rayapati, P., and Moran, M. A. (2010). Genes for transport and metabolism of spermidine in *Ruegeria pomeroyi* DSS-3 and other marine bacteria. *Aquat. Microb. Ecol.* 58, 311–321. doi: 10.3354/ame01367

Mou, X., Vila-Costa, M., Sun, S., Zhao, W., Sharma, S., and Moran, M. A. (2011). Metatranscriptomic signature of exogenous polyamine utilization by coastal bacterioplankton. *Environ. Microbiol. Rep.* 3, 798–806. doi: 10.1111/j.1758-2229.2011.00289.x

Noell, S. E., Barrell, G. E., Suffridge, C., Morré, J., Gable, K. P., Graff, J. R., et al. (2021). SAR11 cells rely on enzyme multifunctionality to metabolize a range of polyamine compounds. *MBio* 12:e0109121. doi: 10.1128/mBio.01091-21

Offre, P., Kerou, M., Spang, A., and Schleper, C. (2014). Variability of the transporter gene complement in ammonia-oxidizing archaea. *Trends Microbiol.* 22, 665–675. doi: 10.1016/j.tim.2014.07.007

Pachiadaki, M. G., Sintes, E., Bergauer, K., Brown, J. M., Record, N. R., Swan, B. K., et al. (2017). Major role of nitrite-oxidizing bacteria in dark ocean carbon fixation. *Science* 358, 1046–1051. doi: 10.1126/science.aan8260

Palatinszky, M., Herbold, C., Jehmlich, N., Pogoda, M., Han, P., von Bergen, M., et al. (2015). Cyanate as an energy source for nitrifiers. *Nature* 524, 105–108. doi: 10.1038/nature14856

Palomo, A., Pedersen, A. G., Fowler, S. J., Dechesne, A., Sicheritz-Pontén, T., and Smets, B. F. (2018). Comparative genomics sheds light on niche differentiation and the evolutionary history of comammox Nitrospira. *ISME J.* 12, 1779–1793. doi: 10.1038/s41396-018-0083-3

Pearson, W. R. (2013). An introduction to sequence similarity ("homology") searching. *Curr Protoc Bioinform* 42, 3.1.1–3.1.8. doi: 10.1002/0471250953.bi0301s42

Qin, W., Amin, S. A., Martens-Habbena, W., Walker, C. B., Urakawa, H., Devol, A. H., et al. (2014). Marine ammonia-oxidizing archaeal isolates display obligate mixotrophy and wide ecotypic variation. *Proc. Natl. Acad. Sci.* 111, 12504–12509. doi: 10.1073/pnas.1324115111

Qin, W., Heal, K. R., Ramdasi, R., Kobelt, J. N., Martens-Habbena, W., Bertagnolli, A. D., et al. (2017). Nitrosopumilus maritimus gen. Nov., sp. nov., Nitrosopumilus cobalaminigenes sp. nov., Nitrosopumilus oxyclinae sp. nov., and Nitrosopumilus ureiphilus sp. nov., four marine ammonia-oxidizing archaea of the phylum Thaumarchaeota. *Int. J. Syst. Evol. Microbiol.* 67, 5067–5079. doi: 10.1099/ijsem.0.002416

Rasche, M. E., Hyman, M. R., and Arp, D. J. (1991). Factors limiting aliphatic chlorocarbon degradation by *Nitrosomonas europaea*: cometabolic inactivation of ammonia monooxygenase and substrate specificity. *Appl. Environ. Microbiol.* 57, 2986–2994. doi: 10.1128/aem.57.10.2986-2994.1991

Raunser, S., Mathai, J. C., Abeyrathne, P. D., Rice, A. J., Zeidel, M. L., and Walz, T. (2009). Oligomeric structure and functional characterization of the urea transporter from *Actinobacillus pleuropneumoniae*. *J. Mol. Biol.* 387, 619–627. doi: 10.1016/j.jmb.2009.02.005

Ren, M., Feng, X., Huang, Y., Wang, H., Hu, Z., Clingenpeel, S., et al. (2019). Phylogenomics suggests oxygen availability as a driving force in Thaumarchaeota evolution. *ISME J.* 13, 2150–2161. doi: 10.1038/s41396-019-0418-8

Rittstieg, K., Robra, K.-H., and Somitsch, W. (2001). Aerobic treatment of a concentrated urea wastewater with simultaneous stripping of ammonia. *Appl. Microbiol. Biotechnol.* 56, 820–825. doi: 10.1007/s002530100696

Rohwerder, T. (2020). New structural insights into bacterial sulfoacetaldehyde and taurine metabolism. *Biochem. J.* 477, 1367–1371. doi: 10.1042/BCJ20200079

Rycovska, A., Hatahet, L., Fendler, K., and Michel, H. (2012). The nitrite transport protein NirC from *Salmonella typhimurium* is a nitrite/proton antiporter. *Biochim Biophys Acta Biomemb* 1818, 1342–1350. doi: 10.1016/j.bbamem.2012.02.004

Sauder, L. A., Albertsen, M., Engel, K., Schwarz, J., Nielsen, P. H., Wagner, M., et al. (2017). Cultivation and characterization of Candidatus Nitrosocosmicus exaquare, an ammonia-oxidizing archaeon from a municipal wastewater treatment system. *ISME J.* 11, 1142–1157. doi: 10.1038/ismej.2016.192

Sauder, L. A., Engel, K., Lo, C.-C., Chain, P., and Neufeld, J. D. (2018). "Candidatus Nitrosotenuis aquarius," an Ammonia-oxidizing archaeon from a freshwater aquarium biofilter. *Appl. Environ. Microbiol.* 84, e01430–e01418. doi: 10.1128/AEM.01430-18

Seitzinger, S. P., Sanders, R., and Styles, R. (2002). Bioavailability of DON from natural and anthropogenic sources to estuarine plankton. *Limnol. Oceanogr.* 47, 353–366. doi: 10.4319/lo.2002.47.2.0353

Shakhman, Y., and Harries, D. (2021). How glycine betaine modifies lipid membrane interactions. *Chem Syst Chem* 3:e2100010. doi: 10.1002/syst.202100010

Sheridan, P. O., Raguideau, S., Quince, C., Holden, J., Zhang, L., Consortium, T., et al. (2020). Gene duplication drives genome expansion in a major lineage of Thaumarchaeota. *Nat. Commun.* 11:5494. doi: 10.1038/s41467-020-19132-x

Sipler, R. E., Bronk, D. A., Seitzinger, S. P., Lauck, R. J., McGuinness, L., Kirkpatrick, G. J., et al. (2013). Trichodesmium-derived dissolved organic matter is a source of nitrogen capable of supporting the growth of toxic red tide Karenia brevis. *Mar. Ecol. Prog. Ser.* 483, 31–45. doi: 10.3354/meps10258

Sliekers, A. O., Haaijer, S., Schmid, M., Harhangi, H., Verwegen, K., Kuenen, J. G., et al. (2004). Nitrification and anammox with urea as the energy source. *Syst. Appl. Microbiol.* 27, 271–278. doi: 10.1078/0723-2020-00259

Soliman, M., and Eldyasti, A. (2018). Ammonia-oxidizing Bacteria (AOB): opportunities and applications—a review. *Rev. Environ. Sci. Biotechnol.* 17, 285–321. doi: 10.1007/s11157-018-9463-4

Solomon, C. M., Collier, J. L., Berg, G. M., and Glibert, P. M. (2010). Role of urea in microbial metabolism in aquatic systems: a biochemical and molecular review. *Aquat. Microb. Ecol.* 59, 67–88. doi: 10.3354/ame01390

Spang, A., Poehlein, A., Offre, P., Zumbrägel, S., Haider, S., Rychlik, N., et al. (2012). The genome of the ammonia-oxidizing Candidatus Nitrososphaera gargensis: insights into metabolic versatility and environmental adaptations. *Environ. Microbiol.* 14, 3122–3145. doi: 10.1111/j.1462-2920.2012.02893.x

Stahl, D. A., and de la Torre, J. R. (2012). Physiology and diversity of ammonia-oxidizing archaea. *Annu. Rev. Microbiol.* 66, 83–101. doi: 10.1146/annurev-micro-092611-150128

Taubert, M., Grob, C., Howat, A. M., Burns, O. J., Pratscher, J., Jehmlich, N., et al. (2017). Methylamine as a nitrogen source for microorganisms from a coastal marine environment. *Environ. Microbiol.* 19, 2246–2257. doi: 10.1111/1462-2920.13709

Thompson, J. D., Higgins, D. G., and Gibson, T. J. (1994). CLUSTAL W: improving the sensitivity of progressive multiple sequence alignment through sequence weighting, position-specific gap penalties and weight matrix choice. *Nucleic Acids Res.* 22, 4673–4680. doi: 10.1093/nar/22.22.4673

Tolar, B. B., Ross, M. J., Wallsgrove, N. J., Liu, Q., Aluwihare, L. I., Popp, B. N., et al. (2016). Contribution of ammonia oxidation to chemoautotrophy in Antarctic coastal waters. *ISME J.* 10, 2605–2619. doi: 10.1038/ismej.2016.61

Tourna, M., Stieglmeier, M., Spang, A., Könneke, M., Schintlmeister, A., Urich, T., et al. (2011). Nitrososphaera viennensis, an ammonia oxidizing archaeon from soil. *Proc. Natl. Acad. Sci.* 108, 8420–8425. doi: 10.1073/pnas.1013488108

Uemura, T., Kashiwagi, K., and Igarashi, K. (2007). Polyamine uptake by DUR3 and SAM3 in *Saccharomyces cerevisiae*. *J. Biol. Chem.* 282, 7733–7741. doi: 10.1074/jbc.M611105200

Valladares, A., Montesinos, M. L., Herrero, A., and Flores, E. (2002). An ABC-type, high-affinity urea permease identified in cyanobacteria. *Mol. Microbiol.* 43, 703–715. doi: 10.1046/j.1365-2958.2002.02778.x

Van Kessel, M. A., Speth, D. R., Albertsen, M., Nielsen, P. H., Op den Camp, H. J., Kartal, B., et al. (2015). Complete nitrification by a single microorganism. *Nature* 528, 555–559. doi: 10.1038/nature16459

Veaudor, T., Cassier-Chauvat, C., and Chauvat, F. (2019). Genomics of urea transport and catabolism in cyanobacteria: biotechnological implications. *Front. Microbiol.* 10:2052. doi: 10.3389/fmicb.2019.02052

Vijayan, A., Vattiringal Jayadradhan, R. K., Pillai, D., Prasannan Geetha, P., Joseph, V., and Isaac Sarojini, B. S. (2021). Nitrospira as versatile nitrifiers: taxonomy, ecophysiology, genome characteristics, growth, and metabolic diversity. *J. Basic Microbiol.* 61, 88–109. doi: 10.1002/jobm.202000485

Voss, M., Bange, H. W., Dippner, J. W., Middelburg, J. J., Montoya, J. P., and Ward, B. (2013). The marine nitrogen cycle: recent discoveries, uncertainties and the potential relevance of climate change. *Philos Transac Roy Soc B Biol Sci* 368:20130121. doi: 10.1098/rstb.2013.0121

Wang, W. H., Köhler, B., Cao, F. Q., Liu, G. W., Gong, Y. Y., Sheng, S., et al. (2012). Rice DUR3 mediates high-affinity urea transport and plays an effective role in improvement of urea acquisition and utilization when expressed in Arabidopsis. *New Phytol.* 193, 432–444. doi: 10.1111/j.1469-8137.2011.03929.x

Wargo, M. J. (2013). Homeostasis and catabolism of choline and glycine betaine: lessons from *Pseudomonas aeruginosa*. *Appl. Environ. Microbiol.* 79, 2112–2120. doi: 10.1128/AEM.03565-12

Wetzel, K. J., Bjorge, D., and Schwan, W. R. (2011). Mutational and transcriptional analyses of the *Staphylococcus aureus* low-affinity proline transporter OpuD during in vitro growth and infection of murine tissues. *FEMS Immunol Med Microbiol* 61, 346–355. doi: 10.1111/j.1574-695X.2011.00781.x

Wiechert, M., and Beitz, E. (2017). Mechanism of formate–nitrite transporters by dielectric shift of substrate acidity. *EMBO J.* 36, 949–958. doi: 10.15252/embj.201695776

Woebken, D., Lam, P., Kuypers, M. M., Naqvi, S. W. A., Kartal, B., Strous, M., et al. (2008). A microdiversity study of anammox bacteria reveals a novel Candidatus Scalindua phylotype in marine oxygen minimum zones. *Environ. Microbiol.* 10, 3106–3119. doi: 10.1111/j.1462-2920.2008.01640.x

Wright, C. L., Schatteman, A., Crombie, A. T., Murrell, J. C., and Lehtovirta-Morley, L. E. (2020). Inhibition of ammonia monooxygenase from ammonia-oxidizing archaea by linear and aromatic alkynes. *Appl. Environ. Microbiol.* 86, e02388–e02419. doi: 10.1128/AEM.02388-19

Xiong, Z., Zhang, N., Xu, L., Deng, Z., Limwachiranon, J., Guo, Y., et al. (2023). Urease of aspergillus fumigatus is required for survival in macrophages and virulence. *Microbiol Spectr* 11, e03508–e03522. doi: 10.1128/spectrum.03508-22

Yang, Y., Daims, H., Liu, Y., Herbold, C. W., Pjevac, P., Lin, J.-G., et al. (2020). Activity and metabolic versatility of complete ammonia oxidizers in full-scale wastewater treatment systems. *MBio* 11, e03175–e03119. doi: 10.1128/mBio.03175-19

Yang, Y., Zhang, C., Lenton, T. M., Yan, X., Zhu, M., Zhou, M., et al. (2021). The evolution pathway of ammonia-oxidizing archaea shaped by major geological events. *Mol. Biol. Evol.* 38, 3637–3648. doi: 10.1093/molbev/msab129

Zhang, L., Lan, S., Dou, Q., Hao, S., Wang, Y., Wang, X., et al. (2023). Metagenomic insights into responses of microbial population and key functional genes to fulvic acid during partial nitritation. *J. Environ. Sci.* 124, 952–962. doi: 10.1016/j.jes.2022.03.003

frontiers | Frontiers in Microbiology

TYPE Original Research
PUBLISHED 04 September 2024
DOI 10.3389/fmicb.2024.1410251

OPEN ACCESS

EDITED BY
Wei Qin,
University of Oklahoma, United States

REVIEWED BY
Xianhui Wan,
Princeton University, United States
Man-Young Jung,
Jeju National University, Republic of Korea

*CORRESPONDENCE
Elisa Hernández-Magaña
✉ elisa@biology.sdu.dk
Beate Kraft
✉ bkraft@biology.sdu.dk

RECEIVED 31 March 2024
ACCEPTED 15 August 2024
PUBLISHED 04 September 2024

CITATION
Hernández-Magaña E and Kraft B (2024) Nitrous oxide production and consumption by marine ammonia-oxidizing archaea under oxygen depletion.
Front. Microbiol. 15:1410251.
doi: 10.3389/fmicb.2024.1410251

Nitrous oxide production and consumption by marine ammonia-oxidizing archaea under oxygen depletion

Elisa Hernández-Magaña* and Beate Kraft*

Nordcee, Department of Biology, Faculty of Sciences, University of Southern Denmark, Odense, Denmark

Ammonia-oxidizing archaea (AOA) are key players in the nitrogen cycle and among the most abundant microorganisms in the ocean, thriving even in oxygen-depleted ecosystems. AOA produce the greenhouse gas nitrous oxide (N_2O) as a byproduct of ammonia oxidation. Additionally, the recent discovery of a nitric oxide dismutation pathway in the AOA isolate *Nitrosopumilus maritimus* points toward other N_2O production and consumption pathways in AOA. AOA that perform NO dismutation when exposed to oxygen depletion, produce oxygen and dinitrogen as final products. Based on the transient accumulation of N_2O coupled with oxygen accumulation, N_2O has been proposed as an intermediate in this novel archaeal pathway. In this study, we spiked N_2O to oxygen-depleted incubations with pure cultures of two marine AOA isolates that were performing NO dismutation. By using combinations of N compounds with different isotopic signatures ($^{15}NO_2^-$ pool $+^{44}N_2O$ spike and $^{14}NO_2^-$ pool $+^{46}N_2O$ spike), we evaluated the N_2O spike effects on the production of oxygen and the isotopic signature of N_2 and N_2O. The experiments confirmed that N_2O is an intermediate in NO dismutation by AOA, distinguishing it from similar pathways in other microbial clades. Furthermore, we showed that AOA rapidly reduce high concentrations of spiked N_2O to N_2. These findings advance our understanding of microbial N_2O production and consumption in oxygen-depleted settings and highlight AOA as potentially important key players in N_2O turnover.

KEYWORDS

oxygen depletion, anoxia, NO dismutation, ammonia-oxidizing archaea, nitrous oxide, nitrous oxide reduction

Introduction

Environments with low oxygen concentrations are major sources of the greenhouse gas nitrous oxide (N_2O). Nearly half of the net yearly production of N_2O in the open ocean occurs in hypoxic and oxygen-depleted waters (Codispoti, 2010). N_2O has a warming potential approximately 300 times higher than CO_2 and contributes to stratospheric ozone destruction (IPCC, 2014). In order to understand the dynamics of N_2O emissions from oxygen-depleted environments, it is crucial to disentangle the contributions of different microbial pathways of N_2O production and consumption.

Ammonia-oxidizing archaea (AOA) are key players in the nitrogen cycle, performing the first step of nitrification. They are among the most abundant microorganisms in the ocean, and in some cases, they can represent up to 40% of the total picoplankton in the water column

(Karner et al., 2001). Oceanic ammonia oxidation is almost entirely performed by AOA, and they have been suggested to be an important source of N_2O in the ocean (Santoro et al., 2011; Löscher et al., 2012). Here, N_2O is mainly formed as a byproduct of ammonia oxidation in a process named hybrid formation. In this process, hydroxylamine from NH_4^+ reacts with NO, which is produced from NO_2^- (Stieglmeier et al., 2014; Kozlowski et al., 2016; Prosser et al., 2020; Wu et al., 2020; Stein et al., 2021).

Until the recent discovery of the NO-dismutation pathway in AOA upon oxygen depletion, AOA were assumed to be inactive when oxygen was absent. In this NO-dismutation pathway, AOA reduces NO_2^-, which is the product of aerobic ammonia oxidation, to NO. Then, NO is dismutated to O_2 and N_2O, which is reduced to N_2 (Kraft et al., 2022). The dismutation step is thermodynamically favorable ($2NO \rightarrow N_2O + 0.5O_2$, $\Delta G0' = -165 kJ/mol\ O_2$), and AOA can use the produced oxygen to fuel ammonia oxidation (Kraft et al., 2022). N_2O is proposed to be an intermediate based on the transient accumulation of $^{15,15}N$-labeled N_2O from ^{15}N-nitrite in parallel to oxygen production (Kraft et al., 2022; Hernández-Magaña et al., 2023). NO dismutation has been observed previously in the methane-oxidizing bacterium *Ca. Methylomirabilis oxyfera*, which also produces O_2 and N_2 as final products of the pathway (Ettwig et al., 2010). However, there is no evidence of N_2O production or reduction associated with this process. A further difference is that in the case of *Ca. M. oxyfera*, the oxygen produced is immediately utilized to oxidize methane and other microbial processes (Ettwig et al., 2010). In the case of AOA, the oxygen produced during NO dismutation is used for ammonia oxidation and respiration, but the coupling between production and consumption is not that tight, and oxygen accumulates (Kraft et al., 2022).

AOA are highly abundant in environments with low or undetectable oxygen concentrations, such as anoxic basins such as the Black Sea (Sollai et al., 2019) or oceanic oxygen minimum zones (OMZs) (Francis et al., 2005; Lam et al., 2007; Beman et al., 2008; Peng et al., 2015; Bristow et al., 2016). The discovery of NO dismutation in AOA provides a potential explanation for their presence in these environments, suggesting that AOA may contribute to N_2O cycling if N_2O indeed is an intermediate in NO dismutation.

To date, N_2O production from nitrite in anoxic environments has been solely attributed to denitrification. Denitrification, the stepwise reduction of nitrate to dinitrogen ($NO_3^- \rightarrow NO_2^- \rightarrow NO \rightarrow N_2O \rightarrow N_2$), can be performed by a phylogenetically diverse group of organisms, including bacteria, archaea, and eukaryotes (Thomson et al., 2012). Some denitrifiers possess only some of the enzymes and can only carry out incomplete denitrification; organisms that cannot reduce N_2O to N_2 lead to the accumulation of N_2O (Babbin et al., 2015), while some microorganisms that only reduce N_2O to N_2 become net sinks of N_2O in the system (Jones et al., 2013). Biogeochemical rate measurements based on ^{15}N-stable isotope labeling would not be able to distinguish between denitrification and NO dismutation as sources for N_2O and N_2 production because, in both processes, the two N atoms originate from nitrite.

To test the role of N_2O as an intermediate in the NO dismutation pathway by AOA, we carried out incubations under oxygen depletion with pure cultures of the AOA strains, *N. maritimus* and *Nitrosopumilus piranensis*. The oxygen-depleted incubations were combined with the use of ^{15}N-stable isotope-labeled compounds to track the origin and fate of the nitrogen gases N_2O and N_2 during NO dismutation. The N_2 and N_2O accumulation patterns from different experiments support the role of N_2O as an intermediate in the formation of N_2 upon oxygen depletion. Furthermore, solid evidence for the N_2O reduction to N_2 by two marine AOA isolates is presented.

Materials and methods

Growth conditions

Axenic 5 L batch pre-cultures of the AOA strains *N. maritimus* SCM1 and *N. piranensis* D3C (JCM 32271, DSM 106147, and NCIMB 15115) were grown at 28°C in the dark in synthetic Crenarchaeota medium (SCM) HEPES-buffered (pH 7.8), as described by Könneke et al. (2005) and Martens-Habbena et al. (2009), modified with a 6 mM final concentration of sodium bicarbonate (Kraft et al., 2022).

Oxygen-depleted incubations

The oxygen-depleted incubations were prepared by sparging the aerobically grown batch culture with argon gas (99.99%) for 45 min to reduce the oxygen concentration in the culture. The culture was sterilely transferred into 330-ml custom-made glass bottles designed to avoid oxygen intrusion with a glass capillary and a port for inserting a microsensor (Tiano et al., 2014) through a glass tube connection, using the overpressure generated in the argon-sparged culture bottle. All bottles were filled without headspace and closed with glass stoppers. The bottles were continuously stirred with glass-coated stirring bars (VWR, United Kingdom) at 300 rpm. The bottles were incubated in a water bath at 28°C in the dark. Control incubations with the custom-made bottles and killed controls with $HgCl_2$ have been previously reported in Kraft et al. (2022), showing no oxygen intrusion from the atmosphere.

Oxygen was monitored constantly during the incubations with trace fluorescence oxygen sensors, also referred to as optodes, with a detection limit of 0.5 nM (Lehner et al., 2015). The optodes were previously glued to the glass bottles. NO was monitored with microsensors (Unisense, Denmark), inserted into the sensor ports of the bottles, which were previously sterilized with 70% ethanol, and rinsed with autoclaved ASTM1a water. NO was observed to cause a small and predictable interference with the optodes (up to 17%). Therefore, the oxygen concentration measurements were corrected for NO interference, as in Kraft et al. (2022). All bottles, stirring bars, tube connections, and materials used for the incubation were previously autoclaved.

N_2O as an intermediate in dinitrogen production via NO dismutation

Two sets of experiments with ^{15}N-stable isotope compounds were used for the identification of the intermediates in dinitrogen and oxygen production via NO dismutation.

For the first experimental setup, batch cultures of *N. maritimus* and *N. piranensis* were grown aerobically with ^{15}N-labeled ammonium ($^{15}NH_4^+$) until it was completely oxidized to $^{15}NO_2^-$, and thus cultures

contained a pool of 1 mM of $^{15}NO_2^-$ (late exponential phase). Prior to the incubation, more than 500 µM of $^{14}NH_4^+$ was added to the culture to ensure the survival (ammonia oxidation) of the cultures during the experiment and to capture traces of $^{15}NH_4^+$ that could have remained in a large pool of $^{14}NH_4^+$. The incubations under oxygen depletion were set up, as described in the section "oxygen-depleted incubations." The sets of replicates (at least 3 bottles of 330 mL each per incubation) were spiked with 1.2 µM of unlabeled N_2O ($^{44}N_2O$) after 30 h in the case of *N. maritimus* and with 3 µM after 6 h and 1.2 µM after 30 h in the case of *N. piranensis*. Three incubation replicates were kept without the addition of N_2O as a control. A killed control was performed by adding mercury chloride to the incubation.

In the second set of experiments, an aerobically grown batch culture of *N. piranensis* was maintained with $^{14}NH_4^+$ until it was completely oxidized to $^{14}NO_2^-$. Then, the batch culture contained a pool of approximately 1 mM of $^{14}NO_2^-$ (the late exponential phase). Prior to the incubation, more than 500 µM of $^{14}NH_4^+$ was added to the culture to ensure the survival (ammonia oxidation) of the cultures during the experiment. The oxygen-depleted incubation was started, as described in the section "oxygen-depleted incubations." One set of replicates (at least three bottles of 330 mL each) was spiked with 40 nM of ^{15}N-labeled N_2O ($^{46}N_2O$) at 8 h and with 90 nM at 42 h. Three incubation replicates were kept without the addition of $^{46}N_2O$ as a control.

Sample collection and analysis

Samples were collected with gas-tight syringes (Hamilton, United States) that were connected to stainless steel needles (Ochs, Germany) through the capillaries of the incubation bottles. When collecting the samples, the volume collected was simultaneously replaced with deoxygenated sterile culture media to avoid headspace formation in the incubation bottle. The samples were collected in 3-ml gas-tight exetainers, headspace-free, and preserved with 50 µL of saturated $HgCl_2$ solution. The isotopic signature of N_2 and N_2O was analyzed by coupled gas chromatography–isotope ratio mass spectrometry (GC-IRMS) on a Thermo Delta V Plus isotope ratio mass spectrometer (Dalsgaard et al., 2012). Total N_2O concentrations were analyzed using a gas chromatograph (GC-TRACE1300, Thermo Scientific) equipped with an electron capture detector. Concentrations were plotted as the average of at least three replicates, with error bars representing the standard deviation. Rates were calculated from the change in concentration over time, with $r^2 > 0.9$.

Results

Reduction of N_2O to N_2 by *N. maritimus* and *N. piranensis* under oxygen depletion

The AOA strains *N. maritimus* and *N. piranensis* were previously observed to conduct NO dismutation upon oxygen depletion (Kraft et al., 2022; Hernández-Magaña et al., 2023), in which they produced oxygen and ultimately N_2 from NO_2^-. Transient accumulation of N_2O in both strains was reported in the cited publications, suggesting that AOA can produce N_2O under oxygen depletion and further reduce it to N_2. To assess the role of N_2O as an intermediate in NO dismutation by AOA and, therefore, the AOA's potential to reduce N_2O, we performed incubations under oxygen depletion with pure cultures of *N. maritimus* and *N. piranensis*. The first set of incubations was started with a pool of $^{15}NO_2^-$ and spiked with 1.2–1.5 µM of unlabeled nitrous oxide ($^{44}N_2O$) at 30 h for both AOA strains and additionally with 3 µM of $^{44}N_2O$ at 6 h only for *N. piranensis*.

A striking decrease in the total N_2O concentration was observed after the spike in all the incubations. N_2O consumption was especially fast within the first 3 h after the spike (Figure 1). For example, *N. piranensis* consumed on average 497 nM/h in the first 3 h after the 6-h spike and 198 nM/h after the 30-h spike. Overall, strikingly fast N_2O consumption after the spikes was consistently observed in all the incubations. After this first fast decrease in N_2O, N_2O consumption slowed down. Then, *N. maritimus* had the highest consumption rate of 48 nM/h, followed by the incubation of N. piranensis after the spike at 6 h, which had a rate of 41 nM/h. Finally, the same strain after the spike at 30 h consumed all spiked N_2O in approximately 30 h at a rate of 28 nM/h. The accumulation of $^{46}N_2O$ from $^{15}NO_2^-$ started within the first hours of the oxygen-depleted incubations, followed by a linear production of $^{30}N_2$ (Figure 2, controls). In *N. maritimus* incubations, the production of $^{30}N_2$ increased at approximately 20 h, while in *N. piranensis* N_2 production was linear from the beginning of the oxygen-depleted incubation. Another subtle difference between the strains was the transient accumulation of N_2O, which was maintained throughout the whole incubation period for *N. maritimus*. For *N. piranensis*, the N_2O accumulation started quickly after oxygen depletion, reaching its maximum within the first 20 h and decreasing almost totally after 40 h of oxygen depletion. Despite these differences in accumulation patterns between strains, there is consistency in the transient accumulation of $^{46}N_2O$ and in the formation of $^{46}N_2O$ only from $^{15}NO_2^-$ via NO, which is consistent with previous observations (Kraft et al., 2022; Hernández-Magaña et al., 2023).

If N_2O is a free intermediate in the NO-dismutation pathway (a product of the NO-dismutation step), which is reduced to N_2 and not a byproduct, an increase in the pool of $^{44}N_2O$ over $^{46}N_2O$ ($^{44}N_2O$ spike) would lead to an increase in $^{28}N_2$ production instead of $^{30}N_2$ production compared to the control incubations, in which only $^{46}N_2O$ is available. Thus, the reduction of N_2O from a pool enriched with $^{44}N_2O$ would be observed as a slowing of $^{30}N_2$ accumulation. For the incubation with *N. maritimus* in which $^{44}N_2O$ was spiked at 30 h (Figure 1A), $^{30}N_2$ accumulation stopped until the spiked $^{44}N_2O$ was consumed (55 h) and then $^{30}N_2$ accumulation started again (Figure 2A), demonstrating the direct reduction of N_2O to N_2 and the role of N_2O as an intermediate in the NO-dismutation pathway. For the incubations with *N. piranensis*, a similar pattern in $^{30}N_2$ production was observed after the spike of $^{44}N_2O$ at 6 h of the incubation (Figure 2C). In the case of the spiked incubations of *N. piranensis* at 30 h, the effect of the $^{44}N_2O$ spike on the $^{30}N_2$ production was more difficult to notice in the averaged trend (Figure 2B) and easier to distinguish in the trends of the individual replicates (Supplementary Figure S1A). The replicate with the fastest total N_2O consumption (Supplementary Figure S1B) was the only replicate with no visible effect on the $^{30}N_2$ production after the 30-h spike (Supplementary Figure S1A), suggesting that the N_2O pool was consumed too fast to capture the N_2O produced from nitrite. Additionally, no production of $^{30}N_2$ or $^{46}N_2O$ or consumption of N_2O after a spike of $^{44}N_2O$ was detected in the killed control with *N. maritimus* (Supplementary Figure S2), indicating that the consumption of N_2O was performed by active cells of AOA.

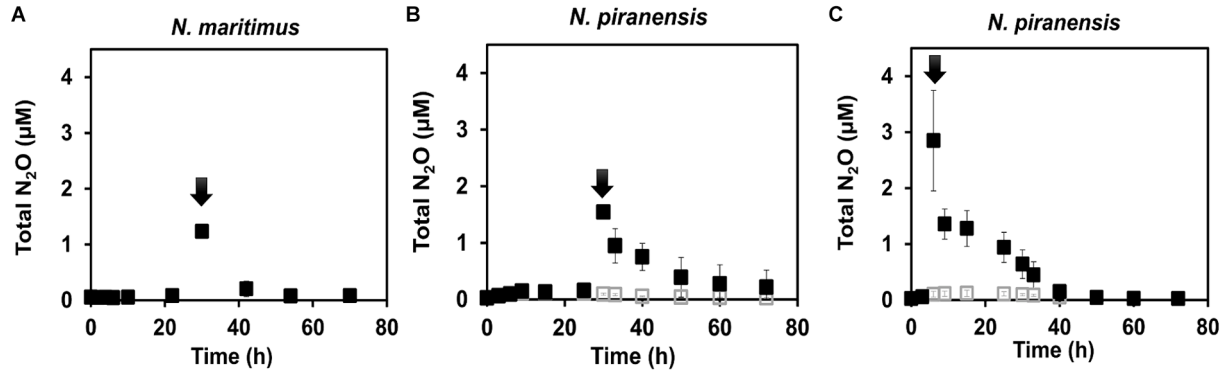

FIGURE 1
N_2O consumption in oxygen-depleted incubations of AOA cultures receiving a spike of N_2O (black arrows). **(A)** *N. maritimus* spiked with 1.2 μM of $^{44}N_2O$ at 30 h of incubation. **(B)** *N. piranensis* spiked with 1.5 μM of $^{44}N_2O$ at 30 h of incubation. **(C)** *N. piranensis* spiked with 3 μM of $^{44}N_2O$ at 6 h. Filled squares show the spiked incubations, while open squares are control replicates (without spike). Symbols represent averages of triplicates, and error bars represent the standard deviation. Some error bars are smaller than the symbols.

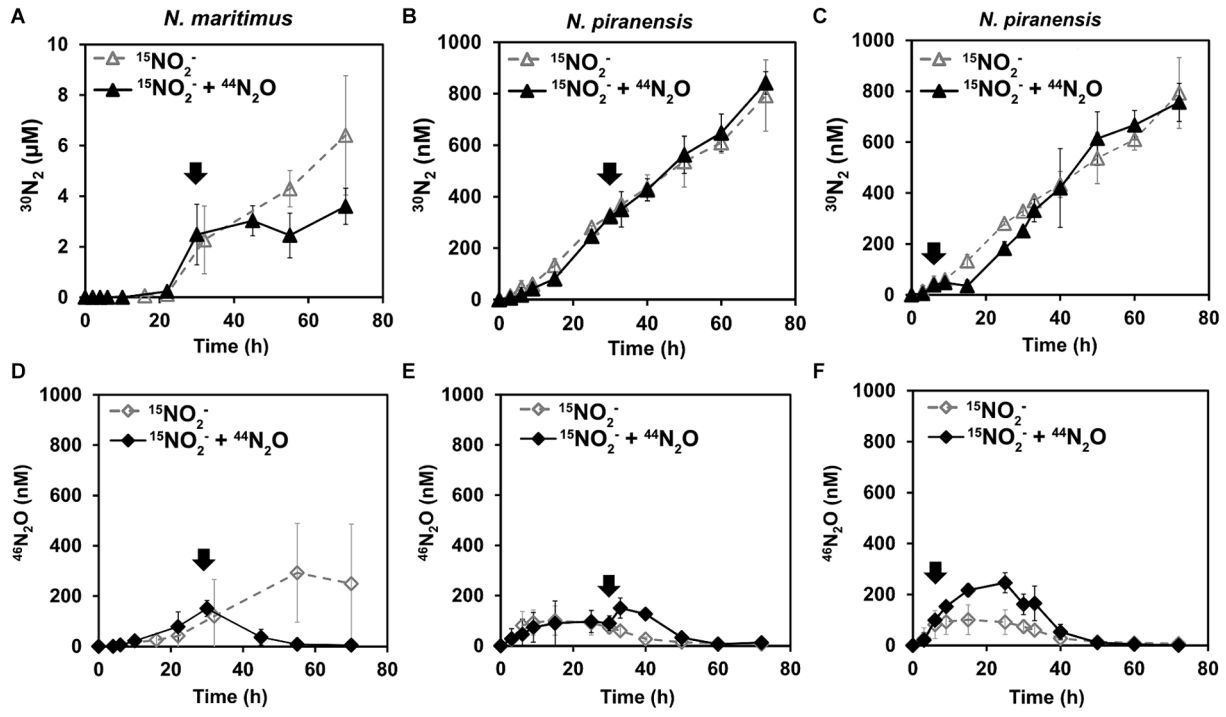

FIGURE 2
Effect of $^{44}N_2O$ spikes on $^{30}N_2$ and $^{46}N_2O$ accumulation by AOA under oxygen depletion. All incubations started with a pool of $^{15}NO_2^-$, and $^{44}N_2O$ was spiked (marked by arrows). The top panels show the accumulation trends of $^{30}N_2$, while the bottom panels show the parallel $^{46}N_2O$ accumulation for the same set of incubations: **(A,D)** from *N. maritimus* with $^{44}N_2O$ spiked at 30 h **(B,E)** from *N. piranensis* with $^{44}N_2O$ spiked at 30 h, and **(C,F)** from *N. piranensis* with $^{44}N_2O$ spiked at 6 h. Open symbols represent control incubations (only $^{15}NO_2^-$ pool), while black symbols show the spiked treatment. The average values of at least three replicates are presented; error bars represent the standard deviation. Some error bars are smaller than the symbols and are therefore not visible.

Complementary incubations to the previous ones were performed to further explore the ability of AOA to reduce N_2O to dinitrogen. *N. piranensis* was selected based on the observations in previous incubations that pointed toward a faster N_2O turnover during NO dismutation. For these incubations, the concentration of spiked N_2O was reduced so that the total N_2O concentration remained in the range in which *N. piranensis* was previously observed to accumulate, to better simulate the conditions under which the reduction of N_2O to N_2 naturally takes place. To track the outcome of the small spikes of N_2O in this set of incubations, the ^{15}N-labeled compound was N_2O and not nitrite. Oxygen-depleted incubations were performed with a batch culture with a pool of $^{14}NO_2^-$. After 8 h, 40 nM of $^{46}N_2O$ was spiked into the incubation bottles. The added $^{46}N_2O$ was completely consumed approximately 24 h after the spike at a rate of approximately 1.5 nM/h (Figure 3A). After 42 h of incubation, a second addition of $^{46}N_2O$ was made, this time aiming for a final concentration of

approximately 90 nM. The $^{46}N_2O$ added was rapidly consumed again the second time at a rate of approximately 3.5 nM/h.

$^{30}N_2$ production was only observed in the replicates spiked with $^{46}N_2O$ (Figure 3B) and was within the expected range. After the second spike, up to 106 ± 2 nM of $^{30}N_2$ was produced by the end of the incubation (Figure 3B), indicating a complete conversion of the spiked $^{46}N_2O$ to N_2. The measured $^{46}N_2O$ spike was 38 ± 9 nM in the first spike and 89 ± 4 nM in the second spike. Thus, the incubation received a total of 127 ± 9 nM $^{46}N_2O$. Every time a sample was collected, the volume was replaced with anoxic sterile medium (see Materials and Methods), leading to a dilution of the added $^{46}N_2O$ and the produced $^{30}N_2$. Taking this into account, the expected concentration of $^{15\text{-}15}N$ compounds at the end of the incubation was 106 nM (see Supplementary material), consistent with the $^{30}N_2$ accumulated by the end of the incubation. To summarize, the spiked $^{46}N_2O$ was completely reduced to and recovered as $^{30}N_2$.

In the controls that did not receive any ^{15}N-labeled compounds, accumulation of neither $^{30}N_2$ nor $^{46}N_2O$ was observed. In these incubations, the accumulation of unlabeled N_2O started in all replicates at the beginning of the incubation and continued until the spike. After the $^{46}N_2O$ spike, the total N_2O concentration ($^{44}N_2O + ^{46}N_2O$) was slightly higher in the spiked replicates compared to the controls. Overall, the total N_2O concentration remained within the natural range in which *N. piranensis* would normally accumulate (Supplementary Figure S3). Taken together, the results of both sets of incubations present solid evidence for N_2O turnover by AOA under oxygen depletion and support its role as an intermediate in the NO-dismutation metabolic pathway.

Oxygen accumulation dynamics in *N. maritimus* and *N. piranensis*

In order to resolve trends in oxygen consumption and accumulation, oxygen concentrations were measured during all incubations with sensors that can resolve oxygen concentrations in the nanomolar range (Lehner et al., 2015). In all incubations, the oxygen was respired within the first few minutes after the transfer to the incubation bottles. For *N. maritimus*, shortly after the oxygen was depleted, oxygen started to accumulate, coupled with NO accumulation (Figure 4A). This pattern of oxygen accumulation has been reported previously by Kraft et al. (2022) for *N. maritimus* and for other AOA species, including *N. piranensis*, by Hernández-Magaña et al. (2023). When samples were collected, despite the precautions taken (see methodology), the sampling was always accompanied by a small intrusion of oxygen, hereafter referred to as oxygen pulses. Immediately after the oxygen pulses caused by the sampling, oxygen was respired until depletion and oxygen accumulation started again, which was consistently within the nanomolar range and coupled with the transient N_2O accumulation and N_2 production described in the previous section.

In addition to the overall oxygen trends described, there was some variability between strains and among incubations. In the incubations with *N. maritimus,* sometimes there was a decrease in oxygen accumulation toward the end of the incubations (Figure 4A and Supplementary Figure S4A), as also observed by Kraft et al. (2022). NO accumulated coupled with oxygen accumulation, especially within the first 20 h of the incubation, reached its highest concentration during this time. Like oxygen, NO accumulation decreased toward the end of the incubation (Supplementary Figure S4B). Oxygen was still consumed following oxygen pulses, indicating the culture's activity. The cessation of oxygen accumulation should not necessarily be interpreted as a lack of oxygen production, but most likely as a more efficient use of it, as in the case of the methane oxidizer *Ca. Methylomirabilis oxyfera*, which internally consumes all the oxygen produced via NO dismutation (Ettwig et al., 2010).

In the case of *N. piranensis,* variability in oxygen accumulation trends between different culture batches was observed. In some incubations, oxygen accumulated after its consumption (Figure 4B), but in other cases, no oxygen accumulation was observed (Figures 4C,D). However, NO, N_2O, and N_2 accumulation from NO_2 were still observed during these incubations. A possible explanation for the lack of oxygen accumulation while the production of N_2 continued is that NO dismutation continued and the produced oxygen was used more efficiently, as mentioned above. A possible contamination of the culture, which could also lead to the consumption of oxygen produced during incubation, was excluded by fluorescence microscopy.

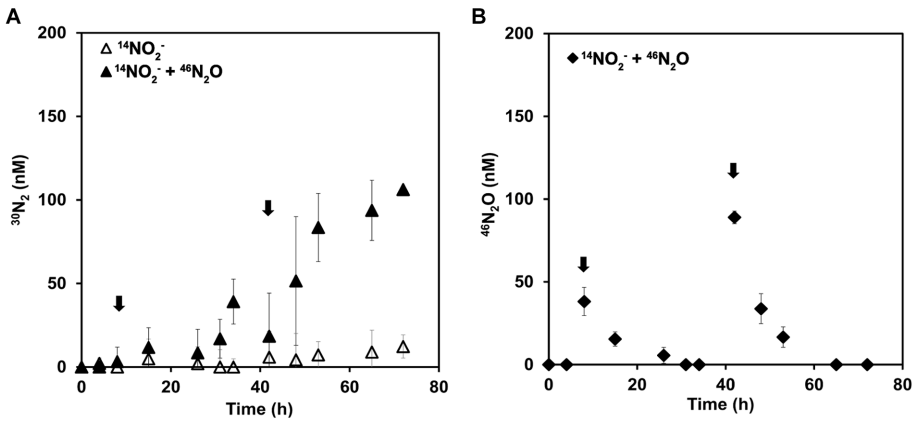

FIGURE 3
$^{46}N_2O$ turnover in oxygen-depleted incubation of *N. piranensis* under oxygen depletion. Incubations started with a pool of $^{14}NO_2^-$ and $^{46}N_2O$ was spiked at 6 h and 42 h (black arrows). **(A)** $^{30}N_2$ production. Black triangles represent incubations into which $^{46}N_2O$ was spiked; open triangles indicate controls without spikes. **(B)** $^{46}N_2O$ concentration measured in the incubation. Black diamonds represent the incubations in which $^{46}N_2O$ was added. $^{46}N_2O$ was undetectable in the control replicates; thus, symbols are not presented. The average of at least three replicates is presented; error bars represent the standard deviation. Some error bars are smaller than the symbols and therefore not visible.

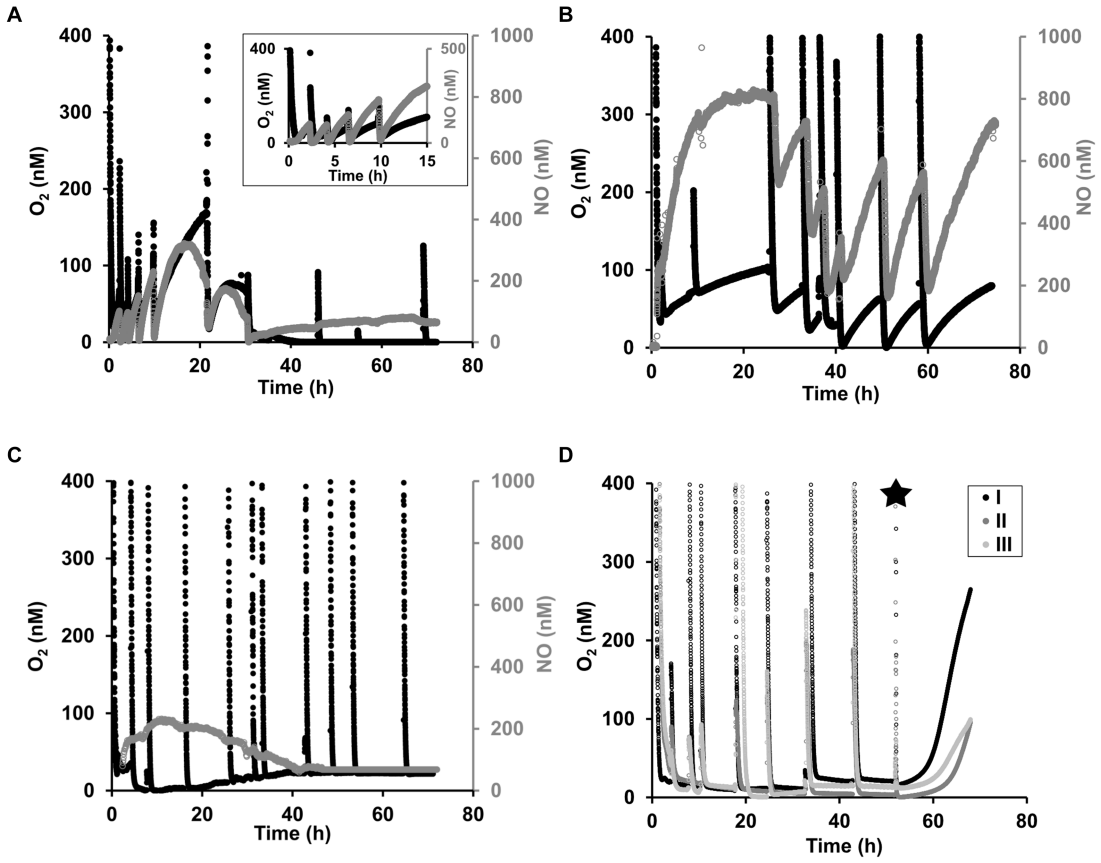

FIGURE 4
Oxygen dynamics in the nanomolar range in oxygen-depleted incubations for *N. maritimus* and *N. piranensis*. **(A)** Oxygen accumulation (black) and NO accumulation (gray) by *N. maritimus* under oxygen depletion. This example of oxygen accumulation corresponds to the incubations of *N. maritimus* started with a $^{15}NO_2^-$ pool and a spike of $^{44}N_2O$ at 30 h (Figures 1, 2). One out of three reproducible replicates is shown, and the other replicates are shown in Supplementary Figure S4, S5. **(B)** *N. piranensis* accumulated oxygen (black) and NO (gray) in different batch incubations. One out of three reproducible replicates is shown here, and the other replicates are shown in Supplementary Figure S6. This incubation was not used for the N_2O spike experiments reported in the present study, but the starting conditions were the same (NO_2^- pool and oxygen depletion). In some batches of *N. piranensis*, oxygen was quickly respired but not accumulated after depletion. **(C)** Shows an example of this. Transient N_2O accumulation and N_2 production were observed in parallel (Figures 1, 2, *N. piranensis*). The example here corresponds to the control incubations with $^{14}NO_2^-$ without spike (The other replicates are shown in Supplementary Figure S7A). The spike of $^{46}N_2O$ at 8 h and at 42 h (Supplementary Figure S6B) did not show differences in oxygen trends. **(D)** After KCN addition (black star), oxygen builds up in incubations with *N. piranensis*. The example here corresponds to the control of the incubations with $^{15}NO_2^-$ without spike. No differences in oxygen trends between control and N_2O spiked replicates were observed (Supplementary Figure S8). Transient N_2O accumulation and N_2 production were observed in parallel (*N. piranensis*, Figures 1, 2).

To test whether *N. piranensis* consumed oxygen more efficiently and thus prevented its accumulation, in some sets of incubations, 0.5 mM of potassium cyanide was added to inhibit oxygen respiration by heme–copper oxygen reductases (Wilson et al., 1994). Indeed, after cyanide addition, oxygen accumulated rapidly (Figure 4D and Supplementary Figure S8A), confirming that oxygen was still being produced but was consumed directly, preventing the accumulation of detectable oxygen concentrations.

Discussion

Marine ammonia-oxidizing archaea reduce N_2O to dinitrogen under oxygen depletion

Oxygen and dinitrogen production through NO dismutation has been observed so far in several different marine and terrestrial AOA isolates, including *N. maritimus* (Kraft et al., 2022) and *N. piranensis* (Hernández-Magaña et al., 2023), which we selected to study the pathway in more detail. In the proposed NO-dismutation pathway, the product of ammonia oxidation, NO_2^-, is reduced to NO, which is dismutated. The proposed products of the dismutation step are N_2O and O_2. N_2O is then further reduced to N_2, making it an intermediate in the NO-dismutation pathway. Transient N_2O accumulation was observed from the beginning of the incubations, followed by N_2 accumulation when *N. maritimus* and *N. piranensis* were exposed to oxygen depletion (this study, Kraft et al., 2022; Hernández-Magaña et al., 2023). The production of N_2O and oxygen from NO dismutation by AOA is a substantial difference from the other known NO-dismutation metabolism by *Ca. M. oxyfera*. This bacterium directly produces N_2 and oxygen via NO dismutation without N_2O as an intermediate (Ettwig et al., 2010). By using a combination of oxygen-depleted incubations with different ^{15}N-labeled compounds and N_2O spikes with different isotopic signatures, we confirmed that

N_2O is the direct intermediate of NO dismutation by AOA. Furthermore, the investigated AOA isolates not only turn over N_2O from NO dismutation but rapidly reduce externally supplied N_2O to N_2.

Although the production and accumulation of N_2O by AOA had been previously reported (Santoro et al., 2011; Löscher et al., 2012), they had been mainly attributed to hybrid formation from ammonia oxidation products and nitrite in oxic incubations (Stieglmeier et al., 2014; Kozlowski et al., 2016; Hink et al., 2017). The N_2O produced in the mentioned studies showed a hybrid isotopic signature, suggesting that one of the N atoms originated from hydroxylamine and one from NO_2. A recent study by Wan et al. (2023), using dual-isotope labeling, assessed multiple N_2O formation mechanisms by *N. maritimus* and suggested ammonia as the main source of N atoms in N_2O under oxic conditions. The same study also found that the production of N_2O from nitrite only occurred by hybrid formation when ammonia and oxygen were present. Under the oxygen concentrations used by Wan et al. (2023), the $^{46}N_2O$ formation from $^{15}NO_2^-$ was negligible, and the authors suggested that the production of N_2O by NO dismutation in AOA is restricted to anoxia. In our experiments, the isotopic signature of the N_2O accumulated by *N. maritimus* and *N. piranensis* upon oxygen depletion ($^{46}N_2O$) indicates that the origin of both N atoms in N_2O is the pool of $^{15}NO_2^-$, suggesting that under oxygen depletion, NO_2^- is the only source of N atoms for N_2O formation, which is consistent with the observations by Kraft et al. (2022). It is worth highlighting that oxygen depletion is required for NO accumulation and, consequently, for NO dismutation to take place. At higher oxygen concentrations, NO would not accumulate to the concentrations observed in the incubations presented here because it reacts with oxygen via autooxidation, producing NO_2^- (Ford et al., 1993; Hickok et al., 2013).

During the incubations with a pool of $^{15}NO_2^-$, *N. maritimus* and *N. piranensis* accumulated oxygen, NO, and $^{46}N_2O$ and produced $^{30}N_2$. In the incubations of *N. piranensis* with a pool of $^{14}NO_2^-$, the spiked $^{46}N_2O$ resulted in the accumulation of $^{30}N_2$, with N_2O being the only source of ^{15}N atoms to form dinitrogen. The quick consumption of the spiked N_2O shows that *N. maritimus* and *N. piranensis* quickly turn over the N_2O pool to N_2 when exposed to oxygen depletion. This evidence supports the role of N_2O as an intermediate in the NO-dismutation pathway. To the best of our knowledge, this is the first time that direct N_2O reduction to dinitrogen by AOA has been shown in physiology experiments.

When exposed to anoxia, NO dismutation is advantageous for AOA because it constitutes an alternative pathway to sustain energy generation and provides alternative electron acceptors and oxygen that can sustain ammonia oxidation at nanomolar ranges (Kraft et al., 2022). While the NO-dismutation reaction is electron-neutral, the other N-conversion steps in the pathway require electrons. The reduction of NO_2^- to NO requires one electron per molecule of NO produced, and the reduction of N_2O to N_2 requires two electrons per molecule of N_2 produced. While the electrons could be partly supplied by ammonia oxidation, the source of the remaining electrons has yet to be discovered. Potential electron donors are organic compounds naturally accumulated in the culture medium during aerobic cell growth (Bayer et al., 2019, 2022).

If AOA were capable of using alternative electron donors other than ammonia, N_2O could serve as the sole electron acceptor under anoxia. The rapid conversion of N_2O to N_2 in the two AOA isolates investigated here supports this possibility. Metabolic activity and growth with N_2O as the only electron acceptor are common in many different denitrifying and non-denitrifying microorganisms, with a NosZ N_2O reductase (Mania et al., 2016; Conthe et al., 2018; Lycus et al., 2018; Read-Daily et al., 2022). Given the incubation times in the present study, cell growth was not expected to be observed. During aerobic ammonia oxidation under oxic and optimal conditions, AOA grow at a relatively slow rate. Generation times of *N. maritimus* and *N. piranensis* are at a minimum of 19 and 27 h, respectively (Qin et al., 2017; Bayer et al., 2019). Growth rates under anoxic conditions are expected to drop. Therefore, to detect cell growth when AOA perform NO dismutation under oxygen depletion, future research should explore alternatives to cell counts, such as using activity proxies like the incorporation of specifically labeled substrates (Musat et al., 2012; Hatzenpichler et al., 2020).

Although nitrite reduction to NO is most likely performed by the NirK nitrite reductase (Bartossek et al., 2010; Kozlowski et al., 2016), the enzymes responsible for NO dismutation and the further reduction of N_2O by AOA remain to be identified. No genes encoding potential NO dismutases or N_2O reductases have been identified in the genomes of *N. maritimus*, *N. piranensis,* or other AOA species (Walker et al., 2010; Qin et al., 2020). All known nitrous oxide reductases belong to the NosZ family. However, the existence of N_2O reductases outside of this family has been proposed multiple times, as reduction of N_2O has been observed in pure microbial cultures that lack a NosZ enzyme (Arciero et al., 2002; Fernandes et al., 2010). Recently, the cytochrome P450 was suggested to be involved in the production of N_2O via NO reduction by the AOA *Nitrosocosmicus oleophilus* MY3, based on N_2O production measurements coinciding with higher expression of the cytochrome (Jung et al., 2019). These observations were made under oxic conditions and low pH (5.5), in contrast to the conditions used in the current study (oxygen depletion and media HEPES buffered at a pH of 7.6). In *Ca. M. oxyfera*, quinol-dependent NO reductases (qNORs) have been identified as putative NO dismutases encoded by the *nod* gene (Ettwig et al., 2010, 2012; Zhu et al., 2019), but AOA do not possess these genes. To date, the potential for NO dismutation followed by N_2O reduction to N_2 by AOA would therefore be overlooked in comparative genomic analyses.

In physiological studies, NO dismutation by AOA would also have been easily overlooked because AOA cultures were not exposed long enough to oxygen depletion, and nitrogen compounds were studied with lower-resolution methods. The lowest oxygen concentrations examined in previous physiological studies of AOA were approximately 1 µM in the headspace (0.1%) (Qin et al., 2015, 2017), and ammonia oxidation was no longer detectable with colorimetric assays. These oxygen concentrations greatly exceed the concentrations at which we observed NO dismutation and oxygen accumulation. At the oxygen concentrations of the present study, the ammonia oxidation rates are in the range of 40 nM/h and would only be detectable by using ^{15}N-tracers, as shown by Kraft et al. (2022). Furthermore, the rates of N_2 production via NO dismutation are also low and would not be detectable without the use of ^{15}N-tracers.

Variability in oxygen accumulation trends in marine AOA

In oxygen-depleted incubations in which oxygen accumulation was observed in all replicates, oxygen accumulation often decreased toward the end of the incubation, similar to previous observations

(Kraft et al., 2022; Hernández-Magaña et al., 2023). The quick oxygen respiration after oxygen pulses, despite oxygen not being accumulated, indicates respiratory activity of the AOA cells (Figure 4). Moreover, the reduction of N_2O and constant production of N_2 in these incubations continued despite the apparent lack of oxygen accumulation. In the specific case of *N. piranensis,* oxygen did not accumulate in some incubation bottles (Figures 4C,D). After cyanide addition, a rapid increase in oxygen concentration was observed (Figure 4D and Supplementary Figure S7A). These observations, taken together, suggest that the cultures most likely continued to produce oxygen via NO dismutation, but all of it was utilized immediately, leading to no accumulation at detectable concentrations. Therefore, the lack of oxygen accumulation does not imply a lack of activity or absence of oxygen production, but most likely a more efficient usage of the oxygen produced, which prevents accumulation from being detected.

These observations point toward a change in the efficiency of the coupling between oxygen production and its use: at the beginning of the incubation, oxygen is produced faster than it is used, and later the production and consumption processes become more tightly coupled, or in the case of *N. piranensis*, some culture batches may have a faster response to oxygen depletion, which leads to a tighter coupling between oxygen production and consumption. Tightly coupled oxygen production and consumption takes place in cultures of the methane oxidizer *Ca. M. oxyfera*: no oxygen accumulates during NO dismutation, as it is immediately utilized intracellularly for methane oxidation (Ettwig et al., 2010). In *Ca. M. oxyfera*, the detection of oxygen produced via NO dismutation was only possible after the inhibition of the oxygen-consuming methane mono-oxygenase complex (pMMO) by acetylene (Ettwig et al., 2010, 2012; Wu et al., 2011), which is comparable to our observation of oxygen accumulation after cyanide addition.

Whether AOA are capable of producing oxygen via the NO-dismutation pathway in the environment is still unknown and challenging to detect, as any trace of oxygen produced in the environment would be immediately used by the microbial community (Garcia-Robledo et al., 2017), and because the isotopic signature of ^{15}N-tracer methods to detect NO dismutation is indistinguishable from denitrification. Therefore, it is important to perform investigations in environmental settings to unveil the potential influence of AOA activity on the oxygen and nitrogen metabolism of natural communities in oxygen-depleted ecosystems.

Conclusion

We confirmed that in the NO-dismutation pathway performed by AOA under oxygen depletion, N_2O is indeed an intermediate and demonstrated that NO is dismutated to oxygen and nitrous oxide, which is then further reduced to dinitrogen. Through incubations with combinations of different N compounds with different isotopic signatures ($^{15}NO_2^-$ pool +$^{44}N_2O$ spike and $^{14}NO_2^-$ pool +$^{46}N_2O$ spike), we showed that N_2O is rapidly turned over by AOA and that AOA are capable of reducing N_2O to N_2 at high rates. The observations made here highlight the importance of a new pathway of N_2O turnover by AOA, whose potential in the environment needs to be further investigated. AOA have been shown to be abundant in environments with short or extended periods of anoxia, such as marine OMZs or anoxic basins. Experimental evidence of AOA activity at such sites is crucial to determining the extent to which this pathway should be included among the potential sources and sinks of N_2O in the environment.

Data availability statement

The original contributions presented in the study are included in the article/Supplementary material, further inquiries can be directed to the corresponding authors.

Author contributions

EH-M: Conceptualization, Data curation, Formal analysis, Investigation, Methodology, Visualization, Writing – original draft, Writing – review & editing. BK: Conceptualization, Funding acquisition, Investigation, Supervision, Writing – original draft, Writing – review & editing, Methodology.

Funding

The author(s) declare that financial support was received for the research, authorship, and/or publication of this article. This study was funded by the Villum Foundation (grant no. 00025491) to Beate Kraft.

Acknowledgments

We thank Bo Thamdrup and Laura Bristow for their valuable advice when processing samples on the IRMS.

Conflict of interest

The authors declare that the research was conducted in the absence of any commercial or financial relationships that could be construed as a potential conflict of interest.

Publisher's note

Supplementary material

The Supplementary material for this article can be found online at: https://www.frontiersin.org/articles/10.3389/fmicb.2024.1410251/full#supplementary-material

References

Arciero, D. M., Pierce, B. S., Hendrich, M. P., and Hooper, A. B. (2002). Nitrosocyanin, a red Cupredoxin-like protein from *Nitrosomonas europaea*. *Biochemistry* 41, 1703–1709. doi: 10.1021/bi015908w

Babbin, A. R., Bianchi, D., Jayakumar, A., and Ward, B. B. (2015). Rapid nitrous oxide cycling in the Suboxic Ocean. *Science* 348, 1127–1129. doi: 10.1126/science.aaa8380

Bartossek, R., Nicol, G. W., Lanzen, A., Klenk, H.-P., and Schleper, C. (2010). Homologues of nitrite reductases in ammonia-oxidizing archaea: diversity and genomic context. *Environ. Microbiol.* 12, 1075–1088. doi: 10.1111/j.1462-2920.2010.02153.x

Bayer, B., Hansman, R. L., Bittner, M. J., Noriega-Ortega, B. E., Niggemann, J., Dittmar, T., et al. (2019). Ammonia-oxidizing archaea release a suite of organic compounds potentially fueling prokaryotic heterotrophy in the ocean. *Environ. Microbiol.* 21, 4062–4075. doi: 10.1111/1462-2920.14755

Bayer, B., McBeain, K., Carlson, C. A., and Santoro, A. E. (2022). Carbon content, carbon fixation yield and dissolved organic carbon release from diverse marine nitrifiers. *Limnol. Oceanography* 68, 84–96. doi: 10.1002/lno.12252

Beman, J. M., Popp, B. N., and Francis, C. A. (2008). Molecular and biogeochemical evidence for ammonia oxidation by marine Crenarchaeota in the Gulf of California. *ISME J.* 2, 429–441. doi: 10.1038/ismej.2007.118

Bristow, L. A., Dalsgaard, T., Tiano, L., Mills, D. B., Bertagnolli, A. D., Wright, J. J., et al. (2016). Ammonium and nitrite oxidation at nanomolar oxygen concentrations in oxygen minimum zone waters. *Proc. Natl. Acad. Sci.* 113, 10601–10606. doi: 10.1073/pnas.1600359113

Codispoti, L. A. (2010). Interesting times for marine N_2O. *Science* 327, 1339–1340. doi: 10.1126/science.1184945

Conthe, M., Wittorf, L., Kuenen, J. G., Kleerebezem, R., van Loosdrecht, M. C. M., and Hallin, S. (2018). Life on N_2O: deciphering the ecophysiology of N_2O respiring bacterial communities in a continuous culture. *ISME J.* 12, 1142–1153. doi: 10.1038/s41396-018-0063-7

Dalsgaard, T., Thamdrup, B., Farías, L., and Revsbech, N. P. (2012). Anammox and denitrification in the oxygen minimum zone of the eastern South Pacific. *Limnol. Oceanogr.* 57, 1331–1346. doi: 10.4319/lo.2012.57.5.1331

Ettwig, K. F., Butler, M. K., Le Paslier, D., Pelletier, E., Mangenot, S., Kuypers, M. M. M., et al. (2010). Nitrite-driven anaerobic methane oxidation by oxygenic bacteria. *Nature* 464, 543–548. doi: 10.1038/nature08883

Ettwig, K. F., Speth, D. R., Reimann, J., Wu, M. L., Jetten, M. S. M., and Keltjens, J. T. (2012). Bacterial oxygen production in the dark. *Front. Microbiol.* 3:273. doi: 10.3389/fmicb.2012.00273

Fernandes, A. T., Damas, J. M., Todorovic, S., Huber, R., Baratto, M. C., Pogni, R., et al. (2010). The multicopper oxidase from the archaeon *Pyrobaculum aerophilum* shows nitrous oxide reductase activity. *FEBS J.* 277, 3176–3189. doi: 10.1111/j.1742-4658.2010.07725.x

Ford, P. C., Wink, D. A., and Stanbury, D. M. (1993). Autoxidation kinetics of aqueous nitric oxide. *FEBS Lett.* 326, 1–3. doi: 10.1016/0014-5793(93)81748-O

Francis, C. A., Roberts, K. J., Beman, J. M., Santoro, A. E., and Oakley, B. B. (2005). Ubiquity and diversity of ammonia-oxidizing archaea in water columns and sediments of the ocean. *Proc. Natl. Acad. Sci.* 102, 14683–14688. doi: 10.1073/pnas.0506625102

Garcia-Robledo, E., Padilla, C. C., Aldunate, M., Stewart, F. J., Ulloa, O., Paulmier, A., et al. (2017). Cryptic oxygen cycling in anoxic marine zones. *Proc. Natl. Acad. Sci.* 114, 8319–8324. doi: 10.1073/pnas.1619844114

Hatzenpichler, R., Krukenberg, V., Spietz, R. L., and Jay, Z. J. (2020). Next-generation physiology approaches to study microbiome function at single cell level. *Nat. Rev. Microbiol.* 18, 241–256. doi: 10.1038/s41579-020-0323-1

Hernández-Magaña, A. E., Canfield, D. E., and Kraft, B. (2023). Oxygen production via NO dismutation in different ammonia oxidizers. *BioRxiv. [Preprint]*. doi: 10.1101/2023.06.07.544047

Hickok, J. R., Vasudevan, D., Jablonski, K., and Thomas, D. D. (2013). Oxygen dependence of nitric oxide-mediated signaling. *Redox Biol.* 1, 203–209. doi: 10.1016/j.redox.2012.11.002

Hink, L., Lycus, P., Gubry-Rangin, C., Frostegård, Å., Nicol, G. W., Prosser, J. I., et al. (2017). Kinetics of NH_3-oxidation, NO-turnover, N2O-production and electron flow during oxygen depletion in model bacterial and archaeal ammonia oxidisers. *Environ. Microbiol.* 19, 4882–4896. doi: 10.1111/1462-2920.13914

Jones, C. M., Graf, D. R., Bru, D., Philippot, L., and Hallin, S. (2013). The unaccounted yet abundant nitrous oxide-reducing microbial community: a potential nitrous oxide sink. *ISME J.* 7, 417–426. doi: 10.1038/ismej.2012.125

Jung, M.-Y., Gwak, J.-H., Rohe, L., Giesemann, A., Kim, J.-G., Well, R., et al. (2019). Indications for enzymatic denitrification to N2O at low pH in an ammonia-oxidizing archaeon. *ISME J.* 13, 2633–2638. doi: 10.1038/s41396-019-0460-6

Karner, M. B., DeLong, E. F., and Karl, D. M. (2001). Archaeal dominance in the mesopelagic zone of the Pacific Ocean. *Nature* 409, 507–510. doi: 10.1038/35054051

Könneke, M., Bernhard, A. E., de la Torre, J. R., Walker, C. B., Waterbury, J. B., and Stahl, D. A. (2005). Isolation of an autotrophic ammonia-oxidizing marine archaeon. *Nature* 437, 543–546. doi: 10.1038/nature03911

Kozlowski, J. A., Stieglmeier, M., Schleper, C., Klotz, M. G., and Stein, L. Y. (2016). Pathways and key intermediates required for obligate aerobic ammonia-dependent chemolithotrophy in bacteria and Thaumarchaeota. *ISME J.* 10, 1836–1845. doi: 10.1038/ismej.2016.2

Kraft, B., Jehmlich, N., Larsen, M., Bristow, L. A., Könneke, M., Thamdrup, B., et al. (2022). Oxygen and nitrogen production by an ammonia-oxidizing archaeon. *Science* 375, 97–100. doi: 10.1126/science.abe6733

Lam, P., Jensen, M. M., Lavik, G., McGinnis, D. F., Müller, B., Schubert, C. J., et al. (2007). Linking crenarchaeal and bacterial nitrification to anammox in the Black Sea. *Proc. Natl. Acad. Sci.* 104, 7104–7109. doi: 10.1073/pnas.0611081104

Lehner, P., Larndorfer, C., Garcia-Robledo, E., Larsen, M., Borisov, S. M., Revsbech, N.-P., et al. (2015). LUMOS - a sensitive and reliable Optode system for measuring dissolved oxygen in the Nanomolar range. *PLoS One* 10:e0128125. doi: 10.1371/journal.pone.0128125

Löscher, C. R., Kock, A., Könneke, M., LaRoche, J., Bange, H. W., and Schmitz, R. A. (2012). Production of oceanic nitrous oxide by ammonia-oxidizing archaea. *Biogeosciences* 9, 2419–2429. doi: 10.5194/bg-9-2419-2012

Lycus, P., Soriano-Laguna, M. J., Kjos, M., Richardson, D. J., Gates, A. J., Milligan, D. A., et al. (2018). A bet-hedging strategy for denitrifying bacteria curtails their release of N_2O. *Proc. Natl. Acad. Sci.* 115, 11820–11825. doi: 10.1073/pnas.1805000115

Mania, D., Heylen, K., van Spanning, R. J. M., and Frostegård, Å. (2016). Regulation of nitrogen metabolism in the nitrate-ammonifying soil bacterium bacillus vireti and evidence for its ability to grow using N_2O as electron acceptor. *Environ. Microbiol.* 18, 2937–2950. doi: 10.1111/1462-2920.13124

Martens-Habbena, W., Berube, P. M., Urakawa, H., de la Torre, J. R., and Stahl, D. A. (2009). Ammonia oxidation kinetics determine niche separation of nitrifying Archaea and Bacteria. *Nature* 461, 976–979. doi: 10.1038/nature08465

Musat, N., Foster, R., Vagner, T., Adam, B., and Kuypers, M. M. M. (2012). Detecting metabolic activities in single cells, with emphasis on nanoSIMS. *FEMS Microbiol. Rev.* 36, 486–511. doi: 10.1111/j.1574-6976.2011.00303.x

IPCC, (2014). *Climate change 2014: Synthesis report. Contribution of working groups I, II and III to the fifth assessment report of the intergovernmental panel on climate change.* Eds. R. K. Pachauri and L. A. Meyer (Geneva, Switzerland: IPCC) pp. 151.

Peng, X., Fuchsman, C. A., Jayakumar, A., Oleynik, S., Martens-Habbena, W., Devol, A. H., et al. (2015). Ammonia and nitrite oxidation in the eastern tropical North Pacific. *Glob. Biogeochem. Cycles* 29, 2034–2049. doi: 10.1002/2015GB005278

Prosser, J. I., Hink, L., Gubry-Rangin, C., and Nicol, G. W. (2020). Nitrous oxide production by ammonia oxidizers: physiological diversity, niche differentiation and potential mitigation strategies. *Glob. Chang. Biol.* 26, 103–118. doi: 10.1111/gcb.14877

Qin, W., Carlson, L. T., Armbrust, E. V., Devol, A. H., Moffett, J. W., Stahl, D. A., et al. (2015). Confounding effects of oxygen and temperature on the TEX86 signature of marine Thaumarchaeota. *Proc. Natl. Acad. Sci.* 112, 10979–10984. doi: 10.1073/pnas.1501568112

Qin, W., Meinhardt, K. A., Moffett, J. W., Devol, A. H., Armbrust, E. V., Ingalls, A. E., et al. (2017). Influence of oxygen availability on the activities of ammonia-oxidizing archaea. *Environ. Microbiol. Rep.* 9, 250–256. doi: 10.1111/1758-2229.12525

Qin, W., Zheng, Y., Zhao, F., Wang, Y., Urakawa, H., Martens-Habbena, W., et al. (2020). Alternative strategies of nutrient acquisition and energy conservation map to the biogeography of marine ammonia-oxidizing archaea. *ISME J.* 14, 2595–2609. doi: 10.1038/s41396-020-0710-7

Read-Daily, B., Ben Maamar, S., Sabba, F., Green, S., and Nerenberg, R. (2022). Effect of nitrous oxide (N_2O) on the structure and function of nitrogen-oxide reducing microbial communities. *Chemosphere* 307:135819. doi: 10.1016/j.chemosphere.2022.135819

Santoro, A. E., Buchwald, C., McIlvin, M. R., and Casciotti, K. L. (2011). Isotopic signature of N2O produced by marine Ammonia-oxidizing Archaea. *Science* 333, 1282–1285. doi: 10.1126/science.1208239

Sollai, M., Villanueva, L., Hopmans, E. C., Reichart, G.-J., and Sinninghe Damsté, J. S. (2019). A combined lipidomic and 16S rRNA gene amplicon sequencing approach reveals archaeal sources of intact polar lipids in the stratified Black Sea water column. *Geobiology* 17, 91–109. doi: 10.1111/gbi.12316

Stein, L. Y., Klotz, M. G., Lancaster, K. M., Nicol, G. W., Qin, W., Schleper, C., et al. (2021). Comment on"a critical review on nitrous oxide production by Ammonia-oxidizing Archaea" by Lan Wu, Xueming Chen, Wei Wei, Yiwen Liu, Dongbo Wang, and Bing-Jie Ni. *Environ. Sci. Technol.* 55, 797–798. doi: 10.1021/acs.est.0c06792

Stieglmeier, M., Mooshammer, M., Kitzler, B., Wanek, W., Zechmeister-Boltenstern, S., Richter, A., et al. (2014). Aerobic nitrous oxide production through N-nitrosating hybrid formation in ammonia-oxidizing archaea. *ISME J.* 8, 1135–1146. doi: 10.1038/ismej.2013.220

Thomson, A. J., Giannopoulos, G., Pretty, J., Baggs, E. M., and Richardson, D. J. (2012). Biological sources and sinks of nitrous oxide and strategies to mitigate emissions. *Philos. Trans. R. Soc. Lond. Ser. B Biol. Sci.* 367, 1157–1168. doi: 10.1098/rstb.2011.0415

Tiano, L., Garcia-Robledo, E., and Revsbech, N. P. (2014). A new highly sensitive method to assess respiration rates and kinetics of natural planktonic communities by use of the switchable trace oxygen sensor and reduced oxygen concentrations. *PLoS One* 9:e105399. doi: 10.1371/journal.pone.0105399

Walker, C. B., de la Torre, J. R., Klotz, M. G., Urakawa, H., Pinel, N., Arp, D. J., et al. (2010). Nitrosopumilus maritimus genome reveals unique mechanisms for nitrification and autotrophy in globally distributed marine crenarchaea. *Proc. Natl. Acad. Sci.* 107, 8818–8823. doi: 10.1073/pnas.0913533107

Wan, X. S., Hou, L., Kao, S.-J., Zhang, Y., Sheng, H.-X., Shen, H., et al. (2023). Pathways of N_2O production by marine ammonia-oxidizing archaea determined from dual-isotope labeling. *Proc. Natl. Acad. Sci.* 120:e2220697120. doi: 10.1073/pnas.2220697120

Wilson, M. T., Antonini, G., Malatesta, F., Sarti, P., and Brunori, M. (1994). Probing the oxygen binding site of cytochrome c oxidase by cyanide. *J. Biol. Chem.* 269, 24114–24119. doi: 10.1016/S0021-9258(19)51055-9

Wu, L., Chen, X., Wei, W., Liu, Y., Wang, D., and Ni, B.-J. (2020). A critical review on nitrous oxide production by Ammonia-oxidizing Archaea. *Environ. Sci. Technol.* 54, 9175–9190. doi: 10.1021/acs.est.0c03948

Wu, M. L., Ettwig, K. F., Jetten, M. S. M., Strous, M., Keltjens, J. T., and Van Niftrik, L. (2011). A new intra-aerobic metabolism in the nitrite-dependent anaerobic methane-oxidizing bacterium Candidatus '*Methylomirabilis oxyfera*'. *Biochem. Soc. Trans.* 39, 243–248. doi: 10.1042/BST0390243

Zhu, B., Wang, J., Bradford, L. M., Ettwig, K., Hu, B., and Lueders, T. (2019). Nitric oxide dismutase (nod) genes as a functional marker for the diversity and phylogeny of methane-driven oxygenic Denitrifiers. *Front. Microbiol.* 10:1577. doi: 10.3389/fmicb.2019.01577

frontiers | Frontiers in Microbiology

TYPE Correction
PUBLISHED 28 October 2024
DOI 10.3389/fmicb.2024.1506979

OPEN ACCESS

APPROVED BY
Frontiers Editorial Office,
Frontiers Media SA, Switzerland

*CORRESPONDENCE
Elisa Hernández-Magaña
✉ elisa@biology.sdu.dk
Beate Kraft
✉ bkraft@biology.sdu.dk

RECEIVED 06 October 2024
ACCEPTED 09 October 2024
PUBLISHED 28 October 2024

CITATION
Hernández-Magaña E and Kraft B (2024) Corrigendum: Nitrous oxide production and consumption by marine ammonia-oxidizing archaea under oxygen depletion.
Front. Microbiol. 15:1506979.
doi: 10.3389/fmicb.2024.1506979

Corrigendum: Nitrous oxide production and consumption by marine ammonia-oxidizing archaea under oxygen depletion

Elisa Hernández-Magaña* and Beate Kraft*

Nordcee, Department of Biology, Faculty of Sciences, University of Southern Denmark, Odense, Denmark

KEYWORDS

oxygen depletion, anoxia, NO dismutation, ammonia-oxidizing archaea, nitrous oxide, nitrous oxide reduction

A Corrigendum on
Nitrous oxide production and consumption by marine ammonia-oxidizing archaea under oxygen depletion

by Hernández-Magaña, E., and Kraft, B. (2024). *Front. Microbiol.* 15:1410251. doi: 10.3389/fmicb.2024.1410251

In the published article, there was an error in affiliation 1. Instead of "Nordcee, Department of Biology, Faculty of Sciences, Nordcee, University of Southern Denmark, Odense, Denmark", it should be "Nordcee, Department of Biology, Faculty of Sciences, University of Southern Denmark, Odense, Denmark".

In the published article, there was an error. The name of a microbial isolate was spelled incorrectly.

A correction has been made to **Materials and methods**, *Growth conditions*. This sentence previously stated:

"Axenic 5 L batch pre-cultures of the AOA strains *N. maritimus* SCM1 and *N. piranensis* DC3 (JCM 32271, DSM 106147, and NCIMB 15115) were grown at 28°C in the dark in synthetic Crenarchaeota medium (SCM) HEPES-buffered (pH 7.8), as described by Könneke et al. (2005) and Martens-Habbena et al. (2009), modified with a 6 mM final concentration of sodium bicarbonate (Kraft et al., 2022)."

The corrected sentence appears below:

"Axenic 5 L batch pre-cultures of the AOA strains *N. maritimus* SCM1 and *N. piranensis* D3C (JCM 32271, DSM 106147, and NCIMB 15115) were grown at 28°C in the dark in synthetic Crenarchaeota medium (SCM) HEPES-buffered (pH 7.8), as described by Könneke et al. (2005) and Martens-Habbena et al. (2009), modified with a 6 mM final concentration of sodium bicarbonate (Kraft et al., 2022)."

The authors apologize for this error and state that this does not change the scientific conclusions of the article in any way. The original article has been updated.

Publisher's note

All claims expressed in this article are solely those of the authors and do not necessarily represent those of their affiliated organizations, or those of the publisher, the editors and the reviewers. Any product that may be evaluated in this article, or claim that may be made by its manufacturer, is not guaranteed or endorsed by the publisher.

frontiers | Frontiers in Microbiology

TYPE Original Research
PUBLISHED 23 September 2024
DOI 10.3389/fmicb.2024.1433224

OPEN ACCESS

EDITED BY
Ivan A. Berg,
University of Münster, Germany

REVIEWED BY
Nicole Buan,
University of Nebraska-Lincoln, United States
Rafael Bargiela,
Instituto de Catálisis y Petroleoquímca (ICP-CSIC), Spain

*CORRESPONDENCE
Filipa L. Sousa
✉ filipa.sousa@univie.ac.at

RECEIVED 15 May 2024
ACCEPTED 28 August 2024
PUBLISHED 23 September 2024

CITATION
Karavaeva V and Sousa FL (2024) Navigating the archaeal frontier: insights and projections from bioinformatic pipelines.
Front. Microbiol. 15:1433224.
doi: 10.3389/fmicb.2024.1433224

Navigating the archaeal frontier: insights and projections from bioinformatic pipelines

Val Karavaeva[1,2] and Filipa L. Sousa[1]*

[1]Genome Evolution and Ecology Group, Department of Functional and Evolutionary Ecology, University of Vienna, Vienna, Austria, [2]Vienna Doctoral School of Ecology and Evolution, University of Vienna, Vienna, Austria

Archaea continues to be one of the least investigated domains of life, and in recent years, the advent of metagenomics has led to the discovery of many new lineages at the phylum level. For the majority, only automatic genomic annotations can provide information regarding their metabolic potential and role in the environment. Here, genomic data from 2,978 archaeal genomes was used to perform automatic annotations using bioinformatics tools, alongside synteny analysis. These automatic classifications were done to assess how good these different tools perform in relation to archaeal data. Our study revealed that even with lowered cutoffs, several functional models do not capture the recently discovered archaeal diversity. Moreover, our investigation revealed that a significant portion of archaeal genomes, approximately 42%, remain uncharacterized. In comparison, within 3,235 bacterial genomes, a diverse range of unclassified proteins is obtained, with well-studied organisms like *Escherichia coli* having a substantially lower proportion of uncharacterized regions, ranging from <5 to 25%, and less studied lineages being comparable to archaea with the range of 35–40% of unclassified regions. Leveraging this analysis, we were able to identify metabolic protein markers, thereby providing insights into the metabolism of the archaea in our dataset. Our findings underscore a substantial gap between automatic classification tools and the comprehensive mapping of archaeal metabolism. Despite advances in computational approaches, a significant portion of archaeal genomes remains unexplored, highlighting the need for extensive experimental validation in this domain, as well as more refined annotation methods. This study contributes to a better understanding of archaeal metabolism and underscores the importance of further research in elucidating the functional potential of archaeal genomes.

KEYWORDS

archaea, energy metabolism, microbial dark matter, microbial ecology, microbial diversity

1 Introduction

Archaea, as a domain of life, has been a source of continual surprises (Cavicchioli, 2010; Jarrell et al., 2011), with ongoing discoveries helping us to understand the processes conserved in all domains of life and revealing novel types and unique features of metabolism (DiMarco et al., 1990; Weiss and Thauer, 1993; Verhees et al., 2003; Siebers and Schönheit, 2005; Thauer et al., 2008), unique structural features (Nickell et al., 2003; Moissl et al., 2005; Walsby, 2005; Matsumi et al., 2011; Zillig et al., 1981), and new genomes (Mara

et al., 2023; Zhang I. H. et al., 2024), and novel lineages at the highest rank. Examples of those would be the new supergroups of archaea such as DPANN (Dombrowski et al., 2019; Zhang R. Y. et al., 2024) and Asgard (Spang et al., 2015; Zaremba-Niedzwiedzka et al., 2017; Imachi et al., 2020; Rodrigues-Oliveira et al., 2023). Moreover, the archaeal domain continuously reveals new sides to already known aspects of microbial metabolism, with novel metabolic capabilities for old enzymes, such as the case of McrA, previously a marker for methanogenesis and anaerobic methane oxidation (Friedrich, 2005), whose role in metabolism of higher carbon compounds was shown (Goenrich et al., 2004; Scheller et al., 2013; Laso-Pérez et al., 2016; Musat et al., 2024) in agreement with early *in vitro* experiments with higher carbons (Gunsalus et al., 1978), or the discovery of the metabolic potential of *Ca.* Korarchaeota for dissimilatory sulfite reduction (McKay et al., 2019). Notably, Archaea have played a pivotal role in the evolution of eukaryotes, indicating their significance in the history of life on Earth (Spang et al., 2015; Mac Leod et al., 2019; Imachi et al., 2020; López-García and Moreira, 2020; Eme et al., 2023; Spang, 2023, to name a few). The presence of eukaryotic signature proteins within Asgard genomes also led to an increased interest in the archaeal cell biology in the last few years, with a myriad of papers published on the topic (van Wolferen et al., 2022; Charles-Orszag et al., 2024; Makarova et al., 2024).

Archaea are everywhere, including the gut and skin of humans and other animals (Thomas C. M. et al., 2022; Moissl-Eichinger et al., 2017), with possibly a beneficial role. Yet, primarily due to methodological limitations (Taffner et al., 2019; Song et al., 2019), and possibly the biases in funding towards pathogens or biotechnologically relevant organisms (Lasken and McLean, 2014), the role of archaea with their host and other microorganisms remains largely unknown. Furthermore, archaea are present in plants, where, besides ammonia-oxidizing archaea (AOA) in the rhizosphere and leaves (Taffner et al., 2019; Song et al., 2019), methanogens (Taffner et al., 2019; Taffner et al., 2018) and halophilic (salt-loving) archaea can also be found (Taffner et al., 2018; Yadav et al., 2015; Al-Mailem et al., 2010). Thus, besides the impact of AOA and their role in increasing plant yield, using metagenomic sequencing techniques, indirect roles in plant growth-promoting traits, such as auxin production and production of secondary metabolites to aid against pathogens, abiotic, and biotic stress, were proposed (Taffner et al., 2018). These examples clearly show the archaeal versatile roles across different ecosystems. Whether thriving in extreme environments (*Sulfolobales, Halobacteria*) or existing in more common settings (*Nitrososphaerota*; Chaban et al., 2006), archaea remain enigmatic due to their unique adaptations and historical research biases towards the study of (pathogenic) bacteria. For instance, so far, no one really knows all enzymes involved in archaeal ammonia oxidation (Schleper and Nicol, 2010).

Since the origin of life on our planet, archaeal microorganisms continue to be fundamental to biogeochemical cycles, profoundly influencing ecosystems and environmental processes (Falkowski et al., 2008; Zhang C. et al., 2023; Qi et al., 2024; Lyons et al., 2024; Baker et al., 2020). Archaea contribute significantly to cycles involving sulfur (S; Offre et al., 2013; Neukirchen et al., 2023), nitrogen (N; Huang et al., 2021; Offre et al., 2013; Leigh, 2000), carbon (C; Boetius et al., 2000; Offre et al., 2013; Fuchs, 2011; Zhang X. et al., 2023; Justice et al., 2012; Kaster et al., 2011; Thauer et al., 1977; Thauer et al., 2008), oxygen (O; Bandeiras et al., 2005; Teske, 2018; Luo et al., 2024), iron (Fe, Dong et al., 2021; Auernik and Kelly, 2008; Malik and Hedrich, 2022), and arsenic (As; Zhang C. et al., 2023; van Lis et al., 2013) across various habitats. Their metabolic versatility and resilience in extreme environments make archaea indispensable for maintaining the equilibrium of these elemental cycles, impacting nutrient availability, greenhouse gas emissions, and overall ecosystem health (Falkowski et al., 2008; Zhang X. et al., 2023; Qi et al., 2024; Lyons et al., 2024).

Methanogens, halophiles, thermophilic *Euryarchaeota* and *Thermoproteota* have become valuable model systems in molecular biology and biotechnology (Allers and Ngo, 2003; Kletzin, 2007; Soppa, 2006; Leigh et al., 2011; Costa and Whitman, 2023; De Lise et al., 2023; Pfeifer et al., 2021; Aparici-Carratalá et al., 2023), and currently these four groups of archaea boast well-established genetic systems. This advancement renders them ideal for use as model organisms and facilitates the expanded exploration of the functions of archaeal genes. However, the biotechnological potential of recently discovered archaeal lineages remains to be explored.

At the heart of archaeal diversity lies their genomic repertoire, comprising a finite set of protein building blocks, organized into pathways that facilitate biochemical reactions. One prominent example is methanogenesis, a pathway wherein certain archaea produce methane through anaerobic metabolism, essential for carbon cycling in environments like wetlands, alkaline hydrothermal vents, and animal digestive tracts (Angle et al., 2017; Jones et al., 1983; ver Eecke et al., 2012; Thomas P. D. et al., 2022), and that is proposed to have had an important role at the origin of Life (Martin and Russel, 2007). Additionally, many archaea engage in chemolithotrophy, deriving energy by oxidizing inorganic compounds such as hydrogen, sulfur, or iron (Thauer et al., 1977; Edwards et al., 2000; Pereira et al., 2011; Colman et al., 2020).

With the advent of metagenomics, many novel lineages have been discovered, for which mainly only metagenomic information is available for metabolic reconstructions using functional annotation pipelines. However, most of these are biased toward bacterial knowledge, with archaeal proteins many times falling out of the established cutoffs due to their natural diversity. Thus, it is important to assess how much of this diversity can be retrieved semi-automatically using functional annotation pipelines. Moreover, this approach can, in a systematic way, pinpoint gaps in knowledge, driving for the experimental characterization of archaeal proteins, as well as a redefinition of model design. Several studies regarding microbial dark matter, particularly Archaea, have been put forward, where the ratios vary between 30 and 80% (e.g., Makarova et al., 2019; Rinke et al., 2013; Jiao et al., 2020). More recently, deep learning was applied to genomes to get insights from microbial dark matter, showing how relevant the characterization of microbial dark matter is (Hoarfrost et al., 2022).

The question put out in this paper is: do existing automated prediction tools perform as well at assigning gene functions to archaea as to bacteria? Thus, to deepen our understanding of archaeal biology and metabolism, we performed a comprehensive mapping of genomic data from 2,978 archaeal genomic assemblies, belonging to 27 phyla (including unclassified Archaea) and compared the results to the ones obtained from a similar number of bacterial assemblies (175 phyla). This initiative aims to assess the gaps in predicted knowledge about archaea, and compare it to bacteria. Through

systematic exploration and analysis, we can pinpoint gaps in predictive knowledge and guide experimental studies with the aim of further understanding the diverse metabolic capabilities and ecological significance of archaea.

2 Materials and methods

2.1 Genomic dataset

A subset of our in-house dataset (over 190,000 genomes, 2,629 of which are archaeal; downloaded from NCBI in November 2019 with two *Acidianus ambivalens* and one *Ca. Lokiarchaeum ossiferum* assemblies added later; Supplementary Table 1; Rodrigues-Oliveira et al., 2023) was created by filtering these assemblies by completeness and contamination (calculated using the "Rinke method," Rinke et al., 2013), excluding all with contamination >20%. In addition, assemblies containing more than 10% contamination were excluded unless there were only two or less representatives per genus. Assemblies with low contamination were filtered for completeness: if the genus had more than two representatives, those with <40% completeness were excluded. In case of DPANN archaea, genomes were excluded only if their completeness was <20% and they had more than one representative per genus. To capture the recent sequenced diversity of archaea, additional genomes were downloaded from JGI (1,731 genomes). For this study, the total of 2,978 archaeal assemblies, belonging to 27 phyla (incl. "unclassified Archaea") were obtained. In addition, a set of 3,235 bacterial genomes, belonging to 175 phyla (2 representatives per genus) used for comparison (Supplementary Table 1).

2.2 Functional annotation

The 2,978 archaeal and the 3,235 bacterial genomic assemblies were functionally annotated using KEGG HMM profiles (version 2024-02-28, Kanehisa and Goto, 2000; using HMMER version 3.4, hmmer.org). The resulting hits were filtered first by cutoffs provided by KEGG for each model, and second, by lowering the KEGG cutoffs by 20% for most models, except for cytochrome *bc1* complex models, where the previously established in-house cutoffs were used (Supplementary Table 2). The cutoffs were lowered to account for the fact that the standard KEGG cutoffs do not always work for the archaeal sequences. If no KEGG cutoff was provided for a model, a cutoff of 50 was used to ensure the hits for these KOs of acceptable quality were still included in the analysis. The KEGG name, module and pathway information was mapped to the resulting annotations.

The dataset was additionally annotated using Interproscan (version 5.66–98.0; Jones et al., 2014), which includes the following databases: CDD (NCBI Conserved Domain Database; Lu et al., 2020), PFAM (Mistry et al., 2007), Gene3D (Lees et al., 2012), PANTHER (Thomas C. M. et al., 2022), SUPERFAMILY (Gough and Chothia, 2002; Wilson et al., 2009), ProSitePatterns and ProSiteProfiles (Expasy Prosite; Sigrist et al., 2013), NCBIfam (also known and further referred to as TIGRFAM, Li et al., 2021), FunFam (Sillitoe et al., 2013), Hamap (Pedruzzi et al., 2015), PIRSF (Wu et al., 2004), Coils (Lupas et al., 1991), MobiDB-lite (Necci et al., 2021), SMART (Letunic et al., 2021), PRINTS (Attwood et al., 2012). PANTHER annotations were further filtered to eliminate uncharacterized proteins, domains of unknown functions (DUF) and annotations solely as "membrane protein" or "conserved protein."

Furthermore, the archaeal genomes were annotated using the information obtained from DiSCo (Neukirchen and Sousa, 2021). Diamond Blast searches were also performed to assign arCOG (Makarova et al., 2015; Liu et al., 2021) classification to all genomes, by selecting best hits using as cutoffs >= 25% identity and E-value of <= 0^{-10}.

2.3 Sequence classification into "characterized" and "uncharacterized"

The resulting annotated hits were split into "characterized" and "uncharacterized" sets using the following strategy (as described in Supplementary Figure 1): If the sequence has a KEGG annotation with a KEGG pathway annotation "Function unknown," then it is classified as "uncharacterized"; if the KEGG pathway annotation is different, then the sequence is classified as "characterized." If the sequence has no KEGG annotation, then the PANTHER annotation is checked. If a PANTHER annotation is present and it is not in the curated list of uncharacterized PANTHERs (Supplementary Table 3), the sequence is classified as "characterized"; if it is in the list, the sequence is "uncharacterized." If no PANTHER annotation is present, then the NCBIfam (TIGRFAM) annotation is checked. If a TIGRFAM annotation is present in the curated list of "uncharacterized TIGRFAMs" (Supplementary Table 3), then the sequence is classified as "uncharacterized"; otherwise, it is assigned as "characterized." If no TIGRFAM annotation is available, the Hamap annotation is checked: if it is present, the sequence is classified as "characterized," otherwise, it is classified as "uncharacterized."

Sequences without any annotations were automatically classified as "uncharacterized." The order of the steps is partially arbitrary, and, starting with KEGG annotations, the classification steps can be run in a different order if preferred. The reason for selecting KEGG as initial step is three-fold: KEGG is a widely used database in which metabolic maps were constructed manually, and KEGG orthology is usually based on characterized enzymes or proteins. Lastly, KEGG provides modules and higher classifications of metabolism which are of interest for this analysis. This pipeline is available at https://github.com/valkaravaeva/protein_classification_tool.

2.4 Analysis of "uncharacterized" sequences

The mean, median, maximum, and minimum numbers of uncharacterized sequences were calculated per taxon (in percent of uncharacterized vs. total CDS per genome) at a phylum level. The PFAM annotations of archaea were analyzed, in terms of most common occuring domains per taxon (supergroup or phylum). The values per lineage were plotted as a boxplot using "ggplot2" package in R.

2.5 Comparison between "uncharacterized" archaeal sequences and ArCOGs

ArCOG annotation was used as a comparison to the pipeline in terms of uncharacterized proteins. Sequences without arCOG

annotation or with the functional model belonging to "S_Function_unknown," "4_Poorly_Characterised" and "R_General_Function_Prediction_only" category, or having no category were classified as "uncharacterized." The mean, median, max, and min percentages per phylum of "uncharacterized" sequences based on arCOGs were computed and plotted, as described in section 2.4. The intersection between uncharacterized proteins between both methods as well as the method specific were analyzed. The values per lineage were plotted as a boxplot using "ggplot2" package in R.

2.6 Analysis of "characterized" sequences

The set of "characterized" sequences was analyzed in terms of KEGG module completeness (computed in percent; accounting for alternative KOs and for complexes—see pipeline documentation and files at https://github.com/valkaravaeva/protein_classification_tool and additional files at FigShare: 10.6084/m9.figshare.25782123). Briefly, per assembly, each module, including the different alternatives for each step was considered complete if there were identified proteins for at least one route (100%). If one or more proteins were missing, the ratio of identified proteins versus the number of pathway proteins needed was calculated and multiplied by 100. In the case of complexes, a similar approach was taken, in this case, using the number of identified subunits as numerator. This information was used to analyze the metabolic potential of each genome and *a posteriori*, aggregated by phylum. Further analyses were focused on cofactor biosynthesis and energy metabolism. For this, KOs of selected gene markers were used to represent types of energy metabolism. In addition, in specific cases, existing KEGG modules were manually modified, or created, by either joining several modules for the same pathway or complex, or, as in case of riboflavin biosynthesis, since no KEGG module for the archaeal version is available, by using the BioCyc database entry for *M. jannaschii* (and corresponding KO annotations; Karp et al., 2019). Completeness of these manual modules was assessed in the same way as for original KEGG modules. Completeness of selected modules was plotted as a stacked barchart using "ggplot2" package in R. Taxonomic distribution of selected marker genes was plotted as a heatmap using R package "Pretty heatmaps" (https://cran.r-project.org/web/packages/pheatmap/pheatmap.pdf) and beautified in Inkscape.

3 Results

To determine how much of archaeal proteomes fall into the category of uncharacterized, a pipeline with several different steps was employed (see Supplementary Figure 1 and Materials and Methods). In total, 2,451,799 (40.7%, lowered KEGG cutoffs) out of 6,029,057 of proteins fall into the uncharacterized category, from where newly discovered lineages, such as *Ca.* Heimdallarchaeota and *Ca.* Woesearchaeota, have a mean of ~50% of proteins classified as uncharacterized (Figure 1; Supplementary Table 4). Within Archaea, 16 out of 27 groups (59%; including unclassified Archaea) have more than 40% of its proteins classified as uncharacterized, and only in two groups this ratio falls shortly below 30%. The average of uncharacterized proteins across all analyzed archaeal genomes is 42%. When examining the percentage of uncharacterized proteins per phylum, in bacteria, only 45 out of 175 phyla (25%) have more than 40% uncharacterized proteins (Figure 2, Candidate phyla in Supplementary Figure 2). When comparing model organisms from both domains, and even excluding *E. coli* (12%), there are 31 bacterial phyla where at least one organism has less than 25% uncharacterized proteins. In contrast, among archaea, only the *Candidatus* Bathyarchaeota and *Euryarchaeota* have at least one assembly with less than 25% uncharacterized proteins. Moreover, while lowering KEGG model cutoffs induced a change in the number of archaeal unclassified proteins, it did not affect the number of uncharacterized bacterial proteins, indicating that the models are optimized for this domain (Supplementary Table 4).

The two assemblies of the archaeal group with lowest median percentage of uncharacterized proteins, *Ca.* Nezhaarchaeota, have a low number of proteins (fewer than 1,700) and have completeness scores of 88 and 93%, and contamination of 0.6 and 4.3%, respectively. Their reduced genome, potentially associated with a symbiotic lifestyle, could explain the median percentage of uncharacterized proteins being below 30%. In any case, this value is still roughly three times the one found for model bacteria. This pinpoints the problems in reconstructing the metabolism of newly sequenced archaeal lineages.

Within the 2,451,799 unclassified proteins, 33.8% have PFAM annotation, while 66.2% (1,622,446) lack any annotation. Remarkably, with the exception of *Ca.* Nezhaarchaeota, *Ca.* Hadarchaeota, and *Ca.* Verstraetearchaeota, where 46.6, 55.4, and 59.0% of uncharacterized proteins lack PFAM annotations, respectively, all other archaeal phyla exhibit over 60% of uncharacterized proteins devoid of PFAM annotations, leaving even their domains unidentified. The uncharacterized proteins with PFAM domains have their annotations spread over 16,689 different PFAM entries, from where 3,725 correspond to domains or proteins with unknown functions. The remaining 12,964 PFAM domains are found in 829,353 proteins (33.8%), with 6,602 present in less than 10 proteins.

Notably, the prevalent PFAM among those with annotations is the PIN domain, characterized by three conserved acidic residues but limited conservation otherwise, which in eukaryotes is associated with ribonucleases (Arcus et al., 2011), and in prokaryotes, it is a component of the toxin-antitoxin system (TA; Arcus et al., 2011). In fact, ~44% of those PIN domains are in the proximity of genes annotated as nosB or Vap, being potentially part of a toxin-antitoxin system (TA, Arcus et al., 2011; Bunker et al., 2008) or close to CRISPR-Cas systems. The remaining PIN domains are in the vicinity of enzymes, ribosomal proteins or other uncharacterized genes. The large superfamily of PIN domain proteins was divided into families (Matelska et al., 2017) and a role as endo/exonucleases and/or part of the defense arsenal proposed (Matelska et al., 2017). The second most frequent domain is "LexA-binding inner membrane-associated putative hydrolase," which is found in phospholipases and in proteins belonging to the SOS network, which rescues cells from DNA damage (Zhang and Lin, 2012). The third most frequent domain is the "halobacterial output domain 1," which is specific for haloarchaea and haloviruses, and possibly involved in regulatory processes (Galperin et al., 2018). The fourth most frequent domain overall is the helix-turn-helix domain, usually found in transcriptional regulatory proteins and involved in DNA binding that, in some cases, can also be found in multidomain proteins for nucleotide recruitment, or involved in protein–protein interactions (Menon and Lawrence, 2013). In fact, among the 20 most frequent PFAMs, additional

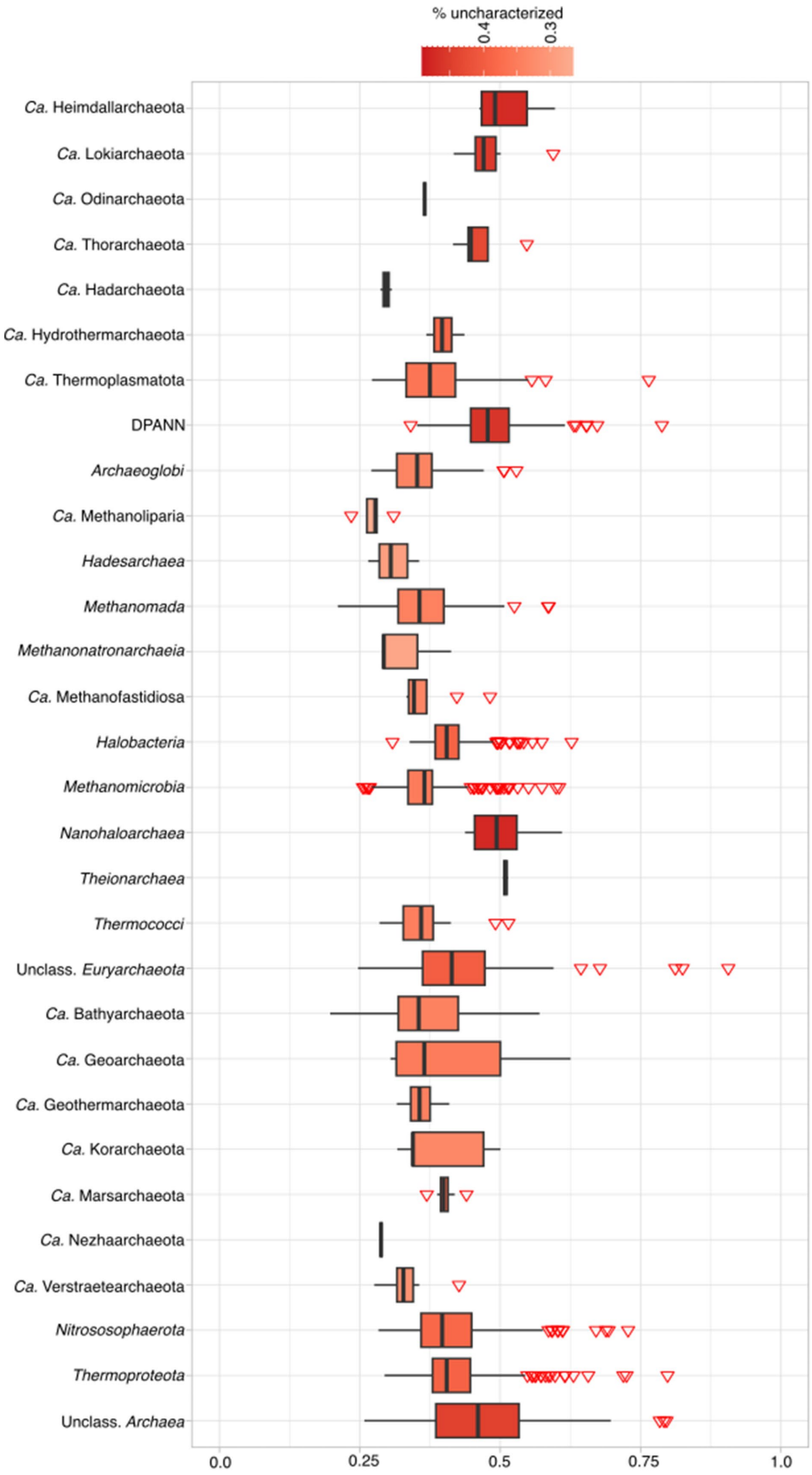

FIGURE 1
Percentage of archaeal unclassified proteins according to the pipeline classification per phylum. For complete taxonomic information see Supplementary Table 1. For exact percentages, see Supplementary Table 4.

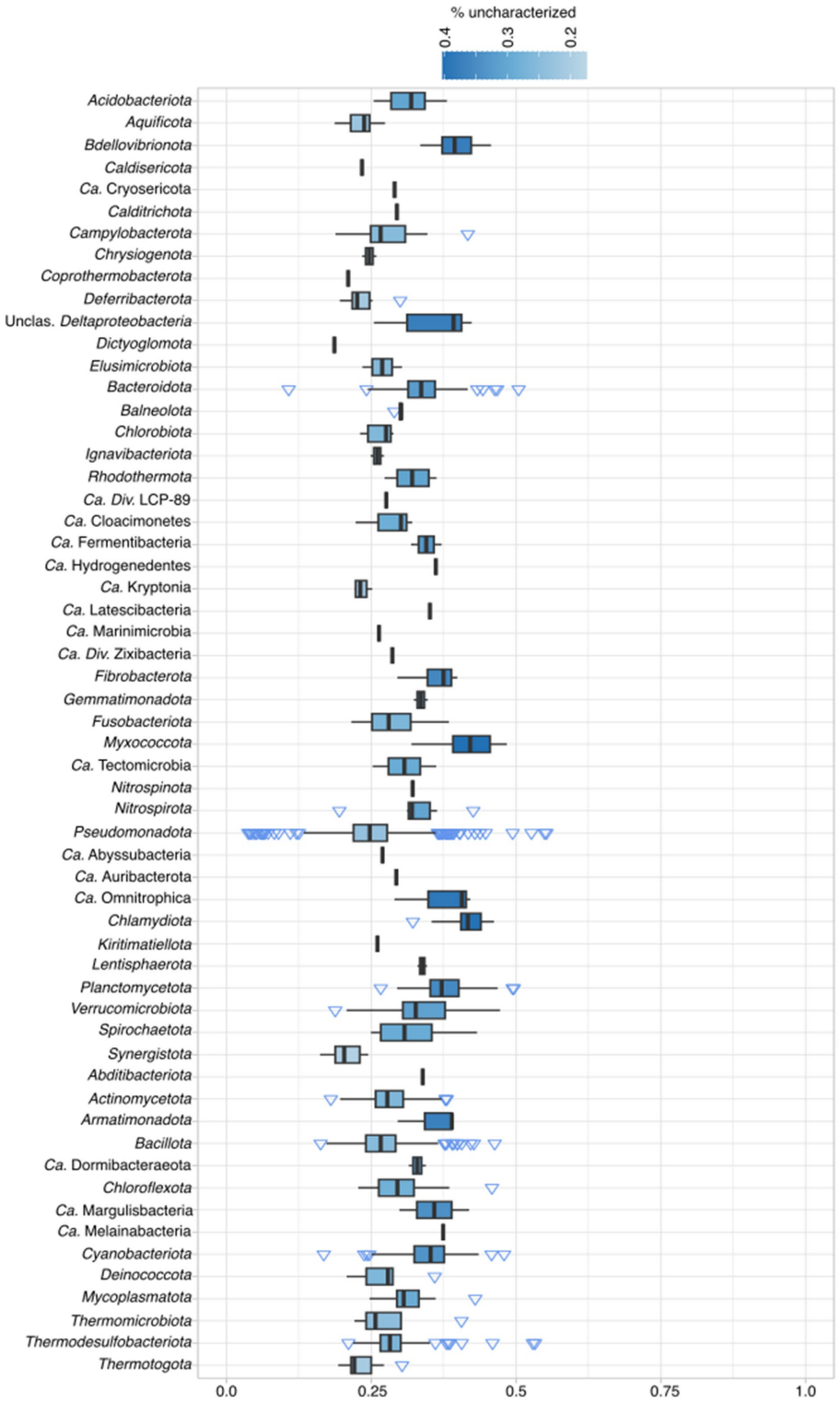

FIGURE 2
Percentage of unclassified bacterial proteins according to pipeline classification (see Materials and Methods) per phylum. For complete taxonomic information see Supplementary Table 1. For exact percentages, see Supplementary Table 4.

DNA-binding annotations emerge, including two winged helix-turn-helix domains, and the transcriptional regulator TrmB (Supplementary Table 5). TrmB, a sugar-specific transcriptional regulator of the trehalose/maltose ABC transporter from the hyperthermophilic archaeon *Thermococcus litoralis*, was previously characterized (Lee et al., 2003). Also, the *H. salinarum* reactive oxidative species regulator (RosR arCOG00006), which was experimentally characterized (Sharma et al., 2012) and whose

crystallographic structure is available (Kutnowski et al., 2019) is annotated as hypothetical protein and has no annotation within KEGG. These examples point to the misidentification of archaeal regulatory networks, in some cases, due to lack of models, in others, due to lack of characterization, as in the case of the ArsR/SmtB family (Lemmens et al., 2019). Moreover, the 6,602 PFAMs identified in fewer than 10 uncharacterized proteins, underscore the vast potential for innovation and diversity within this domain (Supplementary Table 5). Additionally, when examining proteins typically associated with metabolism, over 450 PFAMs (excluding radical SAM enzymes), corresponding to approximately 14,000 proteins, have annotations indicating the presence of hemes, FAD, NADH, molybdopterins, iron–sulfur clusters, oxidoreductases, or quinone-binding. This suggests that a portion of the archaeal metabolism remains not fully understood. A typical example would be the case of molybdopterin enzymes, which are ubiquitously present in prokaryotes, though the function of some is not known (Wells et al., 2020; Roy and Adams, 2002; Bevers et al., 2005).

The synteny analysis of unclassified proteins has shown that in 2,866 assemblies (96.2% of the dataset), there is at least one stretch of five or more genes without any available annotation (no PFAM). This number is even larger when considering the existence of pseudogenes in between uncharacterized ones. As a result, significant portions of the archaeal genomes remain without biological predictions, due to various factors such as the absence of models, assembly artifacts such as technical fusions, fissions or erroneous sequences (Padalko et al., 2024), inadequate CDS predictive methods for archaea (Dimonaco et al., 2022; Meng et al., 2022), or simply lack of biological knowledge. Notably, the uncharacterized genes within these regions are not necessarily involved in the same biological process, as genomic rearrangements frequently occur within genomes (Bobay and Ochman, 2017; Tillier and Collins, 2000; Darmon and Leach, 2014). When focusing on uncharacterized proteins for which PFAMs are available, particularly those which could, *a priori*, give some indication regarding energy metabolism, we observe that, for some cases, the uncharacterized protein's PFAM agrees with the surrounding genes, e.g., PF00507 and PF00420 NADH–ubiquinone/plastoquinone_ oxidoreductase, _chain_3 and 4 L from complex I surrounded by other Complex I subunits (Supplementary Table 6). This indicates that their nonidentification by other methods might be due to the model not accounting for the full range of sequence diversity. In this case, the full predicted complex could, with thorough analysis, be recovered. In other cases, putative complexes have no attributed annotation except PFAM, making their identification more difficult. Those are the cases, for instance, for Complex IV subunits in proximity of each other in known aerobic organisms, such as *Halobacteria*, where both subunit I and subunit II (the catalytic ones) are found within a distance of four or less genes devoid of further annotations. While subunit II tends to be a transmembrane short protein, devoid of cofactors (for exceptions see Pereira et al., 2011; Murali et al., 2022), subunit I is composed of a conserved set of 12 transmembrane helices, containing the ligands for the low-spin heme and for the binuclear center, composed of a high-spin heme and a copper ion. This subunit, outside of the HCO family, has homology only with nitric oxide reductases (Pereira et al., 2011). Thus, the subunit I fold is specific to these enzymes, and, possibly due to sequencing artifacts, falls below the usual model cutoffs. In this way, the complex IV, previously described to be present in *Ca.* Heimdallarchaeota assemblies (Spang et al., 2019; Bulzu et al., 2019), could not be identified. Even though *Halobacteria* thrive in oxic environments (Grant and Ross, 1986; Oren, 1994; Oren and Litchfield, 1999; Cui and Dyall-Smith, 2021), and several Asgard assemblies have been obtained from oxic conditions (Bulzu et al., 2019), additional experimental characterizations are necessary to ascertain whether these "HCOs" can reduce O_2, utilize alternative terminal electron acceptors, or even function effectively.

We compared the results of our pipeline (available at https://github.com/valkaravaeva/protein_classification_tool) with the functional classification given by arCOGs (Makarova et al., 2015; Liu et al., 2021), a tool developed specifically for the identification of archaeal clusters of orthologous groups. Depending on the lineages, either arCOG (18; Figure 3) or our pipeline (4) has less uncharacterized proteins (Figure 1), with 5 phyla achieving similar results (differences below 1%). However, overall, arCOG outperforms our pipeline by identifying approximately 350,000 fewer uncharacterized proteins in total (see Figure 4). This advantage is also evident in lineages with lower overall numbers, such as *Ca.* Woesearchaeota and *Ca.* Heimdallarchaeota, which have mean proportions of 47 and 48% "unclassified" proteins, respectively, compared to 51% for both lineages using our pipeline. Additionally, four out of 27 archaeal phyla show a ratio of unclassified proteins just below 30% using arCOGs, whereas 9 out of 27 have more than 40% uncharacterized sequences.

The large majority of the proteins only classified by arCOGs belong to informational (transcription, translation, replication), defense, mobilome and cellular processes (74%), in agreement with the effort of the authors of arCOGs in improving those modules (Makarova et al., 2015; Liu et al., 2021) combined with the underdevelopment of KEGG in those modules. On the other hand, within the over 350,000 proteins only annotated by our pipeline, and focusing on the ones with KEGG annotations (corresponding to 45% of the proteins only annotated by the pipeline), 62% belong to the metabolism category, with signaling and cellular processes (20%) and informational processes (17%) as following categories. Among the proteins from metabolism are, for instance, 2000 involved in methane metabolism, including several acetyl-CoA synthase and formylmethanofuran dehydrogenase subunits, over 8,300 proteins involved in energy metabolism such as sulfide:quinone oxidoreductases (Brito et al., 2009), thiosulfate:quinone oxidoreductases (Müller et al., 2004), and V/A-type H+/Na+-transporting ATPase subunits, from where the *Methanobrevibacter ruminantium* complex was experimentally validated (McMillan et al., 2011). Therefore, to avoid running both approaches and to standardize the data, the choice of annotation strategy should depend on the specific goals of the study.

However, arCOGs are built from a graph method in which, due to, e.g., gene losses, paralogues can be grouped together. Moreover, there is no relationship between KOs and arCOGs, which renders the mappings of pathways using arCOGs for a database as large as the one used in this paper, an "Herculean" task. Thus, we continued the analysis using KEGG annotations.

The functional classification of archaeal proteins allows to reconstruct their metabolic potential and pinpoint possible gaps within pathways to be further experimentally characterized. Using KEGG modules combined with a strategy to count for their completeness (see Materials and Methods), the full reconstruction of the metabolism of 2,978 genomes is presented in Supplementary Table 7. Out of the 479 modules, 115 had no hit for

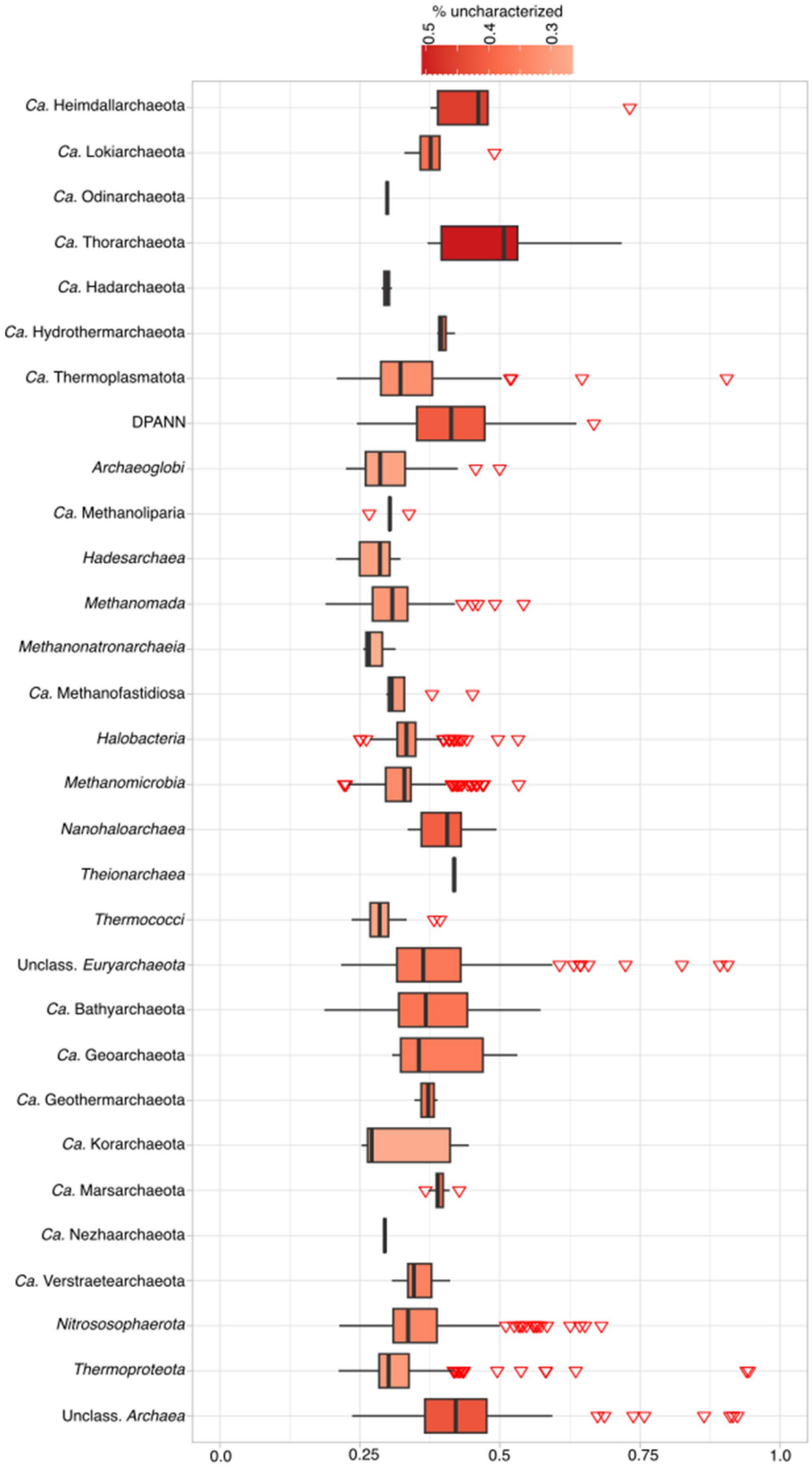

FIGURE 3
Percentage of unclassified archaeal proteins according to arCOG classification per phylum. For complete taxonomic information see Supplementary Table 1. For exact percentages, see Supplementary Table 4.

FIGURE 4
Number of proteins classified as "characterized" only by pipeline (green), only by arCOGs (pink), and by both methods (intersection).

archaeal proteins and only 20 were found to be complete or at least 75% complete in more than 50% of the assemblies in our dataset. These mainly correspond to the building blocks of life, such as nucleotides, amino acids and cofactors biosynthesis, ATP synthesis, lipid biosynthesis as well as carbon metabolism. The rationale behind setting a 75% completeness threshold includes instances where, despite adjustments, specific module components remain elusive. This also accounts for possible assembly incompleteness. Within bacteria, only 44 modules were not present in any of the genomes, and 60 modules found in more than 50% of the bacterial assemblies. The modules specific for bacteria are, for instance, gamma-aminobutyric acid (GABA) biosynthesis, a pathway present in several bacteria (Iorizzo et al., 2023) that has homologues within archaea which perform different functions (Tomita et al., 2014; Falb et al., 2008), or anoxygenic photosynthesis, a process that is absent in archaea (Hohmann-Marriott and Blankenship, 2011). Other modules address specific bacterial systems, such as antibiotic resistance or the synthesis of secondary metabolites unique to certain lineages.

In addition, several KEGG modules were modified to fill in gaps regarding archaeal metabolism not included in the original modules. For instance, in the cobalamin biosynthesis module, the decision to include CbiX, a homologue of CbiK that in some organisms performs the same reaction (Raux et al., 2003), was made to enhance the module's completeness, since this protein was initially absent. However, this adjustment, combined with lowered cutoffs, did not result in the increase of completeness of this module as expected, since there was no identification of other expected proteins within the module, such as the adenosylcobinamide kinase/adenosylcobinamide-phosphate guanylyltransferase CobP/CobU (K02231) because archaea do not have CobP/CobU but rather use CobY (K19712; Rodionov et al., 2003), which is not a part of the KEGG cobalamin biosynthesis modules. Even considering that some archaea might not have cobalamin biosynthesis, this scenario highlights the difficulty of defining a cutoff that accurately reflects the presence of all essential components, especially in complex biosynthetic pathways. Moreover, not all of complexes are part of KEGG modules. This is the case of the Ech and Ehb membrane hydrogenases (Marreiros et al., 2013; Marreiros et al., 2016) present in many methanogens, or the thiol:fumarate reductases (Heim et al., 1998), a complex whose subunits are homologous to the catalytic subunits of Complex II (Lancaster, 2002; Karavaeva and Sousa, 2023). Another problem is the existence of several modules for the same complexes, as, e.g., in the cases of succinate dehydrogenases/fumarate reductases, heme-copper oxygen reductases, and the *bc*1 complex. This leads to the existence of many archaeal complexes that have chimeric classifications according to KEGG modules, i.e., one subunit being part of one module and the other(s) belonging to another module of the same complex. This leads to modular incompleteness and hinders the usage of KEGG modules as a proxy of archaeal metabolism. For the cases mentioned above, we considered the module present if the subunits were identified, regardless of the KO module classification, meaning KEGG modules were merged, and different possible KOs would represent the same subunit. Completing this information with TIGRFam/NCBIFam and BioCyc information for selected modules (as described in Materials and Methods) led to an increase in module and pathway completeness. Still, in most of the cases, modules fall below the 75% completeness cutoffs (Supplementary Table 7). These results suggest that our understanding of the metabolic diversity and the distribution of biosynthetic pathways among archaea is still not included into databases, and the known existing gap between Bacteria and Archaea knowledge is even more pronounced at the level of automatic annotations.

Looking in detail to the different pathways for coenzymes and cofactors biosynthesis, we can observe that regarding heme biosynthesis in archaea (Supplementary Figure 3), the siroheme-dependent route is the most widely distributed, with the coproporphyrin-dependent pathway found to be complete in some *Halobacteria*, as already described (Dailey et al., 2017), as well as in one genome of *Ca.* Hydrothermarchaeota. Interestingly, within *Ca.* Heimdallarchaeota and some unclassified Euryarchaeota, the protoporphyrin-dependent heme biosynthesis was found. *Ca.* Heimdallarchaeota organisms have a mitochondrial-like electron-transport chain, being able to respire oxygen (Zaremba-Niedzwiedzka et al., 2017). This is not found in the majority of the other Asgard lineages and might be the result of HGT events. Since *Ca.* Heimdallarchaeota is also one of the few archaeal groups with protoporphyrin-dependent heme biosynthesis, this pathway might also have been acquired by HGT. Previously, several studies have reported on large events of interdomain HGT for archaea (Koonin and Wolf, 2008; Nelson-Sathi et al., 2012; Nelson-Sathi et al., 2015), and *Ca.* Heimdallarchaeota might be one of these cases. Of note, within our dataset, many other archaea were found to contain partial protoporphyrin-dependent heme biosynthesis pathways. However, this module also contains the universal tetrapyrrole biosynthesis part, common to the biosynthesis of all tetrapyrroles cofactors (heme, cobalamin, siroheme, F_{430}) that are all present in Archaea.

Regarding cobalamin biosynthesis, a full pathway is found in *Ca.* Thermoplasmatota, *Archaeoglobi*, *Ca.* Methanoliparia, *Methanomada, Methanonatronarchaeia, Halobacteria, Methanomicrobia*, *Ca.* Marsarchaeota, *Nitrososphaerota, Thermoproteota*, and unclassified Archaea. However, in most of these lineages, there are genomes that contain only a partial pathway, due to either not passing the cutoffs (especially in the case of CbiJ) or having no KO annotation for a fused protein (e.g., fusions of CbiK/CbiX chelatase and HmbS/HemC in certain *Archaeoglobi* genomes have only the KO annotation for the last protein). Fusion and fission events are a process common in Archaea, as shown in recent large-scale analysis (Padalko et al., 2024).

Complete pathways for the biosynthesis of menaquinone were found in *Ca.* Thermoplasmatota, *Archaeoglobi*, DPANN, *Thermoproteota, Methanomicrobia*, and unclassified Archaea

(Supplementary Figure 4). However, only in *Archaeoglobi* and *Ca.* Hydrothermarchaeota, they were present in the majority of the taxon assemblies. The presence of menaquinone in Archaea has been previously reported for *Thermoproteus tenax* (Thurl et al., 1985). As expected, no archaeal organisms have the complete pathway for ubiquinone biosynthesis. However, many have partial pathways, indicating the presence of several enzymes, homologous to those involved in ubiquinone biosynthesis. Within Archaea, besides menaquinones, several organisms use Caldariella (Schäfer et al., 2002) or sulfoquinone (Elling et al., 2016) as main quinone. Since the biosynthesis of these alternative quinones remains, to our knowledge, not fully resolved, it is not clear if the ubiquinone biosynthesis homologues found in those lineages might play a role in other quinone biosyntheses, and those are good candidates for further experimental validations.

Contrary to menaquinone biosynthesis, riboflavin (incl. FMN/FAD; Figure 5 and Supplementary Figure 4) biosynthesis is found to be partially present in many archaeal lineages, being complete within several lineages, such as *Archaeoglobi, Halobacteria, Methanomada, Theionarchaea, Nitrososphaerota*, and *Thermococci*. FMN/FAD biosynthesis enzymes are present in all lineages, including DPANN. Even with our improved module for FAD biosynthesis, we noticed that the enzyme(s) responsible for converting GTP to 2,5-Diamino-6-(1-D-ribosylamino)pyrimidin-4(3H)-one-5′-phosphate are absent in most archaea, indicating a gap in knowledge that possibly only experimentalists can fill. The biosynthesis of F_{430} is, as expected, present in several methanogenic groups (Figure 6) being less spread than the biosynthesis of F_{420} that besides methanogens, is also found in *Archaeoglobi*, *Ca.* Heimdallarchaeota, *Ca.* Lokiarchaeota, *Halobacteria* and *Theionarchaea*. The dihydrofolate reductase, used as a marker for folate biosynthesis, is mainly found in most assemblies from *Halobacteria* and the related group *Nanohaloarchaea*.

Various types of energy metabolism were investigated using gene markers for arsenic, nitrogen, oxygen and sulfur metabolism (Figure 7). Our findings indicate that organisms capable of detoxifying arsenate include *Methanomada,* as well as unclassified *Euryarchaeota* and *Nitrososphaerota*. Regarding oxygen metabolism, both *bd* oxidases and heme-copper oxidases (Pereira et al., 2001) were detected in *Ca.* Heimdallarchaeota, *Ca.* Thermoplasmatota*, Halobacteria, Methanomicrobia, Ca.* Geoarchaeota, *Nitrososphaerota, Thermoproteota,* unclassified *Euryarchaeota*, and unclassified Archaea. Some lineages have genes that encode only *bd* oxidase (DPANN, *Archaeoglobi, Thermococci, Ca.* Korarchaeota, *Ca.* Geothermarchaeota), while others have only HCO genes (*Ca.* Marsarchaeota). However, many of the hits did not pass the cutoffs, even lowered cutoffs, such as the case for HCOs in *Ca.* Heimdallarchaeota, where, despite earlier evidence of presence of these enzymes in this specific lineage (Spang et al., 2019; Bulzu et al., 2019), only one out of five genomes recovered a partial HCO complex.

Six marker proteins/complexes were selected to cover the diversity of nitrogen metabolism, although not including the ammonia monooxygenase AmoA, which shares a KO with the methane monooxygenase PmoA (K10944), and hence they are difficult to differentiate (Holmes et al., 1995). The hits for K10944 were nonetheless found in the dataset, in *Nitrososphaerota* (ammonia-oxidizers; Pester et al., 2011), as expected. The distribution of the Nif nitrogenase, used as protein marker for nitrogen fixation, recovered a similar distribution to that described in Baker et al. (2020), being found in *Ca.* Thermoplasmatota, *Methanomicrobia*, and *Theionarchaea*. However, in our case, additional 11 lineages had hits for nitrogenases, such as *Archaeoglobi*, *Ca.* Methanoliparia*, Methanomada*. Possible explanations for this difference could be the inclusion of vanadium-dependent nitrogenase Vnf in our results, or our search for all Nif subunits, as compared to Baker et al. (2020) using only NifH as a marker. Other cases, such as nitrite reductases NirK/NirS, did not overlap. For example, none of the lineages analyzed in Baker et al. (2020) were reported to contain NirS, and only *Aigarchaeota* and *Nitrososphaerota* were said to contain NirK. However, while our dataset did not include *Aigarachaeota*, other lineages had a hit for NirK in our dataset (e.g., *Ca.* Heimdallarchaeota, *Ca.* Thermoplasmatota*, Thermoproteota*), and NirS was found in *Halobacteria* (a lineage not included in Baker et al., 2020 analysis). It is possible, however, that additional NirK hits are in fact false positives due to the NirK homology to multicopper oxidases (Bento et al., 2005; Solomon et al., 1996).

To cover dissimilatory sulfur oxidation and reduction in archaea, seven protein markers were selected, ranging from sulfur oxygenase reductase (SOR; Urich et al., 2004; Urich et al., 2006) and thiosulphate:quinone oxidoreductase (TQO; Müller et al., 2004), first characterized in *Acidianus ambivalens* and representing chemolithoautotrophic sulfur-oxidizing metabolism in *Thermoproteales* (*Sulfolobales*, *Acidobales*), to the DsrAB and Qmo proteins to mark the Dsr-dependent dissimilatory sulfate/sulfite reduction in Archaea. The results recapture the known diversity within this dataset (Neukirchen and Sousa, 2021; Anantharaman et al., 2018; Friedrich et al., 2001; Ghosh and Dam, 2009). However, some of the newly discovered archaeal lineages with metabolic potential for Dsr-dependent sulfur metabolism, such as *Ca. Methanodesulfokores washburnensis* (McKay et al., 2019) or Dsr-containing Aigarchaeota (Hua et al., 2018) are absent from our dataset, explaining why this metabolism was not found in those groups. On the contrary, sulfide:quinone oxidoreductases were found to be present across 16 different archaeal groups, such as *Ca.* Heimdallarchaeota, *Halobacteria*, *Ca.* Korarchaeota, and *Thermoproteota*. So far, archaeal Sqrs have only been characterized from *A. ambivalens* (Brito et al., 2009) and *C. maquilingensis* (Lencina et al., 2013), and due to their sequence homology with Ndh-II (Brito et al., 2009), it cannot be excluded that some of these results are false positives, and the distribution of Sqr in Archaea is, in fact, smaller.

Using gene markers for terminal oxidoreductases or central complexes to pinpoint metabolic traits, while effective in uncovering the potential for certain types of energy metabolism in Archaea, falls short of presenting a comprehensive view of the possible variability within energy metabolic strategies. This approach may overlook the emergence of novel complexes formed through the rearrangement of modular protein components into unique architectures, not accounted for in these types of analyses.

4 Discussion

The aim of this paper was straightforward: to conduct a large-scale investigation into what is known and what is yet to be discovered within the archaeal domain, and to assess how much of archaeal metabolism can be reconstructed automatically using computational approaches. However, this turned out to be a much more complex

FIGURE 5
Presence of cofactor biosynthesis in archaea (per phylum for most lineages, per class for Euryarchaeota, with Methanobacteria, Methanococci, and Methanopyri grouped into the Methanomada supergroup), based on modified KEGG modules. **(A)** Presence of NAD biosynthesis (via both Tryptophan and Aspartate). **(B)** Presence of FMN + FAD biosynthesis. **(C)** Presence of cobalamin biosynthesis (excluding the lower ligand synthesis). Dark purple indicates that the full module is present, light purple marks the presence of the incomplete module, white shows the absence of the module in a lineage.

analysis than initially thought, due to the biases of knowledge regarding the other two domains of life, the different pathways of Archaea, and the fact that, with the exponential increase in sequencing projects and discovery of new lineages, their sequence divergency (real or due to sequencing artifacts) cannot be scaled up/incorporated in real time to existing databases. It is well-known that most of the current biological knowledge is based on Bacteria and Eukaryotes, with little attention given to incorporating Archaea and their differences into metabolic modules and pathways. Archaeal metabolism and information processing can be different from the ones present in Bacteria and Eukaryotes, and archaeal unique biochemical pathways enables them to thrive in extreme environments

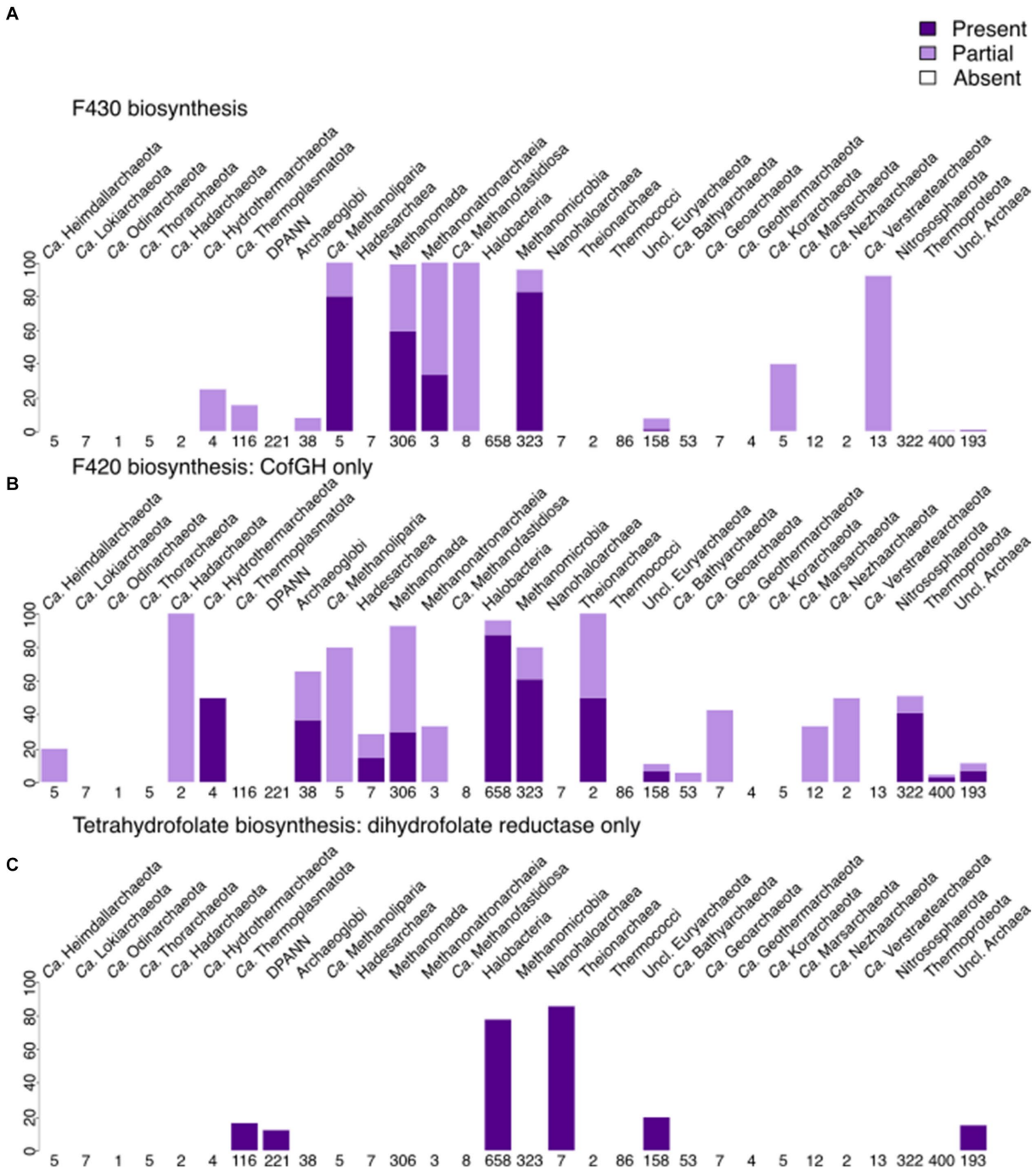

FIGURE 6
Presence of cofactor biosynthesis in archaea (per phylum for most lineages, per class for Euryarchaeota, with Methanobacteria, Methanococci, and Methanopyri grouped into the Methanomada supergroup), based on modified KEGG modules. **(A)** Presence of F_{430} biosynthesis. **(B)** Presence of F_{420} biosynthesis (includes only CofG + CofH as markers). **(C)** Presence of tetrahydrofolate biosynthesis (includes only dihydrofolate reductase as a marker). Dark purple indicates that the full module is present, light purple marks the presence of the incomplete module, white shows the absence of the module in a lineage.

and utilize diverse substrates, often relying on coenzymes and cofactors that necessitate entirely different enzymatic reactions compared to bacterial metabolic pathways. One prominent example is the incorporation of selenocysteine (Stadtman, 1974), often referred to as the 21st amino acid (Böck et al., 1991), that is found in proteins from the three domains of life (Rother and Quitzke, 2018) Selenocysteine is synthesized via a complex mechanism involving a specific tRNA and a dedicated set of enzymes (Chambers et al., 1986), and the archaeal synthesis is more related with the eukaryotic than with the bacterial one (Rother and Quitzke, 2018). This amino acid plays a crucial role in the function of several selenoenzyme families, including glutathione peroxidases and thioredoxin reductases, which

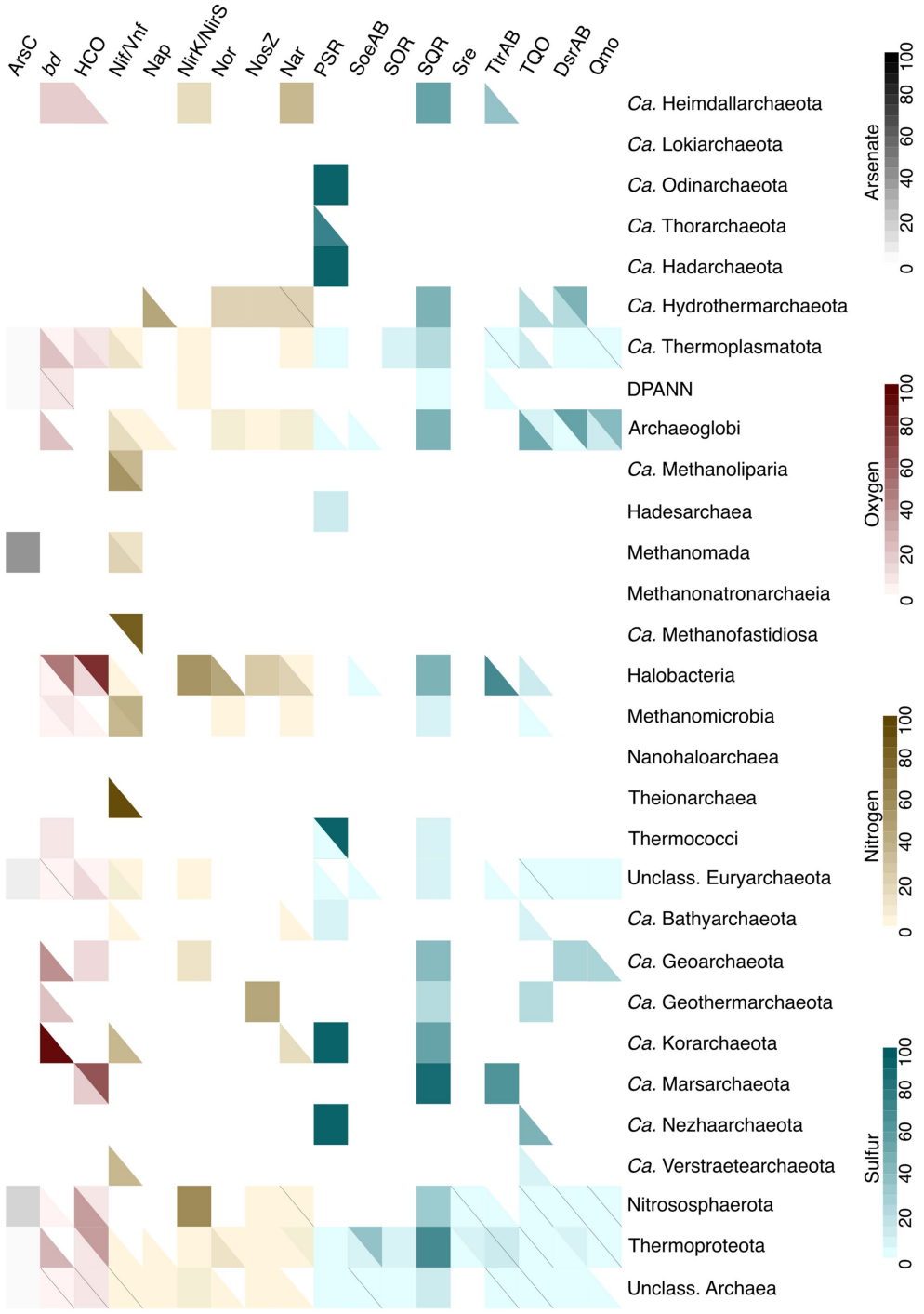

FIGURE 7
Presence of the marker proteins for different types of energy metabolism (KO and DiSCo annotations). Arsenate detoxification is marked in grey, oxygen metabolism in red, nitrogen metabolism in yellow, and sulfur metabolism in blue. ArsC: arsenate reductase, bd: bd oxidase, HCO: heme-copper oxidase, Nif/Vnf: nitrogenase, Nap: nitrate reductase, NirK/NirS: nitrite reductase, Nor: nitric oxide reductase, NosZ: nitrous oxide reductase, Nar: nitrate reductase, PSR: polysulfide reductase, SoeAB: sulfite:quinone dehydrogenase (subunits A and B), SOR: sulfur oxigenase/reductase, SQR: sulfide:quinone oxidoreductase, Sre: sulfur reductase, TtrAB: tetrathionate reductase (subunits A and B), TQO: thiosulfate:quinol oxidoreductase, DsrAB: dissimilatory sulfite reductase (subunits A and B), Qmo: quinone-modifiyng oxidoreductase. A full solid colored square indicates that, if a marker gene is a multisubunit complex, all of the subunits are present in a certain percent of the genomes. In cases where a square is split into two colors, the top part of the square indicates the percentage of genomes containing a full complex, while the bottom part shows the percent of genomes that have incomplete complexes.

are vital for oxidative stress management and redox reactions in archaeal cells (Rother and Quitzke, 2018). Another noteworthy cofactor found in a small number of methylamine-metabolizing archaea as well as a few bacteria (Tharp et al., 2018; Hao et al., 2002; Srinivasan et al., 2002; Borrel et al., 2014) is pyrrolysine, traditionally known as the 22nd amino acid. Pyrrolysine is encoded by the UAG

codon in some methanogenic Archaea (Hao et al., 2002; Srinivasan et al., 2002), and is integral to the activity of methyltransferase enzymes (Soares et al., 2005), which are involved in the final steps of methane production from methylated compounds (Rother and Quitzke, 2018). The existence of pyrrolysine highlights the diversity of genetic codes and implications for protein synthesis in archaea, further underlining their unique metabolic capabilities. Moreover, coenzymes such as coenzyme M (2-mercaptoethanesulfonic acid) and coenzyme F_{430} are central to the metabolic pathways of methanogens and other anaerobic archaea (Kaster et al., 2011), albeit also being found in some bacterial organisms. Coenzyme F_{430}, a nickel-containing porphyrin, plays an essential role in the enzymatic reaction catalyzed by methyl-coenzyme M reductase, where it participates in the final step of methane production, showcasing a highly specialized enzymatic system (Thauer et al., 2008). These unique biochemical components reveal how archaea have evolved distinct metabolic strategies that not only allow them to occupy a wide range of ecological niches but also highlight the evolutionary divergence between archaea and other life forms.

These differences, as well as the usage of non-archaeal sequences in the modules can lead to misassignments or false negatives in terms of functional predictions. For example, HCOs from *Ca.* Heimdallarchaeota fall short of the cutoffs for homology-based annotation. It is possible that this lineage's proteins diverge significantly from those in reference databases. However, this issue is not unique to *Ca.* Heimdallarchaeota; it also applies to halobacterial HCO proteins, indicating that not all divergence can be explained by this alone. Here we have shown 37.6% of the archaeal protein space remains uncharacterized, and that over 96% of archaeal metagenomes contain long stretches of genes, for which not even the protein domains (PFAM) are known. Also, within the uncharacterized proteins with PFAM annotations available, many contain cofactors and metal centers thought to have been playing a pivotal role since the origin of Life (Sanchez-Rocha et al., 2024; Weiss et al., 2016). For these uncharacterized cofactor-containing enzymes, the function is not yet known, and they may be a part of archaeal specific unexplored pathways, whose characterization would increase the diversity of microbial biology.

Enhancing current genomic classification databases and functional predictive models may involve refining them through additional analyses, like synteny analysis or integrating other omics data. This approach requires more sophisticated knowledge and operations rather than simple clicks to access and interpret this information. Some progress has been made regarding sulfur metabolism, where several dedicated tools, such as HMSS2 (Tanabe and Dahl, 2023) or DiSCo (Neukirchen and Sousa, 2021), were carefully built to identify specific types of metabolism, already integrating the current microbial diversity known. Progress has also been made in developing annotation-free strategies for identification of microbial dioxygen utilization from reads data, and in the last years, methods for TF identification from gene-expression data from quantitative phenotyping analysis (Darnell et al., 2017), approaches for a systematic inference of TF activity (Ma and Brent, 2021) and computational models for topological comparison of regulatory networks across the two domains of Life (Robinson and Schmid, 2018) have been developed. Another expanding area is phenomics, with several tools being developed in the last years, such as MicroPIE (Mao et al., 2016) to enable a fast extraction of phenotypic information from text records. Recently, the Functional Annotations of Prokaryotic Taxa (FAPROTAX) database (Louca et al., 2016) was tested for fast-functional screening of microbial metabolism, based on 16S RNA data (Sansupa et al., 2021) with promising results.

However, for an in-depth analysis of large datasets, better and faster tools need to be developed. Here is where statistical information theory (IT) plays an important role. Methods such as Mutual Information (MI; Vinga, 2014), Distance Correlation and its variants (Szé Kely and Rizzo, 2013; Monti et al., 2023) that already are useful to analyze, e.g., gene expression matrices, should be further developed to allow, e.g., comparisons of gene expression levels and inferences across independent samples. Moreover, in a recent study, MI was employed for pathway analysis, and, when applied to single-cell data, yielded robust and meaningful scores (Jeuken and Käll, 2024). For sequence data, IT can provide a broad range of inferences, from TF binding sites to gene mapping and phenotypic predictions, as comprehensively reviewed by Vinga (2014).

Artificial intelligence (AI), particularly machine learning algorithms, can also, in principle, provide valuable insights into archaeal metabolism by analyzing large genomic datasets and by filling in some of the gaps (Hoarfrost et al., 2022). Machine learning can aid in genome annotation (Chen et al., 2024; Khodabandelou et al., 2020), predict enzyme functions (Salas-Nuñez et al., 2024 and references within), and reconstruct metabolic pathways (Libbrecht and Noble, 2015). However, challenges and limitations persist in the field and the accuracy of metabolic reconstructions relies heavily on the quality of genomic and biochemical data available for archaeal species. Missing data and heterogenous datasets can lead to severe overfitting and other problems, as heavily discussed in the literature (Rodrigues, 2019; Xu and Jackson, 2019; Altman and Krzywinski, 2018). Customized models that consider the unique features of archaeal genomes and metabolic pathways can improve the accuracy and specificity of reconstructions. Integrating genomic, transcriptomic, proteomic, and metabolomic data can provide a comprehensive view of archaeal metabolism. AI and machine learning approaches that combine and analyze multi-omics data will facilitate more accurate reconstructions and deeper insights into the metabolic capabilities of Archaea, especially if coupled to statistical information theory. Perhaps this is the way to go in the future. But we must remember that computers only see zeros and ones (much better than we do), so we cannot forget that biology is more than math, and that without proper constraints and curated training data from experimental characterizations, distinguishing real results from artifacts is an almost impossible task. Moreover, as we have shown in this paper, without human manual curation, and extensive literature searches to get experimental archaeal characterized proteins to fill gaps in pathways, the distance between the vast amount of genomic information available and their analysis will only increase. In a perfect world, all data would be of high quality, with consistent information across different platforms. Additionally, linguistic and other barriers would be reduced to unite experimentalists, microbiologists, computational scientists, and mathematicians in the shared goal of closing this gap. Joining bottom-up with state of the art top-down predictive (ML) and inference (IT) approaches—merging the "*in silico*" and "*in vivo/vitro*" could increase the speed

at which we explore the archaeal world and disentangle its mysteries. This strategy would increase our understanding of archaeal metabolism, and life in general, offering new insights and opportunities for further research.

Data availability statement

The files with full annotation, all taxonomic levels for uncharacterized counts, and synteny tables, can be found at Figshare: 10.6084/m9.figshare.25782123. The pipeline (incl. examples of arCOG analysis scripts and plotting scripts) is available on GitHub: https://github.com/valkaravaeva/protein_classification_tool.

Author contributions

VK: Data curation, Formal analysis, Investigation, Methodology, Validation, Visualization, Writing – original draft, Writing – review & editing. FS: Conceptualization, Data curation, Formal analysis, Funding acquisition, Investigation, Supervision, Validation, Writing – original draft, Writing – review & editing.

Funding

The author(s) declare that financial support was received for the research, authorship, and/or publication of this article. This project has received funding from the European Research Council (ERC) under the European Union's Horizon 2020 research and innovation programme (grant agreement no. 803768). FS thanks the Wiener Wissenschafts-, Forschungs-und Technologiefonds (grant agreement VRG15-007) and the European Research Council (ERC) under the European Union's Horizon 2020 Research and Innovation program (grant agreement 803768).

Acknowledgments

The authors thank the Genome Evolution and Ecology group, Sinje Neukirchen, Maximilian Dreer, and Thomas Pribasnig for fruitful discussions. We also thank Brendan Mullins for advising on the pipeline development using Nextflow. Computational infrastructure and support were provided by the Life Science Computer Cluster (LiSC) at the University of Vienna.

Conflict of interest

The authors declare that the research was conducted in the absence of any commercial or financial relationships that could be construed as a potential conflict of interest.

The author(s) declared that they were an editorial board member of Frontiers, at the time of submission. This had no impact on the peer review process and the final decision.

Publisher's note

Supplementary material

The Supplementary material for this article can be found online at: https://www.frontiersin.org/articles/10.3389/fmicb.2024.1433224/full#supplementary-material

References

Allers, T., and Ngo, H. P. (2003). Genetic analysis of homologous recombination in Archaea: *Haloferax volcanii* as a model organism. *Biochem. Soc. Trans.* 31, 706–710. doi: 10.1042/bst0310706

Al-Mailem, D. M., Sorkhoh, N. A., Marafie, M., Al-Awadhi, H., Eliyas, M., and Radwan, S. S. (2010). Oil phytoremediation potential of hypersaline coasts of the Arabian gulf using rhizosphere technology. *Bioresour. Technol.* 101, 5786–5792. doi: 10.1016/j.biortech.2010.02.082

Altman, N., and Krzywinski, M. (2018). The curse (s) of dimensionality. *Nat. Methods* 15, 399–400. doi: 10.1038/s41592-018-0019-x

Anantharaman, K., Hausmann, B., Jungbluth, S. P., Kantor, R. S., Lavy, A., Warren, L. A., et al. (2018). Expanded diversity of microbial groups that shape the dissimilatory sulfur cycle. *ISME J.* 12, 1715–1728. doi: 10.1038/s41396-018-0078-0

Angle, J. C., Morin, T. H., Solden, L. M., Narrowe, A. B., Smith, G. J., Borton, M. A., et al. (2017). Methanogenesis in oxygenated soils is a substantial fraction of wetland methane emissions. *Nat. Commun.* 8:1567. doi: 10.1038/s41467-017-01753-4

Aparici-Carratalá, D., Esclapez, J., Bautista, V., Bonete, M. J., and Camacho, M. (2023). Archaea: current and potential biotechnological applications. *Res. Microbiol.* 174:104080. doi: 10.1016/j.resmic.2023.104080

Arcus, V. L., McKenzie, J. L., Robson, J., and Cook, G. M. (2011). The PIN-domain ribonucleases and the prokaryotic Vap BC toxin-antitoxin array. *Protein Eng. Des. Sel.* 24, 33–40. doi: 10.1093/protein/gzq081

Attwood, T. K., Coletta, A., Muirhead, G., Pavlopoulou, A., Philippou, P. B., Popov, I., et al. (2012). The PRINTS database: a fine-grained protein sequence annotation and analysis resource--its status in 2012. *Database (Oxford)* 2012:bas019. doi: 10.1093/database/bas019

Auernik, K. S., and Kelly, R. M. (2008). Identification of components of electron transport chains in the extremely thermoacidophilic crenarchaeon *Metallosphaera sedula* through iron and sulfur compound oxidation transcriptomes. *Appl. Environ. Microbiol.* 74, 7723–7732. doi: 10.1128/AEM.01545-08

Baker, B. J., De Anda, V., Seitz, K. W., Dombrowski, N., Santoro, A. E., and Lloyd, K. G. (2020). Diversity, ecology and evolution of Archaea. *Nat. Microbiol.* 5, 887–900. doi: 10.1038/s41564-020-0715-z Erratum in: Nat. Microbiol. 2020

Bandeiras, T. M., Pereira, M. M., Teixeira, M., Moenne-Loccoz, P., and Blackburn, N. J. (2005). Structure and coordination of CuB in the *Acidianus ambivalens* aa 3 quinol oxidase heme-copper center. *J. Biol. Inorg. Chem.* 10, 625–635. doi: 10.1007/s00775-005-0012-6

Bento, I., Martins, L. O., Gato Lopes, G., Arménia Carrondo, M., and Lindley, P. F. (2005). Dioxygen reduction by multi-copper oxidases; a structural perspective. *Dalton Trans.* 21, 3507–3513. doi: 10.1039/b504806k

Bevers, L. E., Bol, E., Hagedoorn, P. L., and Hagen, W. R. (2005). WOR5, a novel tungsten-containing aldehyde oxidoreductase from *Pyrococcus furiosus* with a broad substrate specificity. *J. Bacteriol.* 187, 7056–7061. doi: 10.1128/JB.187.20.7056-7061.2005

Bobay, L. M., and Ochman, H. (2017). The evolution of bacterial genome architecture. *Front. Genet.* 8:72. doi: 10.3389/fgene.2017.00072

Böck, A., Forchhammer, K., Heider, J., Leinfelder, W., Sawers, G., Veprek, B., et al. (1991). Selenocysteine: the 21st amino acid. *Mol. Microbiol.* 5, 515–520. doi: 10.1111/j.1365-2958.1991.tb00722.x

Boetius, A., Ravenschlag, K., Schubert, C. J., Rickert, D., Widdel, F., Gieseke, A., et al. (2000). A marine microbial consortium apparently mediating anaerobic oxidation of methane. *Nature* 407, 623–626. doi: 10.1038/35036572

Borrel, G., Gaci, N., Peyret, P., O'Toole, P. W., Gribaldo, S., and Brugère, J. F. (2014). Unique characteristics of the pyrrolysine system in the 7th order of methanogens:

implications for the evolution of a genetic code expansion cassette. *Archaea* 2015:374146. Erratum in: Archaea. 2015: 941836. doi: 10.1155/2015/941836

Brito, J. A., Sousa, F. L., Stelter, M., Bandeiras, T. M., Vonrhein, C., Teixeira, M., et al. (2009). Structural and functional insights into sulfide: quinone oxidoreductase. *Biochemistry* 48, 5613–5622. doi: 10.1021/bi9003827

Bulzu, P. A., Andrei, A. Ş., Salcher, M. M., Mehrshad, M., Inoue, K., Kandori, H., et al. (2019). Casting light on Asgardarchaeota metabolism in a sunlit microoxic niche. *Nat. Microbiol.* 4, 1129–1137. doi: 10.1038/s41564-019-0404-y

Bunker, R. D., McKenzie, J. L., Baker, E. N., and Arcus, V. L. (2008). Crystal structure of PAE0151 from *Pyrobaculum aerophilum*, a PIN-domain (Vap C) protein from a toxin-antitoxin operon. *Proteins* 72, 510–518. doi: 10.1002/prot.22048

Cavicchioli, R. (2010). Archaea--timeline of the third domain. *Nat. Rev. Microbiol.* 9, 51–61. doi: 10.1038/nrmicro2482

Chaban, B., Ng, S. Y., and Jarrell, K. F. (2006). Archaeal habitats--from the extreme to the ordinary. *Can. J. Microbiol.* 52, 73–116. doi: 10.1139/w05-147

Chambers, I., Frampton, J., Goldfarb, P., Affara, N., McBain, W., and Harrison, P. R. (1986). The structure of the mouse glutathione peroxidase gene: the selenocysteine in the active site is encoded by the 'termination' codon. *TGA. EMBO J.* 5, 1221–1227. doi: 10.1002/j.1460-2075.1986.tb04350.x

Charles-Orszag, A., Petek-Seoane, N. A., and Mullins, R. D. (2024). Archaeal actins and the origin of a multi-functional cytoskeleton. *J. Bacteriol.* 206:e0034823. doi: 10.1128/jb.00348-23

Chen, Z., Ain, N. U., Zhao, Q., and Zhang, X. (2024). From tradition to innovation: conventional and deep learning frameworks in genome annotation. *Brief. Bioinform.* 25:bbae138. doi: 10.1093/bib/bbae138

Colman, D. R., Lindsay, M. R., Amenabar, M. J., Fernandes-Martins, M. C., Roden, E. R., and Boyd, E. S. (2020). Phylogenomic analysis of novel Diaforarchaea is consistent with sulfite but not sulfate reduction in volcanic environments on early earth. *ISME J.* 14, 1316–1331. doi: 10.1038/s41396-020-0611-9

Costa, K. C., and Whitman, W. B. (2023). Model organisms to study Methanogenesis, a uniquely archaeal metabolism. *J. Bacteriol.* 205:e0011523. doi: 10.1128/jb.00115-23

Cui, H. L., and Dyall-Smith, M. L. (2021). Cultivation of halophilic archaea (class Halobacteria) from thalassohaline and athalassohaline environments. *Mar. Life Sci. Technol.* 3, 243–251. doi: 10.1007/s42995-020-00087-3

Dailey, H. A., Dailey, T. A., Gerdes, S., Jahn, D., Jahn, M., O'Brian, M. R., et al. (2017). Prokaryotic Heme biosynthesis: multiple pathways to a common essential product. *Microbiol. Mol. Biol. Rev.* 81, e00048–e00016. doi: 10.1128/MMBR.00048-16

Darmon, E., and Leach, D. R. (2014). Bacterial genome instability. *Microbiol. Mol. Biol. Rev.* 78, 1–39. doi: 10.1128/MMBR.00035-13

Darnell, C. L., Tonner, P. D., Gulli, J. G., Schmidler, S. C., and Schmid, A. K. (2017). Systematic discovery of archaeal transcription factor functions in regulatory networks through quantitative phenotyping analysis. *mSystems* 2, e00032–e00017. doi: 10.1128/mSystems.00032-17

De Lise, F., Iacono, R., Moracci, M., Strazzulli, A., and Cobucci-Ponzano, B. (2023). Archaea as a model system for molecular biology and biotechnology. *Biomol. Ther.* 13:114. doi: 10.3390/biom13010114

DiMarco, A. A., Bobik, T. A., and Wolfe, R. S. (1990). Unusual coenzymes of methanogenesis. *Annu. Rev. Biochem.* 59, 355–94. doi: 10.1146/annurev.bi.59.070190.002035

Dimonaco, N. J., Aubrey, W., Kenobi, K., Clare, A., and Creevey, C. J. (2022). No one tool to rule them all: prokaryotic gene prediction tool annotations are highly dependent on the organism of study. *Bioinformatics.* 38, 1198–1207. doi: 10.1093/bioinformatics/btab827

Dombrowski, N., Lee, J.-H., Williams, T., Offre, P., and Spang, A. (2019). Genomic diversity, lifestyles and evolutionary origins of DPANN archaea. *FEMS Microbiol. Lett.* 366:fnz008. doi: 10.1093/femsle/fnz008

Dong, Y., Shan, Y., Xia, K., and Shi, L. (2021). The proposed molecular mechanisms used by Archaea for Fe (III) reduction and Fe (II) oxidation. *Front. Microbiol.* 12:690918. doi: 10.3389/fmicb.2021.690918

Edwards, K. J., Bond, P. L., Gihring, T. M., and Banfield, J. F. (2000). An archaeal iron-oxidizing extreme acidophile important in acid mine drainage. *Science* 287, 1796–1799. doi: 10.1126/science.287.5459.1796

Elling, F. J., Becker, K. W., Könneke, M., Schröder, J. M., Kellermann, M. Y., Thomm, M., et al. (2016). Respiratory quinones in Archaea: phylogenetic distribution and application as biomarkers in the marine environment. *Environ. Microbiol.* 18, 692–707. doi: 10.1111/1462-2920.13086

Eme, L., Tamarit, D., Caceres, E. F., Stairs, C. W., De Anda, V., Schön, M. E., et al. (2023). Inference and reconstruction of the heimdallarchaeial ancestry of eukaryotes. *Nature* 618, 992–999. doi: 10.1038/s41586-023-06186-2

Falb, M., Müller, K., Königsmaier, L., Oberwinkler, T., Horn, P., von Gronau, S., et al. (2008). Metabolism of halophilic archaea. *Extremophiles* 12, 177–196. doi: 10.1007/s00792-008-0138-x

Falkowski, P. G., Fenchel, T., and Delong, E. F. (2008). The microbial engines that drive Earth's biogeochemical cycles. *Science* 320, 1034–1039. doi: 10.1126/science.1153213

Friedrich, M. W. (2005). Methyl-coenzyme M reductase genes: unique functional markers for methanogenic and anaerobic methane-oxidizing Archaea. *Methods Enzymol.* 397, 428–442. doi: 10.1016/S0076-6879(05)97026-2

Friedrich, C. G., Rother, D., Bardischewsky, F., Quentmeier, A., and Fischer, J. (2001). Oxidation of reduced inorganic sulfur compounds by bacteria: emergence of a common mechanism? *Appl. Environ. Microbiol.* 67, 2873–2882. doi: 10.1128/AEM.67.7.2873-2882.2001

Fuchs, G. (2011). Alternative pathways of carbon dioxide fixation: insights into the early evolution of life? *Ann. Rev. Microbiol.* 65, 631–658. doi: 10.1146/annurev-micro-090110-102801

Galperin, M. Y., Makarova, K. S., Wolf, Y. I., and Koonin, E. V. (2018). Phyletic distribution and lineage-specific domain architectures of archaeal two-component signal transduction systems. *J. Bacteriol.* 200, e00681–e00617. doi: 10.1128/JB.00681-17

Ghosh, W., and Dam, B. (2009). Biochemistry and molecular biology of lithotrophic sulfur oxidation by taxonomically and ecologically diverse bacteria and archaea. *FEMS Microbiol. Rev.* 33, 999–1043. doi: 10.1111/j.1574-6976.2009.00187.x

Goenrich, M., Mahlert, F., Duin, E. C., Bauer, C., Jaun, B., and Thauer, R. K. (2004). Probing the reactivity of Ni in the active site of methyl-coenzyme M reductase with substrate analogues. *J. Biol. Inorg. Chem.* 9, 691–705. doi: 10.1007/s00775-004-0552-1

Gough, J., and Chothia, C. (2002). SUPERFAMILY: HMMs representing all proteins of known structure. SCOP sequence searches, alignments and genome assignments. *Nucleic Acids Res.* 30, 268–272. doi: 10.1093/nar/30.1.268

Grant, W. D., and Ross, H. N. M. (1986). The ecology and taxonomy of halobacteria. *FEMS Microbiol. Rev.* 2, 9–15. doi: 10.1111/j.1574-6968.1986.tb01836.x

Gunsalus, R. P., Romesser, J. A., and Wolfe, R. S. (1978). Preparation of coenzyme M analogues and their activity in the methyl coenzyme M reductase system of Methanobacterium thermoautotrophicum. *Biochemistry* 17, 2374–2377. doi: 10.1021/bi00605a019

Hao, B., Gong, W., Ferguson, T. K., James, C. M., Krzycki, J. A., and Chan, M. K. (2002). A new UAG-encoded residue in the structure of a methanogen methyltransferase. *Science* 296, 1462–1466. doi: 10.1126/science.1069556

Heim, S., Künkel, A., Thauer, R. K., and Hedderich, R. (1998). Thiol: fumarate reductase (Tfr) from Methanobacterium thermoautotrophicum--identification of the catalytic sites for fumarate reduction and thiol oxidation. *Eur. J. Biochem.* 253, 292–299. doi: 10.1046/j.1432-1327.1998.2530292.x

Hoarfrost, A., Aptekmann, A., Farfañuk, G., and Bromberg, Y. (2022). Deep learning of a bacterial and archaeal universal language of life enables transfer learning and illuminates microbial dark matter. *Nat. Commun.* 13:2606. doi: 10.1038/s41467-022-30070-8

Hohmann-Marriott, M. F., and Blankenship, R. E. (2011). Evolution of photosynthesis. *Annu. Rev. Plant Biol.* 62, 515–548. doi: 10.1146/annurev-arplant-042110-103811

Holmes, A. J., Costello, A., Lidstrom, M. E., and Murrell, J. C. (1995). Evidence that particulate methane monooxygenase and ammonia monooxygenase may be evolutionarily related. *FEMS Microbiol. Lett.* 132, 203–208. doi: 10.1016/0378-1097(95)00311-r

Hua, Z. S., Qu, Y. N., Zhu, Q., Zhou, E. M., Qi, Y. L., Yin, Y. R., et al. (2018). Genomic inference of the metabolism and evolution of the archaeal phylum Aigarchaeota. *Nat. Commun.* 9:2832. doi: 10.1038/s41467-018-05284-4

Huang, L., Chakrabarti, S., Cooper, J., Perez, A., John, S. M., Daroub, S. H., et al. (2021). Ammonia-oxidizing archaea are integral to nitrogen cycling in a highly fertile agricultural soil. *ISME Commun.* 1:19. doi: 10.1038/s43705-021-00020-4

Imachi, H., Nobu, M. K., Nakahara, N., Morono, Y., Ogawara, M., Takaki, Y., et al. (2020). Isolation of an archaeon at the prokaryote-eukaryote interface. *Nature* 577, 519–525. doi: 10.1038/s41586-019-1916-6

Iorizzo, M., Paventi, G., and Di Martino, C. (2023). Biosynthesis of gamma-aminobutyric acid (GABA) by Lactiplantibacillus plantarum in fermented food production. *Curr. Issues Mol. Biol.* 46, 200–220. doi: 10.3390/cimb46010015

Jarrell, K. F., Walters, A. D., Bochiwal, C., Borgia, J. M., Dickinson, T., and Chong, J. P. J. (2011). Major players on the microbial stage: why archaea are important. *Microbiology* 157, 919–936. doi: 10.1099/mic.0.047837-0

Jeuken, G. S., and Käll, L. (2024). Pathway analysis through mutual information. *Bioinformatics* 40:btad 776. doi: 10.1093/bioinformatics/btad776

Jiao, J. Y., Liu, L., Hua, Z. S., Fang, B. Z., Zhou, E. M., Salam, N., et al. (2020). Microbial dark matter coming to light: challenges and opportunities. *Natl. Sci. Rev.* 8:nwaa280. doi: 10.1093/nsr/nwaa280

Jones, P., Binns, D., Chang, H. Y., Fraser, M., Li, W., McAnulla, C., et al. (2014). Inter pro scan 5: genome-scale protein function classification. *Bioinformatics* 30, 1236–1240. doi: 10.1093/bioinformatics/btu031

Jones, W. J., Leigh, J. A., Mayer, F., Woese, C. R., and Wolfe, R. S. (1983). *Methanococcus jannaschii* sp. nov., an extremely thermophilic methanogen from a submarine hydrothermal vent. *Arch. Microbiol.* 136, 254–261. doi: 10.1007/BF00425213

Justice, N. B., Pan, C., Mueller, R., Spaulding, S. E., Shah, V., Sun, C. L., et al. (2012). Heterotrophic archaea contribute to carbon cycling in low-pH, suboxic

biofilm communities. *Appl. Environ. Microbiol.* 78, 8321–8330. doi: 10.1128/AEM.01938-12

Kanehisa, M., and Goto, S. (2000). KEGG: Kyoto encyclopedia of genes and genomes. *Nucleic Acids Res.* 28, 27–30. doi: 10.1093/nar/28.1.27

Karavaeva, V., and Sousa, F. L. (2023). Modular structure of complex II: an evolutionary perspective. *Biochim. Biophys. Acta Bioenerg.* 1864:148916. doi: 10.1016/j.bbabio.2022.148916

Karp, P. D., Billington, R., Caspi, R., Fulcher, C. A., Latendresse, M., Kothari, A., et al. (2019). The bio Cyc collection of microbial genomes and metabolic pathways. *Brief. Bioinform.* 20, 1085–1093. doi: 10.1093/bib/bbx085

Kaster, A. K., Goenrich, M., Seedorf, H., Liesegang, H., Wollherr, A., Gottschalk, G., et al. (2011). More than 200 genes required for methane formation from H_2 and CO_2 and energy conservation are present in Methanothermobacter marburgensis and *Methanothermobacter thermautotrophicus*. *Archaea* 2011:973848. doi: 10.1155/2011/973848

Khodabandelou, G., Routhier, E., and Mozziconacci, J. (2020). Genome annotation across species using deep convolutional neural networks. *Peer J. Comput. Sci.* 6:e278. doi: 10.7717/peerj-cs.278

Kletzin, A. (2007) in General characteristics and important model organisms. ed. R. C. Archaea (Washington (DC): ASM Press).

Koonin, E. V., and Wolf, Y. I. (2008). Genomics of bacteria and archaea: the emerging dynamic view of the prokaryotic world. *Nucleic Acids Res.* 36, 6688–6719. doi: 10.1093/nar/gkn668

Kutnowski, N., Shmulevich, F., Davidov, G., Shahar, A., Bar-Zvi, D., Eichler, J., et al. (2019). Specificity of protein-DNA interactions in hypersaline environment: structural studies on complexes of *Halobacterium salinarum* oxidative stress-dependent protein hs Ros R. *Nucleic Acids Res.* 47, 8860–8873. doi: 10.1093/nar/gkz604

Lancaster, C. R. (2002). Succinate: quinone oxidoreductases: an overview. *Biochim. Biophys. Acta* 1553, 1–6. doi: 10.1016/s0005-2728(01)00240-7

Lasken, R. S., and McLean, J. S. (2014). Recent advances in genomic DNA sequencing of microbial species from single cells. *Nat. Rev. Genet.* 15, 577–584. doi: 10.1038/nrg3785

Laso-Pérez, R., Wegener, G., Knittel, K., Widdel, F., Harding, K. J., Krukenberg, V., et al. (2016). Thermophilic archaea activate butane via alkyl-coenzyme M formation. *Nature* 539, 396–401. doi: 10.1038/nature20152

Lee, S. J., Engelmann, A., Horlacher, R., Qu, Q., Vierke, G., Hebbeln, C., et al. (2003). Trm B, a sugar-specific transcriptional regulator of the trehalose/maltose ABC transporter from the hyperthermophilic archaeon *Thermococcus litoralis*. *J. Biol. Chem.* 278, 983–990. doi: 10.1074/jbc.M210236200

Lees, J., Yeats, C., Perkins, J., Sillitoe, I., Rentzsch, R., Dessailly, B. H., et al. (2012). Gene 3D: a domain-based resource for comparative genomics, functional annotation and protein network analysis. *Nucleic Acids Res.* 40, D465–D471. doi: 10.1093/nar/gkr1181. Erratum in: Nucleic Acids Res. 40 (10): 4725

Leigh, J. A. (2000). Nitrogen fixation in methanogens: the archaeal perspective. *Curr. Issues Mol. Biol.* 2, 125–131

Leigh, J. A., Albers, S. V., Atomi, H., and Allers, T. (2011). Model organisms for genetics in the domain Archaea: methanogens, halophiles, thermococcales and sulfolobales. *FEMS Microbiol. Rev.* 35, 577–608. doi: 10.1111/j.1574-6976.2011.00265.x

Lemmens, L., Maklad, H. R., Bervoets, I., and Peeters, E. (2019). Transcription regulators in Archaea: homologies and differences with bacterial regulators. *J. Mol. Biol.* 431, 4132–4146. doi: 10.1016/j.jmb.2019.05.045

Lencina, A. M., Ding, Z., Schurig-Briccio, L. A., and Gennis, R. B. (2013). Characterization of the type III sulfide: quinone oxidoreductase from Caldivirga maquilingensis and its membrane binding. *Biochim. Biophys. Acta* 1827, 266–275. doi: 10.1016/j.bbabio.2012.10.010

Letunic, I., Khedkar, S., and Bork, P. (2021). SMART: recent updates, new developments and status in 2020. *Nucleic Acids Res.* 49, D458–D460. doi: 10.1093/nar/gkaa937

Li, W., O'Neill, K. R., Haft, D. H., DiCuccio, M., Chetvernin, V., Badretdin, A., et al. (2021). Ref Seq: expanding the prokaryotic genome annotation pipeline reach with protein family model curation. *Nucleic Acids Res.* 49, D1020–D1028. doi: 10.1093/nar/gkaa1105

Libbrecht, M. W., and Noble, W. S. (2015). Machine learning applications in genetics and genomics. *Nat. Rev. Genet.* 16, 321–332. doi: 10.1038/nrg3920

Liu, Y., Makarova, K. S., Huang, W. C., Wolf, Y. I., Nikolskaya, A. N., Zhang, X., et al. (2021). Expanded diversity of Asgard archaea and their relationships with eukaryotes. *Nature* 593, 553–557. doi: 10.1038/s41586-021-03494-3

López-García, P., and Moreira, D. (2020). The Syntrophy hypothesis for the origin of eukaryotes revisited. *Nat. Microbiol.* 5, 655–667. doi: 10.1038/s41564-020-0710-4

Louca, S., Parfrey, L. W., and Doebeli, M. (2016). Decoupling function and taxonomy in the global ocean microbiome. *Science* 353, 1272–1277. doi: 10.1126/science.aaf4507

Lu, S., Wang, J., Chitsaz, F., Derbyshire, M. K., Geer, R. C., Gonzales, N. R., et al. (2020). CDD/SPARCLE: the conserved domain database in 2020. *Nucleic Acids Res.* 48, D265–D268. doi: 10.1093/nar/gkz991

Luo, Z. H., Li, Q., Xie, Y. G., Lv, A. P., Qi, Y. L., Li, M. M., et al. (2024). Temperature, pH, and oxygen availability contributed to the functional differentiation of ancient Nitrososphaeria. *ISME J.* 18:wrad 031. doi: 10.1093/ismejo/wrad031

Lupas, A., Van Dyke, M., and Stock, J. (1991). Predicting coiled coils from protein sequences. *Science* 252, 1162–1164. doi: 10.1126/science.252.5009.1162

Lyons, T. W., Tino, C. J., Fournier, G. P., Anderson, R. E., Leavitt, W. D., Konhauser, K. O., et al. (2024). Co-evolution of early earth environments and microbial life. *Nat. Rev. Microbiol.* 22, 572–586. doi: 10.1038/s41579-024-01044-y

Ma, C. Z., and Brent, M. R. (2021). Inferring TF activities and activity regulators from gene expression data with constraints from TF perturbation data. *Bioinformatics.* 37, 1234–1245. doi: 10.1093/bioinformatics/btaa947

Mac Leod, F., Kindler, G. S., Wong, H. L., Chen, R., and Burns, B. P. (2019). Asgard archaea: diversity, function, and evolutionary implications in a range of microbiomes. *AIMS Microbiol.* 5, 48–61. doi: 10.3934/microbiol.2019.1.48

Makarova, K. S., Tobiasson, V., Wolf, Y. I., Lu, Z., Liu, Y., Zhang, S., et al (2024). Diversity, origin, and evolution of the ESCRT systems. *mBio* 15:e0033524. doi: 10.1128/mbio.00335-24

Makarova, K. S., Wolf, Y. I., and Koonin, E. V. (2015). Archaeal clusters of orthologous genes (ar COGs): an update and application for analysis of shared features between Thermococcales, Methanococcales, and Methanobacteriales. *Life (Basel)* 5, 818–840. doi: 10.3390/life5010818

Makarova, K. S., Wolf, Y. I., and Koonin, E. V. (2019). Towards functional characterization of archaeal genomic dark matter. *Biochem. Soc. Trans.* 47, 389–398. doi: 10.1042/BST20180560

Malik, L., and Hedrich, S. (2022). Ferric Iron reduction in extreme Acidophiles. *Front. Microbiol.* 12:818414. doi: 10.3389/fmicb.2021.818414

Mao, J., Moore, L. R., Blank, C. E., Wu, E. H., Ackerman, M., Ranade, S., et al. (2016). Microbial phenomics information extractor (Micro PIE): a natural language processing tool for the automated acquisition of prokaryotic phenotypic characters from text sources. *BMC Bioinform.* 17:528. doi: 10.1186/s12859-016-1396-8

Mara, P., Geller-McGrath, D., Edgcomb, V., Beaudoin, D., Morono, Y., and Teske, A. (2023). Metagenomic profiles of archaea and bacteria within thermal and geochemical gradients of the Guaymas Basin deep subsurface. *Nat. Commun.* 14:7768. doi: 10.1038/s41467-023-43296-x

Marreiros, B. C., Batista, A. P., Duarte, A. M., and Pereira, M. M. (2013). A missing link between complex I and group 4 membrane-bound [NiFe] hydrogenases. *Biochim. Biophys. Acta* 1827, 198–209. doi: 10.1016/j.bbabio.2012.09.012

Marreiros, B. C., Calisto, F., Castro, P. J., Duarte, A. M., Sena, F. V., Silva, A. F., et al. (2016). Exploring membrane respiratory chains. *Biochim. Biophys. Acta* 1857, 1039–1067. doi: 10.1016/j.bbabio.2016.03.028

Martin, W., and Russell, M. J. (2007). On the origin of biochemistry at an alkaline hydrothermal vent. *Philos. Trans. R. Soc. Lond. B. Biol. Sci.* 362, 1887–925. doi: 10.1098/rstb.2006.1881

Matelska, D., Steczkiewicz, K., and Ginalski, K. (2017). Comprehensive classification of the PIN domain-like superfamily. *Nucleic Acids Res.* 45, 6995–7020. doi: 10.1093/nar/gkx494

Matsumi, R., Atomi, H., Driessen, A. J., and van der Oost, J. (2011). Isoprenoid biosynthesis in Archaea--biochemical and evolutionary implications. *Res. Microbiol.* 162, 39–52. doi: 10.1016/j.resmic.2010.10.003

McKay, L. J., Dlakić, M., Fields, M. W., Delmont, T. O., Eren, A. M., Jay, Z. J., et al. (2019). Co-occurring genomic capacity for anaerobic methane and dissimilatory sulfur metabolisms discovered in the Korarchaeota. *Nat. Microbiol.* 4, 614–622. doi: 10.1038/s41564-019-0362-4

McMillan, D. G., Ferguson, S. A., Dey, D., Schröder, K., Aung, H. L., Carbone, V., et al. (2011). A1Ao-ATP synthase of *Methanobrevibacter ruminantium* couples sodium ions for ATP synthesis under physiological conditions. *J. Biol. Chem.* 286, 39882–39892. doi: 10.1074/jbc.M111.281675

Meng, K., Chung, C. Z., Söll, D., and Krahn, N. (2022). Unconventional genetic code systems in archaea. *Front. Microbiol.* 13:1007832. doi: 10.3389/fmicb.2022.1007832

Menon, S. K., and Lawrence, C. M. (2013). *Helix-Turn-Helix motif in Brenner's encyclopedia of genetics*. Second Edn, 142–145. Cambridge (MA): Academic Press.

Mistry, J., Bateman, A., and Finn, R. D. (2007). Predicting active site residue annotations in the Pfam database. *BMC Bioinformat.* 8:298. doi: 10.1186/1471-2105-8-298

Moissl, C., Rachel, R., Briegel, A., Engelhardt, H., and Huber, R. (2005). The unique structure of archaeal 'hami', highly complex cell appendages with nano-grappling hooks. *Mol. Microbiol.* 56, 361–370. doi: 10.1111/j.1365-2958.2005.04294.x

Moissl-Eichinger, C., Probst, A. J., Birarda, G., Auerbach, A., Koskinen, K., Wolf, P., et al. (2017). Human age and skin physiology shape diversity and abundance of Archaea on skin. *Sci. Rep.* 7:4039. doi: 10.1038/s41598-017-04197-4

Monti, F., Stewart, D., Surendra, A., Alecu, I., Nguyen-Tran, T., Bennett, S. A. L., et al. (2023). Signed distance correlation (SiDCo): an online implementation of distance correlation and partial distance correlation for data-driven network analysis. *Bioinformatics* 39:btad 210. doi: 10.1093/bioinformatics/btad210

Müller, F. H., Bandeiras, T. M., Urich, T., Teixeira, M., Gomes, C. M., and Kletzin, A. (2004). Coupling of the pathway of sulphur oxidation to dioxygen reduction: characterization of a novel membrane-bound thiosulphate:quinone oxidoreductase. *Mol. Microbiol.* 53, 1147–60. doi: 10.1111/j.1365-2958.2004.04193.x

Murali, R., Hemp, J., and Gennis, R. B. (2022). Evolution of quinol oxidation within the heme-copper oxidoreductase superfamily. *Biochim. Biophys. Acta Bioenerg.* 1863:148907. doi: 10.1016/j.bbabio.2022.148907

Musat, F., Kjeldsen, K. U., Rotaru, A. E., Chen, S. C., and Musat, N. (2024). Archaea oxidizing alkanes through alkyl-coenzyme M reductases. *Curr. Opin. Microbiol.* 79:102486. doi: 10.1016/j.mib.2024.102486

Necci, M., Piovesan, D., Clementel, D., Dosztányi, Z., and Tosatto, S. C. E. (2021). Mobi DB-lite 3.0: fast consensus annotation of intrinsic disorder flavors in proteins. *Bioinformatics* 36, 5533–5534. doi: 10.1093/bioinformatics/btaa1045

Nelson-Sathi, S., Dagan, T., Landan, G., Janssen, A., Steel, M., McInerney, J. O., et al. (2012). Acquisition of 1, 000 eubacterial genes physiologically transformed a methanogen at the origin of Haloarchaea. *Proc. Natl. Acad. Sci. USA* 109, 20537–20542. doi: 10.1073/pnas.1209119109

Nelson-Sathi, S., Sousa, F. L., Roettger, M., Lozada-Chávez, N., Thiergart, T., Janssen, A., et al. (2015). Origins of major archaeal clades correspond to gene acquisitions from bacteria. *Nature* 517, 77–80. doi: 10.1038/nature13805

Neukirchen, S., Pereira, I. A. C., and Sousa, F. L. (2023). Stepwise pathway for early evolutionary assembly of dissimilatory sulfite and sulfate reduction. *ISME J.* 17, 1680–1692. doi: 10.1038/s41396-023-01477-y

Neukirchen, S., and Sousa, F. L. (2021). DiSCo: a sequence-based type-specific predictor of Dsr-dependent dissimilatory Sulphur metabolism in microbial data. *Microb. Genom.* 7:000603. doi: 10.1099/mgen.0.000603

Nickell, S., Hegerl, R., Baumeister, W., and Rachel, R. (2003). Pyrodictium cannulae enter the periplasmic space but do not enter the cytoplasm, as revealed by cryo-electron tomography. *J. Struct. Biol.* 141, 34–42. doi: 10.1016/s1047-8477(02)00581-6

Offre, P., Spang, A., and Schleper, C. (2013). Archaea in biogeochemical cycles. *Ann. Rev. Microbiol.* 67, 437–457. doi: 10.1146/annurev-micro-092412-155614

Oren, A. (1994). The ecology of the extremely halophilic archaea. *FEMS Microbiol. Rev.* 13, 415–439. doi: 10.1111/j.1574-6976.1994.tb00060.x

Oren, A., and Litchfield, C. D. (1999). A procedure for the enrichment and isolation of Halobacterium. *FEMS Microbiol. Lett.* 173, 353–358. doi: 10.1111/j.1574-6968.1999.tb13525.x

Padalko, A., Nair, G., and Sousa, F. L. (2024). Fusion/fission protein family identification in Archaea. *mSystems* 9:e0094823. doi: 10.1128/msystems.00948-23

Pedruzzi, I., Rivoire, C., Auchincloss, A. H., Coudert, E., Keller, G., de Castro, E., et al. (2015). HAMAP in 2015: updates to the protein family classification and annotation system. *Nucleic Acids Res.* 43, D1064–D1070. doi: 10.1093/nar/gku1002

Pereira, I. A., Ramos, A. R., Grein, F., Marques, M. C., da Silva, S. M., and Venceslau, S. S. (2011). A comparative genomic analysis of energy metabolism in sulfate reducing bacteria and archaea. *Front. Microbiol.* 2:69. doi: 10.3389/fmicb.2011.00069

Pereira, M. M., Santana, M., and Teixeira, M. (2001). A novel scenario for the evolution of haem-copper oxygen reductases. *Biochim. Biophys. Acta* 1505, 185–208. doi: 10.1016/s0005-2728(01)00169-4

Pester, M., Schleper, C., and Wagner, M. (2011). The Thaumarchaeota: an emerging view of their phylogeny and ecophysiology. *Curr. Opin. Microbiol.* 14, 300–306. doi: 10.1016/j.mib.2011.04.007

Pfeifer, K., Ergal, İ., Koller, M., Basen, M., Schuster, B., and Rittmann, S. K. R. (2021). Archaea biotechnology. *Biotechnol. Adv.* 47:107668. doi: 10.1016/j.biotechadv.2020.107668

Qi, Y. L., Chen, Y. T., Xie, Y. G., Li, Y. X., Rao, Y. Z., Li, M. M., et al. (2024). Analysis of nearly 3000 archaeal genomes from terrestrial geothermal springs sheds light on interconnected biogeochemical processes. *Nat. Commun.* 15:4066. doi: 10.1038/s41467-024-48498-5

Raux, E., Leech, H. K., Beck, R., Schubert, H. L., Santander, P. J., Roessner, C. A., et al. (2003). Identification and functional analysis of enzymes required for precorrin-2 dehydrogenation and metal ion insertion in the biosynthesis of sirohaem and cobalamin in *Bacillus megaterium*. *Biochem. J.* 370, 505–516. doi: 10.1042/BJ20021443

Rinke, C., Schwientek, P., Sczyrba, A., Ivanova, N. N., Anderson, I. J., Cheng, J. F., et al. (2013). Insights into the phylogeny and coding potential of microbial dark matter. *Nature* 499, 431–437. doi: 10.1038/nature12352

Robinson, N. P., and Schmid, A. K. (2018). Conserved principles of transcriptional networks controlling metabolic flexibility in archaea. *Emerg. Top. Life Sci.* 2, 659–669. doi: 10.1042/ETLS20180036

Rodionov, D. A., Vitreshak, A. G., Mironov, A. A., and Gelfand, M. S. (2003). Comparative genomics of the vitamin B12 metabolism and regulation in prokaryotes. *J. Biol. Chem.* 278, 41148–41159. doi: 10.1074/jbc.M305837200

Rodrigues, T. (2019). The good, the bad, and the ugly in chemical and biological data for machine learning. *Drug Discov. Today Technol.* 32-33, 3–8. doi: 10.1016/j.ddtec.2020.07.001

Rodrigues-Oliveira, T., Wollweber, F., Ponce-Toledo, R. I., Xu, J., Rittmann, S. K. R., Klingl, A., et al. (2023). Actin cytoskeleton and complex cell architecture in an Asgard archaeon. *Nature* 613, 332–339. doi: 10.1038/s41586-022-05550-y

Rother, M., and Quitzke, V. (2018). Selenoprotein synthesis and regulation in Archaea. *Biochim. Biophys. Acta. Gen. Subj.* 1862, 2451–2462. doi: 10.1016/j.bbagen.2018.04.008

Roy, R., and Adams, M. W. (2002). Characterization of a fourth tungsten-containing enzyme from the hyperthermophilic archaeon *Pyrococcus furiosus*. *J. Bacteriol.* 184, 6952–6956. doi: 10.1128/JB.184.24.6952-6956.2002

Salas-Nuñez, L. F., Barrera-Ocampo, A., Caicedo, P. A., Cortes, N., Osorio, E. H., Villegas-Torres, M. F., et al. (2024). Machine learning to predict enzyme-substrate interactions in elucidation of synthesis pathways: a review. *Meta* 14:154. doi: 10.3390/metabo14030154

Sanchez-Rocha, A. C., Makarov, M., Pravda, L., Novotný, M., and Hlouchová, K. (2024). Coenzyme-protein interactions since early life. *eLife* 13:RP94174. doi: 10.7554/eLife.94174.1

Sansupa, C., Wahdan, S. F. M., Hossen, S., Disayathanoowat, T., Wubet, T., and Purahong, W. (2021). Can we use functional annotation of prokaryotic taxa (FAPROTAX) to assign the ecological functions of soil Bacteria? *Appl. Sci.* 11:688. doi: 10.3390/app11020688

Schäfer, G., Anemüller, S., and Moll, R. (2002). Archaeal complex II: 'classical' and 'non-classical' succinate: quinone reductases with unusual features. *Biochim. Biophys. Acta* 1553, 57–73. doi: 10.1016/s0005-2728(01)00232-8

Scheller, S., Goenrich, M., Thauer, R. K., and Jaun, B. (2013). Methyl-coenzyme M reductase from methanogenic archaea: isotope effects on label exchange and ethane formation with the homologous substrate ethyl-coenzyme M. *J. Am. Chem. Soc.* 135, 14985–14995. doi: 10.1021/ja4064876

Schleper, C., and Nicol, G. W. (2010). Ammonia-oxidising archaea--physiology, ecology and evolution. *Adv. Microb. Physiol.* 57, 1–41. doi: 10.1016/B978-0-12-381045-8.00001-1

Sharma, K., Gillum, N., Boyd, J. L., and Schmid, A. (2012). The Ros R transcription factor is required for gene expression dynamics in response to extreme oxidative stress in a hypersaline-adapted archaeon. *BMC Genomics* 13:351. doi: 10.1186/1471-2164-13-351

Siebers, B., and Schönheit, P. (2005). Unusual pathways and enzymes of central carbohydrate metabolism in Archaea. *Curr. Opin. Microbiol.* 8, 695–705. doi: 10.1016/j.mib.2005.10.014

Sigrist, C. J., de Castro, E., Cerutti, L., Cuche, B. A., Hulo, N., Bridge, A., et al. (2013). New and continuing developments at PROSITE. *Nucleic Acids Res.* 41, D344–D347. doi: 10.1093/nar/gks1067

Sillitoe, I., Cuff, A. L., Dessailly, B. H., Dawson, N. L., Furnham, N., Lee, D., et al. (2013). New functional families (Fun Fams) in CATH to improve the mapping of conserved functional sites to 3D structures. *Nucleic Acids Res.* 41, D490–D498. doi: 10.1093/nar/gks1211

Soares, J. A., Zhang, L., Pitsch, R. L., Kleinholz, N. M., Jones, R. B., Wolff, J. J., et al. (2005). The residue mass of L-pyrrolysine in three distinct methylamine methyltransferases. *J. Biol. Chem.* 280, 36962–36969. doi: 10.1074/jbc.M506402200

Solomon, E. I., Sundaram, U. M., and Machonkin, T. E. (1996). Multicopper oxidases and Oxygenases. *Chem. Rev.* 96, 2563–2606. doi: 10.1021/cr950046o

Song, G. C., Im, H., Jung, J., Lee, S., Jung, M. Y., Rhee, S. K., et al. (2019). Plant growth-promoting archaea trigger induced systemic resistance in *Arabidopsis thaliana* against Pectobacterium carotovorum and *Pseudomonas syringae*. *Environ. Microbiol.* 21, 940–948. doi: 10.1111/1462-2920.14486

Soppa, J. (2006). From genomes to function: haloarchaea as model organisms. *Microbiology* 152, 585–590. doi: 10.1099/mic.0.28504-0

Spang, A. (2023). Is an archaeon the ancestor of eukaryotes? *Environ. Microbiol.* 25, 775–779. doi: 10.1111/1462-2920.16323

Spang, A., Saw, J. H., Jørgensen, S. L., Zaremba-Niedzwiedzka, K., Martijn, J., Lind, A. E., et al. (2015). Complex archaea that bridge the gap between prokaryotes and eukaryotes. *Nature* 521, 173–179. doi: 10.1038/nature14447

Spang, A., Stairs, C. W., Dombrowski, N., Eme, L., Lombard, J., Caceres, E. F., et al. (2019). Proposal of the reverse flow model for the origin of the eukaryotic cell based on comparative analyses of Asgard archaeal metabolism. *Nat. Microbiol.* 4, 1138–1148. doi: 10.1038/s41564-019-0406-9

Srinivasan, G., James, C. M., and Krzycki, J. A. (2002). Pyrrolysine encoded by UAG in Archaea: charging of a UAG-decoding specialized tRNA. *Science* 296, 1459–1462. doi: 10.1126/science.1069588

Stadtman, T. C. (1974). Selenium biochemistry. *Science* 183, 915–922. doi: 10.1126/science.183.4128.915

Szé Kely, G. J., and Rizzo, M. L. (2013). The distance correlation t-test of independence in high dimension. *J. Multivar. Anal.* 117, 193–213. doi: 10.1016/j.jmva.2013.02.012

Taffner, J., Cernava, T., Erlacher, A., and Berg, G. (2019). Novel insights into plant-associated archaea and their functioning in arugula (*Eruca sativa* Mill.). *J. Adv. Res.* 19, 39–48. doi: 10.1016/j.jare.2019.04.008

Taffner, J., Erlacher, A., Bragina, A., Berg, C., Moissl-Eichinger, C., and Berg, G. (2018). What is the role of Archaea in plants? New insights from the vegetation of alpine bogs. *mSphere* 3:e0012200118. doi: 10.1128/msphere.00122-18

Tanabe, T. S., and Dahl, C. (2023). HMSS2: an advanced tool for the analysis of sulphur metabolism, including organosulphur compound transformation, in genome and metagenome assemblies. *Mol. Ecol. Resour.* 23, 1930–1945. doi: 10.1111/1755-0998.13848

Teske, A. (2018). Aerobic Archaea in iron-rich springs. *Nat. Microbiol.* 3, 646–647. doi: 10.1038/s41564-018-0168-9

Tharp, J. M., Ehnbom, A., and Liu, W. R. (2018). tRNAPyl: structure, function, and applications. *RNA Biol.* 15, 441–452. doi: 10.1080/15476286.2017.1356561

Thauer, R. K., Jungermann, K., and Decker, K. (1977). Energy conservation in chemotrophic anaerobic bacteria. *Bacteriol. Rev.* 41, 100–180. doi: 10.1128/br.41.1.100-180.1977

Thauer, R. K., Kaster, A. K., Seedorf, H., Buckel, W., and Hedderich, R. (2008). Methanogenic archaea: ecologically relevant differences in energy conservation. *Nat. Rev. Microbiol.* 6, 579–591. doi: 10.1038/nrmicro1931

Thomas, C. M., Desmond-Le Quéméner, E., Gribaldo, S., and Borrel, G. (2022). Factors shaping the abundance and diversity of the gut archaeome across the animal kingdom. *Nat. Commun.* 13:3358. doi: 10.1038/s41467-022-31038-4

Thomas, P. D., Ebert, D., Muruganujan, A., Mushayahama, T., Albou, L. P., and Mi, H. (2022). PANTHER: making genome-scale phylogenetics accessible to all. *Protein Sci.* 31, 8–22. doi: 10.1002/pro.4218

Thurl, S., Buhrow, I., and Schäfer, W. (1985). Quinones from Archaebacteria, I. New types of menaquinones from the thermophilic archaebacterium Thermoproteus tenax. *Biol. Chem. Hoppe Seyler.* 366, 1079–83. doi: 10.1515/bchm3

Tillier, E., and Collins, R. (2000). Genome rearrangement by replication-directed translocation. *Nat. Genet.* 26, 195–197. doi: 10.1038/79918

Tomita, H., Yokooji, Y., Ishibashi, T., Imanaka, T., and Atomia, H. (2014). An archaeal glutamate decarboxylase homolog functions as an aspartate decarboxylase and is involved in β-alanine and coenzyme a biosynthesis. *J. Bacteriol.* 196, 1222–1230. doi: 10.1128/JB.01327-13

Urich, T., Bandeiras, T. M., Leal, S. S., Rachel, R., Albrecht, T., Zimmermann, P., et al. (2004). The Sulphur oxygenase reductase from *Acidianus ambivalens* is a multimeric protein containing a low-potential mononuclear non-haem iron Centre. *Biochem. J.* 381, 137–146. doi: 10.1042/BJ20040003

Urich, T., Gomes, C. M., Kletzin, A., and Frazão, C. (2006). X-ray structure of a self-compartmentalizing sulfur cycle metalloenzyme. *Science* 311, 996–1000. doi: 10.1126/science.1120306

Van Lis, R., Nitschke, W., Duval, S., and Schoepp-Cothenet, B. (2013). Arsenics as bioenergetic substrates. *Biochim. Biophys. Acta* 1827, 176–188. doi: 10.1016/j.bbabio.2012.08.007

Van Wolferen, M., Pulschen, A. A., Baum, B., Gribaldo, S., and Albers, S. V. (2022). The cell biology of archaea. *Nat. Microbiol.* 7, 1744–1755. doi: 10.1038/s41564-022-01215-8

Ver Eecke, H. C., Butterfield, D. A., Huber, J. A., Lilley, M. D., Olson, E. J., Roe, K. K., et al. (2012). Hydrogen-limited growth of hyperthermophilic methanogens at deep-sea hydrothermal vents. *Proc. Natl. Acad. Sci. USA* 109, 13674–13679. doi: 10.1073/pnas.1206632109

Verhees, C. H., Kengen, S. W., Tuininga, J. E., Schut, G. J., Adams, M. W., De Vos, W. M., et al. (2003). The unique features of glycolytic pathways in Archaea. *Biochem. J.* 375, 231–246. doi: 10.1042/BJ20021472. Erratum in: Biochem. J. 2004 Feb 1; 377 (Pt 3): 819-22

Vinga, S. (2014). Information theory applications for biological sequence analysis. *Brief. Bioinform.* 15, 376–389. doi: 10.1093/bib/bbt068

Walsby, A. E. (2005). Archaea with square cells. *Trends Microbiol.* 13, 193–195. doi: 10.1016/j.tim.2005.03.002

Weiss, M. C., Sousa, F. L., Mrnjavac, N., Neukirchen, S., Roettger, M., Nelson-Sathi, S., et al. (2016). The physiology and habitat of the last universal common ancestor. *Nat. Microbiol.* 1:16116. doi: 10.1038/nmicrobiol.2016.116

Weiss, D. S., and Thauer, R. K. (1993). Methanogenesis and the unity of biochemistry. *Cell* 72, 819–822. doi: 10.1016/0092-8674(93)90570-g

Wells, M., Kanmanii, N. J., Al Zadjali, A. M., Janecka, J. E., Basu, P., Oremland, R. S., et al. (2020). Methane, arsenic, selenium and the origins of the DMSO reductase family. *Sci. Rep.* 10:10946. doi: 10.1038/s41598-020-67892-9

Wilson, D., Pethica, R., Zhou, Y., Talbot, C., Vogel, C., Madera, M., et al. (2009). SUPERFAMILY--sophisticated comparative genomics, data mining, visualization and phylogeny. *Nucleic Acids Res.* 37, D380–D386. doi: 10.1093/nar/gkn762

Wu, C. H., Nikolskaya, A., Huang, H., Yeh, L. S., Natale, D. A., Vinayaka, C. R., et al. (2004). PIRSF: family classification system at the protein information resource. *Nucleic Acids Res.* 32, 112D–1114D. doi: 10.1093/nar/gkh097

Xu, C., and Jackson, S. A. (2019). Machine learning and complex biological data. *Genome Biol.* 20:76. doi: 10.1186/s13059-019-1689-0

Yadav, A. N., Sachan, S. G., Verma, P., and Saxena, A. K. (2015). Prospecting cold deserts of north western Himalayas for microbial diversity and plant growth promoting attributes. *J. Biosci. Bioeng.* 119, 683–693. doi: 10.1016/j.jbiosc.2014.11.006

Zaremba-Niedzwiedzka, K., Caceres, E. F., Saw, J. H., Bäckström, D., Juzokaite, L., Vancaester, E., et al. (2017). Asgard archaea illuminate the origin of eukaryotic cellular complexity. *Nature* 541, 353–358. doi: 10.1038/nature21031

Zhang, I. H., Borer, B., Zhao, R., Wilbert, S., Newman, D. K., and Babbin, A. R. (2024). Uncultivated DPANN archaea are ubiquitous inhabitants of global oxygen-deficient zones with diverse metabolic potential. *MBio* 15, e02918–e02923. doi: 10.1128/mbio.02918-23

Zhang, Y., and Lin, K. (2012). A phylogenomic analysis of *Escherichia coli*/Shigella group: implications of genomic features associated with pathogenicity and ecological adaptation. *BMC Evol. Biol.* 12:174. doi: 10.1186/1471-2148-12-174

Zhang, C., Liu, X., Shi, L. D., Li, J., Xiao, X., Shao, Z., et al. (2023). Unexpected genetic and microbial diversity for arsenic cycling in deep sea cold seep sediments. *NPJ Biofilms Microbio.* 9:13. doi: 10.1038/s41522-023-00382-8

Zhang, R. Y., Wang, Y. R., Liu, R. L., Rhee, S. K., Zhao, G. P., and Quan, Z. X. (2024). Metagenomic characterization of a novel non-ammonia-oxidizing Thaumarchaeota from hadal sediment. *Microbiome* 12:7. doi: 10.1186/s40168-023-01728-2

Zhang, X., Zhang, C., Liu, Y., Zhang, R., and Li, M. (2023). Non-negligible roles of archaea in coastal carbon biogeochemical cycling. *Trends Microbiol.* 31, 586–600. doi: 10.1016/j.tim.2022.11.008

Zillig, W., Tu, J., and Holz, I. (1981). Thermoproteales—a third order of thermoacidophilic archaebacteria. *Nature* 293, 85–86. doi: 10.1038/293085a0

frontiers | Frontiers in Microbiology

TYPE Original Research
PUBLISHED 08 January 2025
DOI 10.3389/fmicb.2024.1473270

OPEN ACCESS

EDITED BY
Ivan A. Berg,
University of Münster, Germany

REVIEWED BY
Kensuke Igarashi,
National Institute of Advanced Industrial Science and Technology (AIST), Japan
Meina Neumann-Schaal,
German Collection of Microorganisms and Cell Cultures GmbH (DSMZ), Germany

*CORRESPONDENCE
Tetyana Milojevic
✉ tetyana.milojevic@cnrs-orleans.fr

RECEIVED 30 July 2024
ACCEPTED 19 December 2024
PUBLISHED 08 January 2025

CITATION
Gfellner SV, Colas C, Gabant G, Groninga J, Cadene M and Milojevic T (2025) Improved protocol for metabolite extraction and identification of respiratory quinones in extremophilic Archaea grown on mineral materials.
Front. Microbiol. 15:1473270.
doi: 10.3389/fmicb.2024.1473270

Improved protocol for metabolite extraction and identification of respiratory quinones in extremophilic Archaea grown on mineral materials

Sebastian V. Gfellner[1,2], Cyril Colas[1,2,3], Guillaume Gabant[1,2], Janina Groninga[4], Martine Cadene[1,2] and Tetyana Milojevic[1,2]*

[1]UPR4301 Centre de Biophysique Moléculaire (CBM), Orléans, France, [2]Université d'Orléans, Orléans, France, [3]UMR7311 Institut de Chimie Organique et Analytique (ICOA), Orléans, France, [4]Center for Marine Environmental Sciences, University of Bremen, Bremen, Germany

We investigated the metabolome of the iron- and sulfur-oxidizing, extremely thermoacidophilic archaeon *Metallosphaera sedula* grown on mineral pyrite (FeS_2). The extraction of organic materials from these microorganisms is a major challenge because of the tight contact and interaction between cells and mineral materials. Therefore, we applied an improved protocol to break the microbial cells and separate their organic constituents from the mineral surface, to extract lipophilic compounds through liquid–liquid extraction, and performed metabolomics analyses using MALDI-TOF MS and UHPLC-UHR-Q/TOF. Using this approach, we identified several molecules involved in central carbon metabolism and in the modified Entner-Doudoroff pathway found in Archaea, sulfur metabolism-related compounds, and molecules involved in the adaptation of *M. sedula* to extreme environments, such as metal tolerance and acid resistance. Furthermore, we identified molecules involved in microbial interactions, i.e., cell surface interactions through biofilm formation and cell–cell interactions through quorum sensing, which relies on messenger molecules for microbial communication. Moreover, we successfully extracted and identified different saturated thiophene-bearing quinones using software for advanced compound identification (MetaboScape). These quinones are respiratory chain electron carriers in *M. sedula*, with biomarker potential for life detection in extreme environmental conditions.

KEYWORDS

metabolomics, chemolithotrophs, thiophene-bearing quinones, quorum sensing, organic extraction from minerals

1 Introduction

Analogous to the first microorganisms that inhabited the early Earth, chemolithoautotrophic microorganisms use ancient metabolic pathways to harvest energy either through mineral redox alterations, or directly from inorganic compounds, such as nitrogen, iron, or sulfur (Vargas et al., 1998; Wächtershäuser, 1988, 1990; Weiss et al., 2016; Camprubi et al., 2017; Morrison and Mojzsis, 2021). Archaea from the order Sulfolobales (e.g., *Sulfolobus* spp., *Acidianus* spp. and *Metallosphaera* spp.) are capable of oxidizing Fe and S while thriving under extreme conditions at a pH of 2–3 and temperatures of 65–80°C. These microorganisms can use heterotrophic, chemolithoautotrophic, and mixotrophic ways of generating energy utilizing various substrates, such as complex organic molecules, CO_2

fixation, and oxidation of various metal sulfides (Huber et al., 1989; Clark et al., 1993; Peeples and Kelly, 1995; Schönheit and Schäfer, 1995; Amend and Shock, 2001; Auernik et al., 2008; Auernik and Kelly, 2008, 2010a, 2010b; Maezato et al., 2012; Mukherjee et al., 2012; Kölbl et al., 2017; Wheaton et al., 2019; Blazevic et al., 2019; Milojevic et al., 2021).

The archaeon *Metallosphaera sedula* is known for its potential to mobilize metal sulfides and oxides and a broad range of mineral biotransforming capabilities, which span from Fe and S minerals, such as pyrite FeS_2 (Clark et al., 1993; Schönheit and Schäfer, 1995; Amend and Shock, 2001) and chalcopyrite $CuFeS_2$ (Maezato et al., 2012), to calcium tungstate minerals such as scheelite (Blazevic et al., 2019), uranium (Mukherjee et al., 2012), molybdenum, and vanadium (Wheaton et al., 2019). *M. sedula* was isolated from a sulfataric field in Italy by Huber et al. (1989), and its fully sequenced genome has been intensively studied, with a focus on its bioleaching capabilities (Auernik et al., 2008; Auernik and Kelly, 2008). Moreover, Kölbl et al. (2017) focused on the utilization of extraterrestrial material by *M. sedula* grown on Martian regolith simulants, paving the way for the cultivation of *M. sedula* on the genuine Martian meteorite NWA 7034 by Milojevic et al. (2020).

Bioleaching involves the oxidation of metals and metalloids, accompanied by the release of metal compounds from the mineral matrix (Figure 1); for example, Fe(II) is oxidized to Fe(III). Remarkable is the cellular resistance of acidophilic microorganisms (e.g., *M. sedula*) to heavy metals such as As, Cu, Zn, Cd, and Ni, as reviewed by Dopson et al. (2003). The multimolecular machinery of iron-transforming Archaea is usually represented by clusters of redox-active enzymes associated with respiratory Fe/S oxidation. For instance, for Fe-oxidizing members of the archaeal order Sulfolobales, the existence of the ferrous iron oxidation (fox) gene cluster has been reported (Counts et al., 2022), the products of which include the primary electron acceptor from metal ions and terminal oxidase complex. The surface attachment of mineral-transforming microorganisms and biofilm formation on mineral surfaces are crucial strategies that enhance microbial bioleaching performance and facilitate mineral solubilization, with increasing interest in industrial applications (Rohwerder et al., 2003; Olson et al., 2003). Biofilm formation in Sulfolobales involving attachment, maturation, and dispersal has been described, whereas the bioalteration of mineral materials with extracellular matrices composed of carbohydrates has been observed (Koerdt et al., 2010, 2012; Lewis et al., 2023). The adsorption of microorganisms onto mineral surfaces occurs locally in low-pH microenvironments containing extracellular polymers (Xia et al., 2021). The role of extracellular polymeric substances, mainly neutral sugars and lipids, in attachment to mineral surfaces such as pyrite has been further investigated by Kinzler et al.

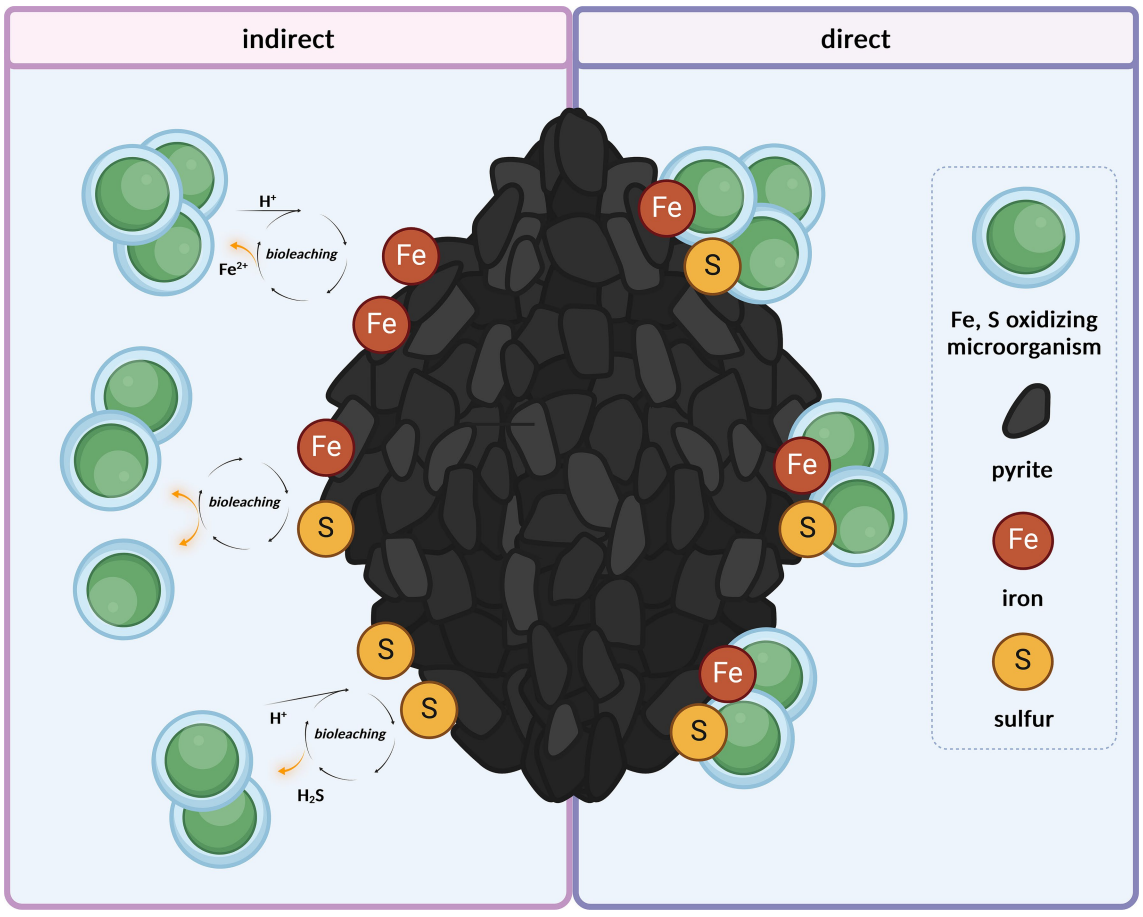

FIGURE 1
Microbial harvest of energy through the oxidation of Fe^{2+} and reduced inorganic sulfur compounds from mineral matrix, either indirectly from ions released in the medium through abiotic acidic leaching (under a pH of 2.0) or directly from the mineral surface. Created with BioRender.com.

(2003), focusing on the bacteria *Acidithibacillus ferrooxidans*, which mediates attachment to the sulfide surface and concentration of Fe due to complexation promoting sulfide oxidation. This was also consistent with the studies by Bromfield et al. (2011), who investigated the mineral adsorption of the extreme thermoacidophilic archaeon *M. hakonensis* onto mineral sulfides, underlining the importance of surface charge rather than hydrophobic interactions.

The detailed biochemical processes involved in the metabolism of *M. sedula* underlying the oxidation of iron and sulfur compounds in the order of Sulfolobales have been described by transcriptome analyses of *M. sedula* grown on various mineral substrates, enabling the comprehensive identification of its electron transport chains (Auernik et al., 2008; Auernik and Kelly, 2008, 2010a, 2010b). This includes the distinct role of isoprenoid quinones, which are part of the membranes of all living organisms (Hiraishi, 1999). They are composed of a hydrophilic head group and an apolar isoprenoid side chain. Therefore, they exhibit amphiphilic properties, which allows them to insert into lipid bilayers. They mainly function as electron and proton carriers in photosynthetic and respiratory electron transport chains, with additional roles as antioxidants (Hiraishi, 1999; Nowicka and Kruk, 2010). Quinone oxidoreductases deliver electrons to terminal oxidase complexes that maintain intracellular pH while generating a proton motive force (thiosulfate:quinone oxidoreductase, e.g., DoxD) through reduced caldariella- or sulfolobus-type quinones (Figure 2) (Auernik and Kelly, 2008). Furthermore, the role of signaling molecules involved in quorum sensing has been intensively investigated, as this cell–cell communication strategy enables cross-species microorganisms to synchronize their gene expression and growth (Ng et al., 2011; Hiblot et al., 2012; Kaur et al., 2018). To date, the best-characterized signaling molecules in Archaea are N-acyl homoserine lactones (AHLs), which potentially promote biofilm formation and, therefore, play an important role in microbe-mineral interactions (Charlesworth et al., 2020; Prescott and Decho, 2020). Additionally, quorum-sensing molecules have been proposed as biocatalysts to increase microbial turnover rates during biomining operations (Ruiz et al., 2008; Bellenberg et al., 2014).

Although the efficient separation of microbial organic molecules from mineral materials is challenging (Direito et al., 2012; Swenson et al., 2015; Swenson and Northen, 2019; Bell et al., 2022), the metabolomics of microbial-mineral interactions is a promising and powerful tool for microbial screening of environmental samples for a number of biotechnological and potential astrobiological applications (Giebel et al., 2010; Das and Dash, 2014; Röling et al., 2015; Abrahamsson and Kanik, 2022; Sharma et al., 2022). However, separation of biologically active molecules from mineral matrices remains problematic because of the strong adsorption of organic substances by iron-rich minerals (Direito et al., 2012; Röling et al., 2015; Swenson et al., 2015; Swenson and Northen, 2019; Abrahamsson and Kanik, 2022; Bell et al., 2022). In this study, we report the successful extraction of metabolites from the chemolithotrophic organism *M. sedula* grown on a mineral source, by adapting a modified lipid extraction protocol and implementing mass spectrometry-based metabolomic analysis. This mass spectrometry-based technique can be further applied to detect thiophene-bearing quinones in environmental and laboratory samples, to resolve metabolic pathway-specific molecules, and to provide insight into the metabolome used in microbe-mineral interactions in *M. sedula*.

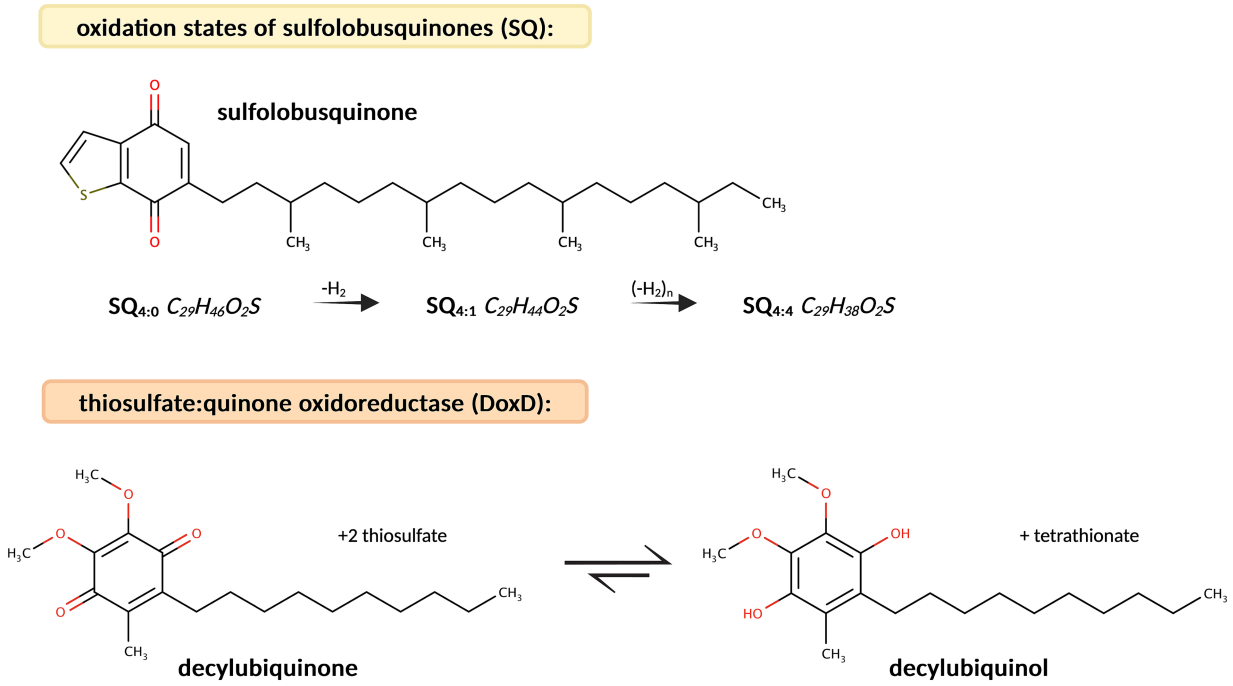

FIGURE 2
Molecular structure of sulfolobusquinone (SQ) and molecular formulas of its different oxidation states ($SQ_{4:0}$, $SQ_{4:1}$, and $SQ_{4:4}$). The reaction pathway of decylubiquinone to decylubiquinol though catalysis by thiosulfate:quinone oxidoreductase (DoxD) is described in the KEGG database.

2 Materials and methods

2.1 Microbial cultivation

Metallosphaera sedula DSM 5348 was cultivated aerobically in DSMZ 88 medium in the presence of pyrite, as described previously (Kölbl et al., 2017; Blazevic et al., 2019; Milojevic et al., 2021), over a period of 140 h in 1 L glassblower modified Schott-bottle bioreactors (Duran DWK Life Sciences GmbH, Wertheim/Main, Germany), unless otherwise noted. The stock culture was stored at −80°C in a mixture of 50% glycerol and DSMZ 88 medium (50, 50, v:v). The DSMZ 88 medium is composed of 9.84 mM $(NH_4)_2SO_4$, 2.06 mM KH_2PO_4, 1.01 mM $MgSO_4 \times 7H_2O$, 0.48 mM $CaCl_2 \times 2H_2O$, and 0.07 mM $FeCl_3 \times 6H_2O$. This was also used as cell resuspension medium. Further, Allen trace element solution was added consisting of 0.91 mM $MnCl_2 \times 4H_2O$, 1.18 mM $Na_2B_4O_7 \times 10H_2O$, 0.08 mM $ZnSO_4 \times 7H_2O$, 0.03 mM $CuCl_2 \times 2H_2O$, 0.01 mM $Na_2MoO_4 \times 2H_2O$, 0.02 mM $VOSO_4 \times 2H_2O$, and 3.56 µM $CoSO_4 \times 7H_2O$. Tryptone (0.1%) was added to the DSMZ 88 medium, as previously described (Kölbl et al., 2017). The pH was adjusted to 2.0, with 5 M H_2SO_4. The pyrite was manually ground using a hand grinder to particles with diameters of 63–100 µm, controlled by 63 µm and 100 µm mesh sieves with a 75:25% distribution of 63 to 100 µm, and baked overnight at 180°C. Pyrite (10 g/L) was added to 800 mL of culture. A 1 L bioreactor was then assembled as described previously (Kölbl et al., 2017; Blazevic et al., 2019; Milojevic et al., 2021) and constantly heated to 73°C with steady stirring. A flow of CO_2 at a total rate of 0.9 L/min (normalized to 1 atm and 0°C) was ensured for the interconnected triplicate bioreactor setup, resulting in a flow rate of 0.3 L/min for each bioreactor. Three biological replicates (A, B, and C) were incubated and harvested before reaching the stationary phase. For inoculation, a frozen (−80°C) glycerol stock of *M. sedula*, previously grown and acclimated to pyrite, was used. To monitor microbial growth, the cultures were sampled continuously during the growth phase and the cells were counted under a microscope (Olympus BX51 equipped with a Pixelink M20C-CYL camera) using a Neubauer Chamber (Carl Roth GmbH & Co. KG, Karlsruhe, Germany) and harvested upon reaching stationary phase. Harvesting was performed by centrifugation in sterile 50 mL Falcon tubes at 3220 × *g* for 40 min. The cell pellets and supernatants were collected separately, snap-frozen in liquid nitrogen, and stored at −20°C until further extraction.

2.2 Lyophilization and hydrolysis

The stored cell/pyrite pellets were thawed and resuspended in cell resuspension medium and transferred into a 50 mL glass vial. The samples were then refrozen and lyophilized overnight. To increase the detection capabilities and promote the separation of cells and minerals, the samples were hydrolyzed before extraction using 1 M HCl in a mixture of methanol (1:1, v/v), and vortexed and ultrasonicated for 10 min. The mixture was then heated to 70°C for 3 h and dried under a stream of N_2 at 60°C. This will be referred to as hydrolyzed cells/pyrite.

2.3 Biomass extraction: cell breakage and liquid–liquid extraction

To increase the yield of metabolites, a protocol originally developed by Bligh and Dyer (1959) for total lipid extraction and modified by Evans et al. (2022) was used to separate organic molecules from the mineral phases. This protocol was applied to dried hydrolyzed cells/pyrite. To burst the microbial cells, separate the cell debris from the minerals and release metabolites into the solution, a volume of 5 mL B&DI solution consisting of methanol, dichloromethane, and 0.1 M potassium phosphate buffer, pH 8.0 (2:1:0.8, v/v/v) was added to 1 g pyrite-equivalent of hydrolyzed cells/pyrite samples. The samples were vortexed, sonicated for 10 min and centrifuged for 10 min at 3220 × *g* in a 50 mL glass vial. The supernatant was decanted into a fresh glass vial and evaporated under a stream of N_2 at 60°C. This step was repeated once with B&DI and twice with B&DII consisting of methanol, dichloromethane, and 0.1 M trichloroacetic acid solution (2:1:0.8, v/v/v). This will be subsequently referred to as B&D extract. To enrich the lipophilic compounds, liquid–liquid extraction was conducted on the B&D extract in 50 mL glass vials. For this, 5 mL ultrapure water and 10 mL dichloromethane were added, followed by vortexing and centrifugation for 5 min at 3220 × *g*. The organic phase at the bottom of the vial was extracted into a fresh glass vial, and the 50 mL glass vials with the aqueous phase were set aside. This liquid–liquid extraction step was repeated four times and the organic fractions were pooled and evaporated under a stream of N_2 at 60°C. The organic fraction of the extract was then transferred using 4 mL dichloromethane into a fresh vial, evaporated under a stream of N_2 at 60°C and resolubilized with 200 µL of methanol and dichloromethane (9:1, v/v). To be able to separately analyze hydrophilic compounds, the aqueous phase in the 50 mL glass vials was further processed. To exclude lipophilic compounds from the aqueous phase, 10 mL of dichloromethane were added, followed by sonication for 10 min and centrifugation for 10 min at 3220 × *g*. Then, the aqueous fraction was collected, transferred with 4 mL of ultrapure water into a fresh vial, evaporated under a stream of N_2 at 60°C and resolubilized with 200 µL of ultrapure water and methanol (9:1, v/v).

2.4 MALDI-TOF mass spectrometry

The exometabolites in *M. sedula* were identified by comparative Matrix Assisted Laser Desorption Ionization – Time of Flight mass spectrometry (MALDI-TOF MS) analysis of a 4.5 L culture of *M. sedula* grown on pyrite. Analysis was conducted of the cell pellet, the corresponding culture supernatant, and the organic extract. MALDI-TOF MS spectra were acquired on an ultrafleXtreme mass spectrometer (Bruker Daltonics GmbH, Bremen, Germany). Samples were mixed in a 1:1 ratio in a solution consisting either of 4-hydroxy-α-cyano-cinnamic acid (HCCA) or 2,5-dihydroxybenzoic acid (DHB) at 1 mg/mL in acetonitrile, ultrapure water, and trifluoroacetic acid (50:47.5:2.5, v/v/v) containing 1 mM NaCl. The matrix-sample solutions were spotted onto an AnchorChip target and air-dried. Spectra were acquired in reflectron positive ion mode (3,000 laser shots) in the 100–4,500 *m/z* range. Calibration of the instrument was performed externally using a neighboring spot with peaks of the matrix and pepmix calibration standard II (Bruker Daltonik GmbH,

Bremen, Germany), with the addition of oxidized insulin B and adrenocorticotropic hormones (clip 1–39). MALDI-TOF MS spectra were processed using the FlexAnalysis v3.4 software (Bruker). After mass spectral comparison, statistical analysis revealed shared masses and masses present only in the cell pellet, the culture supernatant, and the organic extract.

2.5 UHPLC-UHR-Q/TOF mass spectrometry

Analyses were performed using an UltiMate 3000 RSLC system (Dionex, Germering, Germany) connected to a maXis ultra-high resolution quadrupole-TOF mass spectrometer (UHR-Q/TOF MS) (Bruker Daltonics, Bremen, Germany) equipped with an electrospray ion source. Metabolites were separated on an Acquity UPLC BEH C18 1.7 µm 2.1 × 100 mm column (Waters, Saint-Quentin-en-Yvelines, France). For the analysis of the organic phase of the extract, the column was heated at 60°C and the following solvents were used at a flow rate of 500 µL/min: H_2O with 0.1% formic acid as solvent A and a mixture of methanol and isopropanol (50:50, v/v) with 0.1% formic acid as solvent B. Gradient elution was set to 0–2.5 min, 3% B; 2.5–4 min, 6% B; 4–13 min, 85% B; 13.5–19.1 min, 100% B; and 19.1–23 min, 3% B. A volume of 2 µL of the organic extract was injected. To analyze the aqueous phase of the extract, the column was heated at 40°C, and the following solvents were used at a flow rate of 500 µL/min: H_2O with 0.1% formic acid as solvent A and acetonitrile with 0.08% formic acid as solvent B. Gradient elution was set to 0–10 min, 3% B; 10–13 min, 45% B; 13–15 min, 100% B; and 15–18 min, 3% B. A volume of 0.5 µL of the aqueous extract was injected. Mass spectra were acquired in positive ion mode at a frequency of 1 Hz in the 50–1,650 *m/z* range. The ESI source parameters were as follows: nebulizing gas, 2 bar; drying gas, 200°C at a flow rate of 9 L/min; capillary voltage, 4,500 V.

2.6 Data analysis and advanced data processing using MetaboScape®

Data processing was performed using DataAnalysis 4.4 software (Bruker Daltonics, Bremen, Germany). Lock mass calibration was performed at *m/z* 622.0296 [hexakis(2,2-difluoroethoxy)phosphazine; CAS #:186817–57-2], and the peaks (*m/z*) were identified based on mass accuracy, isotope patterns, and retention time. The metabolite analysis was based on the translation of the KEGG pathways of *M. sedula* into target molecules. The purified total lipid extract from Elling et al. (2016) was previously used to identify S-bearing quinones in Sulfolobales, and a database containing the theoretical *m/z* of different oxidation forms of sulfulobusquinones (SQ), caldariellaquinones (CQ), and benzodithiophenequinones (BDTQ) was kindly provided by Felix J. Elling (Leibniz-Laboratory for Radiometric Dating and Isotope Research, Christian-Albrecht University of Kiel, Germany). To verify the feasibility of the method for quinone detection, we applied the quinone detection protocol described by Elling et al. (2016), which was initially reproduced for *S. acidocaldarius* and subsequently adapted it to *M. sedula*. The peaks were then integrated, and the area under the curve (AUC) of the corresponding annotated molecules was compared in biological triplicates, with each biological replicate measured in technical triplicates alongside an additional blank. Further advanced data analysis was conducted using MetaboScape 2024b® (Bruker Daltonics, Bremen, Germany) with its embedded T-ReX® feature finder algorithm, which encompasses retention-time alignment, mass calibration, and peak picking. For feature finding, we set an intensity threshold of 10,000 counts, a minimum peak length of six spectra, and enabled the recursive feature-finding tool to achieve high and reliable coverage. For ion deconvolution, $[M + H]^+$ was set as the primary ion and $[M + NH_4]^+$ and $[M + Na]^+$ were set as potential seed ions. Data filtering ensured that only the features present in at least two samples were recognized and extracted. To automatically annotate our target compounds, we defined and uploaded a target list of sulfur-bearing quinones and performed annotation with a mass tolerance of 2 ppm and a maximum mSigma value (isotopic pattern fit) of 40.

3 Results and discussion

3.1 Microbial cultivation of *Metallosphaera sedula* on pyrite

The *M. sedula* cultures were inoculated in a suspension of pyrite in pH 2.0 growth medium supplemented with air and CO_2 in triplicate bioreactors (A, B, C) as described in the methods section. *M. sedula* cultures were harvested before reaching stationary phase (Supplementary Figure S1).

The cell densities from inoculation to harvest were equivalent in all four bioreactors (Table 1).

3.2 Metabolomic profiling of *Metallosphaera sedula* grown on pyrite

To separate the organic molecules from the mineral pyrite material, the Bligh and Dyer protocol (Bligh and Dyer, 1959) modified by Evans et al. (2022) was applied. Evans et al. concluded that the yield

TABLE 1 Cell densities [cells/mL] of $n = 3$ biological replicates (A, B, and C) of *Metallosphaera sedula* grown on pyrite (10 g/L) at inoculation time point ($t = 0$ h) and harvest time points ($t = 140$ h; $t = 312$ h).

Replicate	Cell density [cells/mL]		
	$t = 0$ h	$t = 140$ h	$t = 312$ h
Initial culture	$7.89 \times 10^6 \pm 3.88 \times 10^6$		$3.37 \times 10^7 \pm 2.43 \times 10^6$
A	$4.71 \times 10^6 \pm 2.55 \times 10^5$	$1.14 \times 10^7 \pm 2.78 \times 10^5$	
B	$5.33 \times 10^6 \pm 3.80 \times 10^3$	$1.08 \times 10^7 \pm 2.56 \times 10^4$	
C	$5.15 \times 10^6 \pm 2.91 \times 10^4$	$9.78 \times 10^6 \pm 1.07 \times 10^5$	

of archaeal lipid extraction was higher with trichloroacetic acid solution than with sodium phosphate buffer. Since potassium phosphate buffer has the potential to chelate soluble metal ions better than sodium phosphate buffer, we further improved the modified Bligh and Dyer protocol by using a potassium phosphate buffer solution (KH_2PO_4). In order to cover a wider range of metabolites, we also decided to alternate acidic and alkaline extraction steps. To enrich the lipophilic compounds, a liquid–liquid extraction step was added to the protocol and the analysis of hydrophilic compounds was made possible by a clean-up step of the aqueous fraction. This additional step was particularly necessary for amino acids.

The protocol for the identification of metabolites, from microbial cultivation to compound identification, is presented in the flowchart in Figure 3. The efficiency of compound identification was increased by combining a reference database with MetaboScape®, an advanced data analysis software. This protocol also has the potential for extracting metabolites from other members of the order of Sulfolobales in the presence of mineral substrates. Indeed, the Bligh and Dyer protocol was developed to separate organic material from mineral materials, and has been used for the extraction of organics from deep-sea sediments to microbial mat systems. In the present study, the quantities of solvents used for Bligh and Dyer extraction were selected based on 1 g of pyrite equivalent of sample material. However, the ability of the protocol to extract compounds may be limited by the solubility of different target molecules. This could be circumvented by adapting the solvents chosen for liquid–liquid extraction.

3.2.1 Distinguishing between metabolites and exometabolites via profiling using MALDI-TOF mass spectrometry

Comparative analysis of the culture supernatant, cell pellet, and organic extract by MALDI-TOF MS can help differentiate between metabolites in the cell and those released into the culture medium, i.e., between metabolites and exometabolites. MALDI-TOF MS analysis is relatively fast to implement and was used as a preliminary step to evaluate the presence of compounds in these fractions. To obtain initial metabolomics data on mineral-adapted *M. sedula*, the microorganism was grown in a 4.5 L bioreactor over a timespan of 312 h. The culture was harvested after reaching the stationary phase under the previously described cultivation and extraction conditions. Comparative analysis using MALDI-TOF MS of culture supernatant, cell pellet, and organic extract revealed 116 measured *m/z* across all biological samples (Supplementary Table S1). 20 compounds were found only in the culture supernatant, 16 in the cell pellet analysis, 19 in the culture supernatant and cell pellet analysis, and 61 were found only in the organic extract. A metabolite screening allowed for the annotation of 13 compounds (Table 2). These annotations were confirmed by UHPLC-UHR-Q/TOF MS analysis. However, the compound lists obtained by MALDI-TOF MS in this initial experiment represent a restricted dataset due to limited sensitivity and dynamic range, which are attributed to competition with the HCCA matrix and the absence of prior HPLC separation. To explore the sample more in depth and gain a more comprehensive and coherent view of the *M. sedula* metabolome, an LC-ESI-based analysis was conducted using the same extraction protocol.

3.2.2 UHPLC-UHR-Q/TOF mass spectrometry

Data annotation and treatment for compound identification for metabolomic profiling was conducted using the DataAnalysis software. For the identification of thiophene-bearing quinone, the advanced data analysis software MetaboScape® was used for molecular assignment. Metabolite analysis by UHPLC-UHR-Q/TOF MS of organic and aqueous fractions of the extracts revealed 48 metabolites (Supplementary Table S2). Based on the results obtained, the

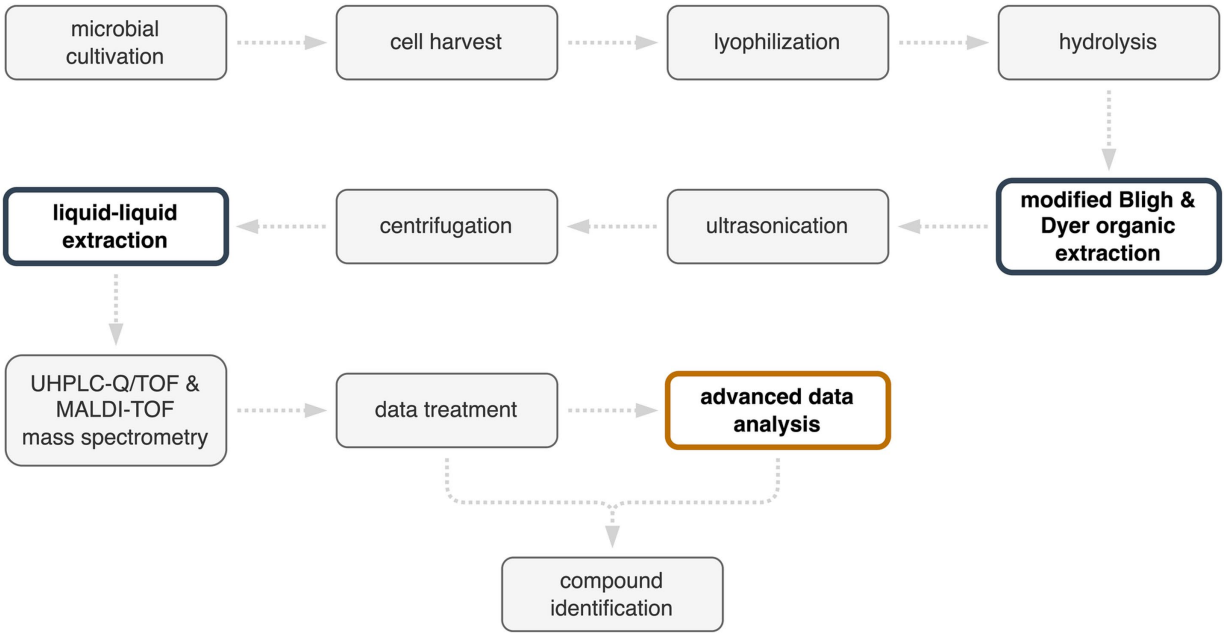

FIGURE 3
Protocol for the identification of *Metallosphaera sedula* metabolites from cells cultivated in a pyrite suspension medium. Improvements in the protocol are highlighted in color.

TABLE 2 Comparative analysis of intra- and extracellular metabolites by MALDI-TOF MS.

Biological sample	Measured compounds	Annotated compounds	Compound annotation
Culture supernatant	20	1	Leucylvaline
Cell pellet	16	0	
Culture supernatant and cell pellet	19	0	
Organic extract	61	12	Gln, Lys, Trp, Pyl, ribose, 2-deoxy-D-ribose, 2-deoxy-D-glucose, hexose, D-glucosamine/galactosamine, phosphoenolpyruvate, 2-dehydro-3-deoxy-6-phospho-D-gluconate, 2-keto-3-deoxygluconate, decylubiquinol

metabolites identified through ESI-based analysis were grouped into structural and functional categories (Figure 4).

Structurally (Figure 4A), the highest number of metabolites was found in the amino acid group, with a total number of 19, followed by 11 carbohydrates, 2 keto acids, 2 lactones, 1 monocarboxylic acid, 1 pterin, 1 dipeptide, 1 aldehyde, 1 modified amino acid, and 9 quinones. However, as the medium contains 0.1% tryptone containing 18 amino acids (Ala, Arg, Asp., Cys, Glu, Gln, His, Leu/Ile, Lys, Met, Phe, Pro, Ser, Thr, Trp, Tyr, and Val), of the identified amino acids in this study, only Asn and Pyl of can be unambiguously ascribed to the contribution of *M. sedula*.

The metabolites were also grouped into functional categories (Figure 4B; Table 3). Their biological functions span from energetic metabolism, anabolism/catabolism, to biofilm formation, cell–cell interactions, and metal complexation.

The modified lipid extraction protocol applied in our study allowed us to identify a wide variety of metabolites and proved to be suitable for separating organics from the mineral material. The dataset also suggested the biological processes underlying these metabolites (Table 3).

Among the metabolites involved in carbon metabolism, the associated metabolites D-glyceraldehyde-3-phosphate, 2-dehydro-3-deoxy-6-phospho-D-gluconate, phosphoenolpyruvate, D-glucosamine/galactosamine, D-glucuronic/galacturonic acid, ribose, 2-deoxy-D-ribose, and 2-deoxy-D-glucose are generally involved in core carbon metabolism and carbohydrate degradation (Fisher, 2001; Bräsen et al., 2014). In contrast, 1,3-bisphosphoglycerate is involved in gluconeogenesis (Siebers and Schönheit, 2005). Since no glucose was added during cultivation, the only identifiable source for glucose-related metabolism might be remnants of glycerol. To store *M. sedula* cultures, we used a mixture of 50% glycerol and DSMZ 88 medium. When inoculated, the residual glycerol could potentially be used by *M. sedula*. Glycerol degradation has been described in halophilic Archaea (Williams et al., 2017) and further proposed in *Sulfolobus acidocaldarius* by Schmerling et al. (2024). Additionally, D-glyceraldehyde-3-phosphate is released in the final step of tryptophan biosynthesis (Tang et al., 2000) and serves as the initial precursor of thiamine biosynthesis (Zaparty et al., 2010).

Archaea in the order Sulfolobales are known for using a modified Entner-Doudoroff (ED) pathway for glucose metabolism. Specifically, utilizing D-gluconate/galactonate, 2-keto-3-deoxygluconate and 2-keto-3-deoxy-6-phosphogluconate, as previously reported for *S. solfataricus*, *S. acidocaldarius* and *Metallosphaera* spp. (Lamble et al., 2003; Nunn et al., 2010; Kim and Lee, 2006; Wang et al., 2020). In hyperthermophilic Archaea, non-, branched-, and semi-phosphorylative ED modifications have been identified (De Rosa et al., 1984; Budgen and Danson, 1986; Selig et al., 1997; Siebers and Schönheit, 2005; Reher and Schönheit, 2006; Sutter et al., 2016). While 2-keto-3-deoxygluconate is used as an intermediate in all three ED pathways, 2-keto-3-deoxy-6-phosphogluconate is involved only in branched and semi-phosphorylative ED (Siebers and Schönheit, 2005; Sutter et al., 2016). However, *S. solfataricus* from the order Sulfolobales utilizes a branched ED pathway (Ahmed et al., 2005). This is congruent with our findings for *M. sedula*, which shares the same order (Sulfolobales) and highlights the usage of unusual sugar degradation pathways in Archaea.

Among sulfur metabolism-related compounds, decylubiquinol is produced from decylubiquinone by enzymes expressed from the sulfur reduction gene cluster (DoxD) (Kletzin et al., 2004; Müller et al., 2004; Auernik and Kelly, 2008), whereas MoCo II is associated with sulfite:acceptor oxidoreductase (SAOR) in *Metallosphaera* spp. (Liu et al., 2014, 2021).

In terms of microbial interactions, cell surface interactions require direct contact resulting in biofilm formation (Lewis et al., 2023). This is mediated by carbohydrates, including hexose, N-acetyl-D-glucosamine/galactosamine, and N-acetylmuramic acid (Koerdt et al., 2010, 2012). Cell–cell interactions, such as quorum sensing, do not require direct cell contact, but relay on messenger molecules (Charlesworth et al., 2020; Prescott and Decho, 2020). We detected N-(3-oxohexanoyl)-L-homoserine lactone, and its indicative lactone ring, as evidence of acyl-homoserine lactone (AHL) quorum sensing, which were characterized in *S. solfataricus* and *S. islandicus* (Ng et al., 2011; Hiblot et al., 2012). Few examples of quorum sensing have been reported only in halophilic and methanogenic Archaea so far (Tommonaro et al., 2012; Zhang et al., 2012).

Of all the identified metabolites, a subgroup can be seen to support the adaptation of *M. sedula* to extreme environments. Two of the detected amino acids, histidine and methionine, have been shown to be involved in tolerance and resistance to copper toxicity in *M. sedula* (Auernik and Kelly, 2008). Leucylvaline can support the growth of *S. islandicus*, promoting its adaptation to extreme and fluctuating environmental conditions in volcanic hot spring habitats (Weitzel et al., 2020). Furthermore, S-adenosylmethionine, a cofactor of methyl transferases, was detected in *M. sedula* in this study. This cofactor was also found in *S. solfataricus* (Cacciapuoti et al., 1996) and *S. acidocaldarius* (Zeng et al., 2018). In extremophiles, S-adenosylmethionine may assist in protein methylation, leading to a higher resistance to aggregation and denaturation at physiological pH

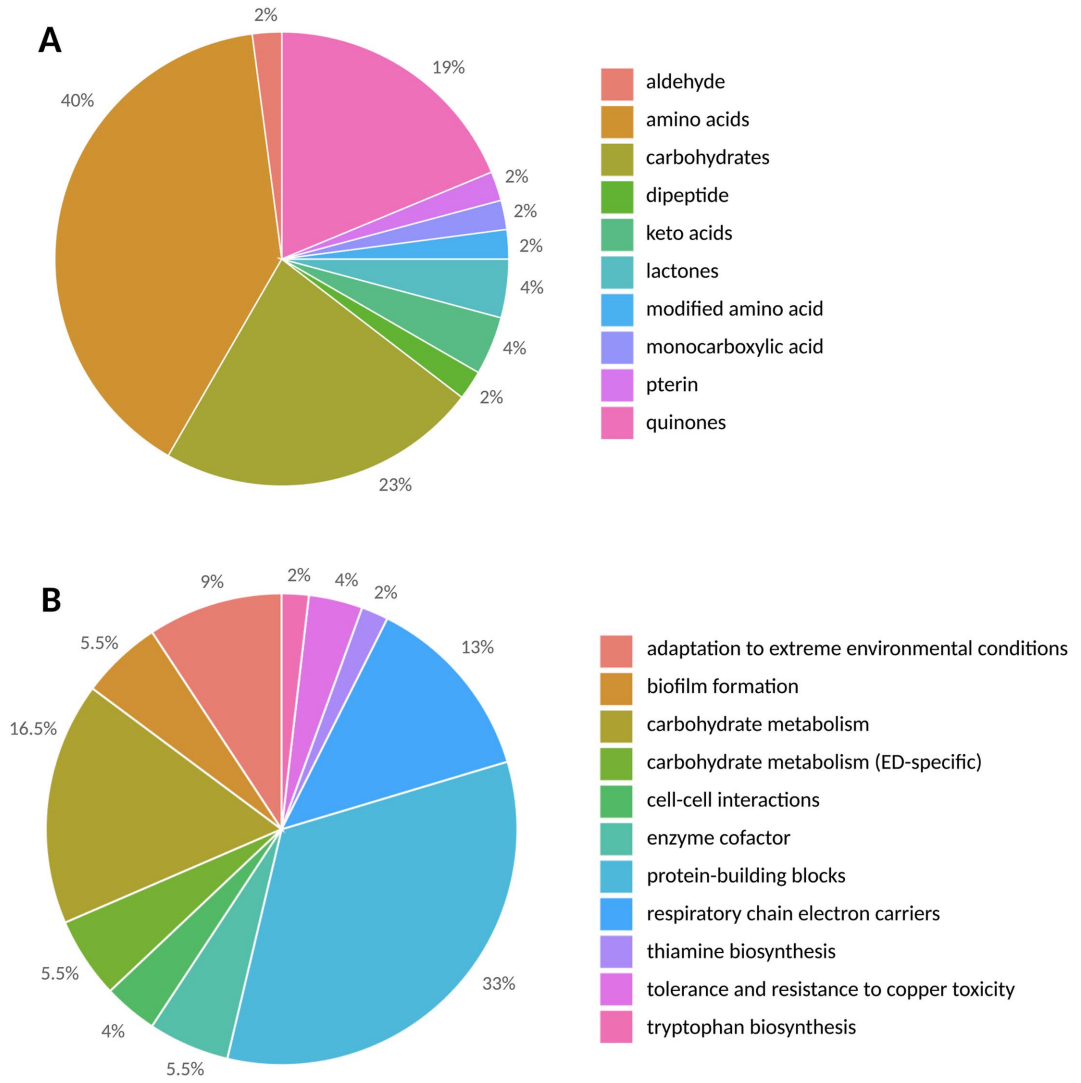

FIGURE 4
The structural **(A)** and functional **(B)** categories of metabolites in *Metallosphaera sedula* triplicates are represented by the number of detected metabolites.

compared to the unmethylated form, and increasing the stability of proteins in high-temperature environments, as shown for *S. solfataricus* (Febbraio et al., 2004).

8-amino-7-oxononanoic acid was downregulated in acid stress tolerance experiments with the bioleaching microorganism *Acidithiobacillus caldus*. It was proposed that *A. caldus* utilizes acid resistance mechanisms via the formation of extracellular polymeric substances and biofilm formation (Feng et al., 2021). The detected N-glycan building blocks, N-acetyl-D-glucosamine/galactosamine and N-acetylmuramic acid, play different roles in Sulfolobales, as they interact with the environment while maintaining cell shape and supporting cell protection under extreme environmental conditions (Jarrell et al., 2014; Palmieri et al., 2013; Van Wolferen et al., 2020).

Different members of the Sulfolobales order have different compositions in saturated quinones in response to their redox environment. Consequently, the quinone distribution of a given member of the Sulfolobales order can be used to reconstruct environmental redox conditions (Brassell et al., 1986; Hiraishi, 1999; Elling et al., 2016; Becker et al., 2018). Therefore, we focused on the composition of the respiratory chain electron carriers in *M. sedula* and the degree of saturation of quinones as an indicative microbial fingerprint.

3.2.3 Focus on thiophene-bearing quinones

The respiratory chain electron carriers were investigated in more detail in terms of their oxidation states (Table 4). To this end, a mass list containing all possible oxidation states of caldariellaquinones, sulfolobusquinones, and benzodithiophenequinones and their corresponding *m/z* values was created, and molecular assignment was performed using the advanced data analysis software MetaboScape®. The main features for molecular assignment were as follows: assign the corresponding *m/z* values within the dataset (over an intensity threshold of 10,000 counts, minimum peak length of six spectra, and distinct isotopic pattern fit) to the molecules defined in the quinone mass list only when they are present in two separate samples.

10.3389/fmicb.2024.1473270

TABLE 3 Grouping of metabolites identified in the present study into functional categories.

Metabolite	Compound class	Functional category
Arg, Asn, Asp., Cys, Glu, Gln, His, Ile/Leu, Lys, Met, Phe, Pro, Ser, Thr, Trp, Tyr, Val, Pyl	Amino acid	Protein-building blocks
His, Met	Amino acid	Tolerance and resistance to copper toxicity
leucylvaline, 8-amino-7-oxononanoic acid, N-acetyl-D-glucosamine/galactosamine*, N-acetylmuramic acid, S-adenosylmethionine	Dipeptide, amino acid, carbohydrate, modified amino acid	Adaptation to extreme environmental conditions
D-glyceraldehyde-3-phosphate, 2-dehydro-3-deoxy-6-phospho-D-gluconate, phosphoenolpyruvate, 1,3-bisphosphoglycerate, D-glucosamine/galactosamine, D-glucuronic/galacturonic acid, ribose, 2-deoxy-D-ribose, 2-deoxy-D-glucose	Aldehyde, monocarboxylic acid, carbohydrate	Carbohydrate metabolism
D-gluconate/galactonate, 2-keto-3-deoxygluconate, 2-keto-3-deoxy-6-phosphogluconate	Keto acid	Carbohydrate metabolism (ed-specific)
D-glyceraldehyde-3-phosphate	Aldehyde	Tryptophan and thiamine biosynthesis
N-(3-oxohexanoyl)-L-homoserine lactone, lactone	Lactone	Cell–cell interactions
hexose, N-acetyl-D-glucosamine/galactosamine*, N-acetylmuramic acid	Carbohydrate	Biofilm formation
MoCo II, decylubiquinone, decylubiquinol	Pterin, quinone	Enzyme cofactor
$CQ_{4:1}$, $CQ_{5:1}$, $SQ_{4:0}$, $SQ_{4:1}$, $SQ_{5:0}$, $SQ_{5:1}$, $BDTQ_{5:0}$	Quinone	Respiratory chain electron carriers

*Identified as N-acetyl-hexosamine.

Thiophene-bearing quinones of *M. sedula* (Table 4) were analyzed and identified in the form of oxidized caldariellaquinones ($CQ_{4:1}$ and $CQ_{5:1}$), sulfolobusquinones ($SQ_{4:0}$, $SQ_{4:1}$, $SQ_{5:0}$, and $SQ_{5:1}$), and benzodithiophenequinones ($BDTQ_{5:0}$). Caldariellaquinones were first described by De Rosa et al. (1977) and adapted by organisms thriving in extreme environments (pH 1.4–2.6; 75–89°C) with a corresponding durable membrane structure found in *Sulfolobus* and *Acidianus* spp. (De Rosa and Gambacorta, 1988). Subsequently, caldariellaquinones have been reported in *S. solfataricus*, and later in *M. sedula* (De Rosa et al., 1983a, 1983b; Lanzotti et al., 1986; Huber et al., 1989), while benzodithiophenequinones have been identified in *S. solfataricus*

TABLE 4 Analytical parameters used for identification of caldariellaquinones (CQ), sulfolobusquinones (SQ), and benzodithiophenequinones (BDTQ) were identified using Metaboscape®.

RT [min]	Observed *m/z*	Theoretical *m/z*	Ions	Observed M	Δ*m/z* [mDa]	Δ*m/z* [ppm]	mSigma	Average integrated peak area	[%]	Molecular formula	Identified compounds
8.91	581.34476	581.34574	$[M + Na]^+$	558.35554	−0.98	−1.685	45.4	36,712	6.9	$C_{34}H_{54}O_2S_2$	$CQ_{5:1}$
10.84	511.26727	511.26749	$[M + Na]^+$	488.27805	−0.22	−0.433	55.2	13,773	2.6	$C_{29}H_{44}O_2S_2$	$CQ_{4:1}$
14.07	459.32844	459.32913	$[M + H]^+$	458.32116	−0.69	−1.505	33.3	14,299	2.7	$C_{29}H_{46}O_2S$	$SQ_{4:0}$
15.10	457.31365	457.31348	$[M + H]^+$	456.30637	0.17	0.377	34.5	357,336	66.7	$C_{29}H_{44}O_2S$	$SQ_{4:1}$
15.41	529.40689	529.40738	$[M + H]^+$	528.39961	−0.49	−0.927	43.8	47,033	8.8	$C_{34}H_{56}O_2S$	$SQ_{5:0}$
15.96	527.39113	527.39173	$[M + H]^+$	526.38385	−0.60	−1.133	53.4	29,716	5.5	$C_{34}H_{54}O_2S$	$SQ_{5:1}$
15.93	543.33195	543.33250	$[M + H]^+$	542.32467	−0.55	−1.014	58.4	36,571	6.8	$C_{33}H_{50}O_2S_2$	$BDTQ_{5:0}$

The mSigma corresponds to the isotopic pattern fit of the software.

(Collins and Langworthy, 1983; Trincone et al., 1986, 1992; Lanzotti et al., 1986). Variations among the produced CQ, SQ, and BDTG molecules are correlated with the presence of oxygen during growth (Trincone et al., 1989; Nicolaus et al., 1992). For the order of Sulfolobales, Elling et al. (2016) showed a distribution of $CQ_{6:0}$ (86.1%), $CQ_{6:1}$ (12.2%) for *S. acidocaldarius*, $CQ_{6:0}$ (85.8%), $CQ_{6:1}$ (13.7%) for *S. solfataricus*, and $SQ_{6:0}$ (42.9%), $CQ_{6:0}$ (36.4%), and $CQ_{6:1}$ (14.6%) for *S. islandicus* as major quinone components, with traces of $BDTQ_{6:0}$ (0.4%) only found in *S. islandicus*. An average semiquantitative distribution among the biological triplicates based on integrated peak area showed percentages of $SQ_{4:0}$ (2.7), $SQ_{4:1}$ (66.7), $SQ_{5:0}$ (8.8), $SQ_{5:1}$ (5.5), $CQ_{4:1}$ (2.6), $CQ_{5:1}$ (6.9), and $BDTQ_{5:0}$ (6.8). Our findings present a shift from CQ to SQ, with $SQ_{4:1}$ being the most abundant, as the preferred quinone with traces of BDTQ. For all three quinones, the detection limit was <2 ppm. These quinones differ in the primary ions detected, i.e., H^+ for SQ and BDTQ, and Na^+ for CQ. Comparing the identified CQs with the SQs, the retention time was reversed: $SQ_{5:1} > SQ_{4:1}$ but $CQ_{5:1} < CQ_{4:1}$. However, the relative proportions of quinones differ between Sulfolobales species. Therefore, adaptations to environmental conditions may be reflected in SQs, CQs, and BDTQs distributions (Elling et al., 2016). Profiling quinones may enable monitoring of shifts in microbial communities from oxic to anoxic conditions and allow archaeal diversity to be characterized, complementing membrane lipid- and gene-based approaches (Brassell et al., 1986; Hiraishi, 1999; Elling et al., 2016; Becker et al., 2018). Furthermore, thiophene-bearing quinones have been proposed to have potential as biomarker for astrobiological life detection owing to their durability and stability over geological timescales (Eigenbrode et al., 2018; Heinz and Schulze-Makuch, 2020; Geisberger et al., 2021). The mass spectrometry-based analysis conducted in our study confirm that it is possible to detect them in *M. sedula* grown on mineral materials.

3.3 Perspectives on environmental metabolomics

In this study, we provided a protocol for the analysis of metabolites from one species of Archaea grown on mineral materials in a laboratory setting. Metabolomics-based technologies have been shown to be useful to monitor biological responses in environmental studies (for examples, see Sardans et al., 2011; Chandran et al., 2020). To set the stage for environmental field studies of chemolithotrophic extremophiles where multiple species and minerals are present, one could perform experiments as an intermediate step, such as monitoring different species, or varying mineral substrates.

Moreover, acidophilic, chemolithotrophic, iron- and sulfur-oxidizing microorganisms are major players in biomining processes and can be used to recover various metals from copper-, uranium-, and gold-bearing minerals and mineral concentrates (Rawlings, 2002, 2005). As the metal recovery rate of biomining is directly linked to the microbial communities involved, multi-omics approaches could be applied to explore microbial diversity, metabolic characteristics, and resistance mechanisms in extreme environments. This way, the corresponding genes, enzymes, metabolites, and active metabolic pathways can be identified (Li and Wen, 2021). With our protocol, it was possible to identify metabolites and draw hypotheses about the metabolic pathways they are involved in, which could at some point lead to similar characterization for microorganisms with the potential for biomining operations.

4 Conclusion

To overcome the challenges associated with the extraction of microbial organic molecules from mineral materials, an improved extraction protocol has been devised and applied. By implementing a metabolomic approach, an overview of the metabolome of the iron- and sulfur-oxidizing archaeon *M. sedula* was proposed. We successfully identified key metabolites of *M. sedula* and ascribed them to their metabolic pathways. We detected molecules indicative of cell surface interactions involved in biofilm formation and acyl-homoserine lactone (AHL) quorum sensing signaling molecules involved in cell–cell communication. Moreover, we successfully analyzed and identified different saturated thiophene-bearing quinones in *M. sedula*. These metabolites are stable, resistant, and preservable biomarker under extreme conditions and can be preserved and extracted in many extreme environmental scenarios. The efficiency of this protocol may be limited by the differences in the solubility of the target molecules. This could be circumvented by adapting the solvents chosen for liquid–liquid extraction. The present study further demonstrates the possibility of extracting metabolites from metallophilic Archaea, paving the way for metabolomics or even multi-omics investigations of microbe-mineral interactions in a number of biotechnological, environmental, and astrobiological applications.

Data availability statement

The original contributions presented in the study are included in the article/Supplementary material, further inquiries can be directed to the corresponding author/s.

Author contributions

SG: Conceptualization, Data curation, Formal analysis, Investigation, Methodology, Visualization, Writing – original draft, Writing – review & editing. CC: Conceptualization, Data curation, Formal analysis, Investigation, Methodology, Resources, Software, Validation, Writing – review & editing. GG: Conceptualization, Data curation, Formal analysis, Investigation, Methodology, Resources, Software, Validation, Writing – review & editing. JG: Data curation, Formal analysis, Investigation, Software, Writing – review & editing. MC: Formal analysis, Investigation, Methodology, Resources, Validation, Writing – review & editing. TM: Conceptualization, Formal analysis, Funding acquisition, Investigation, Project administration, Resources, Supervision, Validation, Visualization, Writing – original draft, Writing – review & editing.

Funding

The author(s) declare that financial support was received for the research, authorship, and/or publication of this article. This

research was funded under the European Union's Horizon 2020 Framework Programme, grant number ERC-2020-COG, Project 101001311 – BIOMAMA and the French National Research Agency (ANR, CPJ n°ANR-22-CPJ1-0066-01) to TM. We thank the Région Centre Val de Loire (SyMBioMS and Malditof grants) and the European FEDER funds (grants nos. 2699–33931 and 2017-EX002979) for supporting MS instruments to MC, and the SALSA and MO2VING platforms. Furthermore, we acknowledge the use of MetaboScape, supported by Germany's Excellence Strategy (EXC-2077) project 390741603 'The Ocean Floor – Earth's Uncharted Interface'.

Acknowledgments

We would like to thank former members of the Exobiology Group at the Center for Molecular Biophysics, Orleans, France, Denise Kölbl and Sebastien Maimbourg for their assistance in the cultivation of *Metallosphaera sedula* and Rebeca Lopez Adams for her supportive analyses. We also sincerely thank Felix J. Elling (Leibniz-Laboratory for Radiometric Dating and Isotope Research, Christian-Albrecht University of Kiel, Kiel, Germany) for the total lipid extract of *Sulfolobus acidocaldarius* and the theoretical quinone *m/z* database provided.

Conflict of interest

The authors declare that the research was conducted in the absence of any commercial or financial relationships that could be construed as a potential conflict of interest.

The author(s) declared that they were an editorial board member of Frontiers, at the time of submission. This had no impact on the peer review process and the final decision.

Publisher's note

Supplementary material

The Supplementary material for this article can be found online at: https://www.frontiersin.org/articles/10.3389/fmicb.2024.1473270/full#supplementary-material

References

Abrahamsson, V., and Kanik, I. (2022). In situ organic biosignature detection techniques for space applications. *Front. Astron. Space Sci.* 9:959670. doi: 10.3389/fspas.2022.959670

Ahmed, H., Ettema, T. J. G., Tjaden, B., Geerling, A. C. M., van der Oost, J., and Siebers, B. (2005). The semi-phosphorylative Entner–Doudoroff pathway in hyperthermophilic archaea: a re-evaluation. *Biochem. J.* 390, 529–540. doi: 10.1042/BJ20041711

Amend, J. P., and Shock, E. L. (2001). Energetics of overall metabolic reactions of thermophilic and hyperthermophilic Archaea and Bacteria. *FEMS Microbiol. Rev.* 25, 175–243. doi: 10.1111/j.1574-6976.2001.tb00576.x

Auernik, K. S., and Kelly, R. M. (2008). Identification of components of Electron transport chains in the extremely Thermoacidophilic Crenarchaeon *Metallosphaera sedula* through Iron and sulfur compound oxidation transcriptomes. *Appl. Environ. Microbiol.* 74, 7723–7732. doi: 10.1128/AEM.01545-08

Auernik, K. S., and Kelly, R. M. (2010a). Impact of molecular hydrogen on chalcopyrite bioleaching by the extremely Thermoacidophilic archaeon *Metallosphaera sedula*. *Appl. Environ. Microbiol.* 76, 2668–2672. doi: 10.1128/AEM.02016-09

Auernik, K. S., and Kelly, R. M. (2010b). Physiological versatility of the extremely Thermoacidophilic archaeon *Metallosphaera sedula* supported by transcriptomic analysis of heterotrophic, autotrophic, and Mixotrophic growth. *Appl. Environ. Microbiol.* 76, 931–935. doi: 10.1128/AEM.01336-09

Auernik, K. S., Maezato, Y., Blum, P. H., and Kelly, R. M. (2008). The genome sequence of the metal-mobilizing, extremely Thermoacidophilic archaeon *Metallosphaera sedula* provides insights into bioleaching-associated metabolism. *Appl. Environ. Microbiol.* 74, 682–692. doi: 10.1128/AEM.02019-07

Becker, K. W., Elling, F. J., Schröder, J. M., Lipp, J. S., Goldhammer, T., Zabel, M., et al. (2018). Isoprenoid Quinones resolve the stratification of redox processes in a biogeochemical continuum from the photic zone to deep anoxic sediments of the Black Sea. *Appl. Environ. Microbiol.* 84, e02736–e02717. doi: 10.1128/AEM.02736-17

Bell, M. A., McKim, U., Sproule, A., Tobalt, R., Gregorich, E., and Overy, D. P. (2022). Extraction methods for untargeted metabolomics influence enzymatic activity in diverse soils. *Sci. Total Environ.* 828:154433. doi: 10.1016/j.scitotenv.2022.154433

Bellenberg, S., Díaz, M., Noël, N., Sand, W., Poetsch, A., Guiliani, N., et al. (2014). Biofilm formation, communication and interactions of leaching bacteria during colonization of pyrite and sulfur surfaces. *Res. Microbiol.* 165, 773–781. doi: 10.1016/j.resmic.2014.08.006

Blazevic, A., Albu, M., Mitsche, S., Rittmann, S. K.-M. R., Habler, G., and Milojevic, T. (2019). Biotransformation of Scheelite CaWO4 by the extreme Thermoacidophile *Metallosphaera sedula*: tungsten–microbial Interface. *Front. Microbiol.* 10:1492. doi: 10.3389/fmicb.2019.01492

Bligh, E. G., and Dyer, W. J. (1959). A rapid method of total lipid extraction and purification. *Can. J. Biochem. Physiol.* 37, 911–917. doi: 10.1139/o59-099

Bräsen, C., Esser, D., Rauch, B., and Siebers, B. (2014). Carbohydrate metabolism in Archaea: current insights into unusual enzymes and pathways and their regulation. *Microbiol. Mol. Biol. Rev.* 78, 89–175. doi: 10.1128/MMBR.00041-13

Brassell, S. C., Lewis, C. A., De Leeuw, J. W., De Lange, F., and Damsté, J. S. S. (1986). Isoprenoid thiophenes: novel products of sediment diagenesis? *Nature* 320, 160–162. doi: 10.1038/320160a0

Bromfield, L., Africa, C.-J., Harrison, S. T. L., and Van Hille, R. P. (2011). The effect of temperature and culture history on the attachment of *Metallosphaera hakonensis* to mineral sulfides with application to heap bioleaching. *Miner. Eng.* 24, 1157–1165. doi: 10.1016/j.mineng.2011.03.019

Budgen, N., and Danson, M. J. (1986). Metabolism of glucose via a modified entner-doudoroff pathway in the thermoacidophilic Archaebacterium*thermoplasma acidophilum*. *FEBS Lett.* 196, 207–210. doi: 10.1016/0014-5793(86)80247-2

Cacciapuoti, G., Porcelli, M., Bertoldo, C., Fusco, S., De Rosa, M., and Zappia, V. (1996). Extremely thermophilic and thermostable 5′-Methylthioadenosine phosphorylase from the archaeon *Sulfolobus solfataricus*: gene cloning and amino acid sequence determination. *Eur. J. Biochem.* 239, 632–637. doi: 10.1111/j.1432-1033.1996.0632u.x

Camprubi, E., Jordan, S. F., Vasiliadou, R., and Lane, N. (2017). Iron catalysis at the origin of life. *IUBMB Life* 69, 373–381. doi: 10.1002/iub.1632

Chandran, H., Meena, M., and Sharma, K. (2020). Microbial biodiversity and bioremediation assessment through omics approaches. *Front. Environ. Chem.* 1:570326. doi: 10.3389/fenvc.2020.570326

Charlesworth, J., Kimyon, O., Manefield, M., Beloe, C. J., and Burns, B. P. (2020). Archaea join the conversation: detection of AHL-like activity across a range of archaeal isolates. *FEMS Microbiol. Lett.* 367:fnaa123. doi: 10.1093/femsle/fnaa123

Clark, T. R., Baldi, F., and Olson, G. J. (1993). Coal Depyritization by the thermophilic archaeon *Metallosphaera sedula*. *Appl. Environ. Microbiol.* 59, 2375–2379. doi: 10.1128/aem.59.8.2375-2379.1993

Collins, M. D., and Langworthy, T. A. (1983). Respiratory Quinone composition of some acidophilic Bacteria. *Syst. Appl. Microbiol.* 4, 295–304. doi: 10.1016/S0723-2020(83)80016-2

Counts, J. A., Vitko, N. P., and Kelly, R. M. (2022). Fox cluster determinants for iron biooxidation in the extremely thermoacidophilic *Sulfolobaceae*. *Environ. Microbiol.* 24, 850–865. doi: 10.1111/1462-2920.15727

Das, S., and Dash, H. R. (2014). Microbial Bioremediation. *Microb. Biodegrad. Bioremed.*, 1–21. doi: 10.1016/B978-0-12-800021-2.00001-7

De Rosa, M., De Rosa, S., Gambacorta, A., Minale, L., Thomson, R. H., and Worthington, R. D. (1977). Caldariellaquinone, a unique benzo[b]thiophen-4,7-quinone from *Caldariella acidophila*, an extremely thermophilic and acidophilic bacterium. *J. Chem. Soc. Perkin Trans.* 1:653. doi: 10.1039/p19770000653

De Rosa, M., and Gambacorta, A. (1988). The lipids of archaebacteria. *Prog. Lipid Res.* 27, 153–175. doi: 10.1016/0163-7827(88)90011-2

De Rosa, M., Gambacorta, A., and Nicolaus, B. (1983a). A new type of cell membrane, in thermophilic archaebacteria, based on bipolar ether lipids. *J. Membr. Sci.* 16, 287–294. doi: 10.1016/S0376-7388(00)81316-2

De Rosa, M., Gambacorta, A., Nicolaus, B., Chappe, B., and Albrecht, P. (1983b). Isoprenoid ethers; backbone of complex lipids of the archaebacterium *Sulfolobus solfataricus*. Biochimica et Biophysica Acta (BBA) - lipids and lipid. *Metabolism* 753, 249–256. doi: 10.1016/0005-2760(83)90014-0

De Rosa, M., Gambacorta, A., Nicolaus, B., Giardina, P., Poerio, E., and Buonocore, V. (1984). Glucose metabolism in the extreme thermoacidophilic archaebacterium *Sulfolobus solfataricus*. *Biochem. J.* 224, 407–414. doi: 10.1042/bj2240407

Direito, S. O. L., Marees, A., and Röling, W. F. M. (2012). Sensitive life detection strategies for low-biomass environments: optimizing extraction of nucleic acids adsorbing to terrestrial and Mars analogue minerals. *FEMS Microbiol. Ecol.* 81, 111–123. doi: 10.1111/j.1574-6941.2012.01325.x

Dopson, M., Baker-Austin, C., Koppineedi, P. R., and Bond, P. L. (2003). Growth in sulfidic mineral environments: metal resistance mechanisms in acidophilic micro-organisms. *Microbiology* 149, 1959–1970. doi: 10.1099/mic.0.26296-0

Eigenbrode, J. L., Summons, R. E., Steele, A., Freissinet, C., Millan, M., Navarro-González, R., et al. (2018). Organic matter preserved in 3-billion-year-old mudstones at Gale crater, Mars. *Science* 360, 1096–1101. doi: 10.1126/science.aas9185

Elling, F. J., Becker, K. W., Könneke, M., Schröder, J. M., Kellermann, M. Y., Thomm, M., et al. (2016). Respiratory quinones in *Archaea*: phylogenetic distribution and application as biomarkers in the marine environment. *Environ. Microbiol.* 18, 692–707. doi: 10.1111/1462-2920.13086

Evans, T. W., Elling, F. J., Li, Y., Pearson, A., and Summons, R. E. (2022). A new and improved protocol for extraction of intact polar membrane lipids from archaea. *Org. Geochem.* 165:104353. doi: 10.1016/j.orggeochem.2021.104353

Febbraio, F., Andolfo, A., Tanfani, F., Briante, R., Gentile, F., Formisano, S., et al. (2004). Thermal stability and aggregation of *Sulfolobus solfataricus* β-glycosidase are dependent upon the N-∈−methylation of specific Lysyl residues. *J. Biol. Chem.* 279, 10185–10194. doi: 10.1074/jbc.M308520200

Feng, S., Qiu, Y., Huang, Z., Yin, Y., Zhang, H., Zhu, D., et al. (2021). The adaptation mechanisms of *Acidithiobacillus caldus* CCTCC M 2018054 to extreme acid stress: bioleaching performance, physiology, and transcriptomics. *Environ. Res.* 199:111341. doi: 10.1016/j.envres.2021.111341

Fisher, M. (2001). Lehninger principles of biochemistry. *Chem. Educ.* 6, 69–70. doi: 10.1007/s00897000455a

Geisberger, T., Sobotta, J., Eisenreich, W., and Huber, C. (2021). Formation of Thiophene under simulated volcanic hydrothermal conditions on earth—implications for early life on extraterrestrial planets? *Life* 11:149. doi: 10.3390/life11020149

Giebel, R., Worden, C., Rust, S. M., Kleinheinz, G. T., Robbins, M., and Sandrin, T. R. (2010). Microbial fingerprinting using matrix-assisted laser desorption ionization time-of-flight mass spectrometry (MALDI-TOF MS). *Adv. Appl. Microbiol.* 71, 149–184. doi: 10.1016/S0065-2164(10)71006-6

Heinz, J., and Schulze-Makuch, D. (2020). Thiophenes on Mars: biotic or abiotic origin? *Astrobiology* 20, 552–561. doi: 10.1089/ast.2019.2139

Hiblot, J., Gotthard, G., Chabriere, E., and Elias, M. (2012). Structural and enzymatic characterization of the lactonase SisLac from *Sulfolobus islandicus*. *PLoS One* 7:e47028. doi: 10.1371/journal.pone.0047028

Hiraishi, A. (1999). Isoprenoid quinones as biomarkers of microbial populations in the environment. *J. Biosci. Bioeng.* 88, 449–460. doi: 10.1016/S1389-1723(00)87658-6

Huber, G., Spinnler, C., Gambacorta, A., and Stetter, K. O. (1989). *Metallosphaera sedula* gen, and sp. nov. represents a new genus of aerobic, metal-mobilizing, Thermoacidophilic Archaebacteria. *Syst. Appl. Microbiol.* 12, 38–47. doi: 10.1016/S0723-2020(89)80038-4

Jarrell, K. F., Ding, Y., Meyer, B. H., Albers, S.-V., Kaminski, L., and Eichler, J. (2014). N-linked glycosylation in Archaea: a structural, functional, and genetic analysis. *Microbiol. Mol. Biol. Rev.* 78, 304–341. doi: 10.1128/MMBR.00052-13

Kaur, A., Capalash, N., and Sharma, P. (2018). Quorum sensing in thermophiles: prevalence of autoinducer-2 system. *BMC Microbiol.* 18:62. doi: 10.1186/s12866-018-1204-x

Kim, S., and Lee, S. B. (2006). Characterization of *Sulfolobus solfataricus* 2-Keto-3-deoxy-*D*-gluconate kinase in the modified Entner-Doudoroff pathway. *Biosci. Biotechnol. Biochem.* 70, 1308–1316. doi: 10.1271/bbb.50566

Kinzler, K., Gehrke, T., Telegdi, J., and Sand, W. (2003). Bioleaching—a result of interfacial processes caused by extracellular polymeric substances (EPS). *Hydrometallurgy* 71, 83–88. doi: 10.1016/S0304-386X(03)00176-2

Kletzin, A., Urich, T., Müller, F., Bandeiras, T. M., and Gomes, C. M. (2004). Dissimilatory oxidation and reduction of elemental sulfur in thermophilic Archaea. *J. Bioenerg. Biomembr.* 36, 77–91. doi: 10.1023/B:JOBB.0000019600.36757.8c

Koerdt, A., Gödeke, J., Berger, J., Thormann, K. M., and Albers, S.-V. (2010). Crenarchaeal biofilm formation under extreme conditions. *PLoS One* 5:e14104. doi: 10.1371/journal.pone.0014104

Koerdt, A., Jachlewski, S., Ghosh, A., Wingender, J., Siebers, B., and Albers, S.-V. (2012). Complementation of *Sulfolobus solfataricus* PBL2025 with an α-mannosidase: effects on surface attachment and biofilm formation. *Extremophiles* 16, 115–125. doi: 10.1007/s00792-011-0411-2

Kölbl, D., Pignitter, M., Somoza, V., Schimak, M. P., Strbak, O., Blazevic, A., et al. (2017). Exploring fingerprints of the extreme Thermoacidophile *Metallosphaera sedula* grown on synthetic Martian regolith materials as the sole energy sources. *Front. Microbiol.* 8:1918. doi: 10.3389/fmicb.2017.01918

Lamble, H. J., Heyer, N. I., Bull, S. D., Hough, D. W., and Danson, M. J. (2003). Metabolic pathway promiscuity in the archaeon *Sulfolobus solfataricus* revealed by studies on glucose dehydrogenase and 2-Keto-3-deoxygluconate aldolase. *J. Biol. Chem.* 278, 34066–34072. doi: 10.1074/jbc.M305818200

Lanzotti, V., Trincone, A., Gambacorta, A., De Rosa, M., and Breitmaier, E. (1986). ^{1}H and ^{13}C NMR assignment of benzothiophenquinones from the sulfur-oxidizing archaebacterium *Sulfolobus solfataricus*. *Eur. J. Biochem.* 160, 37–40. doi: 10.1111/j.1432-1033.1986.tb09936.x

Lewis, A. M., Willard, D. J. H., Manesh, M. J., Sivabalasarma, S., Albers, S.-V., and Kelly, R. M. (2023). Stay or go: Sulfolobales biofilm dispersal is dependent on a Bifunctional VapB antitoxin. *MBio* 14:e0005323. doi: 10.1128/mbio.00053-23

Li, M., and Wen, J. (2021). Recent progress in the application of omics technologies in the study of bio-mining microorganisms from extreme environments. *Microb. Cell Factories* 20:178. doi: 10.1186/s12934-021-01671-7

Liu, L.-J., Jiang, Z., Wang, P., Qin, Y.-L., Xu, W., Wang, Y., et al. (2021). Physiology, taxonomy, and sulfur metabolism of the Sulfolobales, an order of Thermoacidophilic Archaea. *Front. Microbiol.* 12:768283. doi: 10.3389/fmicb.2021.768283

Liu, L.-J., Stockdreher, Y., Koch, T., Sun, S.-T., Fan, Z., Josten, M., et al. (2014). Thiosulfate transfer mediated by DsrE/TusA homologs from Acidothermophilic sulfur-oxidizing archaeon *Metallosphaera cuprina*. *J. Biol. Chem.* 289, 26949–26959. doi: 10.1074/jbc.M114.591669

Maezato, Y., Johnson, T., McCarthy, S., Dana, K., and Blum, P. (2012). Metal resistance and Lithoautotrophy in the extreme Thermoacidophile *Metallosphaera sedula*. *J. Bacteriol.* 194, 6856–6863. doi: 10.1128/JB.01413-12

Milojevic, T., Albu, M., Kölbl, D., Kothleitner, G., Bruner, R., and Morgan, M. L. (2021). Chemolithotrophy on the Noachian Martian breccia NWA 7034 via experimental microbial biotransformation. *Commun. Earth Environ.* 2, 1–10. doi: 10.1038/s43247-021-00105-x

Milojevic, T., Zebec, Z., and Schimak, M. P. (2020). Cultivation with powdered meteorite (NWA 1172) as the substrate enhances low-temperature preservation of the extreme Thermoacidophile *Metallosphaera sedula*. *Front. Astron. Space Sci.* 7:37. doi: 10.3389/fspas.2020.00037

Morrison, P. R., and Mojzsis, S. J. (2021). Tracing the early emergence of microbial sulfur metabolisms. *Geomicrobiol J.* 38, 66–86. doi: 10.1080/01490451.2020.1812773

Mukherjee, A., Wheaton, G. H., Blum, P. H., and Kelly, R. M. (2012). Uranium extremophily is an adaptive, rather than intrinsic, feature for extremely thermoacidophilic *Metallosphaera* species. *Proc. Natl. Acad. Sci. USA* 109, 16702–16707. doi: 10.1073/pnas.1210904109

Müller, F. H., Bandeiras, T. M., Urich, T., Teixeira, M., Gomes, C. M., and Kletzin, A. (2004). Coupling of the pathway of Sulphur oxidation to dioxygen reduction: characterization of a novel membrane-bound thiosulphate:quinone oxidoreductase. *Mol. Microbiol.* 53, 1147–1160. doi: 10.1111/j.1365-2958.2004.04193.x

Ng, F. S. W., Wright, D. M., and Seah, S. Y. K. (2011). Characterization of a Phosphotriesterase-like lactonase from *Sulfolobus solfataricus* and its immobilization for disruption of quorum sensing. *Appl. Environ. Microbiol.* 77, 1181–1186. doi: 10.1128/AEM.01642-10

Nicolaus, B., Trincone, A., Lama, L., Palmieri, G., and Gambacorta, A. (1992). Quinone composition in *Sulfolobus solfataricus* grown under different conditions. *Syst. Appl. Microbiol.* 15, 18–20. doi: 10.1016/S0723-2020(11)80131-1

Nowicka, B., and Kruk, J. (2010). Occurrence, biosynthesis and function of isoprenoid Quinones. *Bioenergetics* 1797, 1587–1605. doi: 10.1016/j.bbabio.2010.06.007

Nunn, C. E. M., Johnsen, U., Schönheit, P., Fuhrer, T., Sauer, U., Hough, D. W., et al. (2010). Metabolism of pentose sugars in the Hyperthermophilic Archaea *Sulfolobus solfataricus* and *Sulfolobus acidocaldarius*. *J. Biol. Chem.* 285, 33701–33709. doi: 10.1074/jbc.M110.146332

Olson, G. J., Brierley, J. A., and Brierley, C. L. (2003). Bioleaching review part B. *Appl. Microbiol. Biotechnol.* 63, 249–257. doi: 10.1007/s00253-003-1404-6

Palmieri, G., Balestrieri, M., Peter-Katalinić, J., Pohlentz, G., Rossi, M., Fiume, I., et al. (2013). Surface-exposed glycoproteins of Hyperthermophilic *Sulfolobus solfataricus* P2 show a common *N*- glycosylation profile. *J. Proteome Res.* 12, 2779–2790. doi: 10.1021/pr400123z

Peeples, T. L., and Kelly, R. M. (1995). Bioenergetic response of the extreme Thermoacidophile *Metallosphaera sedula* to thermal and nutritional stresses. *Appl. Environ. Microbiol.* 61, 2314–2321. doi: 10.1128/aem.61.6.2314-2321.1995

Prescott, R. D., and Decho, A. W. (2020). Flexibility and adaptability of quorum sensing in nature. *Trends Microbiol.* 28, 436–444. doi: 10.1016/j.tim.2019.12.004

Rawlings, D. E. (2002). Heavy metal mining using microbes. *Ann. Rev. Microbiol.* 56, 65–91. doi: 10.1146/annurev.micro.56.012302.161052

Rawlings, D. E. (2005). Characteristics and adaptability of iron- and sulfur-oxidizing microorganisms used for the recovery of metals from minerals and their concentrates. *Microb. Cell Factories* 4:13. doi: 10.1186/1475-2859-4-13

Reher, M., and Schönheit, P. (2006). Glyceraldehyde dehydrogenases from the thermoacidophilic euryarchaeota *Picrophilus torridus* and *Thermoplasma acidophilum*, key enzymes of the non-phosphorylative Entner–Doudoroff pathway, constitute a novel enzyme family within the aldehyde dehydrogenase superfamily. *FEBS Lett.* 580, 1198–1204. doi: 10.1016/j.febslet.2006.01.029

Rohwerder, T., Gehrke, T., Kinzler, K., and Sand, W. (2003). Bioleaching review part a. *Appl. Microbiol. Biotechnol.* 63, 239–248. doi: 10.1007/s00253-003-1448-7

Röling, W. F. M., Aerts, J. W., Patty, C. H. L., Ten Kate, I. L., Ehrenfreund, P., and Direito, S. O. L. (2015). The significance of microbe-mineral-biomarker interactions in the detection of life on Mars and beyond. *Astrobiology* 15, 492–507. doi: 10.1089/ast.2014.1276

Ruiz, L. M., Valenzuela, S., Castro, M., Gonzalez, A., Frezza, M., Soulère, L., et al. (2008). AHL communication is a widespread phenomenon in biomining bacteria and seems to be involved in mineral-adhesion efficiency. *Hydrometallurgy* 94, 133–137. doi: 10.1016/j.hydromet.2008.05.028

Sardans, J., Peñuelas, J., and Rivas-Ubach, A. (2011). Ecological metabolomics: overview of current developments and future challenges. *Chemoecology* 21, 191–225. doi: 10.1007/s00049-011-0083-5

Schmerling, C., Schroeder, C., Zhou, X., Busche, T., Kalinowski, J., Montero, L., et al. (2024). Glycerol degradation in the thermoacidophilic crenarchaeon *Sulfolobus acidocaldarius* involves an unusual glycerol-3-phosphate dehydrogenase. *bioRxiv*. [Preprint]. doi: 10.1101/2024.02.29.582781

Schönheit, P., and Schäfer, T. (1995). Metabolism of hyperthermophiles. *World J. Microbiol. Biotechnol.* 11, 26–57. doi: 10.1007/BF00339135

Selig, M., Xavier, K. B., Santos, H., and Schönheit, P. (1997). Comparative analysis of Embden-Meyerhof and Entner-Doudoroff glycolytic pathways in hyperthermophilic archaea and the bacterium Thermotoga. *Arch. Microbiol.* 167, 217–232. doi: 10.1007/BF03356097

Sharma, P., Bano, A., Singh, S. P., Dubey, N. K., Chandra, R., and Iqbal, H. M. N. (2022). Microbial fingerprinting techniques and their role in the remediation of environmental pollution. *Cleaner Chem. Eng.* 2:100026. doi: 10.1016/j.clce.2022.100026

Siebers, B., and Schönheit, P. (2005). Unusual pathways and enzymes of central carbohydrate metabolism in Archaea. *Curr. Opin. Microbiol.* 8, 695–705. doi: 10.1016/j.mib.2005.10.014

Sutter, J.-M., Tästensen, J.-B., Johnsen, U., Soppa, J., and Schönheit, P. (2016). Key enzymes of the Semiphosphorylative Entner-Doudoroff pathway in the Haloarchaeon *Haloferax volcanii*: characterization of glucose dehydrogenase, gluconate dehydratase, and 2-Keto-3-Deoxy-6-Phosphogluconate aldolase. *J. Bacteriol.* 198, 2251–2262. doi: 10.1128/JB.00286-16

Swenson, T. L., Jenkins, S., Bowen, B. P., and Northen, T. R. (2015). Untargeted soil metabolomics methods for analysis of extractable organic matter. *Soil Biol. Biochem.* 80, 189–198. doi: 10.1016/j.soilbio.2014.10.007

Swenson, T. L., and Northen, T. R. (2019). "Untargeted soil metabolomics using liquid chromatography–mass spectrometry and gas chromatography–mass spectrometry,"" in Microbial Metabolomics. ed. E. E. K. Baidoo (New York, NY: Springer), 97–109.

Tang, X., Ezaki, S., Atomi, H., and Imanaka, T. (2000). Biochemical analysis of a thermostable tryptophan synthase from a hyperthermophilic archaeon. *Eur. J. Biochem.* 267, 6369–6377. doi: 10.1046/j.1432-1327.2000.01721.x

Tommonaro, G., Abbamondi, G. R., Iodice, C., Tait, K., and De Rosa, S. (2012). Diketopiperazines produced by the halophilic archaeon, *Haloterrigena hispanica*, activate AHL bioreporters. *Microb. Ecol.* 63, 490–495. doi: 10.1007/s00248-011-9980-y

Trincone, A., Gambacorta, A., Lanzotti, V., and De Rosa, M. (1986). A new benzo [1, 2-b; 4, 5-b′]dithiophene-4, 8-quinone from the Archaebacterium *Sulfolobus solfataricus*. *J. Chem. Soc. Chem. Commun.* 10:733. doi: 10.1039/C39860000733

Trincone, A., Lanzotti, V., Nicolaus, B., Zillig, W., De Rosa, M., and Gambacorta, A. (1989). Comparative lipid composition of aerobically and anaerobically grown *Desulfwolobus ambivalens*, an autotrophic thermophilic Archaeobacterium. *Microbiology* 135, 2751–2757. doi: 10.1099/00221287-135-10-2751

Trincone, A., Nicolaus, B., Palmieri, G., De Rosa, M., Huber, R., Huber, G., et al. (1992). Distribution of complex and Core lipids within new Hyperthermophilic members of the Archaea domain. *Syst. Appl. Microbiol.* 15, 11–17. doi: 10.1016/S0723-2020(11)80130-X

Van Wolferen, M., Shajahan, A., Heinrich, K., Brenzinger, S., Black, I. M., Wagner, A., et al. (2020). Species-specific recognition of *Sulfolobales* mediated by UV-inducible pili and S-layer glycosylation patterns. *MBio* 11, e03014–e03019. doi: 10.1128/mBio.03014-19

Vargas, M., Kashefi, K., Blunt-Harris, E. L., and Lovley, D. R. (1998). Microbiological evidence for Fe(III) reduction on early earth. *Nature* 395, 65–67. doi: 10.1038/25720

Wächtershäuser, G. (1988). Pyrite formation, the first energy source for life: a hypothesis. *Syst. Appl. Microbiol.* 10, 207–210. doi: 10.1016/S0723-2020(88)80001-8

Wächtershäuser, G. (1990). Evolution of the first metabolic cycles. *Proc. Natl. Acad. Sci. USA* 87, 200–204. doi: 10.1073/pnas.87.1.200

Wang, P., Li, L. Z., Qin, Y. L., Liang, Z. L., Li, X. T., Yin, H. Q., et al. (2020). Comparative genomic analysis reveals the metabolism and evolution of the thermophilic archaeal genus *Metallosphaera*. *Front. Microbiol.* 11:1192. doi: 10.3389/fmicb.2020.01192

Weiss, M. C., Sousa, F. L., Mrnjavac, N., Neukirchen, S., Roettger, M., Nelson-Sathi, S., et al. (2016). The physiology and habitat of the last universal common ancestor. *Nat. Microbiol.* 1, 1–8. doi: 10.1038/nmicrobiol.2016.116

Weitzel, C. S., Li, L., Zhang, C., Eilts, K. K., Bretz, N. M., Gatten, A. L., et al. (2020). Duplication of leucyl-tRNA synthetase in an archaeal extremophile may play a role in adaptation to variable environmental conditions. *J. Biol. Chem.* 295, 4563–4576. doi: 10.1074/jbc.RA118.006481

Wheaton, G. H., Vitko, N. P., Counts, J. A., Dulkis, J. A., Podolsky, I., Mukherjee, A., et al. (2019). Extremely Thermoacidophilic *Metallosphaera* species mediate mobilization and oxidation of vanadium and molybdenum oxides. *Appl. Environ. Microbiol.* 85, e02805–e02818. doi: 10.1128/AEM.02805-18

Williams, T. J., Allen, M., Tschitschko, B., and Cavicchioli, R. (2017). Glycerol metabolism of haloarchaea. *Environ. Microbiol.* 19, 864–877. doi: 10.1111/1462-2920.13580

Xia, L., Ma, L., and Meng, D. (2021). "Adsorption of microorganisms to minerals" in Adsorption at natural minerals/water interfaces. eds. S. Song and B. Li (Cham: Springer International Publishing), 263–303.

Zaparty, M., Esser, D., Gertig, S., Haferkamp, P., Kouril, T., Manica, A., et al. (2010). "Hot standards" for the thermoacidophilic archaeon *Sulfolobus solfataricus*. *Extremophiles* 14, 119–142. doi: 10.1007/s00792-009-0280-0

Zeng, Z., Liu, X.-L., Wei, J. H., Summons, R. E., and Welander, P. V. (2018). Calditol-linked membrane lipids are required for acid tolerance in *Sulfolobus acidocaldarius*. *Proc. Natl. Acad. Sci. USA* 115, 12932–12937. doi: 10.1073/pnas.1814048115

Zhang, G., Zhang, F., Ding, G., Li, J., Guo, X., Zhu, J., et al. (2012). Acyl homoserine lactone-based quorum sensing in a methanogenic archaeon. *ISME J.* 6, 1336–1344. doi: 10.1038/ismej.2011.203

frontiers | Frontiers in Microbiology

TYPE Original Research
PUBLISHED 09 May 2025
DOI 10.3389/fmicb.2025.1455423

OPEN ACCESS

EDITED BY
Ivan A. Berg,
University of Münster, Germany

REVIEWED BY
Shingo Kato,
RIKEN BioResource Research Center (BRC), Japan
Qian Hu,
Beijing Forestry University, China

*CORRESPONDENCE
Robert C. Blake II
✉ rblake@xula.edu

RECEIVED 26 June 2024
ACCEPTED 11 April 2025
PUBLISHED 09 May 2025

CITATION
Blake RC II, Painter RG, Pham N, Griswold O, White B and White RA III (2025) *Metallosphaera sedula* bifurcates into two sizes when it is cultured mixotrophically on soluble iron. *Front. Microbiol.* 16:1455423. doi: 10.3389/fmicb.2025.1455423

Metallosphaera sedula bifurcates into two sizes when it is cultured mixotrophically on soluble iron

Robert C. Blake II[1]*, Richard G. Painter[1], Nghi Pham[1], Olivia Griswold[1], Brooke White[1] and Richard A. White III[2,3,4]

[1]Division of Basic Pharmaceutical Sciences, Xavier University of Louisiana, New Orleans, LA, United States, [2]NCRC, Department of Bioinformatics and Genomics, University of North Carolina at Charlotte, Kannapolis, NC, United States, [3]CIPHER, Department of Bioinformatics and Genomics, University of North Carolina at Charlotte, Charlotte, NC, United States, [4]Australian Centre for Astrobiology, University of New South Wales, Sydney, NSW, Australia

Metallosphaera sedula is a thermoacidophilic archaeon that obtains all of its energy for growth from aerobic respiration and oxidative phosphorylation at the expense of selected organic and inorganic sources of electrons. Initial velocities for the oxidation of soluble ferrous ions by intact cells at 60 °C and pH 1.5 were determined using an integrating cavity absorption meter that permitted accurate absorbance measurements to quantify the increase in soluble ferric iron in the presence of turbid suspensions of the live organisms. *M. sedula* that was cultured on yeast extract either in the absence or the presence of 20 mM soluble ferrous iron exhibited turnover numbers for soluble iron oxidation of 304 ± 26 and 333 ± 31 attamoles/cell/min, respectively. These functional data were consistent with the transcriptomic evidence presented by others, that the proteins presumably responsible for aerobic respiration on soluble iron are expressed constitutively in *M. sedula*. Intact cells of *M. sedula* were characterized by electrical impedance, laser light diffraction, and transmission electron microscopic measurements. All three types of measurements were consistent with the surprising observation that cells cultured on yeast extract in the presence of soluble iron bifurcated into approximately equal numbers of coccoidal cells of two sizes, smaller cells with an average diameter of 0.6 μm and larger cells with an average diameter of 1.35 μm. Cells cultured on the same concentration of yeast extract but in the absence of soluble iron comprised a single cell size with an intermediate average diameter of 1.06 μm. This unexpected bifurcation of a clonal cell population into two demonstrably different sizes when the extracellular nutrient environment changes has not previously been reported for *M. sedula*, or any other single-celled archaeon or eubacterium.

KEYWORDS

***Metallosphaera sedula*, integrating cavity absorption meter, *in situ* kinetics, two cell sizes, phenotypic heterogeneity**

1 Introduction

Metallosphaera sedula is a thermoacidophilic archaeon in the phylum *Crenarchaeota* that was isolated from an acidic hot water pond at Pisciarelli Sulfatata in Naples, Italy (Huber et al., 1989). Cells are regular to slightly irregular cocci, about 0.6 to 1.5 μm in diameter (Huber and Stetter, 2015). Growth occurs at 50 to 80°C (optimal 65 to 75°C) and pH 1.0 to 6.5 (optimal 2.5 to 3.5). *M. sedula* is aerobic and facultatively chemolithoautotrophic. Heterotrophic growth occurs on complex organic compounds such as yeast extract, casamino acids, peptone and tryptone. Autotrophic or mixotrophic

growth occurs in the presence of reduced sulfur compounds, selected sulfide minerals, and soluble ferrous iron. The *Metallosphaera* genus contains six species that are currently recognized (Fuchs et al., 1995; Kurosawa, 2003; Liu et al., 2011; Peng et al., 2015; Kozubal et al., 2011). Other genera within the order *Sulfolobales* that harbor archaea that greatly resemble *M. sedula* include *Acidianus* (5 species) (Segerer et al., 1986; Plumb et al., 2007; Fuchs et al., 1996; He et al., 2004; Yoshida et al., 2006; Urbieta et al., 2017), *Sulfurisphaera* (3 species) (Kurosawa et al., 1998; Suzuki et al., 2002; Tsuboi et al., 2018), *Sulfuracidiflex* (2 species) (Huber and Stetter, 1991; Itoh et al., 2020), and *Sulfodiicoccus* (Sakai and Kurosawa, 2017). All of these thermoacidiphilic archaea are described as lobed or irregular cocci with diameters from 0.5 to 1.8 μm (Liu J. et al., 2021; Liu L. J. et al., 2021; Lewis et al., 2021).

A principal feature of the energy metabolism of these physiologically related *Sulfolobales* is their ability to respire aerobically on soluble reduced iron. Despite the interest in this activity for its contribution to the oxidation and dissolution of minerals within ore bodies, the biomolecules and electron transfer reactions that participate in respiration on soluble iron remain poorly understood. Early studies simply reported the novel spectral properties of presumed electron transfer proteins that were observed in cell-free extracts in archaeal cells that were cultured aerobically on soluble iron (Barr et al., 1990; Blake et al., 1993). A proteomic and transcriptomic study in cell-free extracts of *Sulfuracidiflex* (formerly *Sulfolobus*) *metallicus* first identified proteins and gene products that appeared to be upregulated after the cells were exposed to ferrous iron (Bathe and Norris, 2007). The relevant *fox* genes were subsequently reported from genomic studies to represent terminal heme-copper oxidases whose primary structures were unique to the archaea (Hemp and Gennis, 2008; Sousa et al., 2011). Others have reported further genomic, proteomic, and transcriptomic studies for iron oxidation determinants in the extremely thermoacidophilic archaea (Kozubal et al., 2011; Auernik and Kelly, 2008; Auernik et al., 2008). There is now strong circumstantial evidence that the *fox* gene products, which appear *via* proteomics and transcriptomics to be expressed constitutively in *M. sedula*, are responsible for conducting the electron transfer reactions that comprise aerobic respiration on soluble iron (Counts et al., 2022). An ongoing problem, however, is that accompanying functional assays to quantify iron oxidation by intact cells or cell-free extracts have lagged far behind the elegant genomic, metagenomic, proteomic, and transcriptomic studies. Thus a typical functional measurement consists of a single, fixed-time assay where a sample is removed and treated with 1,10-phenanthroline or a similar organic compound that complexes with ferrous iron and changes color for optical quantification. In order to fully understand and appreciate any biochemical event or reaction, one has to actually monitor the event or reaction as it occurs in real time; simply cataloging the participants, no matter how detailed and thorough is the list, isn't sufficient.

This laboratory has described an integrating cavity absorption meter (ICAM) that permits accurate absorbance measurements to be conducted in turbid media like suspensions of intact cells (Blake and Griff, 2012; Li et al., 2015; Blake et al., 2016; Blake and White, 2020; Blake et al., 2020, 2021). Because ferrous and ferric iron absorb light differently, the ICAM can be exploited to monitor soluble iron oxidation spectrophotometrically as a continuous process. The experimental observations presented below were conducted to quantify the rates of iron oxidation by intact cells of *M. sedula*. In particular, we sought to distinguish between two hypotheses: that the respiratory proteins that are responsible for iron oxidation are expressed constitutively; or that they are induced when the cells are exposed to substrate-level concentrations of soluble iron. Organotrophic and mixotrophic growth on yeast extract in the absence and the presence, respectively, of 20 mM ferrous sulfate produced intact cells that had similar specific activities per intact cell for the rate of iron oxidation. In the process of enumerating and characterizing both populations of cells, we made the unexpected observation that cells cultured in the presence of soluble iron assumed one of two sizes that bracketed the one size assumed by cells cultured in the absence of soluble iron. To our knowledge, no one has reported behavior similar to this in any other iron-oxidizing microorganism, or for that matter, any other microorganism in general.

2 Materials and methods

2.1 Cell culture

M. sedula strain TH2, Deutsche Sammlung von Mikroorganismen und Zellkulturen (DSMZ) 5348^T, was cultured mixotrophically on 20 mM ferrous sulfate plus 0.2% (wt/vol) yeast extract at 60°C. The pH of the medium was adjusted to 1.5 using sulfuric acid; the minimal salts concentrations were those recommended in the DSMZ media guide for the generic *Sulfolobus* medium, number 88. *M. sedula* was cultured heterotrophically in the same medium that omitted the ferrous sulfate. In either case, cells grown to late stationary phase were harvested by centrifugation, washed twice with 0.02 M H_2SO_4, and resuspended in sufficient 0.02 M H_2SO_4 to achieve a stock suspension of approximately 1×10^{10} cells/mL. Each stock suspension was stored at 4°C for no longer than a week while electrical impedance, spectroscopic, or proteomic measurements were conducted on aliquots of the cells.

2.2 Quantification and characterization of microorganisms

Absolute numbers of *M. sedula* cells were determined by electrical impedance measurements in a Multisizer 4 particle counter (Beckman Coulter, Inc., Brea, CA) fitted with a 30-μm aperture (Blake and Griff, 2012; Li et al., 2015; Blake et al., 2020). The instrument was programmed to siphon 50 μL of sample that contained Isoton II as the electrolyte. The current applied across the aperture was 600 μA. Voltage pulses attendant with impedance changes as particles passed through the aperture were monitored with an instrument gain of four. Determinations of particle

Abbreviations: ICAM, integrating cavity absorption meter; DSMZ, Deutsche Sammlung von Mikroorganismen und Zellkulturen; PNNL, Pacific Northwest National Laboratory; SEM, scanning electron microscopy; EDS, energy dispersive x-ray spectroscopy.

diameters, surface areas, and volumes were accomplished with operating and analysis software provided by Beckman Coulter, Inc.

Relative numbers of *M. sedula* cells were determined by photon correlation scattering spectroscopy with a DelsaNano C particle size analyzer, also from Beckman Coulter, Inc. Cell densities were adjusted to $\sim 1 \times 10^7$ cells/mL in 0.02 M sulfuric acid to give an attenuator obscuration of between 45 and 50%. Determination of the relative numbers of light scattering species as a function of particle diameter was accomplished by the time domain method with operating and analysis software provided by Beckman Coulter, Inc.

Transmission electron microscopy was conducted on a model HT7700 Transmission Electron Microscope from Hitachi High-Tech America, Inc., Schaumburg, IL. Washed cells of *M. sedula* cultured mixotrophically were mixed with 1% (w/v) paraformaldehyde for 30 min at room temperature and then air-dried on a Formvar-coated copper grid for whole mounts.

2.3 Initial velocity kinetic measurements

Initial velocity kinetic measurements on the rate of iron oxidation by intact *M. sedula* were obtained by conducting absorbance measurements on the time-dependent appearance of ferric ions using an OLIS-CLARiTY 1000A spectrophotometer (On Line Instrument Systems, Inc., Bogart, GA) that employed a novel integrating cavity absorption meter (Blake and Griff, 2012; Li et al., 2015; Blake et al., 2020). In a typical measurement, identical 8.0- and 7.9-mL solutions that contained sulfuric acid (pH 1.5) were added to both the reference and the sample observation cavities, respectively, of the spectrophotometer. The sample cavity contained an additional 20 μL of a stock cell suspension of cells. After a stable baseline was recorded from 296 to 400 nm, 100 μL that contained soluble ferrous sulfate were added to the cell suspension to initiate subsequent oxidation reactions and absorbance changes within the cavity. These liquid handling operations were conducted manually. The single opening to the otherwise enclosed observation cavity was subsequently fitted with a white, refractive Teflon plug, and data acquisition was then initiated. These latter operations were routinely conducted in 0.5 s, which comprised the operational dead time for any oxidation to proceed before data were obtained.

Raw absorbance spectra, typically 6.2 spectra/s, were collected for appropriate time intervals. Raw absorbance values obtained in the CLARiTY spectrophotometer were converted to equivalent absorbance values/cm using Fry's method (Fry et al., 2010) with analysis software provided by OLIS, Inc. Global fits of absorbance changes as a function of both time and wavelength were accomplished by the singular value decomposition method (DeSa and Matheson, 2004) using analysis software also provided by OLIS, Inc.

2.4 Ribosomal RNA sequence analyses

Sequence analyses of 16S ribosomal RNA were conducted by the Zymo Research Corporation, Irvine, CA. Cells of *M. sedula* that were cultured to stationary phase either heterotrophically or mixotrophically were harvested by centrifugation, washed twice with distilled water to remove excess acid and soluble iron, and resuspended and frozen in sufficient distilled water to achieve samples comprised of 200 mg wet-weight cells in 1.8 mL. Briefly, Zymo Research then extracted the DNA from both samples, prepared the DNA for targeted sequencing using the Quick-16S^{TM} Primer Set, and sequenced the resulting libraries using an Illumina NextSeq2000^{TM} (Illumina, San Diego, CA). Subsequent bioinformatics analyses were conducted using the Dada2 pipeline (Callahan et al., 2016) that was supplemented with the sequence information for *M. sedula* DSMZ 5348^T.

2.5 Scanning electron microscopy and energy dispersive x-ray analyses

Scanning electron microscopy (SEM) and Energy dispersive x-ray spectroscopy (EDS) measurements were conducted by the Drug Discovery and Delivery Core facility at Xavier University of Louisiana, New Orleans, LA. Cells of *M. sedula* that were cultured to stationary phase either heterotrophically or mixotrophically were harvested by centrifugation, washed twice with distilled water to remove excess acid and soluble iron, and resuspended in sufficient distilled water to achieve samples comprised of 900 mg wet-weight cells in 15 mL. Briefly, 20 μL of washed, suspended cells were deposited on the surface of copper tape that was affixed to the sample stub that was positioned in the analysis chamber of a model S-3400N SEM (Hitachi High-Tech America, Inc., Schaumburg, IL) that was equipped with a model EDAX Elite T EDS system (Ametek, Pleasanton, CA). The deposited cells were air-dried and analyzed in a vacuum.

3 Results

3.1 Quantification and size characterization of archaeal cells

Figure 1A shows the size and quantitative measurements that were conducted on cells of *M. sedula* that were cultured heterotrophically on just yeast extract. These measurements were conducted using two methods, electrical impedance and static light scattering. The results from the two methods agreed that the coccoidal cells comprised a single population with an average diameter of 1.06 μm. It must be noted that each method has strengths and weaknesses. The strength of the electrical impedance measurement is that it supplies absolute numbers for the different cell sizes in the culture; the weakness is that the coccoidal archaea with spherical diameters <0.6 μm were underrepresented by the electrical impedance measurements, by which observations were limited to particles with effective diameters between 2 and 60% of the 30-μm aperture employed in the Multisizer. The strength of the static light diffraction measurements is that they are capable of resolving particles with effective diameters as small as 0.1 nm; the weakness is that the light diffraction method does not yield absolute numbers of cells, only relative numbers of cells in the entire population. However, the two types of measurements, when used in conjunction, serve to complement each other to provide a more complete characterization of the entire cell populations.

10.3389/fmicb.2025.1455423

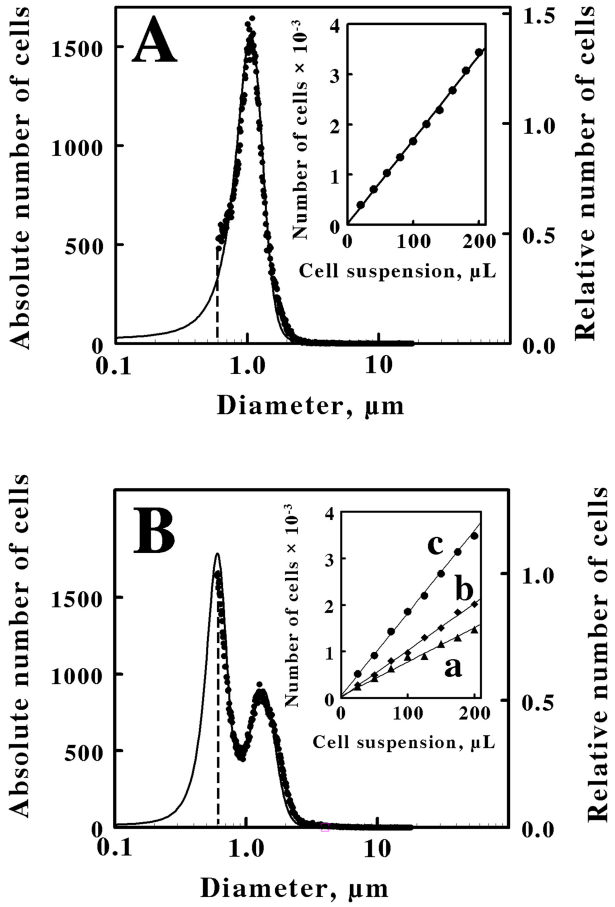

FIGURE 1
Quantification and characterization of intact *M. sedula* cultured heterotrophically on yeast extract **(A)** or mixotrophically on yeast extract plus 20 mM ferrous sulfate **(B)**. Each panel compares cell suspensions by electrical impedance (*data points, left ordinate*) and static light diffraction (*solid curve, right ordinate*) measurement methods. The *dashed vertical lines* in **(A, B)** represent the lower limits of detection for the electrical impedance method. The *insets* in **(A, B)** show the numbers of cells as a function of the microliters of the cell suspension that were derived from the heterotrophic and the mixotrophic cultures, respectively. *Curves a, b,* and *c* in the *inset* of **(B)** represent cell counts for cell diameters of 0.6 to 0.95 µm, 0.95 to 3.0 µm, and 0.6 to 3.0 µm, respectively. Each *datum* in the *insets* of **(A, B)** represents the mean of 6 and 10 determinations, respectively; in all cases, the corresponding standard deviations are within the diameters of the data points.

In the present case, the immediate goal was to quantify the rate of iron oxidation by intact cells. Consequently, the desire was to accurately determine the absolute number of cells to calculate an accurate turnover number per cell in the intact cell-dependent catalytic activity assays. The *inset* in Figure 1A shows the standard curve that was developed to quantify the number of cells present in a stock suspension of washed cells that were derived from the heterotrophic culture of *M. sedula* on yeast extract. Different volumes of the stock suspension were removed and added to the electrolyte solution that was employed in the Multisizer. The numbers of the resulting cells that were present in a prescribed volume of the electrolyte-cell mixture were then plotted as a function of the volumes of the aliquots that were removed from the stock suspension. The number of cells in each aliquot was directly proportional to the volume of the aliquot that was withdrawn from the stock suspension. This standard curve provided the means to quantify the number of cells present in any aliquot taken from the stock suspension for use in subsequent kinetic measurements. It is evident from the data in Figure 1A that a small number of the total cells in the heterotrophic suspension were not counted due to the sensitivity limitation of the electrical impedance measurements. Fortunately, a close correspondence between the electrical impedance and the light diffraction curves was observed down to a diameter of 0.6 µm, indicating that the two instruments were monitoring the same population of particles. Consequently, the numbers of cells that were actually counted by the electrical impedance measurements were increased by 11% to account for the portion of the light diffraction measurements that fell below the limit of detection of the absolute counting method.

Figure 1B shows the size and quantitative measurements that were conducted on cells of *M. sedula* that were cultured mixotrophically on the same concentration of yeast extract amended with 20 mM ferrous sulfate. In this case, the resulting cells comprised two populations of coccoidal cells with different average diameters of 0.6 and 1.35 µm. Once again, a close correspondence between the electrical impedance and the light diffraction curves was observed down to a diameter of 0.6 µm, indicating that the two instruments were monitoring the same population of particles. The *inset* in Figure 1B shows the standard curve that was developed to quantify the numbers and types of cell sizes present in a stock suspension of washed cells that were derived from the mixotrophic culture of *M. sedula*. *Curve c* represents the standard curve for the total number of cells that were quantified in each aliquot. Because the mixotrophic population of cells consisted of two different sizes, a cell diameter of 0.95 µm was arbitrarily chosen as the dividing diameter between the two different cell sizes in the bifurcated mixture. *Curves a* and *b* in the *inset* of Figure 1B thus represent the standard curves for the smaller (0.6 to 0.95 µm cell diameters) and the larger (0.95 to 3.0 µm cell diameters) cells, respectively, within the bifurcated mixture. Although the actual cell counts in the *inset* indicate that the larger cell cohort outnumbered the smaller cell cohort, it is evident that the two curves overlap to a considerable extent. It is also evident in the *main panel* that approximately half of the smaller diameter cells were not quantified by the electrical impedance method. The relative contributions of the two different cell sizes that are evident in Figure 1B to the overall number of cells in the bifurcated mixotrophic cultures were estimated by iterative nonlinear regression analyses of the electrical impedance and the light diffraction measurements (calculations not shown). The result of these calculations was that the small and large cell cohorts contributed ~48 and 52 percent, respectively, to the total cell numbers in the mixotrophic culture. That is, the mixotrophic culture consisted of approximately equal numbers of the two cell sizes.

An alternative hypothesis for the particles that comprise the small sized fraction in Figure 1B is that these smaller particles actually represent exosomes that are produced by *M. sedula* when soluble iron is added to the yeast extract medium. Exosomes, or extracellular vesicles, are membrane-bound particles of variable diameter that are excreted into the extracellular milieu by all three

domains of life (Liu J. et al., 2021; Liu L. J. et al., 2021). *M. sedula* does produce biogeochemically active archaeal membrane vesicles (Johnson et al., 2018). However, energy deprivation was evaluated in *M. sedula* and found to stimulate vesicle synthesis, while energy excess repressed vesicle formation. Thus autotrophic culture on low energy-yielding ferrous sulfate supported vesicle synthesis, while the addition of an organic carbon and energy source (in their case, tryptone) prevented vesicle synthesis as indicated by microscopy and protein quantification. Furthermore, the mean diameter of the vesicles that were produced under autotrophic conditions on soluble iron was only 194 ± 36 nm. The light diffraction measurements in Figures 1A, B show no hint of a population of particles in our cultures that were smaller than a population with a mean diameter of 600 nm. Based on both size and culture condition comparisons, we conclude that the smaller particles in Figures 1B, 2B do not represent extracellular exosomes.

These observations that the same cells could assume one of two cell-size profiles, depending on the medium in which the cells were cultured, were reproducible. Figure 2A shows three representative profiles of cell counts as a function of cell diameters that were obtained when a limited number of cells of M. *sedula* that were cultured mixotrophically were inoculated into fresh media that only contained yeast extract. All three curves were consistent with the pattern observed with cells cultured heterotrophically, like those presented in Figure 1A, where the cell counts were dominated by coccoidal cells that comprised a single population with an average diameter of 1.06 μm. There was no hint of the two different cell sizes that are evident in the culture shown in Figure 1B. The *inset* in Figure 2A shows the corresponding growth curve for *M. sedula* that was taken from a mixotrophic culture and grown in the heterotrophic medium without amended soluble ferrous iron. The cell counts on the *ordinate axis* of the *inset* represent the actual total cell counts obtained when 10 μL of the culture were added to 10 mL of Isoton, and 50 μL of the resulting mixture were subsequently aspirated through the measuring aperture in the instrument. After 14 days, the heterotrophic culture achieved a stationary phase that contained 5.4×10^8 cells/mL.

Figure 2B shows three representative profiles of cell counts as a function of cell diameters that were obtained when a limited number of cells of M. *sedula* that were cultured heterotrophically were inoculated into fresh media that contained yeast extract amended with 20 mM ferrous sulfate. All three curves were consistent with the pattern observed with cells cultured mixotrophically, like those presented in Figure 1B, where the cell counts were dominated by coccoidal cells that comprised two populations of coccoidal cells with different average diameters of 0.6 and 1.35 μm. There was no hint of the single cell size that is evident in the culture shown in Figure 1A. The *inset* in Figure 2B shows the corresponding growth curve for *M. sedula* that was taken from a heterotrophic culture and grown in the mixotrophic medium amended with soluble ferrous iron. After 14 days, the culture had achieved a stationary phase that contained 7.6×10^8 cells/mL.

Independent testimonial evidence that *M. sedula* bifurcates into two cell sizes when it is cultured mixotrophically was obtained by transmission electron microscopy of cells cultured on yeast extract and soluble iron. Figure 3 shows an example of a transmission electron micrograph that contains four coccoidal cells of *M. sedula* that had been cultured mixotrophically. Two of the individual coccoidal cells exhibited diameters <0.6 μm and thus represented examples of the cohort of small cells. One cell had a diameter of 1.22 μm and thus represented an example of the cohort of large cells. Finally, the remaining cell had a diameter of 0.921 μm and thus could represent either type of cell in the bifurcated mixture.

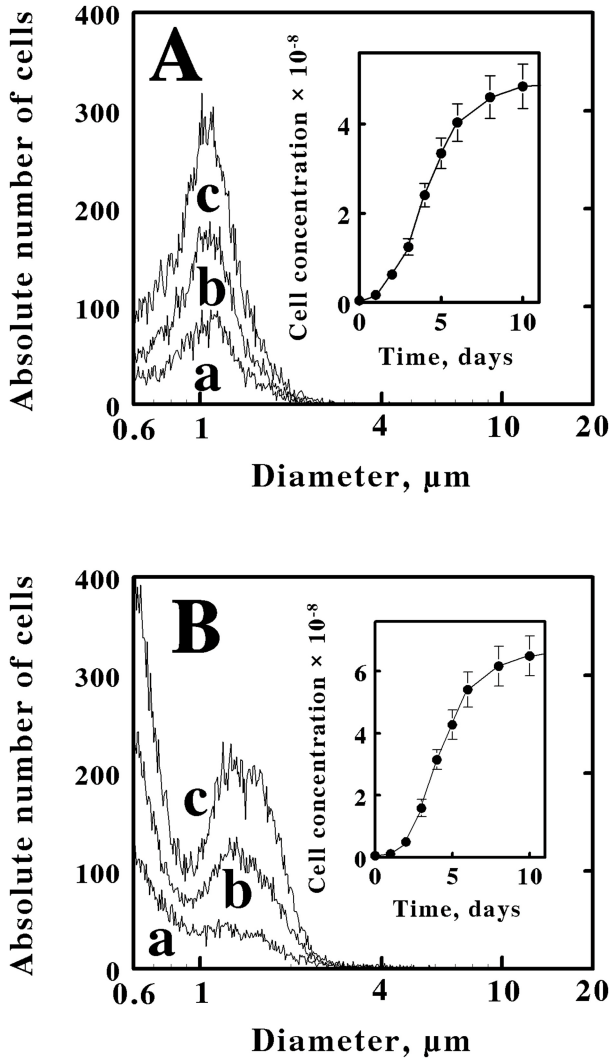

FIGURE 2
Electrical impedance measurements of the time dependencies and cell size characteristics of the cells that were obtained when *M. sedula* was inoculated into different media. **(A)** 6.1×10^6 cells of stationary phase *M. sedula* that were cultured mixotrophically in yeast extract plus soluble ferrous iron were inoculated into fresh media that contained only yeast extract. **(B)** 5.3×10^6 cells of stationary phase *M. sedula* that were cultured heterotrophically in yeast extract were inoculated into fresh media that contained yeast extract amended with soluble ferrous iron. *Curves a*, *b*, and *c* in both panels represent the cell populations present at 3, 4, and 6 days, respectively. The cell numbers in both *insets* represent the concentrations of cells present in the culture at each corresponding time period. Each *datum* in both *insets* represents the mean of 8 determinations; in some cases the corresponding standard deviations are within the diameters of the data points.

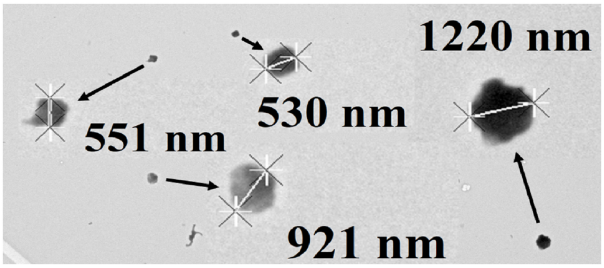

FIGURE 3
Transmission electron micrograph of *Metallosphaera sedula* cultured mixotrophically on yeast extract and 20 mM soluble ferrous ions at pH 1.5. Four coccoid cells of representative sizes are featured. Cell diameters were determined using the "point to point" linear measurement method.

3.2 16S ribosomal RNA sequence analyses

Cells that were cultured either heterotrophically or mixotrophically were subjected to 16S ribosomal RNA sequence analyses to address the hypothesis that our laboratory cultures of *M. sedula* were contaminated with one or more different microorganisms. The 16S rRNA macromolecule is an important structural and functional component of both the bacterial and archaeal 30S ribosomal subunits. Because its primary structure is so highly conserved among species of bacteria and archaea, the 16S rRNA gene has become an important phylogenetic marker, and its sequence is routinely exploited for classification and identification of microorganisms (Woese and Fox, 1977; Woese, 1987; Woese et al., 1990). We sought to test whether changing the culture medium simply permitted one or more members of a hypothetically mixed culture to thrive at the expense of the other members. The sequencing studies revealed that 99.5% of the sequences of the samples cultured in both media were identical to that of *M. sedula* DSM 5348[1] in the database used for the analyses. The remaining 0.5% of the sequences were so low abundance that they were deemed to represent background noise.

3.3 Energy dispersive x-ray spectroscopy

Cells that were cultured either heterotrophically or mixotrophically were subjected to SEM and EDS analyses to address the hypothesis that the particles that are designated as 'small cells' were actually a relatively uniform collection of smaller particles that included flocculated ferric oxy-hydroxide (FeOOH) and sulfate precipitates. Supplementary Figures S1A, B show energy dispersive x-ray spectrographs for washed cells of *M. sedula* that were cultured to stationary phase at pH 1.5 in the absence (Supplementary Figure S1A) and presence (Supplementary Figure S1B), respectively, of 20 mM soluble iron. In both examples, the principal elements that stood out in the elemental analyses were carbon (1 major peak) and copper (3 peaks). The cell samples were deposited and dried on copper tape, so copper could not help but be prominent in the analyses. In either case, there were no discernible peaks associated with either iron or sulfur. Supplementary Figure S1C shows the spectrograph that was obtained for the washed cells that were cultured mixotrophically in 40 mM soluble iron at pH 3.5. In addition to carbon and copper, the spectrograph in Supplementary Figure S1C also exhibited discrete elemental peaks that were associated with iron and sulfur. The combination of a higher concentration of soluble iron and a higher pH value would greatly encourage the coprecipitation of ferric oxy-hydroxide and sulfate. When examined by the electrical impedance and light diffraction methods employed herein, the resulting profile of cell counts *vs.* particle diameters for cells cultured at pH 3.5 had much lower signal-to-noise characteristics than those profiles shown in Supplementary Figures 1B, 2B (data not shown). Given that the numbers associated with the smaller fraction in Figure 1B were comparable to the numbers associated with the larger fraction, we conclude that the absence of discernible iron and sulfur in the EDS spectrograph in Supplementary Figure S1B is consistent with the conclusion that the smaller fraction in Figure 1B is predominantly carbon-based and not inorganic.

3.4 Initial velocity kinetic studies

The formation of product ferric ions was evident as soon as intact cells of *M. sedula* were introduced into an aerobic solution of ferrous ions in sulfuric acid, pH 1.5. Figure 4A shows three representative time courses for the increases in absorbance at 350 nm that were obtained when 1.7×10^9 cells of *M. sedula* that were cultured heterotrophically were mixed with different concentrations of ferrous ions and monitored over time at 60°C. We determined an absorption coefficient of 740 $M^{-1}cm^{-1}$ at 350 nm for oxidized iron in sulfuric acid, pH 1.5 (see the standard curve in Supplementary Figure S1). Initial velocities of the changes in ferric concentration as a function of time were obtained from primary data such as those shown in Figure 4A, and the resulting secondary plot of initial velocity as a function of the starting ferrous ion concentration in shown in Figure 4B. The parameters for the rectangular hyperbola drawn through the *data points* in Figure 4B were derived from a nonlinear least-squares fit of the initial velocity data to the Michaelis-Menten equation. Values for K_M and V_{max} of 140 ± 15 μM and 516 ± 44 nmoles/min, respectively, were obtained from the analysis. That value of V_{max} corresponds to a turnover number of 304 ± 26 attamoles/min/cell.

The schematic illustration shown in Figure 4C represents the minimal kinetic mechanism that is consistent with the initial velocity kinetic data shown in Figure 4B. The iron-dependent reduction of the relevant electron transport proteins in the aerobic respiratory chain in the archaeon is depicted as a relatively rapid reaction, which is consistent with observations that reduction of a colored component within the intact cell is complete within the 0.5 to 1.0 s dead time of the mixing in that instrument (Blake and Griff, 2012; Li et al., 2015; Blake et al., 2016; Blake and White, 2020; Blake et al., 2020). The archaeon with its reduced cellular component(s) then reacts with molecular oxygen to regenerate the oxidized archaeon in a slower reaction that constitutes the rate-limiting catalytic step. When the concentration of intact *M.*

1 https://www.ncbi.nlm.nih.gov/gene/91756283

10.3389/fmicb.2025.1455423

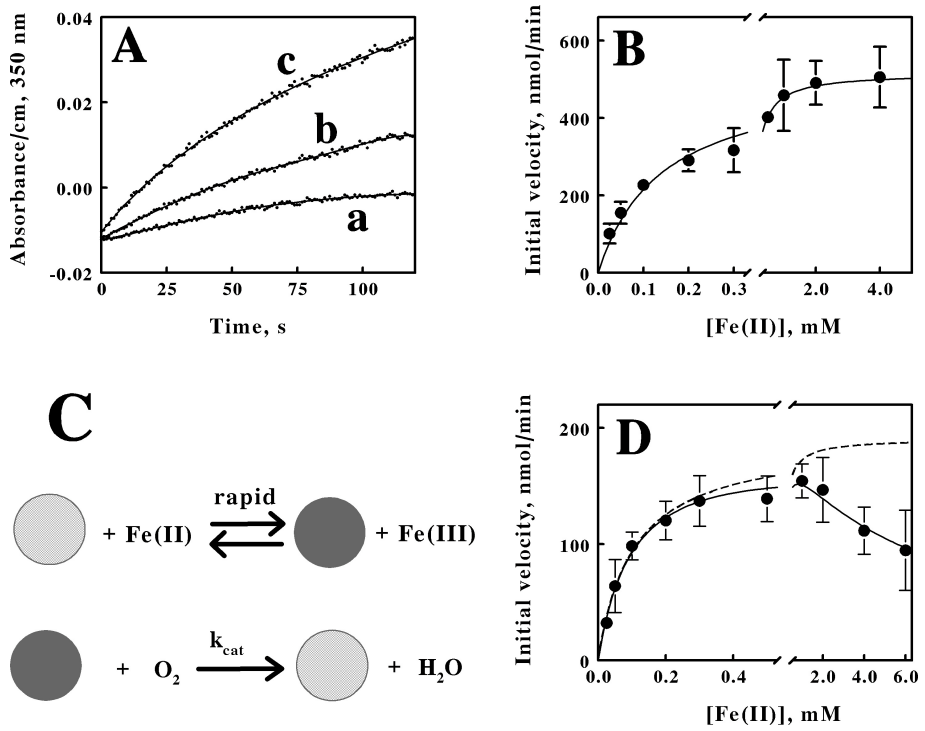

FIGURE 4
Kinetic behavior of aerobic respiration on soluble iron by intact *M. sedula*. **(A)** *curves a, b,* and *c* are representative examples of the increases in the absorbance at 350 nm when *M. sedula* was mixed with 0.025, 0.1, and 4.0 mM soluble ferrous ions, respectively. The parameters for the *curves* drawn through the *data points* were determined by fitting a sextic polynomial to each set of data. **(B)** dependence of the initial velocity of ferric ion production on the concentration of ferrous ions when 1.7×10^9 cells of heterotrophically-grown *M. sedula* were included in 8 mL of sulfuric acid (pH 1.5) at 60°C. The parameters for the *curve* drawn through the data points were determined by a nonlinear regression analysis using the Michaelis-Menten equation. **(C)** schematic representation of the kinetic mechanism for aerobic respiration on soluble iron as catalyzed by intact *M. sedula*. The *cross-hatched* and *solid spheres* represent archaea that contain oxidized and iron-reduced electron transport proteins, respectively. **(D)** dependence of the initial velocity of ferric ion production on the concentration of ferrous ions when 5.7×10^8 cells of mixotrophically-grown *M. sedula* were included in 8 mL of sulfuric acid (pH 1.5) at 60°C. The parameters for the *solid curve* drawn through the data points were determined by a nonlinear regression analysis using the Michaelis-Menten equation amended to include substrate inhibition. Each *datum* in **(B, D)** represents the mean and standard deviation of 4 determinations. The parameters for the *dashed curve* omitted the term in the equation that represented the effect of the substrate inhibition.

sedula cells was limited to that of a catalyst compared with the concentrations of reduced iron and molecular oxygen, aerobic respiration on soluble iron proceeds kinetically in a manner that was consistent with the Michaelis-Menten formalism.

Time courses analogous to those shown in Figure 4A were also obtained when 5.7×10^8 cells of *M. sedula* that were cultured mixotrophically were mixed with different concentrations of ferrous ions and monitored over time at 60°C (primary data not shown). The resulting secondary plot of initial velocities vs. the concentration of reduced iron is shown in Figure 4D. These intact cells also exhibited kinetic behavior that was consistent with the Michaelis-Menten formalism, but with an added deviation. The initial velocity of iron oxidation increased with increasing concentrations of soluble iron up to a point, but the initial velocity then began to decline in value as the concentration of soluble iron increased even further. The *solid curve* drawn through the *data points* in Figure 4D represents the nonlinear regression fit of the data to a velocity equation that represents substrate inhibition (Reed et al., 2010):

$$v_0 = V_{\max}(S)/(K_M + (S) + \frac{(S)^2}{K_I}) \quad (1)$$

where v_0 is the initial velocity and K_I is the equilibrium dissociation constant for the substrate inhibition. Values for K_M, V_{max}, and K_I of 104 ± 13 μM, 190 ± 18 nmoles/min, and 6.3 ± 1.6 mM, respectively, were obtained from the analysis. The *dashed curve* in Figure 4D represents the initial velocity curve that would have been obtained had there been no substrate inhibition. The uninhibited maximum velocity of 190 nmoles/min corresponds to a turnover number of 333 ± 31 attamoles/cell/min. Interestingly, depending on the degree of substrate inhibition that might occur in nature, the effective turnover number per cell is essentially unaffected by whether soluble iron was present at substrate level concentrations in the growth medium. Consequently, the kinetic data are consistent with the hypothesis that the ability to respire aerobically on soluble iron is expressed constitutively in *M. sedula*.

4 Discussion

The original impetus for these studies was to distinguish between two hypotheses: that the respiratory proteins that are responsible for iron oxidation are expressed constitutively; or that the respiratory proteins that are responsible for iron

oxidation are induced when the cells are exposed to substrate-level concentrations of soluble iron. The turnover numbers for respiratory iron oxidation that were determined for cells of *M. sedula* that were cultured in the presence or the absence of soluble reduced iron were within experimental error of each other, an observation that is consistent with the hypothesis that the respiratory proteins that are responsible for iron oxidation are expressed constitutively. Determination of these turnover numbers necessarily required that the intact cells that comprised the catalytic units in these studies had to be quantified with as much accuracy as was possible. The efforts to quantify the intact cells led to the unexpected observations regarding cell sizes that comprise the bulk of the studies presented herein.

Planktonic microorganisms that are cultured from a single clone exhibit a narrow range of sizes and volumes, ranging from smaller, newly-formed "daughter" cells to larger cells that are ready to divide into two daughter cells. This range is typically represented by a log-normal distribution when the cell numbers are plotted as a function of the computed diameter of the cell. That is the behavior that we observed when *M. sedula* was cultured heterotrophically on yeast extract (Figures 1A, 2A). It is generally reported that populations of certain microorganisms can adopt different sizes (Taheri-Araghi et al., 2015; Westfall and Levin, 2017) and even shapes (Young, 2006) when they are cultured on different substrates. The average volume of individual cells within a clonal population generally increases in those cells that are exposed to richer nutrients in the environment or decreases if the cells are exposed to fewer nutrients (Harris and Theriot, 2016, 2018; Taheri-Araghi et al., 2015; Westfall and Levin, 2017). However, that generality applies to the entire population of cells, not to a subset of the population. When *M. sedula* was cultured mixotrophically on yeast extract plus 20 mM ferrous ions, which represents a richer nutritional environment than just yeast extract alone, a reasonable hypothesis was that the average volume of the *M. sedula* cells might increase somewhat. Instead, the population of cells bifurcated into two sizes, one larger and one smaller than that obtained when the cells were cultured on yeast extract in the absence of soluble iron (Figures 1B, 2B, 3). There is little, if any, precedent in the microbiological literature for this surprising observation.

One hypothesis that might account for the two cell sizes that appear when *M. sedula* is cultured under a particular set of solution conditions is that the culture of *M. sedula* is actually contaminated with one or more other microorganisms. Over forty years ago, several laboratories reported that selected cultures of mesophilic, iron-oxidizing, acidophilic eubacteria, known collectively as "*Thiobacillus*" or "*Ferrobacillus*" *ferrooxidans*, could be cultured in successive media that alternated between strictly autotrophic soluble ferrous ions and strictly heterotrophic glucose or some related organic substrate (Shafia et al., 1972; Tabita and Lundgren, 1971; Tuovinen and Nicholas, 1977). In each case, the origins of these growth characteristics were traced to the presence of acidophilic, heterotrophic microorganisms that contaminated the autotrophic iron-oxidizing cultures (Harrison et al., 1980; Johnson and Kelso, 1983; Lobos et al., 1986). It was postulated that the heterotrophic contaminant could survive on a sparce diet of organic materials that either "leaked" from or were transported out of the chemolithotroph that was fixing carbon dioxide into cellular material. So is that sort of scenario an explanation for the unexpected culture behavior reported herein? Was the culture of *M. sedula* in our laboratory contaminated with a slightly smaller thermoacidophilic, coccoidal microorganism whose numbers increased to rival those of the *M. sedula* under certain culture conditions? That hypothesis was not consistent with the 16S rRNA sequencing studies summarized above.

Once we accept the premise that clonal *M. sedula* does indeed bifurcate into roughly equal numbers of two cell sizes when soluble ferrous ions are added to complex organic nutrients in the external medium, then the next question becomes, "Why?" Any rationalization for this unexpected behavior is more speculative at this point than hypothesis-driven. The appearance and existence of a large cell size cohort in a culture medium that was amended with additional nutrients (soluble ferrous ions, in this case) is entirely consistent with published observations conducted on numerous other microorganisms in numerous different culture media. The appearance and existence of a small cell size cohort under the same conditions is not. Where would *M. sedula* encounter high concentrations of soluble reduced iron in its natural habitat? Probably in the close proximity of iron-bearing reduced metal-sulfide minerals such as pyrite, marcasite, arsenopyrite, chalcopyrite, *etc*. Would there be a selective advantage to becoming smaller in the presence of electron-rich solid minerals that could serve as a source of electrons to support aerobic respiration? Perhaps. Unpolished minerals rarely present smooth surfaces at their interfaces with liquid media. Rather, minerals in the rough present irregular surfaces that contain numerous small crevices, cracks, invaginations, and so on. A smaller coccoidal microorganism would enjoy greater access to a larger percentage of the irregular surface area of the uneven mineral than would a larger coccoidal microorganism. The greater the physical contact between the surface of the microorganism and the surface of the rough, semi-conducting mineral solid, the greater is the opportunity for direct electron transfer from one entity to the other. Alternatively, if all of the mineral oxidation occurs *via* an indirect mechanism where the soluble iron serves as the mobile agent to conduct electrons from the surface of the mineral to the plasma membrane of the *M. sedula*, then maximizing the microorganism's proximity to the uneven mineral surface by becoming smaller is still a selective advantage because fewer soluble ferrous ions have the opportunity to diffuse away from the nearby microorganism and be "lost." So why would only a portion of the entire population of planktonic cells transform into a smaller size when the entire population encountered high levels of soluble iron in the medium?

The advent over the last 20 years of methods for quantifying gene expression in individual microbial cells has revealed that populations of genetically identical cells derived from a single clone nonetheless exhibit phenotypic heterogeneity where certain genes are expressed in a non-uniform manner within the population (Ackermann, 2015; Lidstrom and Konopka, 2010; Martins and Locke, 2015; Roberfroid et al., 2016). Consequently, if extracellular environmental conditions change abruptly and unpredictably, at least a small portion of the isogenic population is already pre-adapted and poised to cope with some aspect of the ever-fluctuating environment. On the one hand, this phenotypic heterogeneity may put some or many cells at a disadvantage because they have expressed proteins and capabilities that remain unused and are thus a waste of precious resources at that moment. On the other hand, this practice also means that at least a small portion of the population of cells are in a better position to respond

rapidly to the changing conditions and thereby perpetuate the species. "Bistability" is a term that has been used to represent this phenomenon of the bifurcation of an isogenic population of cells into distinct subpopulations (Dubnau and Losick, 2006).

We hypothesize that the bifurcation of *M. sedula* into two cell sizes is an example of phenotypic heterogeneity that is triggered by exposure of the cells to higher concentrations of soluble ferrous ions. If higher concentrations of soluble iron are indeed harbingers of impending proximity to a rich source of electrons derived from semi-conducting, iron-bearing mineral sulfides with uneven surfaces, then that prospect represents a selective advantage to promote the adaptation of the cells to a smaller size. Interestingly, we have observed that *Sulfobacillus thermosulfidooxidans*, a Gram-negative, moderately thermophilic eubacterium, also appears to exist in two different sizes when it is cultured mixotrophically on yeast extract and soluble iron (unpublished data). We hypothesize that populations of other iron-oxidizing microorganisms that can grow both mixotrophically and heterotrophically may also exhibit analogous size differences when they are cultured on organic media in the absence and presence of soluble iron. Perhaps such size differences exist in many iron-oxidizing acidophiles, but they have heretofore escaped notice because researchers have not specifically looked for them. It will be interesting to see whether other examples of this unexpected behavior appear in the future.

Data availability statement

The datasets presented in this study can be found in online repositories. The names of the repository/repositories and accession number(s) can be found here: https://massive.ucsd.edu/ProteoSAFe/dataset.jsp?task=d034f9f6fddc4877bf305c7479181017, MSV000095146, and https://osf.io/4v62d/.

Author contributions

RB: Conceptualization, Funding acquisition, Investigation, Project administration, Supervision, Writing – original draft. RP: Investigation, Supervision, Writing – review & editing. NP: Investigation, Writing – review & editing. OG: Investigation, Writing – review & editing. BW: Writing – review & editing. RW: Investigation, Writing – review & editing.

Funding

The author(s) declare that financial support was received for the research and/or publication of this article. This work was supported by grant number 2100950 from the National Science Foundation (RB).

Conflict of interest

The authors declare that the research was conducted in the absence of any commercial or financial relationships that could be construed as a potential conflict of interest.

The author(s) declared that they were an editorial board member of Frontiers, at the time of submission. This had no impact on the peer review process and the final decision.

Publisher's note

Supplementary material

The Supplementary Material for this article can be found online at: https://www.frontiersin.org/articles/10.3389/fmicb.2025.1455423/full#supplementary-material

References

Ackermann, M. A. (2015). Functional perspective on phenotypic heterogeneity in microorganisms. *Nat. Rev. Microbiol.* 13, 497–508. doi: 10.1038/nrmicro3491

Auernik, K. S., and Kelly, R. M. (2008). Identification of components of electron transport chains in the extremely thermoacidophilic crenarchaeon *Metallosphaera sedula* through iron and sulfur compound oxidation transcriptomes. *Appl. Environ. Microbiol.* 74, 7723–7732. doi: 10.1128/AEM.01545-08

Auernik, K. S., Maezato, Y., Blum, P. H., and Kelly, R. M. (2008). The genome sequence of the metal-mobilizing, extremely thermoacidophilic archaeon *Metallosphaera sedula* provides insights into bioleaching-associated metabolism. *Appl. Environ. Microbiol.* 74, 682–692. doi: 10.1128/AEM.02019-07

Barr, D. W., Ingledew, W. J., and Norris, P. R. (1990). Respiratory chain components of iron-oxidizing acidophilic bacteria. *FEMS Microbiology Let.* 70, 85–89. doi: 10.1111/j.1574-6968.1990.tb03781.x

Bathe, S., and Norris, P. R. (2007). Ferrous iron- and sulfur-induced genes in *Sulfolobus metallicus*. *Appl. Environ. Microbiol.* 73, 2491–2497. doi: 10.1128/AEM.02589-06

Blake II, R. C., Anthony, M. D., Bates, J. D., Hudson, T., Hunter, K. M., et al. (2016). *In situ* spectroscopy reveals that microorganisms in different phyla use different electron transfer biomolecules to respire aerobically on soluble iron. *Front. Microbiol.* 7:1962. doi: 10.3389/fmicb.2016.01963

Blake II, R. C., and Griff, M.N. (2012). *In situ* spectroscopy on intact *Leptospirillum ferrooxidans* reveals that reduced cytochrome 579 is an obligatory intermediate in the aerobic iron respiratory chain. *Front. Microbiol.* 3:136. doi: 10.3389/fmicb.2012.00136

Blake II, R. C., Guidry, J. J., Anthony, M. D., Ban, B., Smith, K. A., et al. (2020). Oxidation of cytochrome 605 is the rate-limiting step when *Ferrimicrobium acidiphilum* respires aerobically on soluble iron. *Appl. Environ. Microbiol.* 86, e01906–e01920. doi: 10.1128/AEM.01906-20

Blake II, R. C., Nautiyal, A., Smith, K. A., Walton, N. N., Pendleton, B., et al. (2021). *Ferrimicrobium acidiphilum* exchanges electrons with a platinum electrode *via* a cytochrome with reduced absorbance maxima at 448 and 605 nm. *Front. Microbiol.* 12:7051. doi: 10.3389/fmicb.2021.705187

Blake II, R. C., Shute, E. A., Greenwood, M. M., Spencer, G. H., and Ingledew, W.J. (1993). Enzymes of aerobic respiration on iron. *FEMS Microbiol. Rev.* 11, 9–18. doi: 10.1111/j.1574-6976.1993.tb00261.x

Blake II, R. C., and White III, R.A. (2020). *In situ* absorbance measurements: a new means to study respiratory electron transfer in chemolithotrophic

microorganisms. *Adv. Microb. Physiol.* 76, 81–127. doi: 10.1016/bs.ampbs.2020.01.003

Callahan, B. J., McMurdie, P. J., Rosen, M. J., Han, A. W., Johnson, A. J., and Holmes, S. P. (2016). DADA2: high resolution sample inference from illumina amplicon data. *Nat. Methods* 13: 581–583. doi: 10.1038/nmeth.3869

Counts, J. A., Vitko, N. P., and Kelly, R. M. (2022). Fox cluster determinants for iron biooxidation in the extremely thermoacidophilic sulfolobaceae. *Environ. Microbiol.* 24, 850–865. doi: 10.1111/1462-2920.15727

DeSa, R. J., and Matheson, I. B. C. (2004). A practical approach to interpretation of singular value decomposition results. *Methods Enzymol.* 384: 1–8. doi: 10.1016/S0076-6879(04)84001-1

Dubnau, D., and Losick, R. (2006). Bistability in bacteria. *Mol. Microbiol.* 61, 564–572. doi: 10.1111/j.1365-2958.2006.05249.x

Fry, E. S., Kattawar, G. W., Strycker, B. D., and Zhai, P. W. (2010). Equivalent path lengths in an integrating cavity: comment. *Appl. Opt.* 49, 575–577. doi: 10.1364/AO.49.000575

Fuchs, T., Huber, H., Burggraf, S., and Stetter, K. O. (1996). 16S rDNA-based phylogeny of the archaeal order sulfolobales and reclassification of *Desulfurolobus ambivalens* as *Acidianus ambivalens* comb. nov. *Syst. Appl. Microbiol.* 19, 56–60. doi: 10.1016/S0723-2020(96)80009-9

Fuchs, T., Huber, H., Teiner, K., Burggraf, S., and Stetter, K. O. (1995). Metallosphaera prunae, sp. nov., a novel metal-mobilizing, thermoacidophilic archaeum, isolated from a uranium mine in Germany. *System. Appl. Microbiol.* 18, 560–566. doi: 10.1016/S0723-2020(11)80416-9

Harris, L. K., and Theriot, J. A. (2016). Relative rates of surface and volume synthesis set bacterial cell size. *Cell* 165, 1479–1492. doi: 10.1016/j.cell.2016.05.045

Harris, L. K., and Theriot, J. A. (2018). Surface area to volume ratio: a natural variable for bacterial morphogenesis. *Trends Microbiol.* 26, 815–832. doi: 10.1016/j.tim.2018.04.008

Harrison, Jr. A. P., Jarvis, B. W., and Johnson, J. (1980). Heterotrophic bacteria from cultures of autotrophic *Thiobacillus ferrooxidans*: relationships as studied by means of deoxyribonucleic acid homology. *J. Bacteriol.* 143, 448–454. doi: 10.1128/jb.143.1.448-454.1980

He, Z. G., Zhong, H., and Li, Y. (2004). Acidianus tengchongensis sp. nov., a new species of acidothermophilic archaeon isolated from an acidothermal spring. *Curr. Microbiol.* 48, 159–163. doi: 10.1007/s00284-003-4155-9

Hemp, J., and Gennis, R. B. (2008). Diversity of the heme–copper superfamily in archaea: insights from genomics and structural modeling. *Results Probl. Cell Differ.* 45, 1–31. doi: 10.1007/400_2007_046

Huber, G., Spinnler, C., Gambacorta, A., and Stetter, K. O. (1989). *Metallosphaera sedula* gen. and sp. nov. represents a new genus of aerobic, metal-mobilizing, thermoacidophilic archaebacteria. *System. Appl. Microbiol.* 12, 38–47. doi: 10.1016/S0723-2020(89)80038-4

Huber, G., and Stetter, K. O. (1991). Sulfolobus metallicus, sp. nov., a novel strictly chemolithoautotrophic thermophilic archaeal species of metal-mobilizers. *Syst. Appl. Microbiol.* 14, 372–378. doi: 10.1016/S0723-2020(11)80312-7

Huber, H., and Stetter, K. O. (2015). "*Metallosphaera*," In *Bergey's Manual of Systematics of Archaea and Bacteria* Eds. M. E. Trujillo, S. Dedysh, P. DeVos, B. Hedlund, P. Kämpfer, F. A. Rainey and W. B. Whitman (Hoboken, NJ: Wiley).

Itoh, T., Miura, T., Sakai, H. D., Kato, S., Ohkuma, M., and Takashina, T. (2020). *Sulfuracidifex tepidarius* gen. nov., sp. nov. and transfer of *Sulfolobus metallicus* Huber and Stetter 1992 to the genus *Sulfuracidifex* as *Sulfuracidifex metallicus* comb. nov. *Int. J. Syst. Evol. Microbiol.* 70, 1837–1842. doi: 10.1099/ijsem.0.003981

Johnson, D. B., and Kelso, W. I. (1983). Detection of heterotrophic contaminants in cultures of *Thiobacillus ferrooxidans* and their elimination by subculturing in media containing copper sulphate. *J. Gen. Microbiol.* 129, 2969–2972. doi: 10.1099/00221287-129-9-2969

Johnson, T. B., Mach, C., Grove, R., Kelly, R., Van Cott, K., and Blum, P. (2018). Secretion and fusion of biogeochemically active archaeal membrane vesicles. *Geobiology* 16, 659–673. doi: 10.1111/gbi.12306

Kozubal, M. A., Dlakic, M., Macur, R. E., and Inskeep, W. P. (2011). Terminal oxidase diversity and function in *"Metallosphaera yellowstonensis"*: gene expression and protein modeling suggest mechanisms of Fe(II) oxidation in the Sulfolobales. *Appl. Environ. Microbiol.* 77, 1844–1853. doi: 10.1128/AEM.01646-10

Kurosawa, N. (2003). Reclassification of *Sulfolobus hakonensis* Takayanagi *et al.* 1966 as *Metallosphaera hakonensis* comb. nov. based on phylogenetic evidence and DNA G+C content. *Int. J. Syst. Evol. Microbiol.* 53, 1607–1608. doi: 10.1099/ijs.0.02716-0

Kurosawa, N., Itoh, Y. H., Iwai, T., Sugai, A., Uda, I., Kimura, N., et al. (1998). Sulfurisphaera ohwakuensis gen. *nov., sp. nov.*, a novel extremely thermophilic acidophile of the order Sulfolobales. *Int. J. Syst. Bacteriol.* 48, 451–456. doi: 10.1099/00207713-48-2-451

Lewis, A. M., Recalde, A., Brasen, C., Counts, J. A., Nussbaum, P., Bost, J., et al. (2021). The biology of thermoacidophilic archaea from the order *Sulfolobales*. *FEMS Microbiol. Rev.* 45, 1–60. doi: 10.1093/femsre/fuaa063

Li, T. F., Painter, R. G., Ban, B., and Blake II, R. C. (2015). The multi-center aerobic iron respiratory chain of *Acidithiobacillus ferrooxidans* functions as an ensemble with a single macroscopic rate constant. *J. Biol. Chem.* 290, 18293–18303. doi: 10.1074/jbc.M115.657551

Lidstrom, M., and Konopka, M. (2010). The role of physiological heterogeneity in microbial population nov., and acidothermophilic archaeon isolated from a hot spring behavior. *Nat. Chem. Biol.* 6, 705–712. doi: 10.1038/nchembio.436

Liu, J., Cvirkaite-Krupovic, V., Commere, P. H., Yang, Y., Zhou, F., Forterre, P., et al. (2021). Archaeal extracellular vesicles are produced in an ESCRT-dependent manner and promote gene transfer and nutrient cycling in extreme environments. *ISME J.* 15, 2892–2905. doi: 10.1038/s41396-021-00984-0

Liu, L. J., Jiang, Z., Wang, P., Qin, Y. L., Xu, W., Wang, Y., et al. (2021). Physiology, taxonomy, and sulfur metabolism of the Sulfolobales, an order of thermoacidophilic archaea. *Front. Microbiol.* 12:768283. doi: 10.3389/fmicb.2021.768283

Liu, L. J., You, X. Y., Guo, X., Liu, S. J., and Jiang, C. Y. (2011). Metallosphaera cuprina sp. nov., an acidothermophilic, metal-mobilizing archaeon. *Int. J. Syst. Evol. Microbiol.* 61, 2395–2400. doi: 10.1099/ijs.0.026591-0

Lobos, J. H., Chisolm, T. E., Bopp, L. H., and Holmes, D. S. (1986). Acidiphilium organovorum sp. nov., an acidophilic heterotroph isolated from a Thiobacillus ferrooxidans culture. *Int. J. Syst. Evol. Microbiol.* 36, 139–144. doi: 10.1099/00207713-36-2-139

Martins, B. M., and Locke, J. C. (2015). Microbial individuality: how single-cell heterogeneity enables population level strategies. *Curr. Opin. Microbiol.* 24, 104–112. doi: 10.1016/j.mib.2015.01.003

Peng, T. J., Liu, L. J., Liu, C., Yang, Z. F., Liu, S. J., and Jiang, C. Y. (2015). Metallosphaera tengchongensis sp.. *Int. J. Syst. Evol. Microbiol.* 65, 537–542. doi: 10.1099/ijs.0.070870-0

Plumb, J. J., Haddad, C. M., Gibson, J. A. E., and Franzmann, P. D. (2007). Acidianus sulfidivorans sp. nov., an extremely acidophilic, thermophilic archaeon isolated from a solfatata on Lihir Island, Papua New Guinea, and emendation of the genus description. *Int. J. Syst. Evol. Microbiol.* 57, 1418–1423. doi: 10.1099/ijs.0.64846-0

Reed, M. C., Lieb, A., and Nijhout, H. F. (2010). The biological significance of substrate inhibition: a mechanism with diverse functions. *Bioessays* 32, 422–429. doi: 10.1002/bies.200900167

Roberfroid, S., Vanderleyden, J., and Steenackers, H. (2016). Gene expression variability in clonal populations: causes and consequences. *Crit. Rev. Microbiol.* 42, 969–984. doi: 10.3109/1040841X.2015.1122571

Sakai, H. D., and Kurosawa, N. (2017). Sulfodiicoccus acidiphilus gen. nov., sp. nov., a sulfur-inhibited thermoacidophilic archaeon belonging to the order Sulfolobales isolated from a terrestrial acidic hot spring. *Int. J. Syst. Evol. Microbiol.* 67, 1880–1886. doi: 10.1099/ijsem.0.001881

Segerer, A., Neuner, A., Kristjansson, J. K., and Stetter, K. O. (1986). Acidianus infernus gen. nov., sp. nov., and Acidianus brierleyi comb. nov.: facultatively aerobic, extremely acidophilic thermophilic sulfur-metatolizinb archaebacteria. *Int. J. Syst. Evol. Microbiol.* 36, 559–564. doi: 10.1099/00207713-36-4-559

Shafia, F., Brinson, K. R., Heinzman, M. W., and Brady, J. M. (1972). Transition of chemolithotroph *Ferrobacillus ferrooxidans* to obligate organotrophy and metabolic capabilities of glucose-grown cells. *J. of Bacteriol.* 111, 56–65. doi: 10.1128/jb.111.1.56-65.1972

Sousa, F. L., Alves, R. J., Pereira-Leal, J. B., Teixeira, M., and Pereira, M. M. (2011). A bioinformatics classifier and database for heme-copper oxygen reductases. *PLoS One* 6, e19117. doi: 10.1371/journal.pone.0019117

Suzuki, T., Iwasaki, T., Uzawa, T., Hara, K., Nemoto, N., Kon, T., et al. (2002). *Sulfolobus tokodaii* sp. nov. (f. *Sulfolobus* sp. strain 7), a new member of the genus *Sulfolobus* isolated from Beppu Hot Springs, Japan. *Extremophiles* 6, 39–44. doi: 10.1007/s007920100221

Tabita, R., and Lundgren, D. G. (1971). Heterotrophic metabolism of the chemolithotroph *Thiobacillus ferrooxidans*. *J. Bacteriol.* 108, 334–342. doi: 10.1128/jb.108.1.334-342.1971

Taheri-Araghi, S., Bradde, S., Sauls, J. T., Hill, N. S., Levin, P. A., Paulsson, J., et al. (2015). Cell-size control and homeostasis in bacteria. *Curr. Biol.* 25, 385–391. doi: 10.1016/j.cub.2014.12.009

Tsuboi, K., Sakai, H. D., Nur, N., Stedman, K. M., Kurosawa, N., and Suwanto, A. (2018). *Sulfurisphaera javensis* sp. nov., a hyperthermophilic and acidophilic archaeon isolated from Indonesian hot spring, and reclassification of *Sulfolobus tokodaii* Suzuki et al., 2002 as *Sulfurisphaera tokodaii* comb. nov. *Int. J. Syst. Evol. Microbiol.* 68, 1907–1913. doi: 10.1099/ijsem.0.002765

Tuovinen, O. H., and Nicholas, D. J. D. (1977). Transition of *Thiobacillus ferrooxidans* KG-4 from heterotrophic growth on glucose to autotrophic growth on ferrous-iron. *Arch. Microbiol.* 114, 193–195. doi: 10.1007/BF00410784

Urbieta, M. S., Rascovan, N., Vazquez, M. P., and Donati, E. (2017). Genomic analysis of the thermoacidophilic archaeon *Acidianus copahuensis* focusing on

the metabolisms associated to biomining activities. *BMC Genomics* 18, 1–14. doi: 10.1186/s12864-017-3828-x

Westfall, C. S., and Levin, P. A. (2017). Bacterial cell size: multifactorial and multifaceted. *Annu. Rev. of Microbiol.* 71, 499–517. doi: 10.1146/annurev-micro-090816-093803

Woese, C. R. (1987). Bacterial evolution. *Microbiol Rev.* 51, 221–271. doi: 10.1128/mr.51.2.221-271.1987

Woese, C. R., and Fox, G. E. (1977). Phylogenetic structure of the prokaryotic domain: the primary kingdoms. *Proc. Natl. Acad. Sci. U.S.A.* 74, 5088–5090. doi: 10.1073/pnas.74.11.5088

Woese, C. R., Kandler, O., and Wheelis, M. L. (1990). Towards a natural system of organisms: proposal for the domains Archaea, Bacteria, and Eucarya. *Proc. Natl. Acad. Sci. U.S.A.* 87, 4576–4579. doi: 10.1073/pnas.87.12.4576

Yoshida, N., Nakasato, M., Ohmura, N., Ando, A., Saiki, H., Ishii, M., et al. (2006). *Acidianus manzaensis* sp. nov., a novel thermoacidophilic archaeon growing autotrophically by the oxidation of H_2 with the reduction of Fe^{3+}. *Curr. Microbiol.* 53, 406–411. doi: 10.1007/s00284-006-0151-1

Young, K. D. (2006). The selective value of bacterial shape. *MMBR* 70, 660–703. doi: 10.1128/MMBR.00001-06

Frontiers in Microbiology

Explores the habitable world and the potential of microbial life

The largest and most cited microbiology journal which advances our understanding of the role microbes play in addressing global challenges such as healthcare, food security, and climate change.

Discover the latest Research Topics

See more →

Frontiers

Avenue du Tribunal-Fédéral 34
1005 Lausanne, Switzerland
frontiersin.org

Contact us

+41 (0)21 510 17 00
frontiersin.org/about/contact